2017

Static and Dynamic Analysis of Manually Post-Tensioned Timber Rocking Frames with Conical Disc Springs

Safwan Waheed Jaafar Al-Subaihawi
Lehigh University

Static and Dynamic Analysis of Manually Post-Tensioned Timber Rocking Frames with Conical Disc Springs

by

Safwan Waheed Jaafar Al-Subaihawi

A Thesis

Presented to the Graduate and Research Committee

of Lehigh University

In Candidacy for the Degree of

Master of Science

in

Structural Engineering

Lehigh University

May 2017

This thesis is accepted and approved in partial fulfilment of the requirement for the Master of Science.

_____

Date

_____

Dr. Stephen Pessiki

Thesis Advisor

_____

Dr. Panayiotis Diplas

Chairperson of Departme

TABLE OF CONTENTS

LIST OF FIGURES

LIST OF TABLES

ABSTRACT

This research proposes a new low damage seismic resistant system that implements a manual post-tensioning procedure by inserting a spring element at the post-tensioning steel anchorage. This system is aimed at the following: (1) eliminate the need for specialized post-tensioning equipment and the associated highly trained workers required in the construction of the conventional rocking systems; and, (2) promote more sustainable seismic systems by combing with renewable materials.

This report derives a set of closed form expressions that provide a useful tool for understanding the behavior of the proposed system. Also, it develops a finite element model to capture the response of the system under static pushover loads. The report also conducts an extensive parametric study using the closed form expressions and the finite element model to understand the effects of certain parameters on the lateral displacement response of the proposed system. These parameters are: (1) the axial stiffness of the spring element; (2) the length of the rocking frame; (3) the initial stress of the post-tensioning steel; and, (4) the height of the post-tensioning steel. The results of this parametric study show that the closed form expressions display an excellent agreement with the finite element results. Also, even though a rocking timber frame has constant member dimensions and post-tensioning steel area, connecting the post-tensioning steel in series with a flexible spring element could significantly increase the drift capacity of the rocking frame.

This report also develops a finite element model to capture the response of the proposed system under actually recorded ground motions. Several prototype frames were subjected to 22-pair ground motions, and the results of different prototype frames were plotted and

compared. The results show that even though significant ground shakes are applied to the prototype frames, the residual post-tensioning force after the earthquake of frames having flexible spring element is always more than other frames with no spring element. In fact, the frames with flexible spring elements never experienced yielding in any of the ground shakes in this study, while some frames with stiff spring element experienced significant yielding. It was also noticed from the dynamic analyses that the moment hysteresis loop for frames with flexible spring element is likely to be flat after the frame decompression (i.e. no moment increase), while the hysteresis loop of frames with stiff spring element is steeper (moment increases) under the same circumstances.

CHAPTER 1

INTRODUCTION

Conventional lateral force resistant systems subjected to high-intensity seismic loads are designed to dissipate energy and reach significant drift by damage through inelastic deformation. Figure 1-a shows a reinforced concrete wall, which is a conventional lateral force resistant system subjected to a cyclic lateral load that could develop during earthquakes. The lateral load causes the wall to deform laterally and increases the stress at the reinforcing bars and concrete. The increased stress causes cracking of the concrete in tension, yielding of the reinforcing bars, and softening of the concrete in compression. The force-deformation response of the wall indicates that the wall encountered damage by inelastic deformations that are difficult and challenging to repair.

Lehigh University has been working on developing low damage lateral force resistant systems that accomplish the goal of providing large drift capacity and reducing the permanent lateral displacements after extreme events. Figure 1-b shows a scheme of the unbonded post-tensioned walls (also called rocking concrete walls) that were investigated by Lehigh University (Kurama 1997, Perez 2004, Srivastava 2013, and chancellor 2014). The idea is to use post-tensioning steel to provide re-centering force, besides introducing a gap opening mechanism at the base of the wall. Under the normal operation of the building, the clamping force of the post-tensioning (PT) bars provides compression at the base, and thus the gap at the base is closed. However, extreme seismic loads could overcome the clamping force of the PT bars leading to the gap opening and softening of the wall. When

the seismic loads are removed, the PT force will bring back the wall to its original position, and this is the reason it is called self-centering system.

Recent work has been emphasizing the use bonded mild steel that crosses the gap at the base of the wall to provide the energy dissipation mechanism as shown in Figure 1-c. The PT steel is still unbonded and expected to give the self-centering force, but the mild steel is bonded and supposed to yield under extreme seismic loads.

Figure 1.2 shows the time history response of the three systems shown in Figure 1.1. While the conventional reinforced concrete wall is shown to have residual drift by the end of the earthquake, the self-centering systems undergo limited residual drift since the PT steel recentres the system. However, the self-centering system with mild steel has shown to reach lower peak response because of the damping provided by yielding of the mild steel.

The goal of this report is to introduce a simple lateral force resistant system that implements a manual post-tensioning procedure as shown in Figures 1.3 and 1.4. This system would eliminate the need for specialized post-tensioning equipment and the associated highly trained workers. The idea is to introduce a spring element that is connected in series with the PT bar aimed to facilitate the manual post-tensioning process. Moreover, another goal is to combine with renewable materials to make more sustainable seismic systems (Pessiki, 2017).

1.1 OBJECTIVE

The objective of this research is to investigate the lateral force behavior of the unbonded post-tensioned rocking frames with disc springs at the PT bar anchorage under static and dynamic loads.

1.2 APPROACH

The research approach was comprised of the following 5 tasks:

1. Derive closed-form expressions (CFE) that describe the key stages in the response under lateral loads. This will provide a useful tool to understand the behavior of the system.
2. Develop a finite element model (FE) model to capture the response under static pushover loads. Open SEES (Mazzoni et al., 2006) is used to develop the FE model. Then, the model is used to conduct a parametric study to understand the effects of certain parameters on the response.
3. Conduct a parametric study and compare the results of the CFE and the FE. This would be helpful in verifying the CFE's results.
4. Develop an FE model for dynamic analyses using actually recorded ground motions.
5. Analyze the response of the system to a set of ground motions.

1.3 ORGANIZATION OF REPORT

The report has the following organization: Chapter 2 provides the background information about the rocking systems, the usage of the disc springs and their behavior under loads. Chapter 3 discusses the derivation of the closed-form expressions to predict the backbone curve. Chapter 4 develops the FE model to capture the response under static pushover loads. Chapter 5 discusses the prototype building used in this study. Chapter 6 compares the results of the CFE and the FE. Chapter 7 conducts the dynamic analysis of the proposed system under a set of ground motions. Chapter 8 provides the summary and conclusions and outlines future research needs.

1.4 NOTATION

The following notation is used in this report:

a_1 = stiffness proportional damping coefficient

a_o = mass proportional damping coefficient

A_{p1} = area of the post-tensioning (PT) steel at location 1

A_{p2} = area of the post-tensioning (PT) steel at location 2

DEC = limit state correlated with the decompression of the frame base

Ep = elastic modulus of the PT steel

F_C = force required to bring the spring stack to its flat position

FC = limit state at clamping of the spring stack

Fn = normal force at the coulomb friction damper

FP = limit state at fracture of PT steel

F_{p1i} = initial stress of PT group 1

F_{p2i} = initial stress of PT group 2

F_{pu} = ultimate strength of the PT steel

F_{py} = yielding strength of the PT steel

F_{sl} = loading force on the hysteresis loop of the spring stack

F_{su} = unloading force on the hysteresis loop of the spring stack

H_f = height of the frame

ho = height of the disc spring

H_{unb} = unbonded length of the post-tensioning steel

Kbar = axial stiffness of PT bar

$Kbar^T$ = axial stiffness of PT bar based on the tangent stiffness

K_{c1} = axial stiffness of PT group 1

K_{c2} = axial stiffness of PT group 2

Keff = effective stiffness of the assembly (spring stack plus PT bar in series)

K_s = stiffness of spring stack

K_{s1} = stiffness of the spring stack at PT group 1

K_{s2} = stiffness of the spring stack at PT group 2

Ksp = stiffness of spring stack

L_{c1} = length of the spring stack at fully flat position at location 1

L_{c2} = length of the spring stack at fully flat position at location 2

L_f = length of the frame

LLP = limit state where PT steel yielded

L_{o1} = height of the unloaded spring stack at location 1

L_{o2} = height of the unloaded spring stack at location 2

L_{p1} = distance from right side of the frame to the first PT group

L_{p2} = distance from the right side of the frame to the second PT group

L_{s1} = measured height of the 1st spring stack when lateral load is applied

L_{s1o} = measured height of the 1st spring stack (no lateral load is applied)

L_{s2} = measured length of the 2nd spring stack when lateral load is applied

L_{s2o} = measured length of the 2nd spring stack (no lateral load is applied)

M_{dec} = moment at the frame base at decompression

M_{FC} = moment at the frame base when the spring stack clamps

M_{FP} = moment at the frame base when the PT steel fractures

M_{LLP} = moment at the frame base when the PT steel yields

N = gravity loads applied to the frame

n1 = number of springs in parallel at first PT group

n2 = numb of springs in parallel at the second PT group

t = thickness of the disc spring

T_{p1i} = initial force at PT group 1

T_{p1u} = force at fracture of PT group 1

T_{p1y} = force at yielding of PT group 1

T_{p2i} = initial force at PT group 2

T_{p2u} = force at fracture of PT group 2

T_{p2y} = force at yielding of PT group 2

u = displacement of the spring stack under compression load

V_{dec} = base shear at the DEC limit state

V_{FC} = base shear at the FC limit state

V_{FP} = base shear at the FP limit state

V_{LLP} = base shear at the LLP limit state

W = structure weight used in seismic calculations

Θ_{dec} = drift at the DEC limit

Θ_{FC} = drift at the FC limit

Θ_{FP} = drift at the FP limit

Θ_{LLP} = drift at the LLP limit

γ_k = relative stiffness of the spring stack

Δ_{DEC} = roof displacement at the DEC limit

Δ_{FC} = roof displacement at the FC limit

Δ_{FP} = roof displacement at the FP limit

Δ_{LLP} = roof displacement at the LLP limit

ΔT_{p1} = change in PT force due to the applied loads (PT group 1)

ΔT_{p2} = change in PT force due to the applied loads (PT group 2)

Δ_{v1} = gap height under of PT group 1

Δ_{v2} = gap height under of PT group 2

ε_{pu} = strain of PT steel at the fracture

ε_{py} = strain of PT steel at the yielding

μm = coefficient of friction between the contact faces of the disc springs

μr = coefficient of friction at the contact face of the applied load

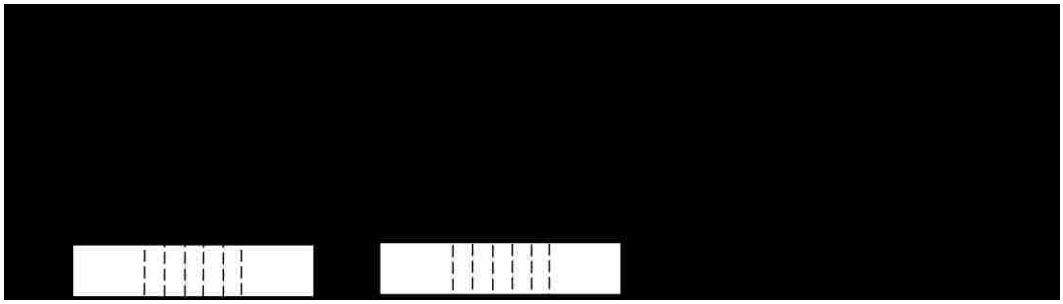

(a): ACI complaint cast in place shear wall

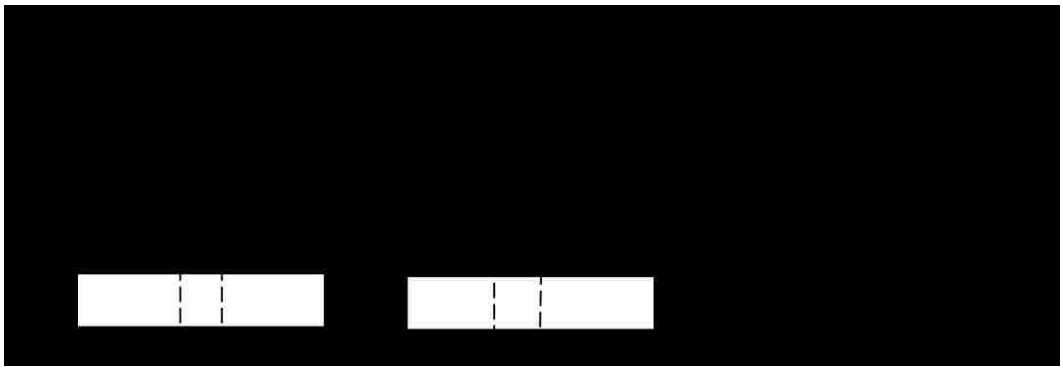

(b): Unbonded post-tensioned precast concrete wall

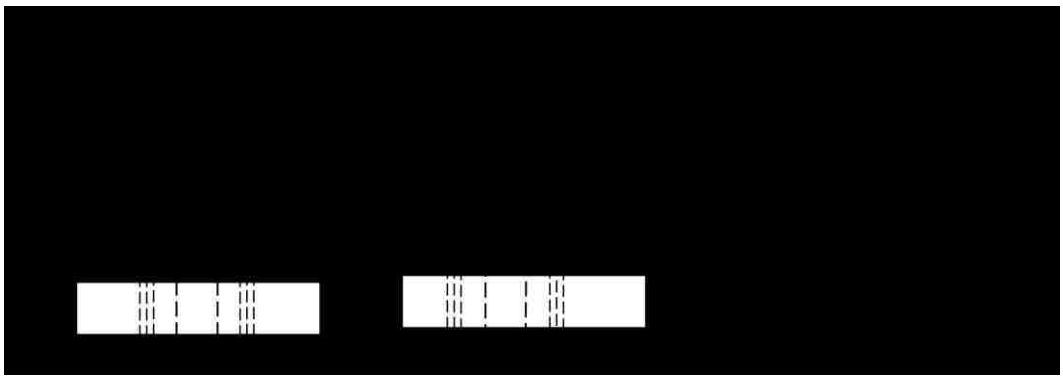

(c): Unbonded post tensioned precast concrete wall with mild steel

Figure 1.1: Walls under lateral load (Srivastava, 2013).

Figure 1.2: Idealized time history response of different walls.

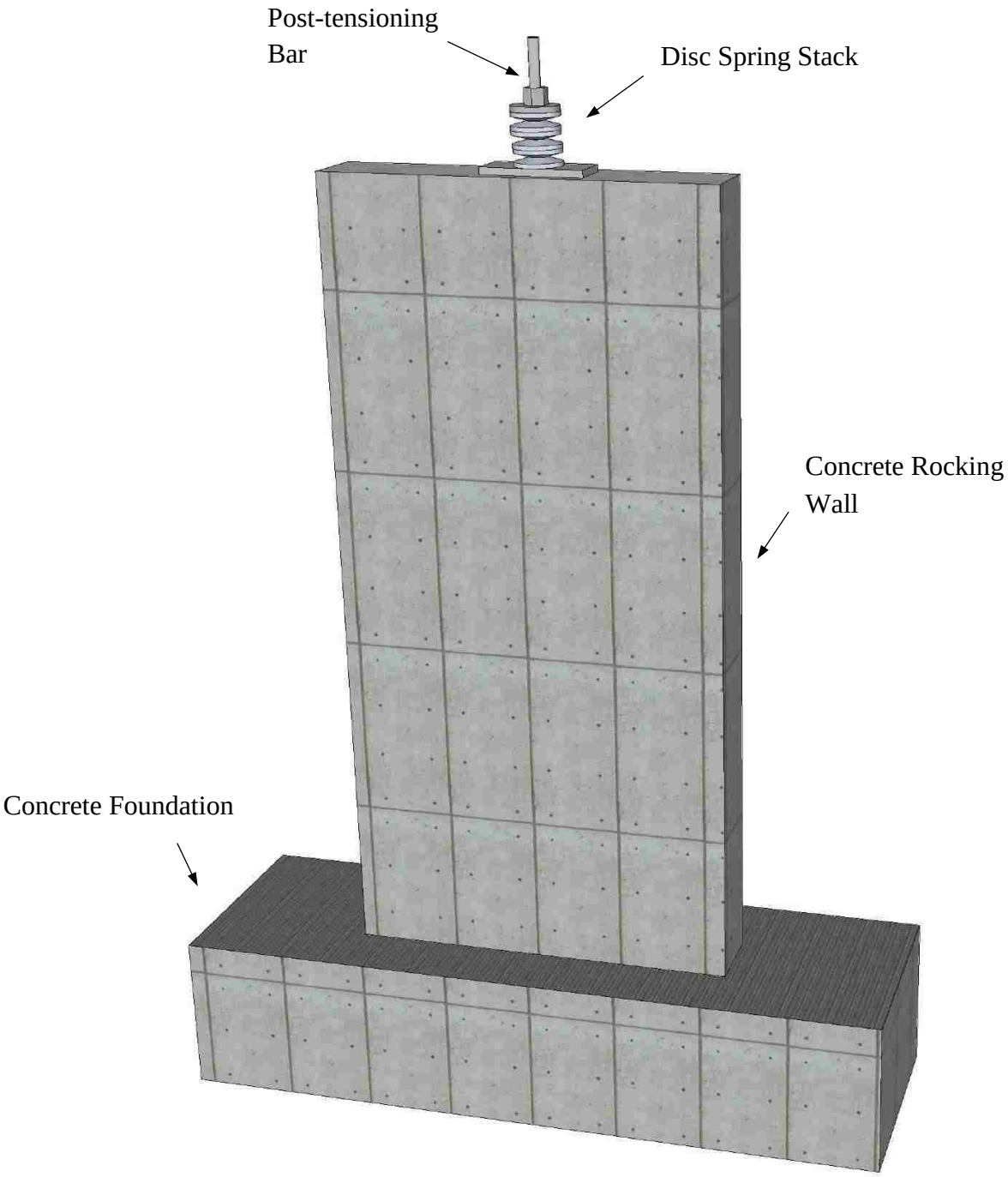

Figure 1.3: Proposed concept for a concrete rocking wall.

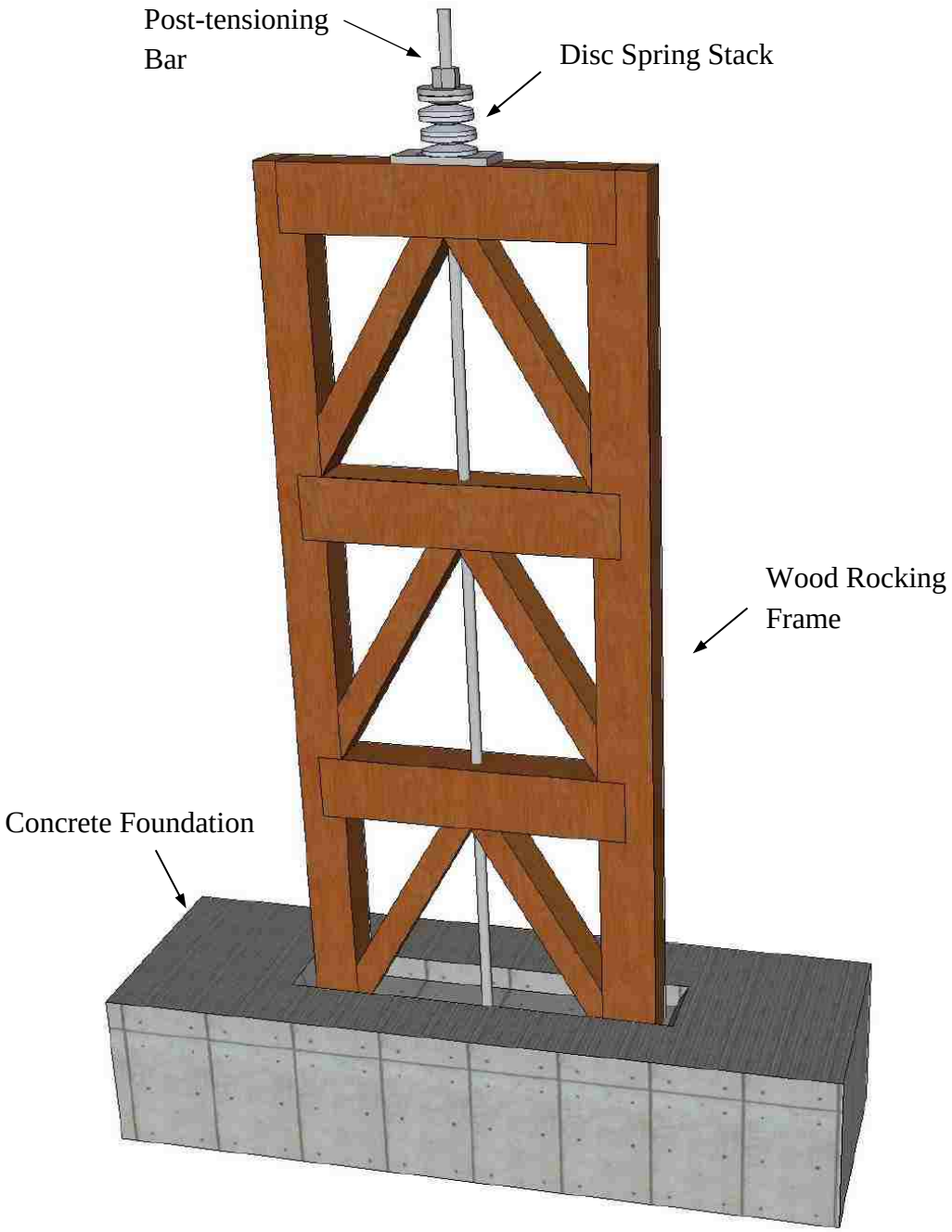

Figure 1.4: Proposed concept for a wood rocking frame.

CHAPTER 2

BACKGROUND

2.1 INTRODUCTION

This chapter presents the background information on the relevant topics. The chapter starts with a description of the rocking systems and their behavior. After that, the chapter discusses the work that has been conducted on self-centering timber systems. Finally, the chapter ends with a description of the behavior of the disc springs followed by the definition of the expected limit states used in this report.

2.2 UPT LATERAL FORCE RESISTANT SYSTEMS

2.2.1 General behavior of conventional lateral force resistant systems

The goal of seismic design is to offer life safety of the occupants and to prevent the collapse of the structure. Hence, designing the building to remain elastic during severe earthquakes could be uneconomical.

Buildings subjected to severe earthquakes are expected to develop large seismic forces that can cause damage and residual drift. Usually, damage and residual drift need expensive and challenging repairs, but the time required to perform these repairs might affect the business and the occupants of the building, which further increases the loss.

2.2.2 Wall systems

2.2.2.1 Concrete

Figure 2.1 shows a conventional reinforced concrete wall. The construction process of the wall starts by placing deformed bars and casting concrete. The service load is applied to the wall when the hardening of the concrete occurs. Note that in this case the longitudinal steel is bonded to the surrounding concrete because bars are deformable, and thus offer full interaction with the concrete. The longitudinal steel is confined with stirrups to resist shear forces on the wall.

Figure 2.1 also shows the cyclic overturning moment versus roof drift of a conventional concrete wall. Under small lateral load, the wall is deforming elastically and is expected to go back to its original straight position. However, once the lateral load is increased, the wall behaves in non-linear manner due to three reasons: (1) cracking of the concrete in the tension side; (2) yielding of the PT steel; (3) crushing of the concrete in the compression side. Note that the wall could have significant drift and energy dissipation capacities, but damage to the wall provides that drift and energy disspation. This damage could be expensive and challenging to repair, adding to that the downtime needed to get the damage fixed.

Figure 2.1: Conventional concrete wall (Srivastava, 2013).

Designing these conventional concrete shear walls to remain elastic under extreme seismic hazards might be possible, yet it is impractical due to the associated cost of over design.

2.2.2.2 Masonry walls

Masonary walls are built by bonding brick or block units using cement mortar. The primary goal of external masonry walls is to offer shelter for the occupants from the outside weather, while the internal walls are often used to partition the available space. Load bearing walls carry loads from the upper floors in addition to their weight, and they can also carry lateral loads. The cyclic force displacement history for a brick wall is tested as shown in Figure 2.2-a, and the hysteresis loop is shown in Figure 2.2-b. The masonry wall could have several failure modes under the applied lateral load (Naraine and Sinha 1989), including: (1) failure of the brick-mortar interface; (2) cracking of the brick.

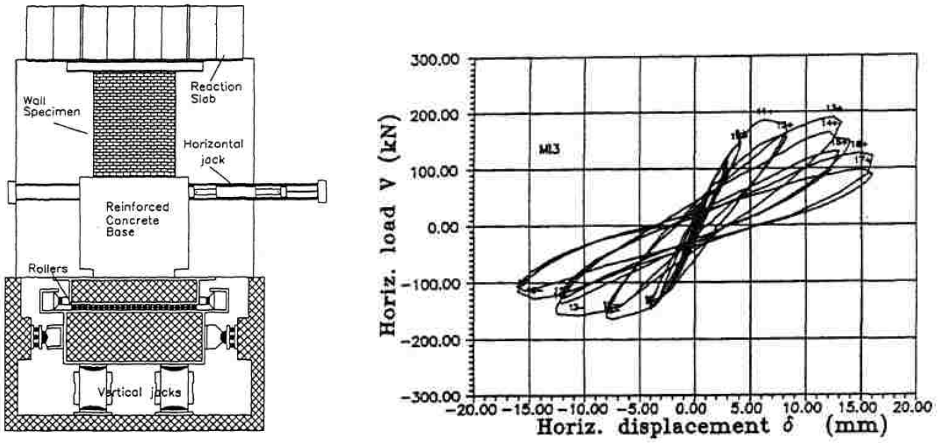

Figure 2.2: Masonry wall: (a) Test setup; (b) Hysteresis loop of the wall (Naraine and Sinha 1989).

2.2.2.3 CLT walls

Cross-laminated timber (CLT) walls are used more widely in recent years because of their favorable weight to strength ratio, and their ductile behavior that could be achieved by proper design of connections, fasteners, and joints (Ceccotti et al. 2013).

CLT walls subjected to lateral force could deform in several ways (Gavric et al. 2014): (1) vertical uplifting of the panel (rocking); (2) horizontal slipping; and, (3) shear and bending deformations as seen in Figure 2.3. When the applied load is increased, the wall could uplift and rotate as a rigid body. Also, the shear and bending deformations may vary depending on the dimensions of the wall and the intensity of the applied load. Since the wall is held down by mechanical connections, fasteners, angles, etc., slipping could happen if these elements have little lateral stiffness.

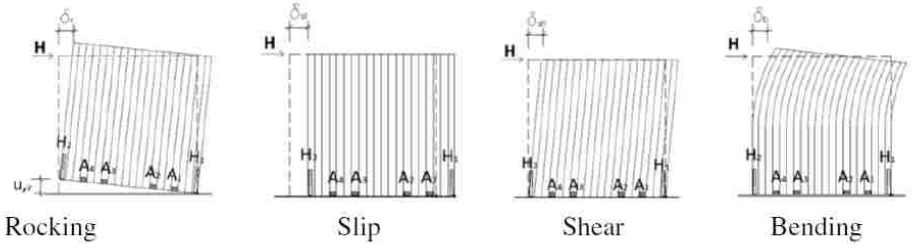

Figure 2.3: Deflection components of CLT panels (Gavric et al. 2014).

Figure 2.4 shows the lateral force-displacement response of CLT walls. Gavric et al. mentioned that the first wall has lateral displacement dominated by the rocking part, and it failed by excessive uplifting and crushing of the compression side of the wall. This wall demonstrates the self-centering behavior. The second wall has lateral displacement dominated by a combination of rocking and sliding, and it failed by the increased lateral force causing yielding of the mechanical fasteners. The third wall has lateral displacement

dominated by the sliding, and but it failed by the shear failure of angle bracket connector. Noted that the panel is not expected to return to its original position for two reasons: (1) the damage to the mechanical connection is not recoverable; and, (2) it is likely that the CLT is expected to undergo nonlinear response (i.e. permanent deformations), and thus it suffers permanent deformation. This is the same problem with the conventional concrete shear walls where extreme lateral loads could cause damage and residual drift. In the next section, a new type of lateral force resistant systems that implement self-centering and elastic-softening mechanisms to reduce damage and residual drift are reviewed.

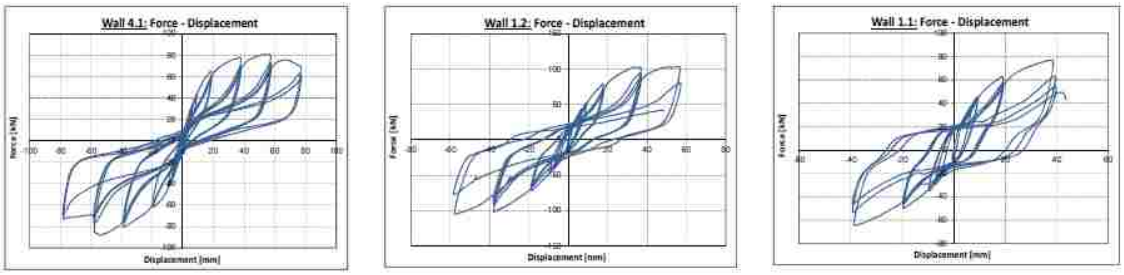

Figure 2.4: Force-lateral displacement response of a CLT panel: (a) Rocking; (b) Rocking and sliding; (c) Sliding (Gavric et al. 2014).

2.2.3 Rocking frame systems

Conventional lateral force resistant systems such as concrete shear walls and braced steel frames are expected to be damaged by severe earthquakes. This was the motivation of several researchers in Lehigh University to investigate low damage lateral force resistant systems that accomplish the following goals (Chancellor et al. 2014):

1. Reduce damage under severe earthquakes;

2. Provide a gap opening mechanism to assure softening of the systems and thus limit the increase in the lateral force under large lateral loads;

3. Utilize PT force to re-center the building after the ground motion and reduce the residual drift;

4. Flexibility in integrating several energy dissipation devices that could be replaced easily after the earthquake.

three systems were investigated in the literature: First, the unbonded post-tensioned precast concrete walls (Perez et al. 2004). Second, the self-centering rocking steel frames (Chancellor 2014). Third, the self-centering timber walls (Sarti et al. 2016) A review of these three systems is presented in the next sections.

2.2.3.1 Concrete rocking wall systems

The concrete rocking wall systems achieve two goals (Perez et al. 2004): (1) implement self-centering mechanism to bring back the wall to its vertical position and reduce the residual drift. This is achieved by integrating post tensioning (PT) steel that is placed in ducts (i.e. to remain unbonded to the concrete) inside the concrete wall and extended from the foundation and usually to the roof. Note that when the wall is displaced laterally, the PT steel will return the wall to its original vertical position, but this assumes that the PT steel is still elastic as yielding could reduce this recentering force. The PT steel is usually designed to still be elastic during the design based earthquake; and, (2) offer elastic-softening mechanism under extreme loads by placing a gap at the base of the wall during the construction stage of the wall. The PT steel causes a clamping force to the wall (i.e. the

gap is closed) during service loads and the usual operation of the building. However, during extreme events, the lateral forces could overcome this clamping force and lead to the gap opening at the base and softening of the system. Note that the lateral stiffness of the wall is expected to reduce after the gap opening (softening mechanism) and this could control the seismic loads that develop in the system.

Figure 2.5-a shows a scheme of the unbonded post-tensioned concrete walls, and Figure 2.5-b shows the typical backbone curve.

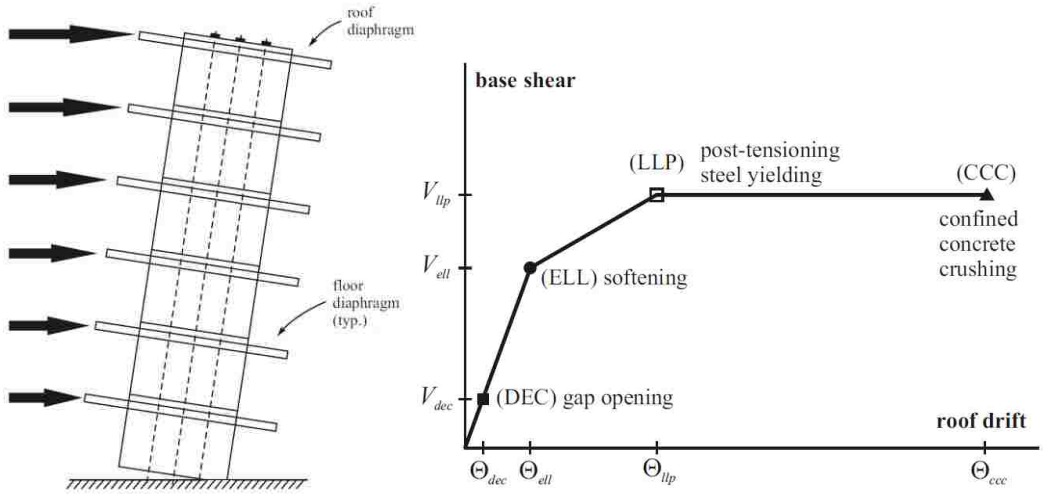

Figure 2.5: (a) Unbonded post tensioned precast concrete wall scheme; (b) Idealized base shear-lateral drift curve (Perez et al., 2004).

2.2.3.2 Steel rocking frame

According to Chancellor (2014) steel rocking frames are meant to reduce damage under severe earthquakes with little or no residual drift. In an analogous manner to the unbonded post-tensioned concrete walls, the rocking steel frames use PT steel to provide self-

centering force. However, the columns at the base of the rocking frame are capable of uplifting to assure the elastic-softening mechanism as shown in Figure 2.6.

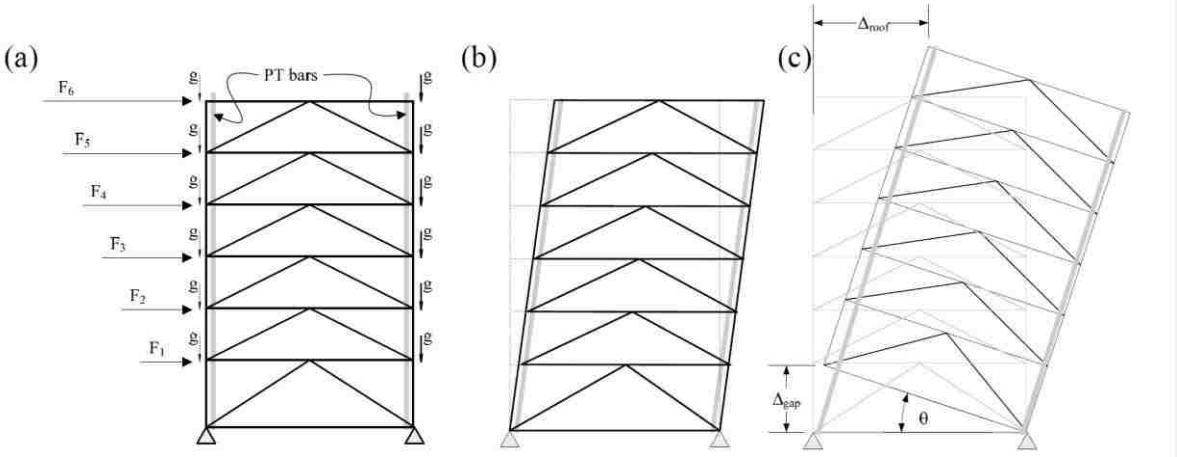

Figure 2.6: Steel rocking frame: (a) load and configuration; (b) elastic displacement before the gap opening; (c) gap opening mechanism (Sause et al. 2010).

Note that the post-tensioning force is causing a clamping force onto the gap under each column. Thus, the lateral deformations in this stage are elastic, and the frame works like the traditional braced frames under the normal operation of the building. Under severe earthquakes, the lateral force developed could overcome the clamping force at the base of the frame leading to opening of the gap at the base of the frame and softening of the systems. Note that the system could go back to its original position by the help of the PT steel. An idealized overturning moment versus roof drift curve of the steel rocking frames is shown in Figure 2.7 and includes the expected limit states.

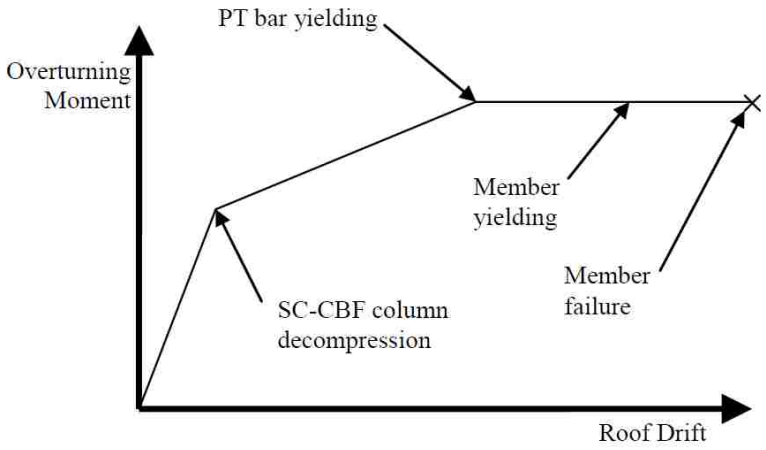

Figure 2.7: Idealized overturning moment vs. roof drift steel rocking frame systems (Nathen et al. 2014).

2.2.3.3 Timber self-centering systems

The use of the self-centering systems made of timber is enabled with the introduction of new products like the Glued Laminated Timber (Glulam) and the Laminated Veneer Lumber (LVL) (Sarti, Palermo, and Pampanin 2016a). These engineering wood products provide substantial resistance to compression loads developed during the post-tensioning process (Sarti, Palermo, and Pampanin 2016a). Figure 2.8 shows examples of timber structures that implement a self-centering system.

In the literature, the performance of self-centering timber walls has been investigated by (Sarti, Palermo, and Pampanin 2016a). The study included two third scale wall specimen under cyclic pushover loads as shown in Figure 2.9. The results of this test revealed that the wall could resist the design loads with little damage.

Figure 2.8: Implementation of wood self-centering systems (Sarti, Palermo, and Pampanin 2016a).

Figure 2.9: Test set up as reported by (Sarti et al. 2016).

2.3 DISC SPRINGS

A key component in this research is the inclusion of disc springs in the post-tensioning steel anchorage. This section reviews the properties of disc springs.

2.3.1 Axial Behavior

Figure 2.10-a shows a disc spring stack assembled from a series of discs around a central pin. Figure 2.10-b shows a single conical disc spring and illustrates the geometric properties. The outside diameter of the disc spring is OD while the inside diameter is ID. The thickness is t, total height is H, and the clear height is ho.

The geometry of the conical disc spring determines its force deformation response. For example, the force deformation response of the spring stack is not always linear as shown in Figure 2.11. Indeed, the shape of the response depends on the ratio of the height of the

spring ho to the thickness of the disc t. As ho/t becomes small, the response is nearly linear but the response becomes nonlinear as the ratio ho/t gets larger as shown in Figure 2.11.

Figure 2.10: Disc spring (Spirol 2017, Shigley, J. E., & Mischke, C. R. 1996).

Figure 2.11: Force deformation of a single disc spring (adapted from Shigley, J. E., & Mischke, C. R. 1996).

Disc springs provide designers with a flexible way to attain various force-deformation responses by combining multiple springs differently (Schnorr, 2003). For instance, an assembly of two or more disc springs could be arranged in many ways as shown in Figure 2.12. Disc springs could be stacked in parallel, series or a combination of both leading to a different force-deformation response as shown in Figure 2.13. We can see that the first case in Figure 2.12 has four disc springs stacked in parallel. As shown in Figure 2.13, this lead to increase in the loading capacity of the stack by four times over a single spring, but the deformation capacity (travel capacity) remains the same as a single spring. On the other hand, the second case in Figure 2.12 is having four disc springs stacked in series. As shown in Figure 2.13, the load capacity remains the same as for a single spring, but the travel capacity increased four times over that of a single spring. Lastly, the last case in Figure 2.12 shows that it is possible to arrange disc springs in a combination of series and parallel.

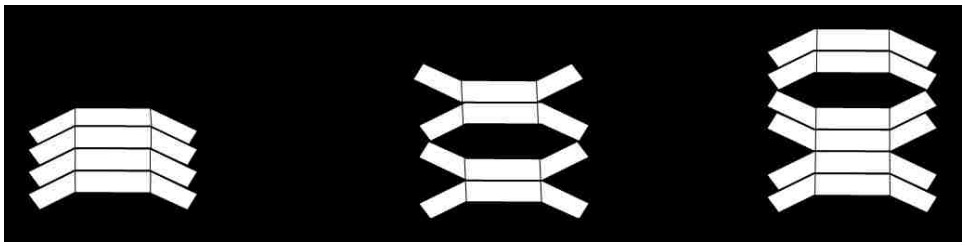

Figure 2.12: Different stack arrangement (adapted from Schnorr, 2003).

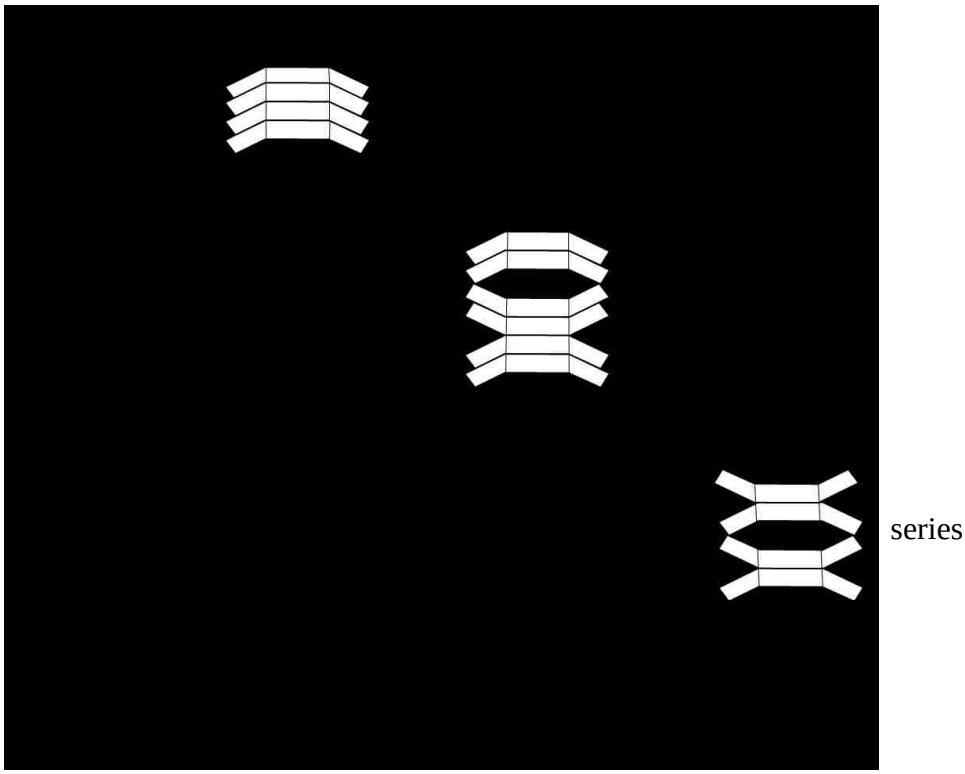

Figure 2.13: Force deformation of different spring stack arrangement (adapted from Schnorr, 2003).

2.3.2 Hysteresis behavior of the disc springs

Figure 2.14 shows the hysteresis loop of a disc spring stack. Three main sources of energy dissipation are causing this hysteretic behavior (Schnorr, 2003). First, friction of the disc springs with the supporting surface. Second, internal friction between the disc springs. Third, the energy dissipated by the disc springs material itself. It worth mentioning that the DIN 2092 standards give a range for the friction coefficients of these springs.

According to (Schnorr, 2003), the area of the hysteretic loop is proportional to the number of disc springs stacked in parallel. This could be explained by the increase of area subjected

to friction as the disc springs deform under the load. However, the applications where energy dissipation from friction is not wanted, disc springs are usually lubricated to reduce this friction in the mechanical application (Schnorr, 2003). Maintenance of this lubricant in long term applications envisioned in this research may not be necessary since friction may be beneficial.

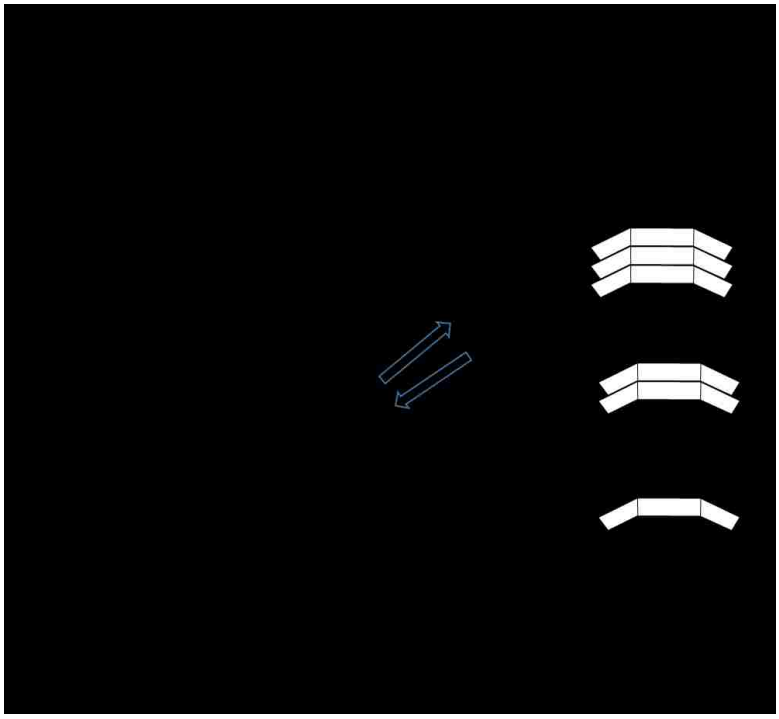

Figure 2.14: Hysteretic behavior of the disc spring stack (adapted from Schnorr, 2003).

2.3.3 Effects of springs on the pre-stressing loss

The use of disc springs to reduce the post tensioning (PT) loss was investigated in a project to rehabilitate a small wooden bridge in Ontario (Accorsi and Sarisley 1990). Disc springs were placed between the side of the bridge and the anchorage plate as shown in Figures

2.15 and 2.16. Then, rods were subjected to PT force causing the wooden deck to creep, and the reduction in the PT force with time was measured.

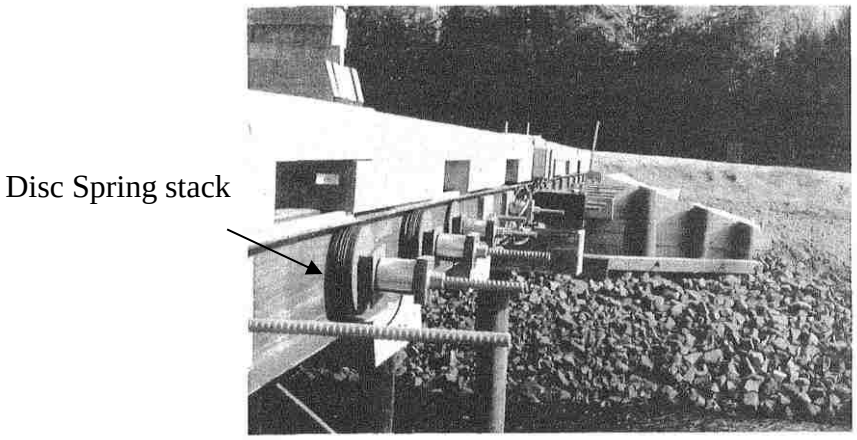

(a): Test set up

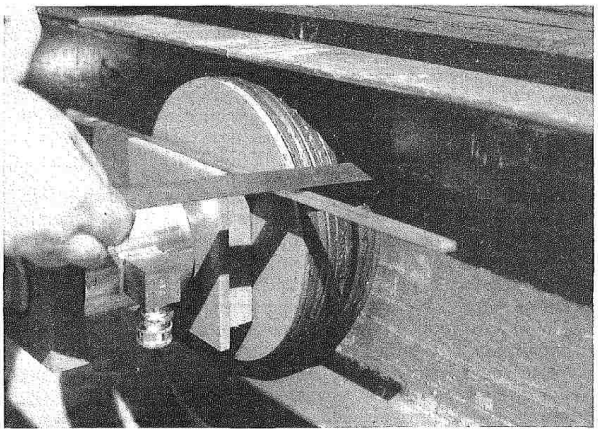

(b): Measuring the PT force

Figure 2.15: Disc spring stack and rods assembly (Accorsi and Sarisley 1990).

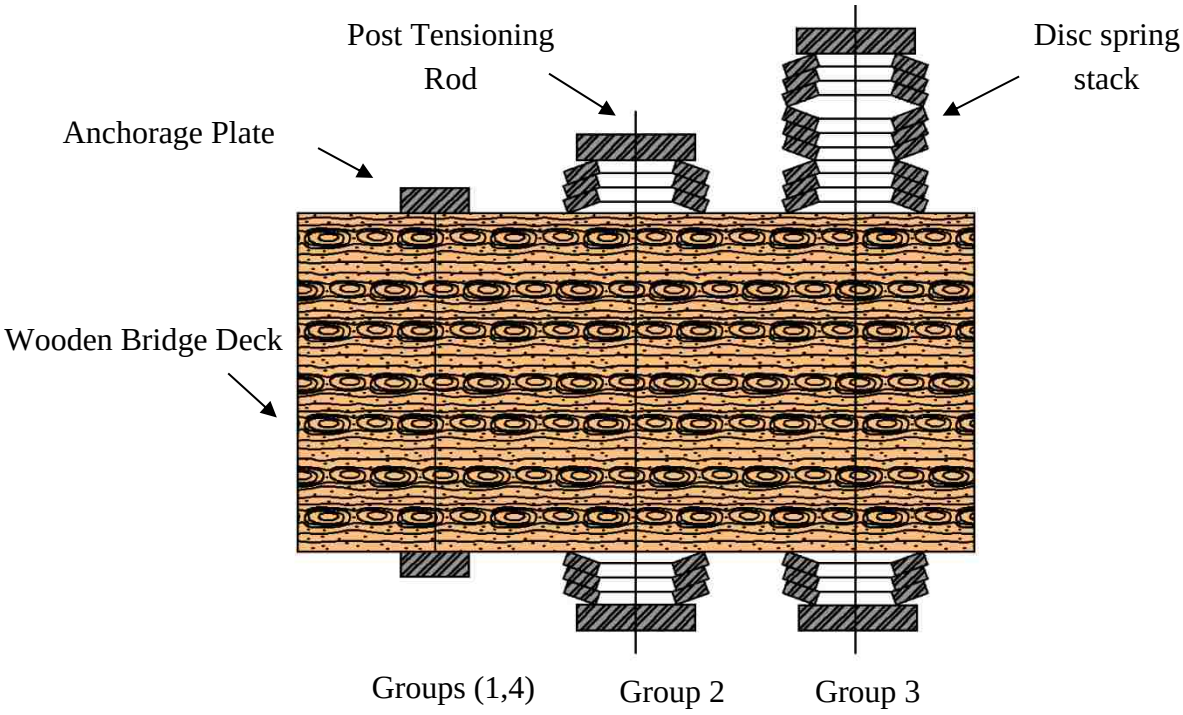

Figure 2.16: Test setup (Accorsi and Sarisley 1990)

To evaluate the influence of the disc spring stack, Accorsi et al. included four scenarios as shown in Table 2.1. The first case had no springs. The second case had 6 springs (three in parallel and two in series). The third case had 12 springs (three in parallel and four in series). The last case had no springs, but a small initial PT force.

Table 2.1: Types of assemblies.

Group	Description
1	Regular (no springs)
2	6 springs
3	12 springs
4	No springs (small force)

.

Figure 2.17 presents the results of this experiment. The results show that the third group had the least drop in PT force with time, while the first group had the largest. The author

mentions that the third group had the lowest PT loss since it had the lowest effective stiffness due to the attribute of the disc spring stack (Accorsi and Sarisley 1990).

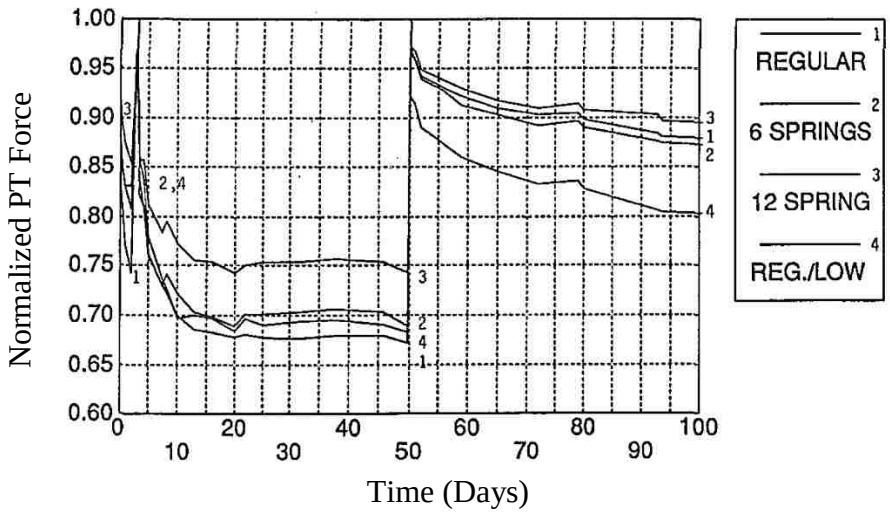

Figure 2.17: Averaged and normalized PT force (Accorsi and Sarisley 1990).

The experiment described above suggests that the proposed system shown in Figure 1.4 will experience the same phenomena leading to alleviation of PT loss with time. This would make it possible to implement various types of wood in the construction of the proposed system.

2.4 EXPECTED LIMIT STATES

Rocking frames exhibit several limit states under the action of lateral force. However, the discussion of these limit states in this report is limited to what is needed to keep the text focused. Four limit states are considered in this report as shown in Figure 2.18:

1. Decompression of the base (DEC);

2. Full clamping of the spring stack (FC);

3. Linear limit of post-tensioning steel (LLP);

4. Fracture of PT steel (FP).

Figure 2.18: Expected limit states.

2.4.1 Decompression (DEC)

The base of the rocking frame is expected to be in compression due to axial force from two sources. First, the gravity loads are collected by the columns down to the foundation leading to compression force at the base of the frame. Second, the force from the prestressing bars also causes compression at the base because it follows the same load path as the gravity loads.

We define the DEC as the state where the reaction at the extreme side of the frame becomes zero. The base shear and the drift at this state limit are denoted by $V_{dec}, and\ \Theta_{dec}$.

2.4.2 Linear limit of post tensioning steel (LLP)

As more lateral load is applied to the frame, not only the does gap at the base of the frame open, but the force at the PT bars is mostly expected to increase. The force at the PT bars could reach the yield stress (F_{py}) of the PT bars.

Accordingly, we can define the LLP as the state where the PT bars have reached their yield stress (F_{py}). The base shear and the drift are denoted by $V_{LLP}\ , and\ \Theta_{LLP}$ at this limit state.

2.4.3 Fracture of PT steel (FP)

After yielding of the PT bars, the force at the PT bars could increase, and more stress is developed due to the strain hardening of the PT steel. However, the steel has finite travel capacity, and as a result, PT bars could fracture.

For this reason, we define the FP as the state where the PT bars have reached their fracture stress (F_{pu}). The base shear and the drift are denoted by $V_{FP}, and\ \Theta_{FP}$ at this state limit.

2.4.4 Full clamping of spring stack (FC)

Full clamping of the spring stack, if it occurs, could happen between any of the previous state limits. This is considered in developing the closed expressions as will be shown later in the next chapter.

The full clamping of the spring stack (FC) limit state is defined as the state where the spring stack has reached its maximum travel capacity, and the surfaces of adjacent disc springs come into full contact and no more deformation is possible. The base shear the drift are denoted by $V_{FC}, and\ \Theta_{FC}$ at this limit state.

2.5 SUMMARY

1. Disc springs provide a flexible way to attain various force-deformation responses by combining multiple springs differently.
2. The literature shows that using a spring element connected in series with the PT bars could reduce the PT loss associated with time dependent deformations like creep and shrinkage.

CHAPTER 3

DERIVATION OF CLOSED FORM EXPRESSIONS

3.1 INTRODUCTION

This chapter develops closed form expressions to describe the key stages in the force deformation response of rocking frames with disc springs. These closed form expressions provide a useful tool to understand the behavior of the proposed system. These closed form expressions are also used to check the validity of the FEA response in Chapter 6

In deriving these closed form expressions (CFE), several assumptions were made:

1. The frame is considered rigid;
2. Sliding at the base of the frame does not occur;
3. Frame has symmetric post-tensioning (PT) bars and spring stack layouts;
4. PT bars are unbonded, deformable, and have a bilinear stress-strain relation as shown in Figure 3.1;
5. PT force does not change before the decompression of the frame base;
6. Friction between the disc springs is neglected;
7. The clamped spring stack undergoes no further deformation as shown in Figure 3.2;
8. Stability failure of the frame does not occur.

The derivations of the closed form expressions are presented for two cases: The first case is where the PT bars are expected to yield and fracture before the spring stack fully

compresses and thus has no more travel capacity; and the second case is where the PT bars are expected to yield after the spring stack fully compresses.

3.2 EXPECTED LIMIT STATES

The proposed system exhibits four limit states as shown in Figures 3.3 and 3.4. These four limit states represent the key stages in the response that the frame is expected to encounter under the action of quasi-static pushover loads. It is important to note that these limit states are for a frame that was treated as a rigid body for simplicity, and we would expect more limit states to be considered if we have an elastic frame instead. These four limit states are discussed more in detail in Chapter 2.

3.3 PUSHOVER CURVES

Figures 3.3 and 3.4 show idealizations of the most likely cases of the pushover curve of the proposed system. Note that the LLP and FP limit states have tag numbers 1 or 2. Limit states that end with 1 (i.e. LLP-1 and FP-1 shown in Figure 3.3) refer to the first case where the spring stack does not clamp, while limit states that end with 2 (i.e. LLP-2 and FP-2 shown in Figure 3.4) refer to the second case where the spring stack clamps. However, the DEC limit state does not have a tag number because it is not affected by the clamping of the spring stack. As Figures 3.3 and 3.4 show, the spring stack clamping governs the shape of the pushover curve.

In the first case illustrated in Figure 3.3, the first limit state reached in the frame is decompression DEC. Then, the force at the PT bars increases and reaches yielding LLP-1. Afterward, the PT bar reaches its maximum travel capacity and fractures FP-1. Note that the spring stack does not fully clamp in this first case.

In the second case shown in Figure 3.4, the first limit state reached in the frame is decompression DEC. Then, the spring stack reaches its maximum travel capacity FC. Afterward, yielding of the PT bar LLP-2 is followed by fracture FP-2. In this second case, the spring stack reaches it maximum travel capacity between the DEC and the LLP-2 limit states.

3.4 DEVELOPMENT OF CLOSED FORM EXPRESSIONS

A set of closed form expressions (CFE) is derived here to describe the backbone curve of the two cases explained in Section 3.3. Figure 3.5 presents the geometry notations used in the upcoming equations. In this figure, H_{unb} refers to the length of the PT bar, H_f is the height of the frame, L_{p1} and L_{p2} are the distance from the right support to the location of the first and second PT bars respectively, L_f is the length of the frame, L_{s10} and L_{s2o} refer to the initial height of the disc spring stack at locations 1 and 2.

Figure 3.6 illustrates the forces and the corresponding deformations. Δ_{v1} and Δ_{v2} are the height of the gap under the first and the second PT bars. Θ is the drift and Δ is the roof displacement. L_{s1} and L_{s2} are the height of the disc spring stacks at locations 1 and 2. V is the base shear and N is the gravity load. T_{p1} and T_{p2} are the axial forces of the PT bars at

locations 1 and 2. The derivation of the CFE follows the assumptions mentioned at the beginning of this chapter.

3.4.1 Decompression (DEC)

The frame is expected to behave in an elastic manner at normal load levels. However, at larger loads, the gap at the base of the frame opens leading to a reduction in the lateral stiffness of the frame (Sause et al. 2010). Closed form expressions are derived in this section to predict the behavior of the DEC limit state. The following steps show the derivation process.

We start with the basic compatibility principle. Thus, the gap under each PT bar at decompression is zero since the frame is treated as a rigid body as shown in Figure 3.7.

$$\Delta_{v1} = 0 \tag{3.1}$$

$$\Delta_{v2} = 0 \tag{3.2}$$

Now, since the gap underneath each PT bar is zero, the change in length of each PT bar is also zero. Therefore, the change in force at each PT bar is zero.

$$\Delta T_{p1} = 0 \tag{3.3}$$

$$\Delta T_{p2} = 0 \tag{3.4}$$

By summing the moments about point O, the moment that causes decompression of frame base is:

$$M_{DEC} = \left(T_{p1i} + \Delta T_{p1}\right)L_{p1} + \left(T_{p2i} + \Delta T_{p2}\right)L_{p2} + N\ L_f/2 \tag{3.5}$$

The roof displacement at decompression is zero since the frame is considered rigid:

$$\Delta_{dec} = 0 \tag{3.6}$$

The frame drift at decompression is zero:

$$\Theta_{dec} = 0 \tag{3.7}$$

3.4.2 Full clamping of spring stack (FC)

This limit state happens if the spring stack reaches its maximum travel capacity before the PT bar yields as shown in Figure 3.8. This derivation assumes that the spring stack undergoes no additional deformations after clamping as shown in Figure 3.2.

Using the deformation compatibility, the gap underneath each PT bar is:

$$\Delta_{v1} = \frac{L_{p1}}{L_{p2}}\ \Delta_{v2} \tag{3.8}$$

$$\Delta_{v2} = \frac{F_c - T_{p2i}}{K_{c2}} + \left(L_{o2} - L_{c2} - \frac{T_{p2i}}{K_{s2}}\right) \tag{3.9}$$

where F_c is the force required to bring the spring stack to its flat position. K_{c2} is the axial stiffness of PT bar at location 2. L_{o2} is the initial length of the spring stack. L_{c2} is the length of the clamped spring stack at location 2. K_{s2} is the axial stiffness of the spring stack at location 2. The change in force at each PT bar is:

$$\Delta T_{p1} = \Delta_{v1} \left(\frac{1}{K_{c1}} + \frac{1}{K_{s1}} \right)^{-1} \tag{3.10}$$

$$\Delta T_{p2} = F_c - T_{p2i} \tag{3.11}$$

where K_{c1} and K_{s1} are the axial stiffness of the PT bar, and the spring stack respectively. T_{p2i} is the initial force at PT bar in location 2. Summing the moment about point O yields:

$$M_{FC} = \left(T_{p1i} + \Delta T_{p1}\right) L_{p1} + \left(T_{p2i} + \Delta T_{p2}\right) L_{p2} + N\, L_f/2 \tag{3.12}$$

The roof displacement and drift at this state limit are:

$$\Delta_{FC} = \Delta_{v2} \frac{H_w}{L_{p2}} \tag{3.13}$$

$$\Theta_{FC} = \tan^{-1} \frac{\Delta_{v2}}{L_{p2}} \tag{3.14}$$

3.4.3 Linear limit of PT steel (LLP)

As shown in Figures 3.3 and 3.4, the LLP limit state could happen in two forms: LLP-1 where the spring stack does not clamp during pushover loads, and LLP-2 where the spring stack does collapse. The formulation for these two different cases is shown below.

In the first instance, LLP-1 illustrated in Figure 3.9, the force at the PT bars is expected to increase after the gap opening at the base of the frame. In fact, the force is likely to reach the yield stress of steel (F_{py}). At this point, the lateral stiffness of the frame is expected to reduce due to yielding of the PT bars as shown later in Chapter 6.

We start with the deformation compatibility at the base of the frame:

$$\Delta_{v1} = \Delta_{v2} \frac{L_{p1}}{L_{p2}} \tag{3.15}$$

$$\Delta_{v2} = \left(\varepsilon_{py} - \frac{T_{p2i}}{A_{p2}E_p}\right) H_{unb} + \left(\frac{f_{py}A_{p2} - T_{p2i}}{K_{s2}}\right) \tag{3.16}$$

where ε_{py} is the strain of PT steel at yielding. A_{p2} is the cross-sectional area of the PT steel at location 2. E_p is the modulus of elasticity of the PT steel. F_{py} is the stress at yielding of the PT bar.

It is noted that Equation 3.16 assumes that the PT bar and the spring stack represent two springs connected in series as shown in Figure 3.10. Therefore, the expected gap at the base of the frame is the sum of the PT bar elongation and the spring stack shortening.

Now, the change in force at each PT bar is determined using the gap height at the location of each PT bar.

$$\Delta T_{p1} = \Delta_{v1} \left(\frac{1}{K_{c1}} + \frac{1}{K_{s1}}\right)^{-1} \tag{3.17}$$

$$\Delta T_{p2} = (f_{py} A_{p2} - T_{p2i}) \tag{3.18}$$

The moment at this limit state is:

$$M_{LLP-1} = \left(T_{p1i} + \Delta T_{p1}\right) L_{p1} + \left(T_{p2i} + \Delta T_{p2}\right) L_{p2} + N\, L_f/2 \tag{3.19}$$

The roof displacement and drift at this limit state are:

$$\Delta_{LLP-1} = \Delta_{v2}\, \frac{H_w}{L_{p2}} \tag{3.20}$$

$$\Theta_{LLP-1} = \tan^{-1} \frac{\Delta_{LLP-1}}{H_w} \tag{3.21}$$

In the second instance, LLP-2 shown in Figure 3.11, the force at the PT bars will continue to increase after the full clamping of the spring stack and could reach yielding. We now derive the force deformation response at this limit state. Using the strain compatibility and the rigid frame assumption, the gap at the location each PT bar is determined by the following equations:

$$\Delta_{v1} = \Delta_{v2} \frac{L_{p1}}{L_{p2}} \tag{3.22}$$

$$\Delta_{v2} = \left(\varepsilon_{py} - \frac{T_{p2i}}{A_{p2} Ep} \right) Hunb + (L_{o2} - L_{c2} - \frac{T_{p2i}}{K_{s2}}) \tag{3.23}$$

The above equation shows that the spring stack no longer deforms after clamping; one of the assumptions proposed at the beginning of this chapter as shown in Figure 3.2. Now, the change in force at each PT bar is:

$$\Delta T_{p1} = \Delta_{v1} \left(\frac{1}{K_{c1}} + \frac{1}{K_{s1}} \right)^{-1} \tag{3.24}$$

$$\Delta T_{p2} = F_{py} A_{p2} - T_{p2i} \tag{3.25}$$

Equation 3.24 assumes that the first spring stack is still deformable, but otherwise different approach should be taking by implementing the scheme shown in Figure 3.12 or Figure 3.13. Now, the moment at the base is:

$$M_{LLP-2} = \left(T_{p1i} + \Delta T_{p1}\right) L_{p1} + \left(T_{p2i} + \Delta T_{p2}\right) L_{p2} + N\, L_f/2 \tag{3.26}$$

The roof displacement is:

$$\Delta_{LLP-2} = \Delta_{v2} \frac{H_w}{L_{p2}} \tag{3.27}$$

The drift at this state limit is:

$$\Theta_{LLP-2} = \tan^{-1} \frac{\Delta_{LLP-2}}{H_w} \tag{3.28}$$

3.4.4 Fracture of PT steel (FP)

In a similar manner to the LLP limit state, the FP limit state could also happen in two different forms as shown in Figures 3.3 and 3.4. The first case FP-1 where the spring stack does not clamp during pushover loads, and the second case FP-2 where the spring stack does clamp**.**

In the first case, FP-1, the PT bar is expected to reach its ultimate capacity (F_{pu}). The following expressions were derived to predict the response at this limit state. The following steps explain the derivation process.

Starting with the deformation compatibility in Figure 3.14, we can find the gap height at the location of each PT bar:

$$\Delta_{v1} = \Delta_{v2} \frac{L_{p1}}{L_{p2}} \tag{3.29}$$

$$\Delta_{v2} = \left(\varepsilon_{pu} - \frac{T_{p2i}}{A_{p2}E_p}\right) H_{unb} + \left(\frac{f_{pu}A_{p2} - T_{p2i}}{K_{s2}}\right) \tag{3.30}$$

Where ε_{pu} and f_{pu} are the strain and stress at fracture of the PT bar.

In a similar manner to Equation 3.16, the above Equation 3.30 assumes that the spring stack and the PT bar are two springs connected in series. Consequently, the gap at the location of each PT bar is the sum of the bar elongation and the spring stack shortening. This assumption holds only if the spring stack has not reached its maximum travel capacity.

Now, we can find the increase in the force at each PT bar using the gap height at the location of each PT bar.

$$\Delta T_{p1} = \Delta_{v1} \left(\frac{1}{K_{c1}} + \frac{1}{K_{s1}} \right)^{-1} \tag{3.31}$$

$$\Delta T_{p2} = (f_{pu} A_{p2} - T_{p2i}) \tag{3.32}$$

Equation 3.31 is valid for the elastic ranges only. For example, if Δ_{v1} is larger than the gap height under PT1 at yielding, Δ_{v1} found using Equation 3.29 should be used to find the inelastic force at PT1 where Equation 3.17 no longer holds. Note that Figure 3.12 or Figure 3.13 could be used for this purpose.

Now, the moment at the base of the frame represents the sum of the moments of the base:

$$M_{FP-1} = \left(T_{p1i} + \Delta T_{p1}\right) L_{p1} + \left(T_{p2i} + \Delta T_{p2}\right) L_{p2} + N\, L_f/2 \tag{3.33}$$

The roof displacement at this stage is:

$$\Delta_{FP-1} = \Delta_{v2} \frac{H_w}{L_{p2}} \tag{3.34}$$

The drift of the frame at this stage is:

$$\Theta_{FP-1} = \tan^{-1} \frac{\Delta_{FP-1}}{H_w} \tag{3.35}$$

In the second case FP-2 shown in Figure 3.15, after yielding of the PT bar, the bar could fracture due to the increased load, and to predict the response, the followings equations apply.

$$\Delta_{v1} = \Delta_{v2} \frac{L_{p1}}{L_{p2}} \tag{3.36}$$

$$\Delta_{v2} = \left(\varepsilon pu - \frac{T_{p2i}}{A_{p2} Ep} \right) Hunb + (L_{o2} - L_{c2} - \frac{T_{p2i}}{K_{s2}}) \tag{3.37}$$

The change in force at each PT group is:

$$\Delta T_{p1} = \Delta_{v1} \left(\frac{1}{K_{c1}} + \frac{1}{K_{s1}} \right)^{-1} \tag{3.38}$$

$$\Delta T_{p2} = F_{pu} A_{p2} - T_{p2i} \tag{3.39}$$

In a similar manner to Equation 3.31, the above Equation 3.38 is valid for elastic ranges and assumes that the spring stack has not clamped. Otherwise, we would have two scenarios.

1. The first PT assembly has a clamped spring stack, but the PT bar has not yielded. As shown in Figure 3.14, this scenario lies between the spring stack clamping and yielding of the PT bar.
2. The first PT assembly has a clamped spring stack, but the PT bar has yielded. As shown in Figure 3.13, this lies between the PT bar yielding and fracture.

In both scenarios stated above, the stiffness of the assembly could be traced to find the force corresponding to Δ_{v1} calculated by Equation 3.36.

The moment at the base is:

$$M_{FP-2} = \left(T_{p1i} + \Delta T_{p1}\right)L_{p1} + \left(T_{p2i} + \Delta T_{p2}\right)L_{p2} + N\ L_f/2 \tag{3.40}$$

The roof displacement is:

$$\Delta_{FP-2} = \Delta_{v2}\frac{H_w}{L_{p2}} \tag{3.41}$$

The drift at this state limit is:

$$\Theta_{FP-2} = \tan^{-1}\frac{\Delta_{FP-2}}{H_w} \tag{3.42}$$

In summary, Figure 3.16 shows the expected limit states and the order they might occur. Also, Tables 3.1, 3.2, 3.3, 3.4, and 3.5 summarize the CFE in a tabulated form.

Table 3.1: Summary of the CFE for the decompression limit state (DEC).

Decompression (DEC)	**CFE**
Δ_{v1}	0
Δ_{v2}	0
ΔT_{P1}	0
ΔT_{p2}	0
M_{DEC}	$(T_{p1i} + \Delta T_{p1})L_{p1} + (T_{p2i} + \Delta T_{p2})L_{p2} + N\ L_f/2$
Δ_{DEC}	0
Θ_{DEC}	0

Table 3.2: Summary of the CFE for the full clamping of the spring stack limit state (FC).

Full Clamping of The Springs Stack (FC)	**CFE**
Δ_{v1}	$\frac{L_{p1}}{L_{p2}}\ \Delta_{v2}$
Δ_{V2}	$\frac{F_c - T_{p2i}}{K_{c2}} + (L_{o2} - L_{c2} - \frac{T_{p2i}}{K_{s2}})$
ΔT_{P1}	$\Delta_{v1}\left(\frac{1}{K_{c1}} + \frac{1}{K_{s1}}\right)^{-1}$
ΔT_{p2}	$F_c - T_{p2i}$
M_{FC}	$(T_{p1i} + \Delta T_{p1})L_{p1} + (T_{p2i} + \Delta T_{p2})L_{p2} + N\ L_f/2$
Δ_{FC}	$\Delta_{v2}\frac{H_w}{L_{p2}}$
Θ_{FC}	$\tan^{-1}\frac{\Delta_{v2}}{L_{p2}}$

Table 3.3: Summary of the CFE for the linear limit of the PT steel limit state (LLP-1).

Linear Limit of Post Tensioning Steel (LLP-1)	**CFE**
Δ_{v1}	$\frac{L_{p1}}{L_{p2}}\,\Delta_{v2}$
Δ_{v2}	$\left(\varepsilon_{py}-\frac{T_{p2i}}{A_{p2}E_p}\right)H_{unb}+(\frac{f_{py}A_{p2}-T_{p2i}}{K_{s2}})$
ΔT_{P1}	$\Delta_{v1}\left(\frac{1}{K_{c1}}+\frac{1}{K_{s1}}\right)^{-1}$
ΔT_{p2}	$(f_{py}A_{p2}-T_{p2i})$
M_{LLP-1}	$(T_{p1i}+\Delta T_{p1})L_{p1}+(T_{p2i}+\Delta T_{p2})L_{p2}+N\,L_f/2$
Δ_{LLP-1}	$\Delta_{v2}\frac{H_w}{L_{p2}}$
Θ_{LLP-1}	$\tan^{-1}\frac{\Delta_{LLP-1}}{H_w}$

Table 3.4: Summary of the CFE for the linear limit of the PT steel limit state (LLP-2).

Linear Limit of Post Tensioning Steel (LLP-2)	**CFE**
Δ_{v1}	$\frac{L_{p1}}{L_{p2}}\,\Delta_{v2}$
Δ_{v2}	$\left(\varepsilon py-\frac{T_{p2i}}{A_{p2}Ep}\right)Hunb+(L_{o2}-L_{c2}-\frac{T_{p2i}}{K_{s2}})$
ΔT_{P1}	$\Delta_{v1}\left(\frac{1}{K_{c1}}+\frac{1}{K_{s1}}\right)^{-1}$
ΔT_{p2}	$F_{py}A_{p2}-T_{p2i}$
M_{LLP-2}	$(T_{p1i}+\Delta T_{p1})L_{p1}+(T_{p2i}+\Delta T_{p2})L_{p2}+N\,L_f/2$
Δ_{LLP-2}	$\Delta_{v2}\frac{H_w}{L_{p2}}$
Θ_{LLP-2}	$\tan^{-1}\frac{\Delta_{LLP-2}}{H_w}$

Table 3.5: Summary of the CFE for the fracture of the PT steel limit state (FP-1).

Fracture of Post Tensioning Steel (FP-1)	**CFE**
Δ_{v1}	$\frac{L_{p1}}{L_{p2}}\,\Delta_{v2}$
Δ_{v2}	$\left(\varepsilon_{pu}-\frac{T_{p2i}}{A_{p2}E_p}\right)H_{unb}+(\frac{f_{pu}A_{p2}-T_{p2i}}{K_{s2}})$
ΔT_{P1}	$\Delta_{v1}\left(\frac{1}{K_{c1}}+\frac{1}{K_{s1}}\right)^{-1}$
ΔT_{p2}	$(f_{pu}A_{p2}-T_{p2i})$
M_{FP-1}	$(T_{p1i}+\Delta T_{p1})L_{p1}+(T_{p2i}+\Delta T_{p2})L_{p2}+N\,L_f/2$
Δ_{FP-1}	$\Delta_{v2}\frac{H_w}{L_{p2}}$
Θ_{FP-1}	$\tan^{-1}\frac{\Delta_{FP-1}}{H_w}$

Table 3.6: Summary of the CFE for the fracture of the PT steel limit state (FP-2).

Fracture of Post Tensioning Steel (FP-2)	**CFE**
Δ_{v1}	$\frac{L_{p1}}{L_{p2}}\,\Delta_{v2}$
Δ_{v2}	$\left(\varepsilon pu-\frac{T_{p2i}}{A_{p2}Ep}\right)Hunb+(L_{o2}-L_{c2}-\frac{T_{p2i}}{K_{s2}})$
ΔT_{P1}	$\Delta_{v1}\left(\frac{1}{K_{c1}}+\frac{1}{K_{s1}}\right)^{-1}$
ΔT_{p2}	$F_{pu}A_{p2}-T_{p2i}$
M_{FP-2}	$(T_{p1i}+\Delta T_{p1})L_{p1}+(T_{p2i}+\Delta T_{p2})L_{p2}+N\,L_f/2$
Δ_{FP-2}	$\Delta_{v2}\frac{H_w}{L_{p2}}$
Θ_{FP-2}	$\tan^{-1}\frac{\Delta_{FP-2}}{H_w}$

Figure 3.1: Idealized post-tensioning reinforcement stress-strain curve (Kurama 1997).

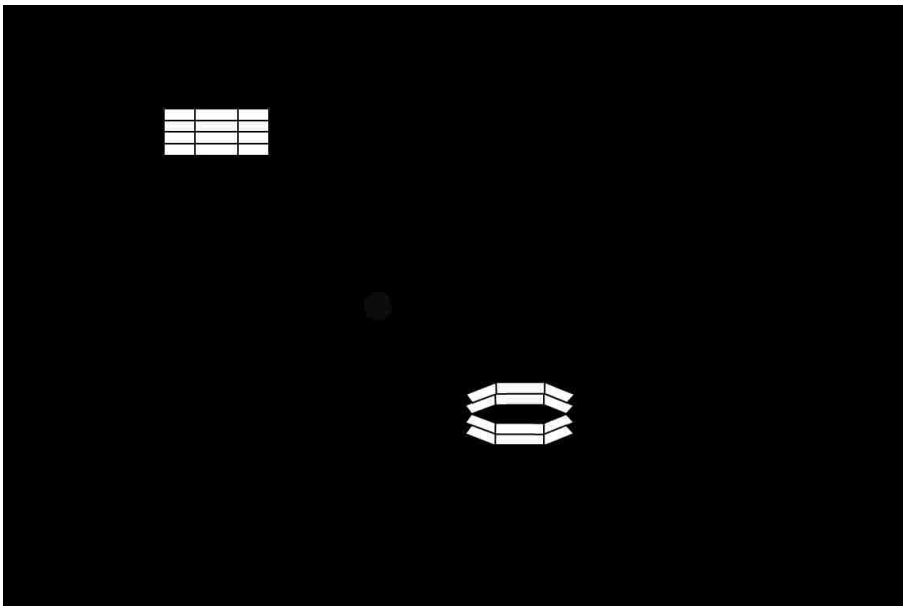

Figure 3.2: Force-deformation curve of typical spring stack (Schnorr, 2003).

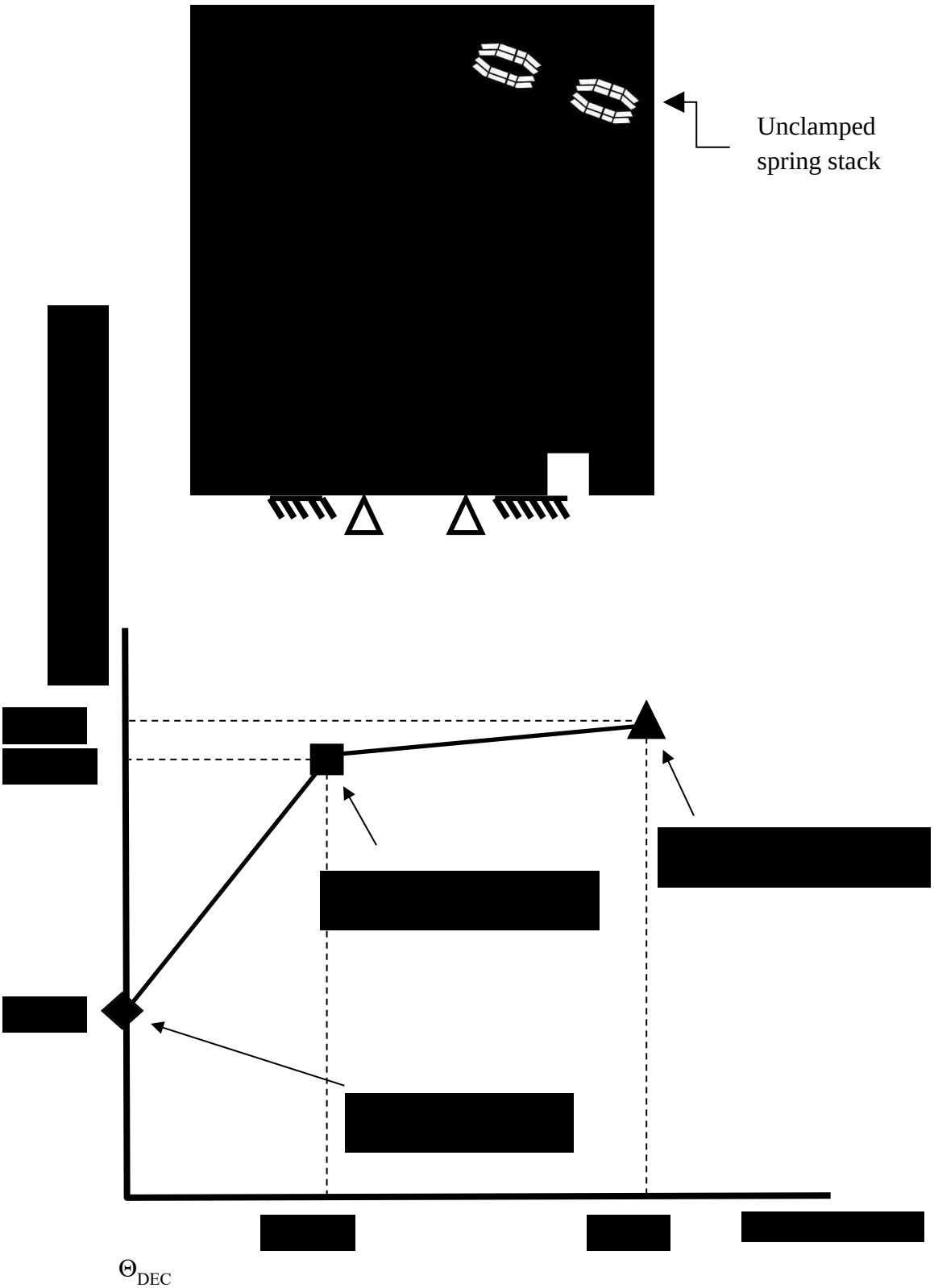

Figure 3.3: Overview of the rocking frame limit states (spring stack does not clamp).

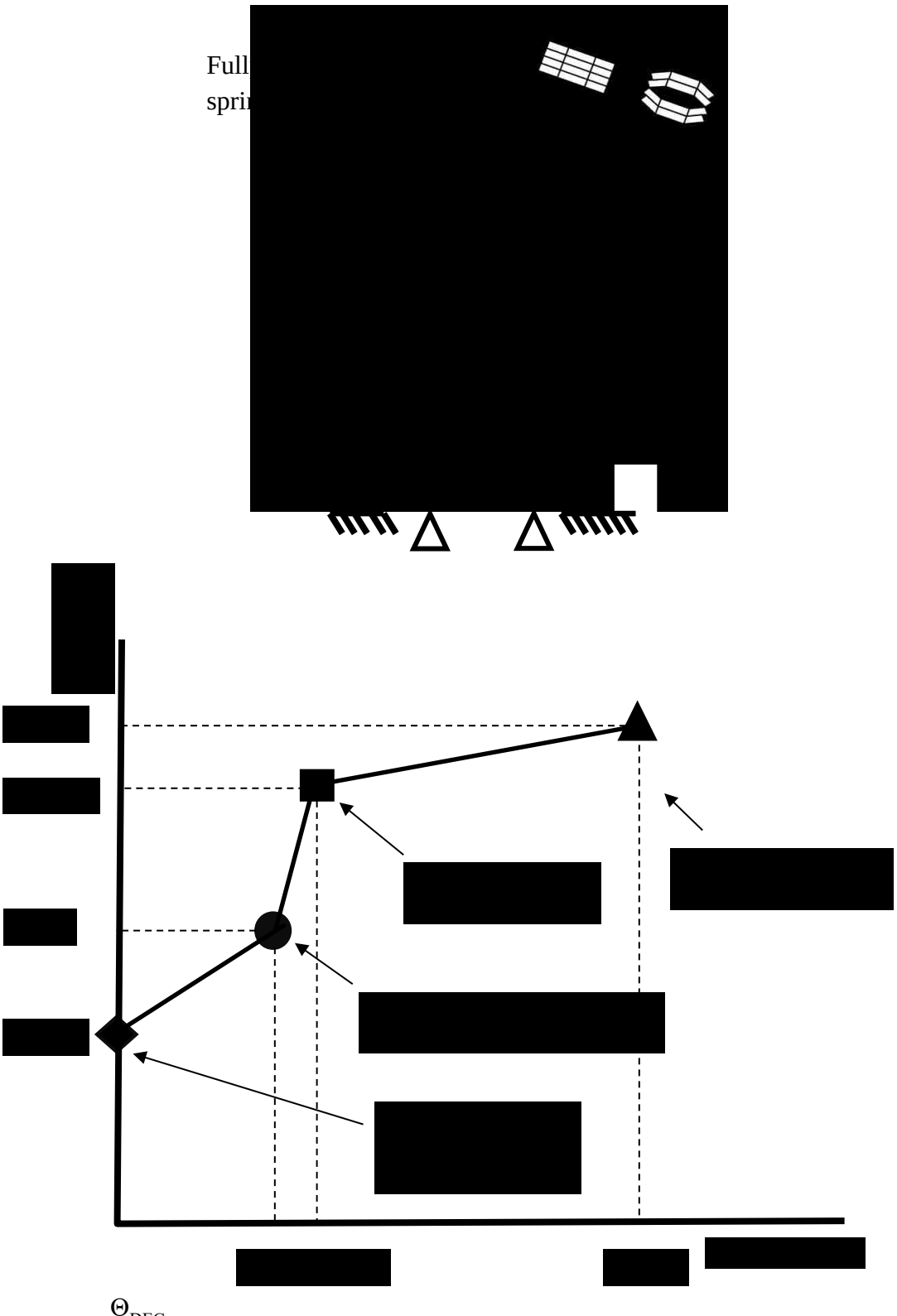

Figure 3.4: Overview of the rocking frame limit states (cpring stack does clamp).

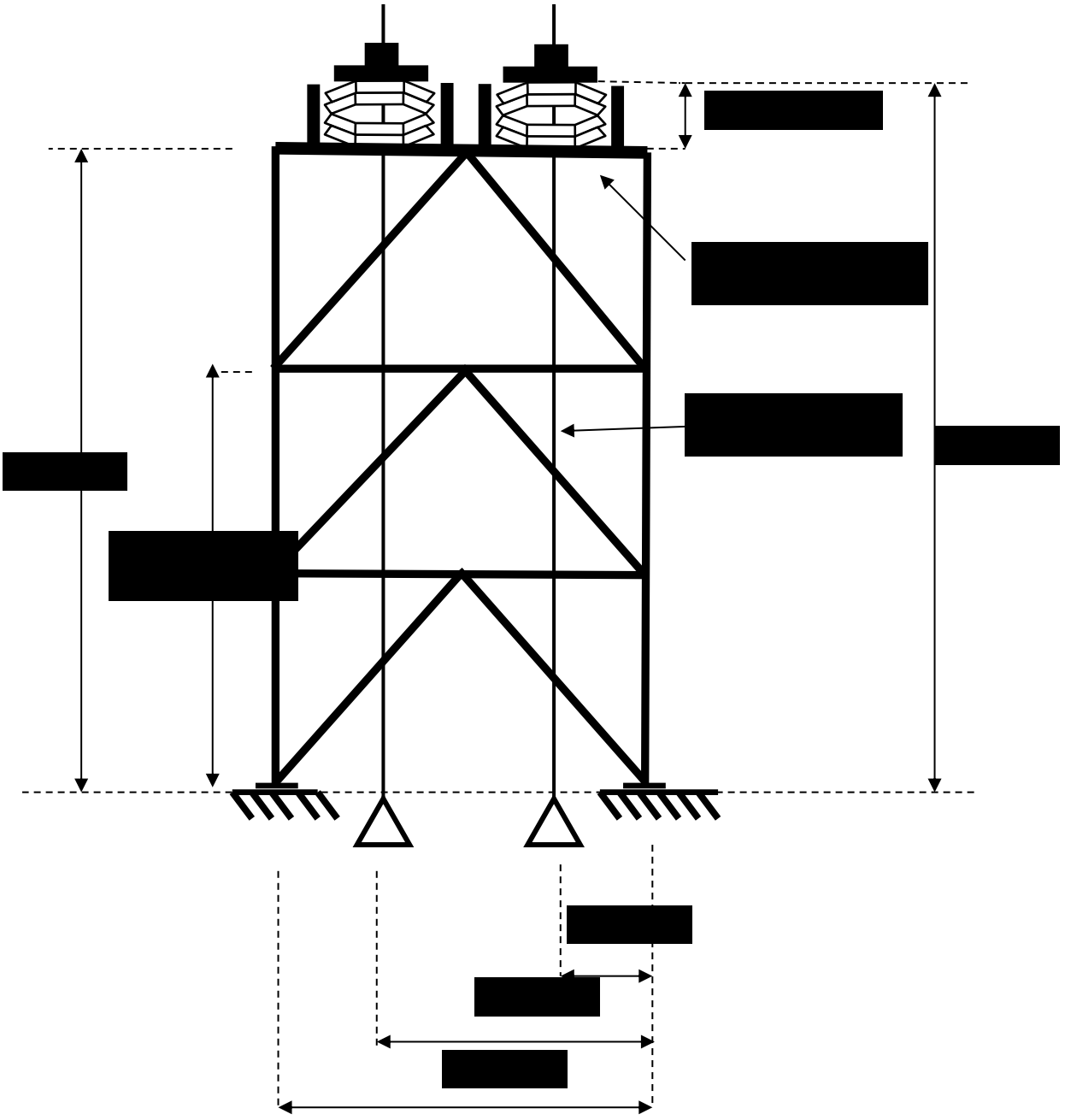

Figure 3.5: Rocking frame geometry and notation.

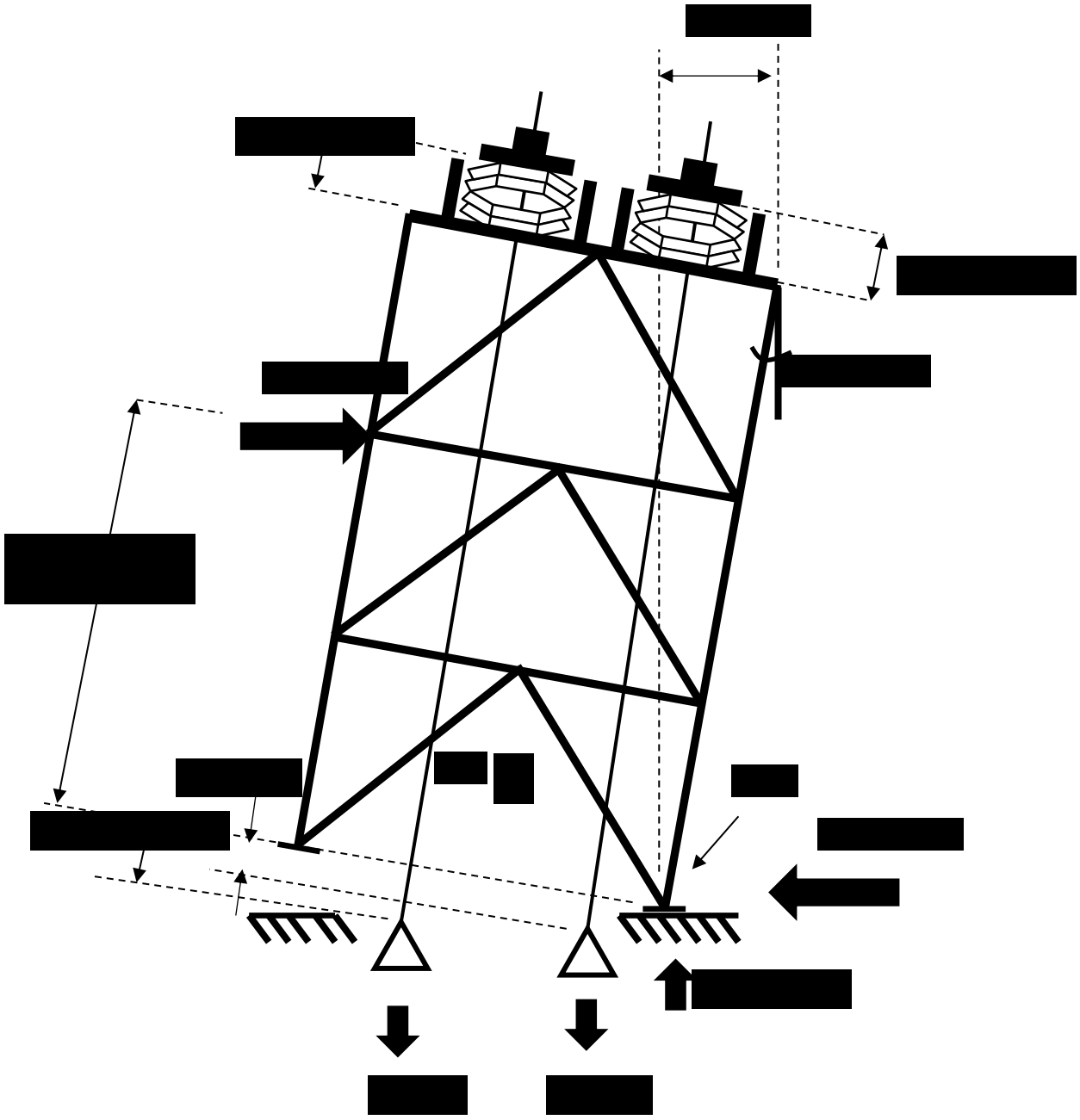

Figure 3.6: Notation for the rocking frame forces and deformations.

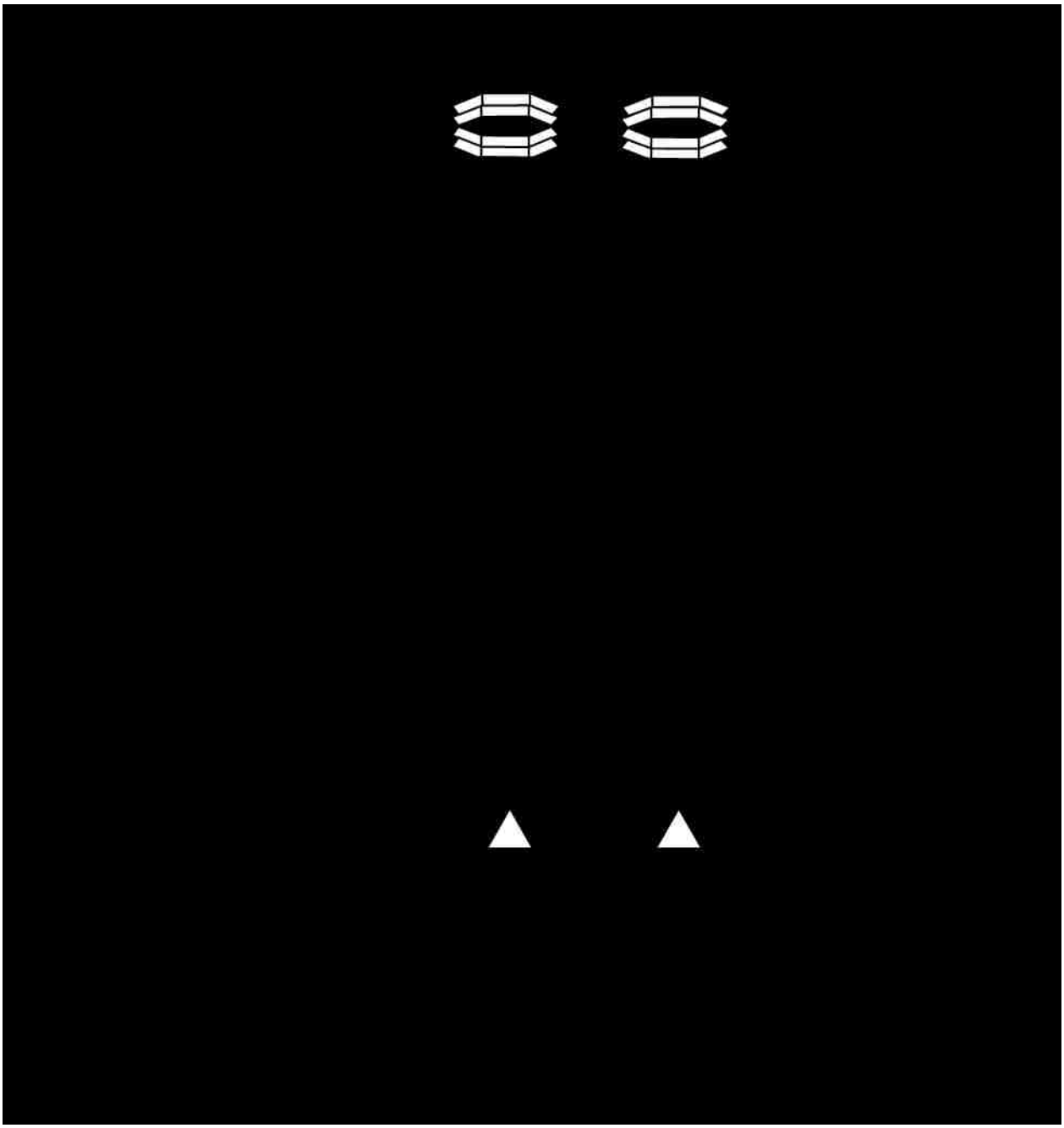

Figure 3.7: Decompression of the base (DEC).

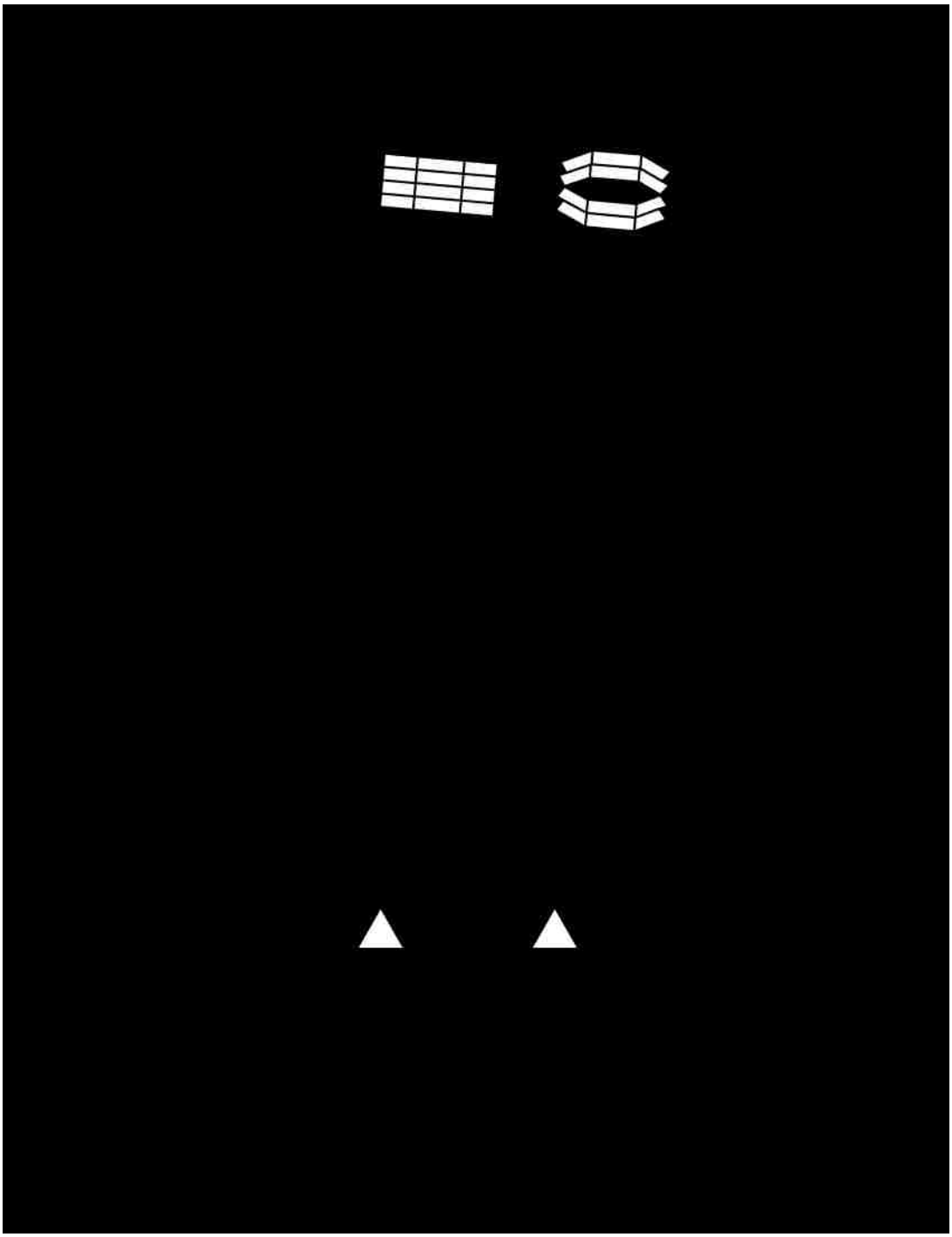

Figure 3.8: Full clamping of the spring stack (FC).

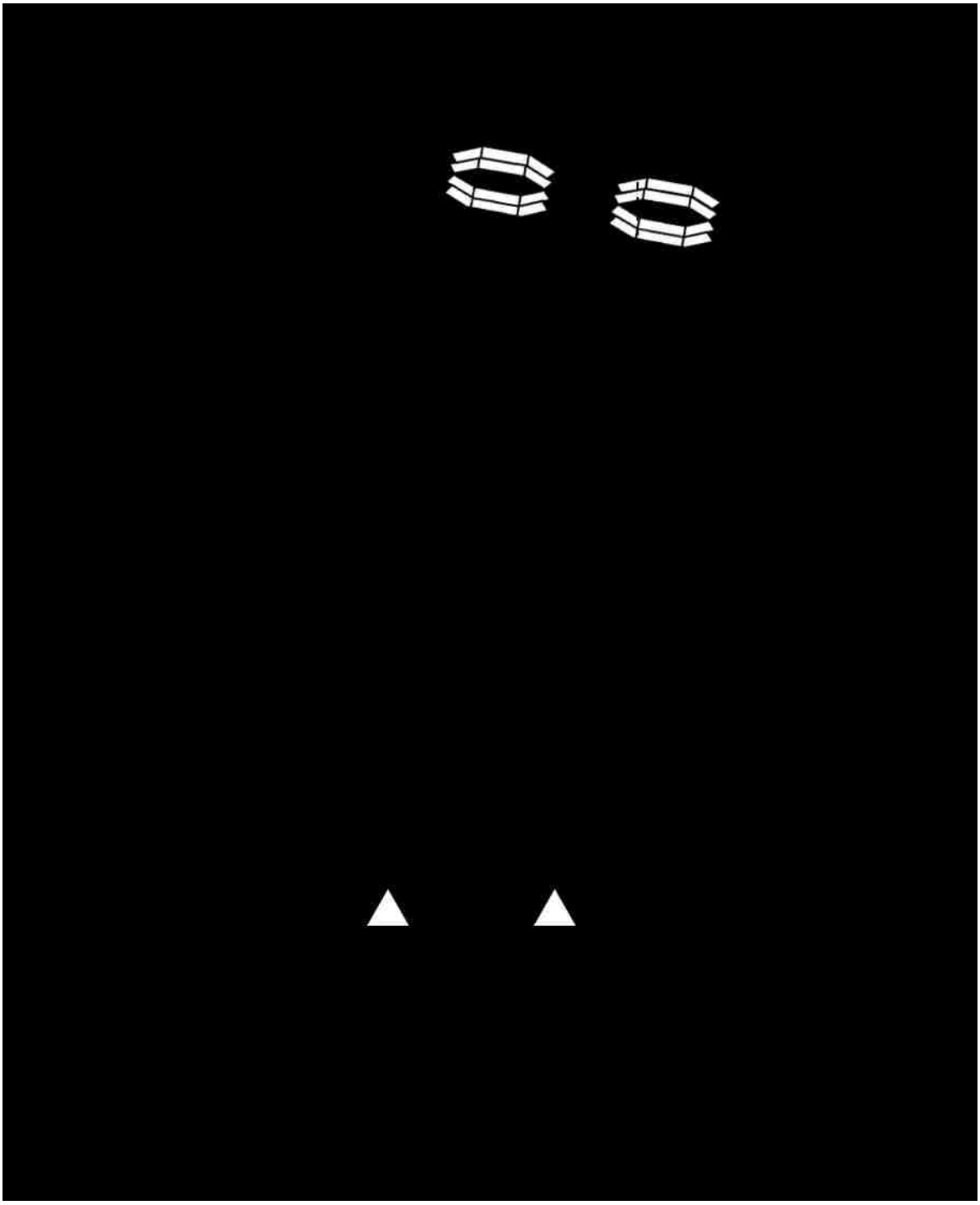

Figure 3.9: Linear limit of the post-tensioning steel (LLP-1).

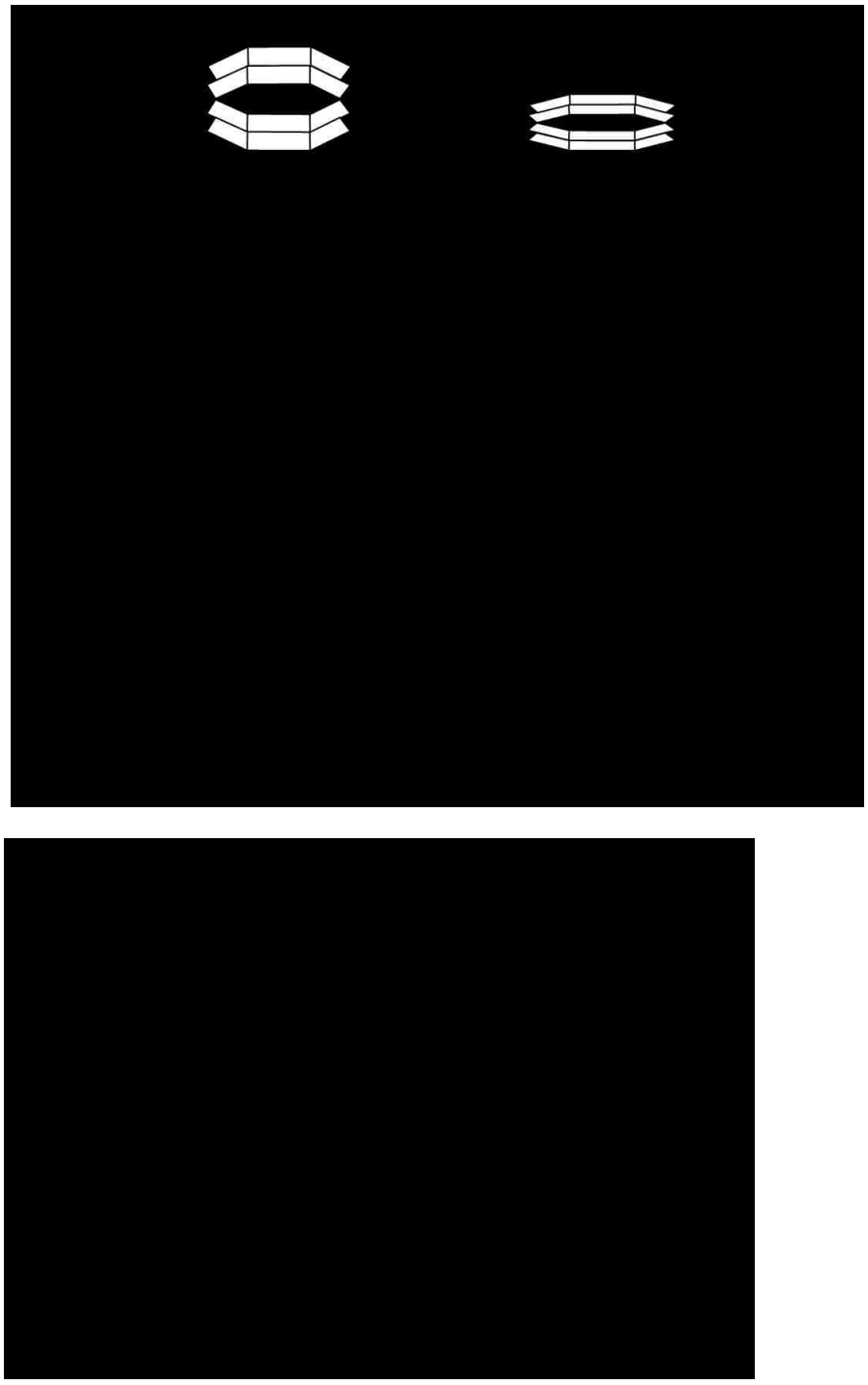

Figure 3.10: Force-deformation of the PT bar and the spring stack assembly (spring stack does not clamp).

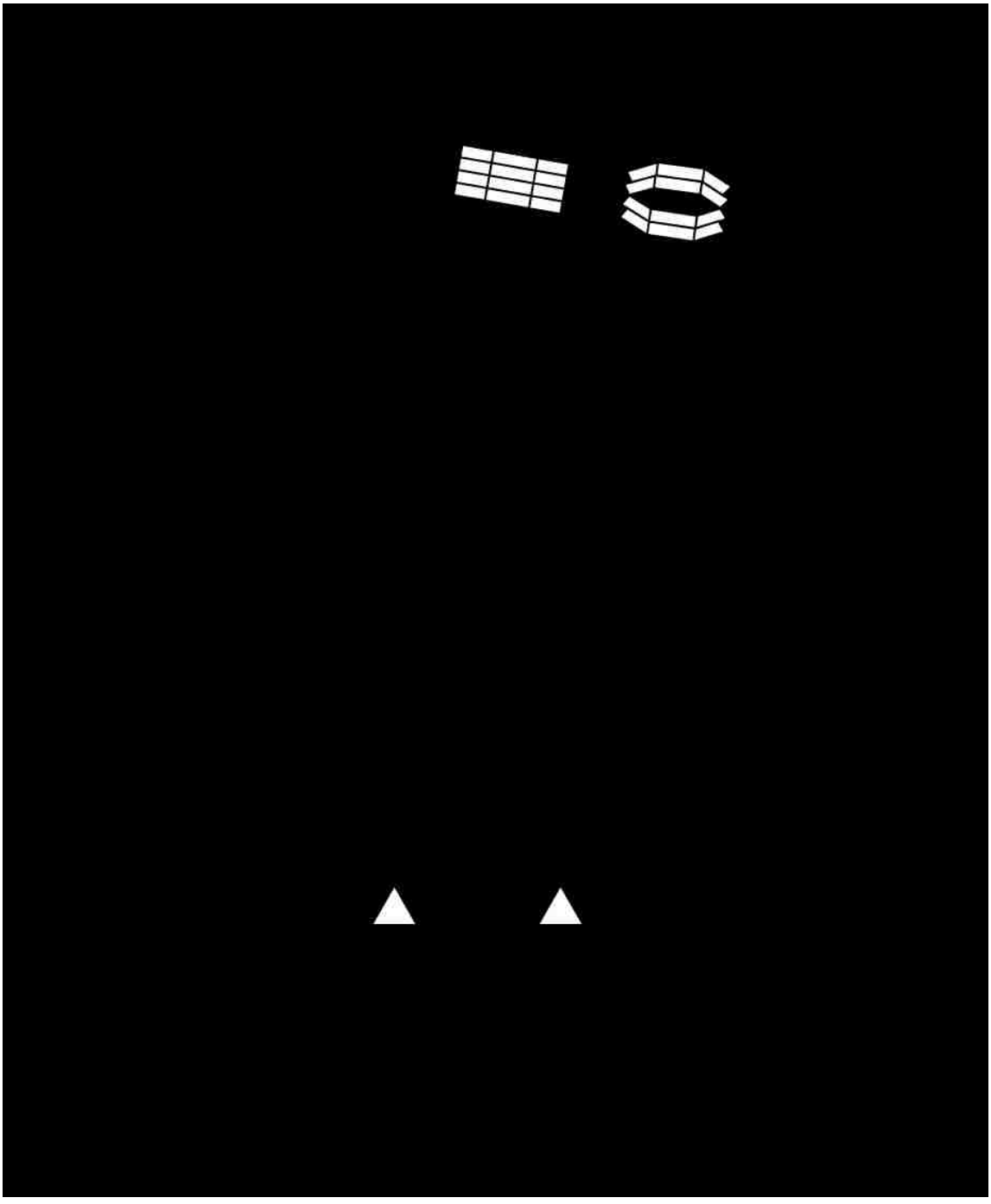

Figure 3.11: Linear limit of post-tensioning steel (LLP-2).

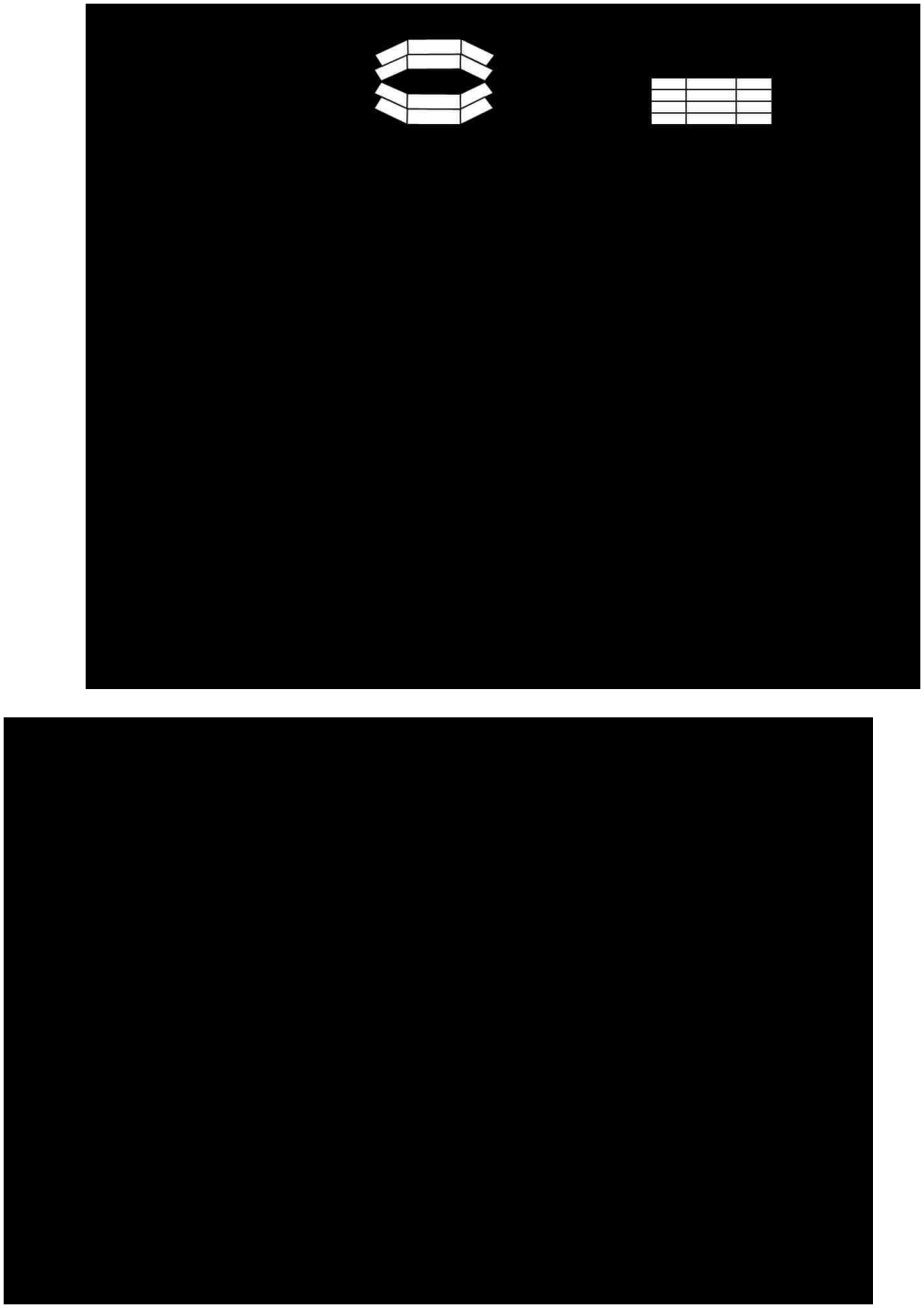

Figure 3.12: Force-deformation of the PT bar and the spring stack assembly (spring stack does clamp).

Figure 3.13: Deformation of the assembly in the inelastic range (spring stack does clamp).

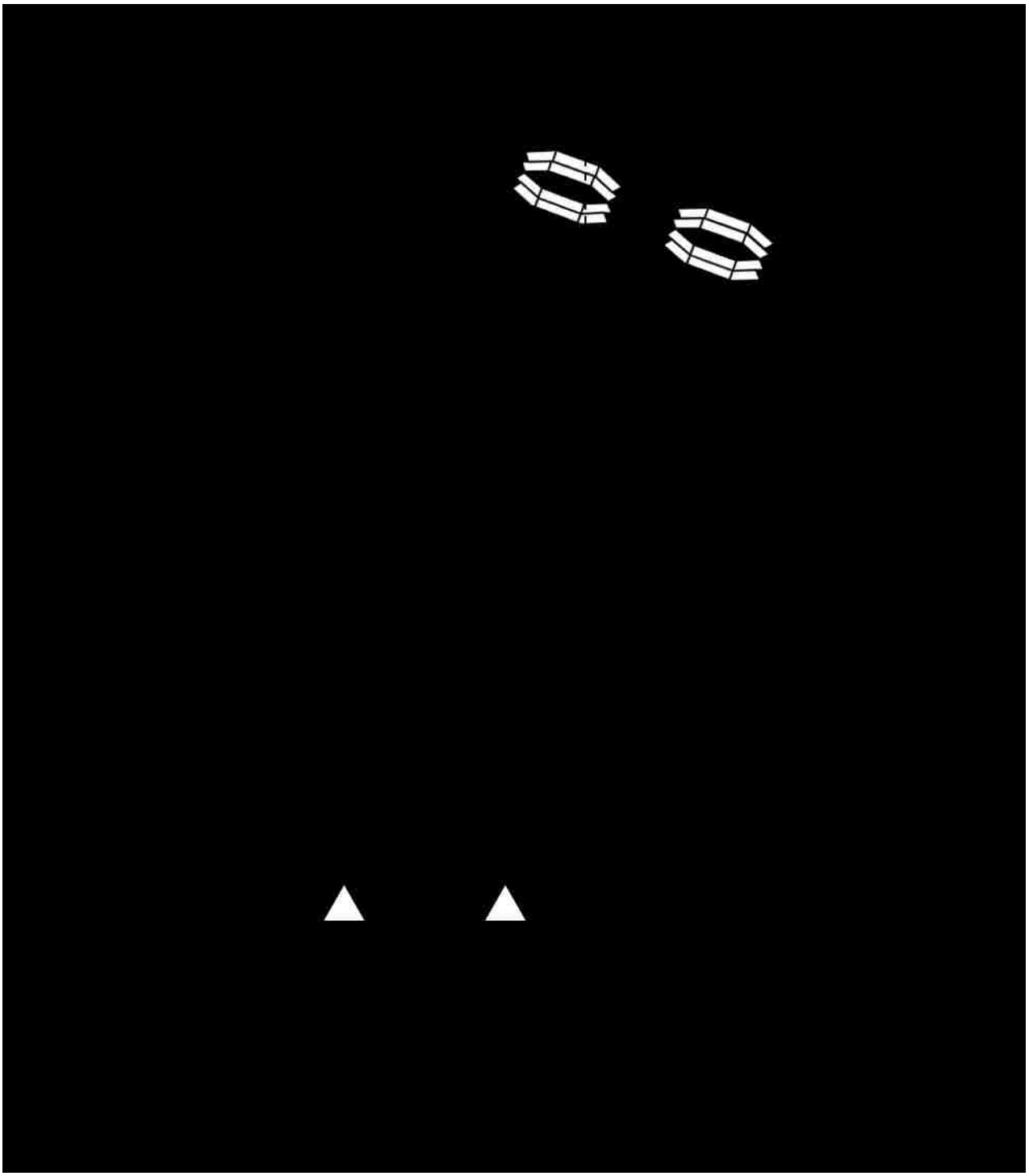

Figure 3.14: Fracture of post-tensioning steel (FP-1).

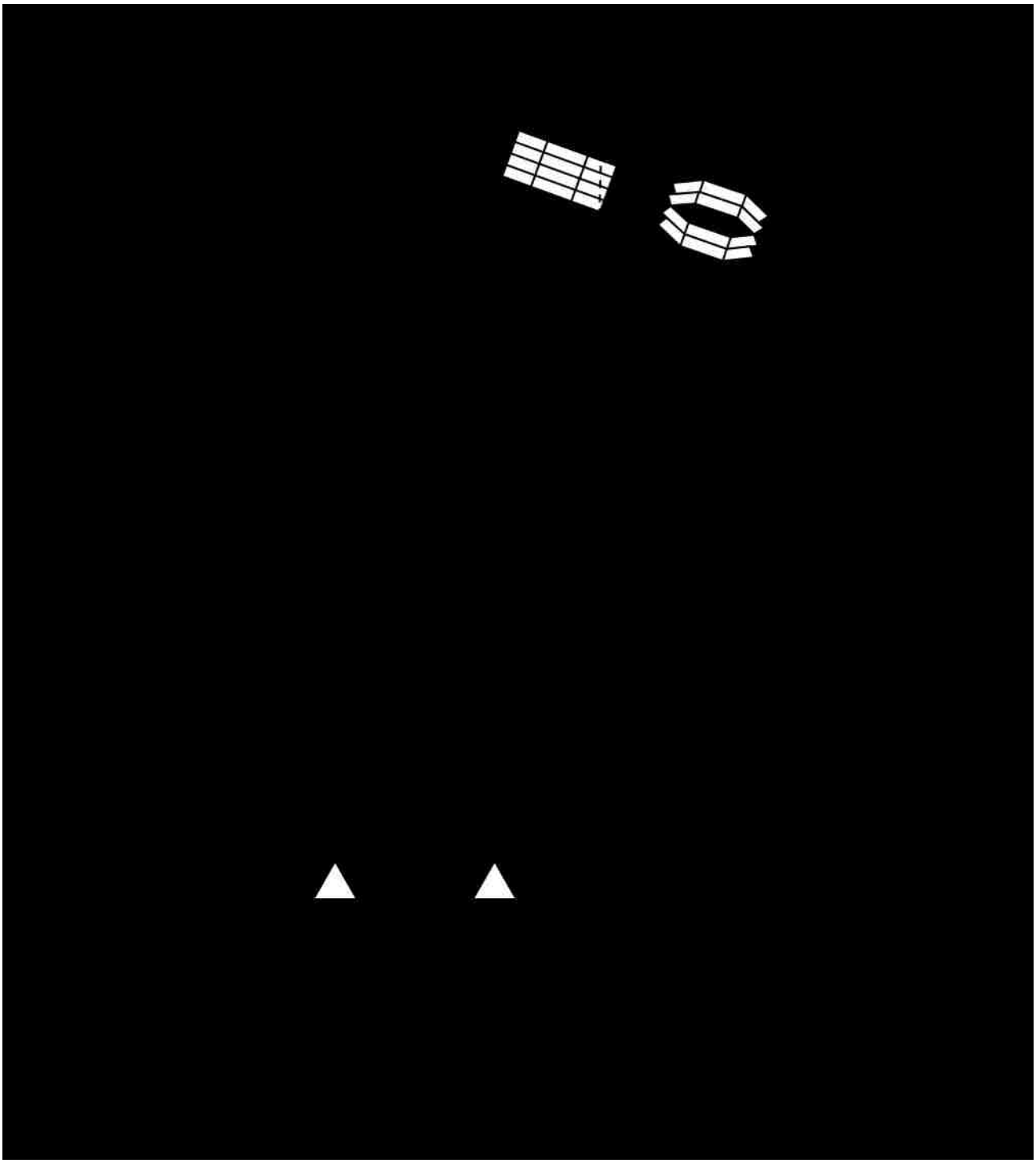

Figure 3.15: Fracture of post-tensioning steel (FP-2).

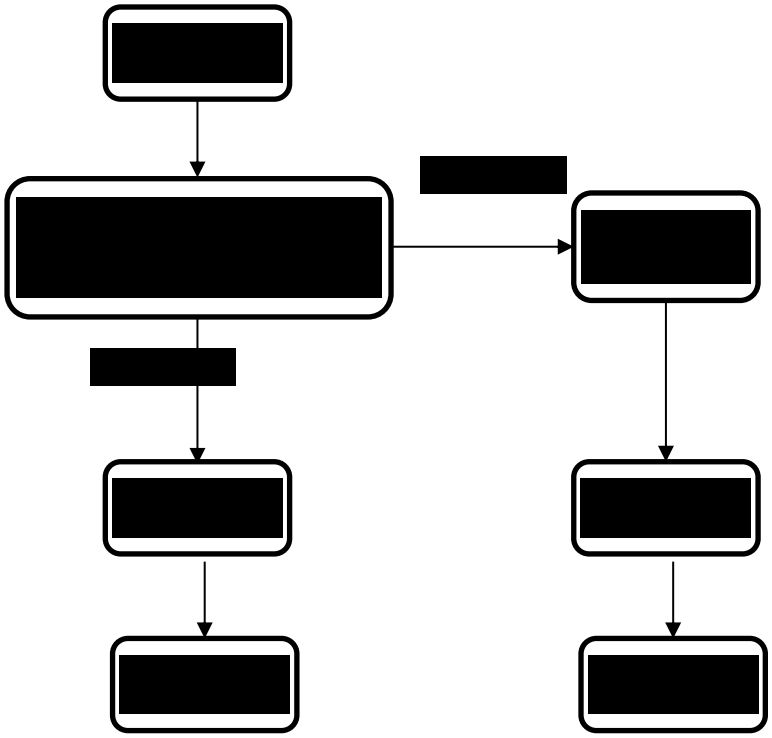

Figure 3.16: Summary of the expected pushover curves.

CHAPTER 4

FINITE ELEMENT MODEL

4.1 INTRODUCTION

This chapter develops a finite element model (FE) that is used to conduct the parametric study presented in Chapter 6. The finite element software OpenSEES (Mazzoni et al. 2006) is used to develop the FE model and to execute the parametric study. The results of the FE analysis are compared with CFE models for the same parameters to examine the error between the finite element solution and the solution predicted by the closed form expressions.

In developing this FE, the same assumptions made in deriving the CFE are used. A summary of these assumptions follows:

1. The frame is considered rigid;
2. The post tension bars are considered deformable;
3. The friction between the disc springs is neglected;
4. Stability failure does not occur;
5. No sliding at the base of the frame occurs;
6. The PT bars are unbonded;
7. The disc spring stack remains elastic.

4.2 ELEMENTS USED IN THE FE MODEL

The FE model is comprised of five main components:

1. Beam column element to model the rocking frame and its braces;
2. Zero length spring (ZLS) to model the disc spring stack;
3. Truss element to model the PT bars;
4. Zero length spring (ZLS) to model the gap opening mechanism;
5. Gap element to model the spring stack clamping.

4.3 DETAILED FE MODEL

This section discusses the FE model in detail by describing the nodes, elements used their connectivity, the initial and the boundary conditions, the loading application, and the recorded responses of interest.

4.3.1 Nodes

As shown in Figures 4.1, 4.2, 4.3, and 4.4, the proposed FE models contain several nodes connecting the various elements employed. However, we can see that the first and the second models have 17 nodes, whereas the third and the fourth models have 21 nodes.

OpenSEES command manual explains the method of creating nodes by assigning the node tag number, and the coordinates of the nodes (Mazzoni et al. 2006). It is seen that each

node in the FE models has a unique tag number, and thus elements could be uniquely defined between the nodes.

4.3.2 Model Components

4.3.2.1 Rocking frame members

The rocking frame and its braces are modeled using beam-column elements as shown in Figures 4.1, 4.2, 4.3, and 4.4. These elements have three degrees of freedom per node and as the name indicates, elastic beam column elements will remain elastic during the analysis.

Each elastic beam column element needs the following to be defined (Mazzoni et al. 2006): (1) unique tag number; (2) starting node number; (3) end node number; (4) cross-sectional area; (5) modulus of elasticity; (6) shear modulus; (7) moment of inertia about the x and the y-axes; and, (8) the coordinate transformation for the element.

To model the frame as a rigid assembly and keep the consistency between the FE and CFE results, large values for the elements inputs were given. In that case, OpenSEES (Mazzoni et al. 2006) will use these large inputs to calculate the elements stiffness matrices, and accordingly, the elements will be practically rigid. With this intention, most of the elastic deformations are almost zero, and the consistency of the of the FE and the CFE solutions is maintained.

4.3.2.2 PT bars

The PT bars are modeled using truss elements. These truss elements can carry axial loads only, and they can capture the nonlinear response due to yielding of the steel. Hence, the material of the PT bars is modeled as steel 01 in OpenSEES (Mazzoni et al. 2006) with a bilinear stress-strain curve as shown in Figure 3.1.

4.3.2.3 Spring stack

The disc spring stack is modeled using a zero-length spring (ZLS) connecting two nodes as shown in Figures 4.1, 4.2, 4.3, and 4.4. This element represents the force deformation response of the spring stack. OpenSEES (Mazzoni et al. 2006) requires a uniaxial material to be assigned with this ZLS. Thus, a hysteretic material is implemented to represent the stiffness of the spring stack. However, it is noted that it is crucial to use only the elastic portion of the hysteretic curve to obtain a linear spring. The hysteretic curve does not capture the effects of friction between springs. As shown in Figures 4.1, 4.2, 4.3, and 4.4, the ZLS connects the truss element to the roof and this assembly depicts the physical behavior of a PT bar connected in series to a disc spring stack as explained in Figure 3.14.

Keep in mind that the ZLS would have a symmetric force deformation response, and thus it should give wrong results if it goes under the circumstance shown Figure 4.5. The figure indicates that the assembly of the truss and the ZLS is valid only if the truss element is in tension, but it is invalid if the truss goes in compression since the physical model would behave differently.

4.3.2.4 Zero length spring (zls) to model the gap opening mechanism

Zero length spring (ZLS) was used to capture the gap opening mechanism at the base of the frame as shown in Figures 4.1, 4.2, 4.3, and 4.4. Elastic-no-tension uniaxial material was assigned to this element to prevent it from resisting uplift while providing vertical reaction when the gap is closed. It was required to assign large value for the compression stiffness of the uniaxial material to prevent downward displacement; the same approach used by a previous study on the rocking steel frames (Chancellor 2014).

4.3.2.5 Gap element to model the spring stack clamping

Gap element is used to model the clamping of the spring stack as illustrated in Figures 4.2 and 4.4. This gap element is connected in parallel with the ZLS representing the stiffness spring stack, and it simply limits the travel capacity of the ZLS. Once the gap element is activated, the ZLS undergoes no further deformation as shown in Figure 4.7. The Elastic gap material is assigned to this element to provide a locking mechanism as shown in Figure 4.6.

4.3.3 Elements connectivity

As shown in Figures 4.1, 4.2, 4.3, and 4.4. elements are connected through nodes having unique tag numbers. The following paragraphs describe the connectivity these elements and the direction they are oriented.

Models 1,3

- Zero-length spring (ZLS) connecting nodes 17 and 16 and pointing in the Y-direction represents the gap opening mechanism.
- ZLS at the roof connecting nodes 14 and 11 and oriented in the Y-direction represents the stiffness of disc spring stack.
- Truss element are connecting nodes 15 and 14 and representing the PT bars. The truss element is not connected to the floors; only to node 14 as connecting it to other nodes would give totally different results than the real physical models.
- For model 3 shown in Figure 4.3, additional gap element connecting nodes 14 and 11 and pointing in the y-direction to represent the spring stack clamping. Connecting the gap element using nodes 14 and 11, same nodes connecting the ZLS assures that the ZLS and the gap element work in parallel.
- All the remaining elements are elastic beam columns. Each element passes through two points as shown in Figures 4.1 and 4.3.

Models 2,4

- ZLS connecting nodes 21 and 20 representing the gap opening mechanism.
- ZLS's connecting three pairs of nodes: (17,10), (18,11), and (19,12) representing the disc spring stack (nodes 18 and 19 are not shown in Figure (4.2) or (4.4), but they lie on top of nodes 11 and 12).
- Truss elements connecting three pair of nodes: (14,17); (15, 18), and (16, 19).

- For model 4, all ZLS's on the roof are connected in parallel to gap elements to capture the stack clamping.
- All the remaining are beam column elements connected through the nodes shown in Figures 4.2 and 4.4.

4.3.4 Boundary conditions and constraints

Below is a description of the boundary conditions and the constraints applied to the FE model.

Models 1,3

Models 1,2 have several boundary conditions to prevent rigid body motion of the FE model.

- The base of the right column (node 2) is pinned allowing rotation but no translations. This constraint is only valid for lateral loads acting in the direction seen in Figures 4.1 and 4.2.
- Nodes 15 and 17 are pinned to prevent translations. This would assure that the ends of the truss and the gap elements are prevented from rigid body translations.
- Models 1, 2 have several constraints to the maintain the compatibility of displacement.

- Node 16 is slaved to node 1 in the y-direction. This allows the ZLS to prevent downward displacement of the column tip, but it still provides no resistance to uplifting (Chancellor 2014).
- Node 14 is slaved to node 11 in the x-direction. This assures that node 14 moves horizontally with node 11 as the frame sways laterally.

Models 2,4

Models 2,4 have several boundary conditions to prevent rigid body motion of the FE model.

- The base of the right column (node 2) is pinned allowing rotation but no translations.
- Nodes 14,15,16 and 21 are pinned to prevent translations.
- Models 2, 4 have several constraint to the maintain the compatibility of displacement.
- Node 20 is slaved to node 1 in the y-direction.
- Node 17 is slaved to node 10 in the x-direction; node 18 is slaved to node 11 in the x-direction; and node 19 is slaved to node 12 in the x-direction. (nodes 18 and 19 are not shown, but they lie on top of nodes 11 and 12).

4.3.5 Initial conditions applied to the model

One of the initial conditions that need to be defined is the PT force in the truss element. In fact, even though initial strain could be applied to the truss to reach the required PT force, some of this force would be lost since the truss element is connected in series to a zero-length spring (ZLS) as shown in Figures 4.1, 4.2, 4.3, and 4.4. Therefore, initial strain that causes the required PT force is applied to the truss concurrently with an initial displacement of the ZLS that invokes the same PT as depicted in Figure 4.8. Thus, the force in the truss and the ZLS is now equal (i.e. both truss and the ZLS are in equilibrium, and the assembly maintains the required PT force without loss).

Additionally, it is important to know when to activate the gap element of the spring stack during the push over analysis since it is correlated with the spring stack clamping. The gap element should provide no resistance if the displacement of the ZLS is less than the clamping travel capacity of the spring stack. However, it should completely restrain the displacement once the clamping capacity is reached. Thus, we define the required travel capacity of the gap element as follows: we calculate the displacement that the spring assembly can travel to the clamping and the initial extension of the ZLS due to the initial PT force. Then, the travel capacity of the gap element is the difference between these (the element will not be activated as long the spring displacement is less than the travel capacity). Once this travel capacity is reached, the gap element is activated, and the spring will carry no additional displacement.

4.3.6 Loads and recorders in OpenSEES

Figures 4.1, 4.2, 4.3, and 4.4 show that the pushover load is defined at the two thirds the height of the frame and directed to the right. The load was applied by steps to the FE model to get a smooth pushover curve that includes many points.

A load control integrator is used to apply the load in 1000 steps. Also, the constraints to the mode are applied using the Lagrange option. Additionally, a plain numbered, a general band system with a linear algorithm were used. Finally, the analysis is chosen to be static.

After developing the script that describes the FEM, the outputs of the finite element analysis need to be recorded. OpenSEES (Mazzoni et al. 2006) requires the recorders to be specified in detail inside the script itself. For example, the node number, the type of the force required (axial force for truss element, reaction for supports), the direction of the recorded displacement, and so on. OpenSEES (Mazzoni et al. 2006) will record the results in separate files. Each file represents the response of specific point of interest.

Several recorders in OpenSEES (Mazzoni et al. 2006) script were specified as follows. First, the displacement of the roof in the horizontal direction. This will help in determining the frame drift at each load step. Second, the axial force in each truss element. This will aid in finding the load step where the force in the truss elements reached the yield stress. Third, the force at each spring element. This recorder was specified to assure the consistency of the results, because the force at the truss element must equal the force at the spring element (satisfies equilibrium). Fourth, the force at the gap element. In fact, this will help in determining the decompression load.

After obtaining the outputs from OpenSEES (Mazzoni et al. 2006), the post processing of the results was carried out using MATLAB. It was also used in plotting the results as well.

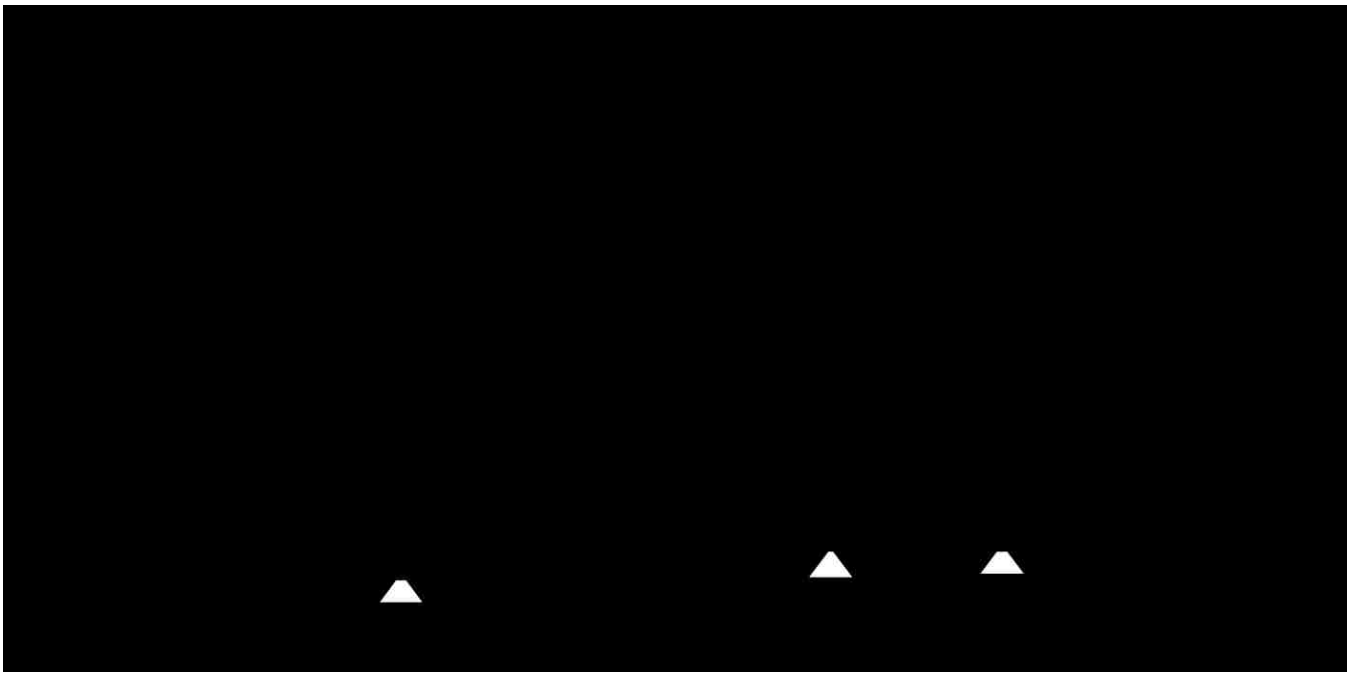

Figure 4.1: FE model for zero eccentricity PT bars (spring stack does not clamp).

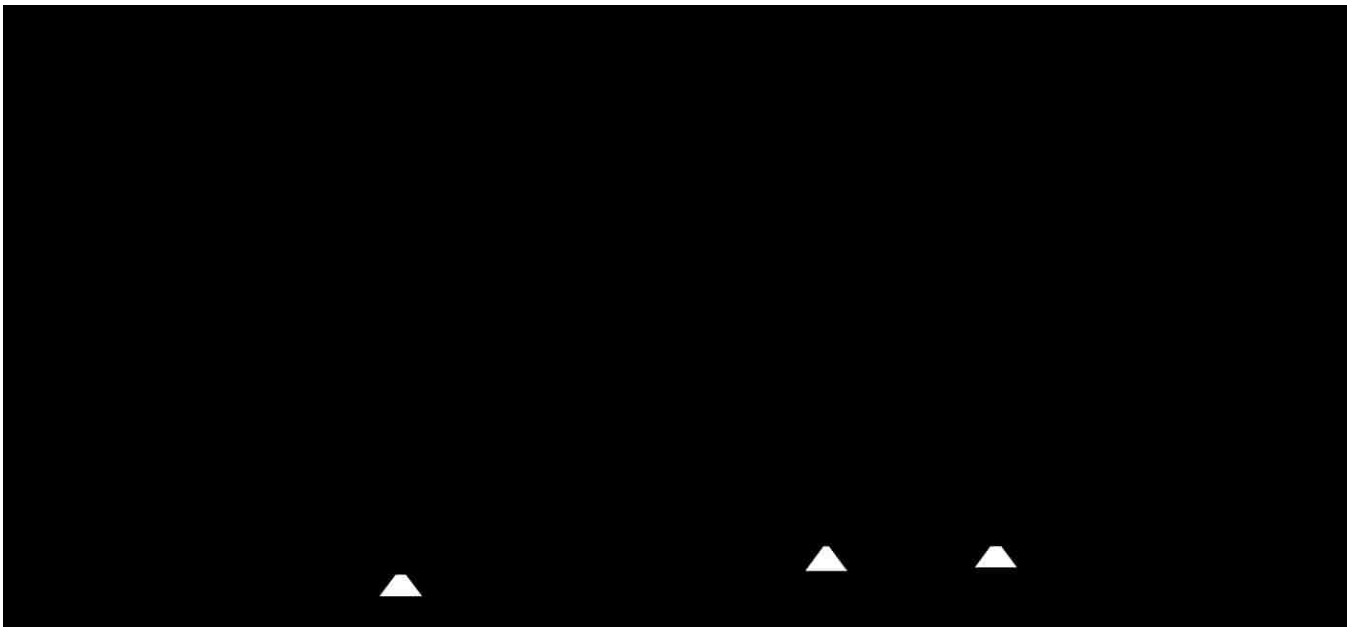

Figure 4.2: FE model for zero eccentricity PT bars (spring stack does clamp).

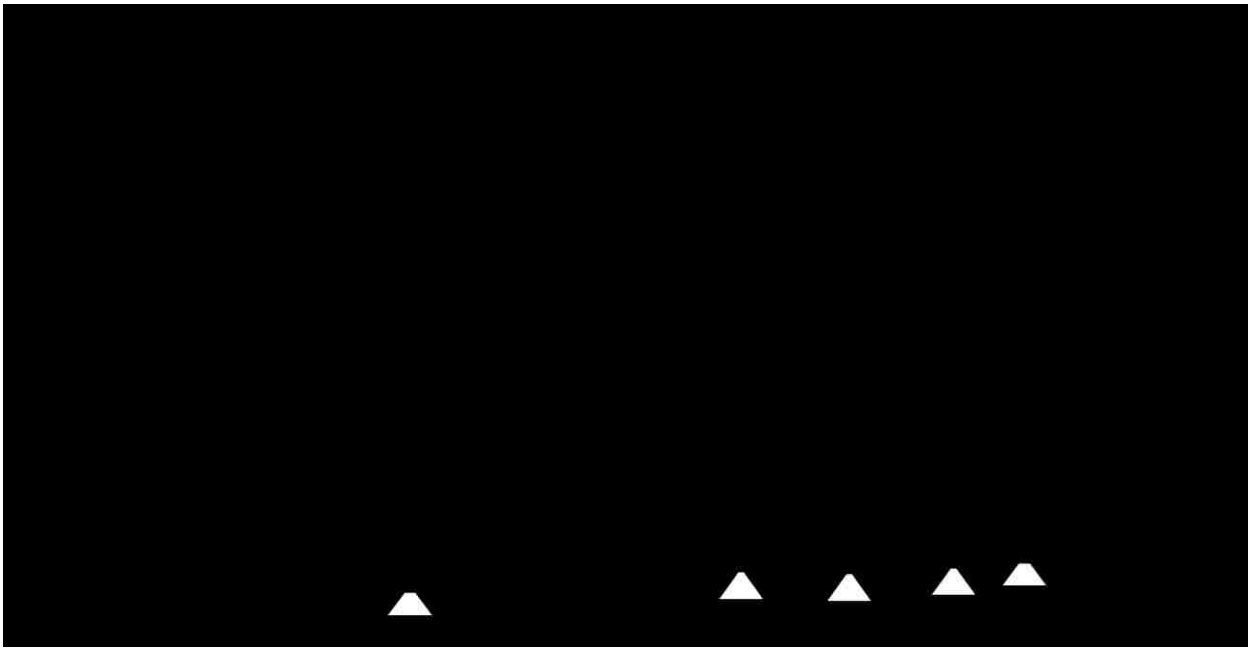

Figure 4.3: FE model for intermediate eccentricity PT bars (spring stack does not clamp).

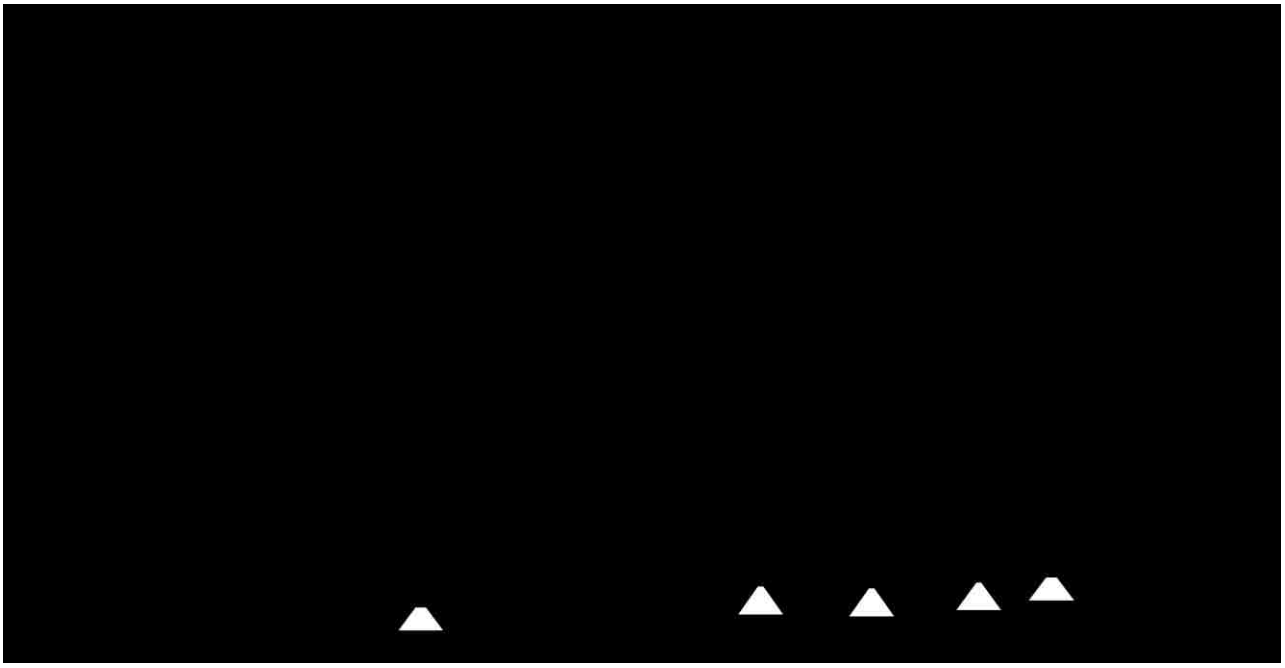

Figure 4.4: FE model for intermediate eccentricity PT bars (spring stack does clamp).

Figure 4.5: Behavior of physical and FE models under compressive load.

Figure 4.6: Gap element force deformation curve (Mazzoni et al. 2006).

Figure 4.7: Force-deformation of ZLS and gap element connected in parallel.

Figure 4.8: Required displacement at the zero-length spring and the initial strain at the truss element to get the required initial PT force.

CHAPTER 5

PROTOTYPE BUILDING

5.1 INTRODUCTION

This chapter provides a description of a prototype building used in this study. The building is made of timber and used here to generate realistic frames for the parametric study. Also, it is used to obtain the analysis matrix for the parametric study in Chapter 6.

5.2 PROTOTYPE BUILDING DESCRIPTION

Figure 5.1 shows a typical floor plan of the prototype building. It consists of three stories (two elevated floors plus the roof). Each story has four bays in the longitudinal direction and three in the transverse direction. In the current study, the analysis focuses on the response of the building in the longitudinal direction, and two rocking frames are used in the longitudinal direction (E-W).

This building is used in the literature to study the traditional post-tensioned walls (Sarti, Palermo, and Pampanin 2016a). It noted that the original building found in the literature has an inclined roof, but it was omitted here for simplicity.

The building represents an office in a region with moderate seismic hazard. It is located in an area with soil type D where the design spectral acceleration is 0.6g for the short period, and 0.2g for the long period. The building system was assumed to have a response

modification factor R=5.5 and an importance factor I=1. The damping ξ is 5% of the critical damping ξ_{cr}.

5.3 PROTOTYPE BUILDING DESIGN

Table 5.1 summarizes the dead loads for the prototype building. Table 5.2 shows the live loads that were determined using the ASCE 7-10 Minimum Design Loads for Buildings and Other Structures. It was assumed that 25% of the live load contributes to the seismic loads. No live load was included on the roof.

The equivalent lateral load force procedure given in ASCE 7-10 is implemented here as follows. We first use the simplified method to calculate the period of the structure (Equation 12.8-7 ASCE7-10).

$$T = ct * h^x = (29.5\ ft)^{0.75} * 0.02 = 0.25\ \text{sec} \tag{5.8}$$

Given the seismic coefficients S_s and S_1 (ASCE 7-10 Figures 22-1 and 22-2), we can determine the "maximum considered earthquake spectral response acceleration parameters."

$$S_{MS} = F_a\ S_s = 0.79 \tag{5.9}$$

$$S_{M1} = F_v\ S_1 = 0.4 \tag{5.10}$$

$$S_{DS} = \left(\frac{2}{3}\right) S_{MS} = 0.52 \tag{5.11}$$

$$S_{D1} = \left(\frac{2}{3}\right) S_{M1} = 0.27 \tag{5.12}$$

$$C_S = \left(\frac{S_{DS}}{\frac{R}{I}}\right) = \left(\frac{0.52}{\frac{5.5}{1}}\right) = 0.096 \tag{5.13}$$

$$C_{S\,min} = \max(0.01, \frac{0.5 * S_1}{\frac{R}{I}}) = 0.018 \tag{5.14}$$

$$C_{s\,max} = \left(\frac{S_{D1}}{\frac{R\,T}{I}}\right) = 0.19 \tag{5.15}$$

$$Base\ shear\ (V) = C_s W = 93\ kips \tag{5.16}$$

The base shear is distributed per ASCE 7-10 Section 12.8.3.

$$V1 = \frac{w_1 h_1^k}{\sum_{n=1} w_i h_i^k}\ V = 19.3\ kips \tag{5.17}$$

$$V2 = \frac{w_2 h_2^k}{\sum_{n=1} w_i h_i^k}\ V = 35.3\ kips \tag{5.18}$$

$$V3 = \frac{w_3 h_3^k}{\sum_{n=1} w_i h_i^k}\ V = 38.4\ kips \tag{5.19}$$

Finally, the overturning moment is

$$Mo = 2256\ kips - ft \tag{5.20}$$

Table 5.1: Floors dead loads.

Element	**Dead Load**
Beams	12.4 psf
Hardwood	4 psf
Wood paneling	2.5 psf
Plywood	3 psf
Plaster	8 psf
Channel suspended system	1 psf
	∑=31 psf

Table 5.2: Roof dead loads.

Element	**Dead Load**
Beams	12.4 psf
Plywood	3 psf
Felt (3 ply)	1.5 psf
Book tile	20 psf
	∑=37 psf

Table 5.3: Floors live loads.

Floor	**Live Load**
First floor	100 psf
Second floor	80 psf

Table 5.4: Seismic weights.

Floor	**Seismic Weight**
First floor	376 kips
Second floor	343 kips
Roof	249 kips

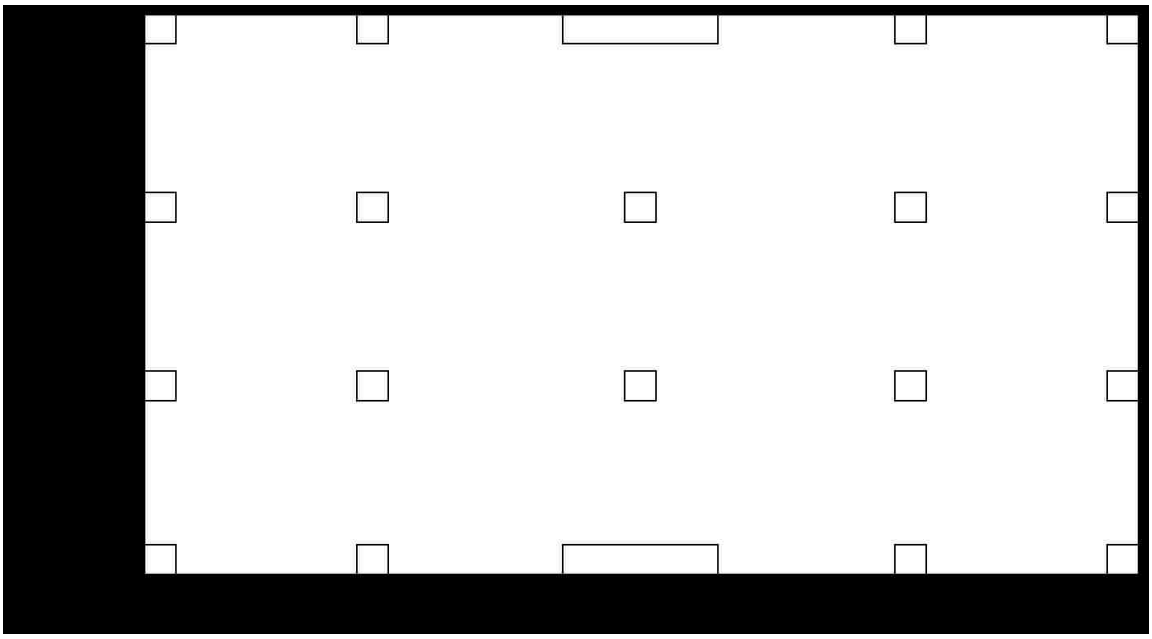

Figure 5.1: Floor plan of the prototype building (Sarti, Palermo, and Pampanin 2016).

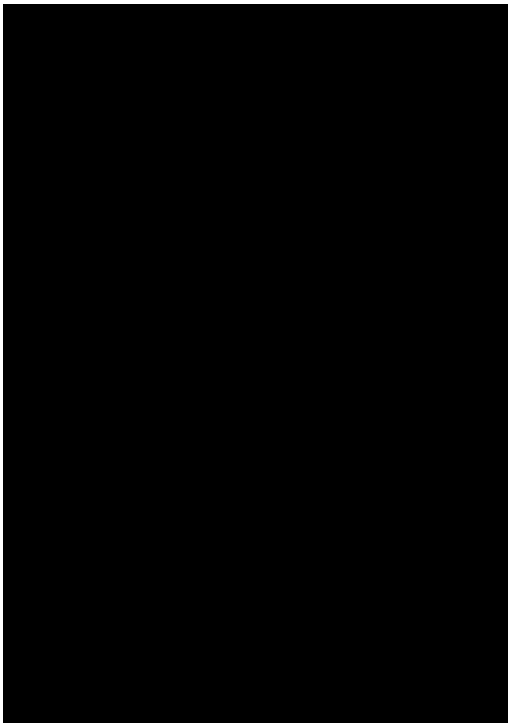

Figure 5.2: Seismic weight distribution for prototype building.

CHAPTER 6

PUSHOVER ANALYSIS RESULTS

6.1 INTRODUCTION

This chapter presents the results of the pushover analyses of a series of prototype frames using the finite element model described in Chapter 4. These prototype frames were subjected to static pushover loads, and the key limit states (e.g. DEC, LLP etc.) were computed and tabulated in this chapter. The limit states were then compared with the limit states determined using the CFE expressions derived in Chapter 3.

6.2 PARAMETRIC STUDY SCHEME

As explained in Chapter 4, the prototype frames were treated as rigid with deformable PT steel. The analyses in this chapter are presented in two groups. The first group is where the spring stack has infinite travel capacity, while the second group is where the spring stack has finite travel capacity and can clamp during pushover loads.

6.3 ANALYSIS ASSUMPTIONS

In the parametric study, several assumptions were made as listed below:

- The pushover loads are modeled as quasi-static, and all the inertial effects are neglected.

- The geometric nonlinearities of the model are neglected.
- The stress-strain curve of the post-tensioning steel is a bilinear curve as shown in Figure 3.1.
- Analyses are performed in a 2D plane.
- The force deformation response of the springs is assumed to be linear.

6.4 PROTOTYPE FRAMES

The prototype building presented in Chapter 5 is used to construct the analysis matrices in this chapter. Remember that Chapter 5 finds the design seismic loads of the prototype building based on the ASCE-10 and using the equivalent lateral force procedure. These seismic loads are used here to tailor the analysis matrices. In the next sections, the term "prototype frames" is used to note the frames in the analysis matrices.

The prototype frames are in two groups: Frames in the first group have spring stacks with infinite travel capacities (i.e. the springs do not clamp during the static pushover analysis). The frames in the second group have spring stacks with finite travel capacities (i.e., the spring stacks do clamp during static pushover analysis). In this report, it is assumed that the clamping of the spring stack takes place at load level corresponding to 0.75 the yielding stress of the PT steel.

Each of the above groups is divided into two sub-groups as shown in Figures 6.1, and 6.2. The first group has PT bars with zero eccentricity (i.e. all the PT bars are positioned at the center of the frame cross-section). The second group has the PT bars with

intermediate eccentricity (i.e. PT bars are placed in three locations along the cross section).

The parametric study in this chapter focuses on the influence of four main parameters: (1) the relative stiffness of the spring stack γ_k; (2) the length of the frame L_f; (3) the initial PT stress F_{pi}; and, (4) the height of the unbonded steel H_{unb}. A description of each parameter is given in the follwing paragraphs.

6.4.1 Relative stiffness of the spring stack (γ_k)

Tables 6.1 and 6.2 are used to study the effects of changing the stiffness of the spring stack on the pushover response. Table 6.1 summarizes the testing matrix of the first group where the spring stack has infinite travel capacity, while Table 6.2 summarizes the testing matrix for the second group where the spring stack has finite travel capacity. In these tables, several parameters need to be defined. Each prototype frame has a unique tag number starting at the beginning of the table. F_{pi} is the initial PT stress. T_{pi} is the initial PT force. H_f is the height of the frame. A_p is the area of the PT bars, and e_p is the distance from center of the frame cross section to the location of the PT bar. L_f is the length of the frame. H_{unb} is the height of the unbonded PT bars. K_p is the axial stiffness of the PT bar, and K_s is the axial stiffness of the spring stack. The relative stiffness of the spring stack (γ_k) is defined as the ratio of the axial stiffness of the spring stack to the stiffness of the PT bar.

$$\gamma_k = \frac{stiffness\ of\ the\ spring\ stack}{stiffness\ of\ the\ post\ tensioning\ bar} \qquad (6.1)$$

The ratio γ_k shows considerable importance since the disc springs can come in different sizes and dimensions. Thus, the designer would have the flexibility to arrange these springs is various ways, leading to different force-deformation behavior.

In this parametric study, the relative stiffness γ_k has the values 0.2, 0.5, 1, 2, 5 as seen in Tables 6.1 and 6.2. The first case, γ_k=0.2 refers to a spring stack that is relatively flexible. However, as γ_k increases, it means the spring stack is increasing in stiffness relative to the axial stiffness of the PT bar.

Tables 6.1 and 6.2 includes two cases F-6 and F-12 where the frames have no spring stacks. These two frames represent the traditional rocking frames, and they were included to provide a reference on how the response is changing as we insert a spring stack.

6.4.2 Length of the frame (L_f)

The length of the frame is defined as the horizontal distance between centerlines of the the columns at the base as shown in Figure 3.3.

The prototype building has a frame length of 120 inches. In the parametric study, we investigate the effects of varying the frame length from to 150 in and 90 in as shown in Figure 6.1. The analysis matrix for this parameter is presented in Table 6.3. Note that all prototype frames in this table have spring stacks with infinite travel capacity.

6.4.3 Initial prestress (F_{pi})

In this parametric study, initial prestress F_{pi} is the stress in the steel prior to application of lateral force. Three values for the initial prestress were considered in this study. These are 0.3, 0.5, and 0.7 the yield stress F_{py} of steel as shown in Table 6.4. Note that all prototype frames in this table have spring stacks with infinite travel capacity.

6.4.3 Height of unbonded steel H_{unb}

The height of unbonded steel H_{unb} is defined as the distance between the two anchorage points of the PT bar as shown in Figure 3.5. The analysis matrix for this parameter is provided in Table 6.5. In all analysis cases, the bottom end of the bar is anchored to the foundation (see Figure 6.2), and the effect of extending these bars to different floors was investigated. As shown in Figure 6.2, the bars are extended to the first, second, and the third floor. Note that all prototype frames in this table have spring stacks with infinite travel capacity.

6.5 RESPONSE QUANTITIES

In the parametric study, several response quantities are of interest as described below.

6.5.1 Moment at decompression (M_{DEC})

The moment at decompression M_{DEC} is defined as the applied moment that causes the vertical reaction at the support to be zero as shown in Figure 3.7.

To determine the decompression moment using the FE model, the axial force of the gap element at the base of the frame shown in Figures 4.1, 4.2, 4.3, 4.4 was recorded. Once the axial force becomes zero, the value of the lateral load that corresponds to this instance is noted and then the moment is determined by multiplying the force by its lever as shown in Figure 3.7.

6.5.2 Drift at decompression (Θ_{DEC})

The drift at decompression Θ_{DEC} is defined as the drift of the frame when decompression occurs at the base of the frame. One of the key assumptions of this parametric study is that the frame is rigid. This is accomplished by assigning very high stiffness values to the FE model. Thus, as noted earlier the drift at decompression will always be zero since elastic deformations are not included.

6.5.3 Moment at yielding of the PT steel (M_{LLP})

The moment at yielding of the PT bar M_{LLP} is defined as the moment at the base of the frame when the force at the PT bar(s) reaches the yield stress. The value for this response was found as follows. The force at the PT steel is recorded, and once it reaches the yield stress, the magnitude of the horizontal load is noted. Now the yielding moment is found by multiplying the force by its arm.

6.5.4 Drift at yielding of the PT steel (Θ_{LLP})

This quantity is defined as the drift of the frame when the PT bar yields. Again, it was determined using the CFE and the FE model simultaneously in this parametric study.

To determine Θ_{LLP} using the FE model, the force at the PT steel is recorded. Once yielding occurs, the corresponding displacement of the roof could be used to determine Θ_{LLP}. On the other hand, the CFE derived in Chapter 3 could also be used to predict this response quantity.

6.5.5 Moment at the fracture of the PT steel (M_{FP})

M_{FP} represents the moment at the base of the frame where the bar on the tension side of the frame fractures. This response quantity is determined the same way as the yielding moment. The method is discussed above in Section 6.5.3, and the only difference is that the force at fracture of the PT bar is noted rather than the yielding force.

6.5.6 Drift at fracture of PT steel (Θ_{FP})

The drift at fracture of the PT steel is defined as the drift of the frame when the PT steel fractures. It was determined using the CFE and the FE model simultaneously. The same procedure to identifying the drift at yielding is used to determine the drift at fracture, but the only change is that we are noting the lateral displacement when the PT bar fractures.

6.6 RESULTS OF THE PARAMETRIC STUDY

This section presents the results of the analyses. The results are divided into two groups. The first group is having spring stack infinite travel capacity. The second group has spring stack with finite travel capacity.

6.6.1 Results for the first group

6.6.1.1 Relative stiffness (γ_K)

Figure 6.3 shows the effects of changing the relative stiffness γ_k of the spring stack on the response of the frames with zero eccentricity. We can see that all the frames decompressed at the same load level. Also, no deformations before the gap opening are seen due to the rigid frame assumption.

The stiffness of the spring seems to influence the response significantly. For example, Table 6.2 shows that F-5 yielded at a drift of 1.1%, whereas F-2 yielded at a drift of 2.8%. The only difference between F-2 and F-5 is that the later one has stiff spring stack (γ_k= 5), whereas frame 2 has flexible spring stack (γ_k=0.2). It seems that adding flexible spring stack increases the drift Θ_{LLP} of the frame because the gap height at the location of the PT bar is the sum of the PT bar elongation and the spring stack shortening (i.e. the spring stack shortening and the gap height at the PT location would be large when flexible spring stack is used, and this increases the drift Θ_{LLP}). Note that for a given PT bar force, the flexible spring stack shortens more that the stiff one and this explains why the gap height at the PT location is larger when flexible spring stack is added.

Figure 6.4 shows the response of F-10 which has intermediate eccentricity. The response starts with decompression of the base. Then, the force at the PT bars is increasing because of the increased lateral load as shown in Figure 6.4. After that, the bar at the end of the frame yields leading to a reduction of the lateral stiffness of the frame. It could also be seen in Figure 6.4 that the bars are yielding successively and the stiffness is decreasing gradually. Moreover, the frame can still carry the load even though one of the bars is damaged by yielding.

Figure 6.5 shows the response the entire group with intermediate eccentricity and some interesting observations are made. First, the group with intermediate eccentricity has concave moment-drift curve due to the successive yielding of the bars. Second, the zero-eccentricity group carries larger moment M_{LLP} at the LLP limit and more drift Θ_{LLP} than the intermediate eccentricity group. Third, the spring stack stiffness plays a major role in determining the backbone of the moment-drift curve. For instance, F-7 yielded at a drift of 3.7%, but F-11 yielded at significantly less drift of 0.7%. The reason for that is because F-11 has stiff spring (γ_k=5). Notice this behavior was seen earlier in frames with zero eccentricity, and this is due to the same reason that flexible spring stack causes more shortening of the spring stack and more Θ_{LLP} accordingly.

A summary of the results for the parameter is shown in Table 6.6. The table summarizes the results presented in Figures 6.3 and 6.5. The table shows that the response obtained by the FE model and predicted by the closed-form expressions are in good agreement. The table demonstrates that the CEF are, in general, accurate in predicting the response for a range of γ_k values. However, the errors increase for the larger drifts corresponding

to the fracture of the PT bars. This is because the closed form equations developed is Chapter 3 were simplified by the use of the small deformations theory. It is noted that the closed form expressions under predict the drift at fracture of the PT reinforcement, and thus may provide a conservative estimate of the drift.

6.6.1.2 Length of the frame (L_f)

Figure 6.6 shows the effects of changing the length of frames with zero eccentricity. The frames have lengths of 90,120, and 150 inches, and spring stacks with γ_k=0.2 (flexible spring stack), and γ_k=5 (stiff spring stack).

Figure 6.6 shows that increasing the frame length and keeping the stiffness of the springs constant increases the decompression moment. Hence, the moment of inertia of frame footprint is larger. Figure 6.6 also showes that the drift at yielding Θ_{LLP} is decreasing as we increase the frame length, and this is because the same gap height would result in smaller drift if the frame length is increased (i.e. the drift angle is the gap height divided by the horizontal distance, and in our case the gap is constant, but the horizontal distance is increasing and leading to smaller drift Θ_{LLP}).

The stiffness of the spring impacts the drift at yielding. In all cases for the same frame length, using flexible spring stack resulted in larger drift at yielding Θ_{LLP} as shown in Figure 6.6.

Figure 6.7 shows the effects of changing the frame length of frames with an intermediate eccentricity. Again, we can see that increasing the frame length increases the

decompression moment and decreases the drift at yielding. Also, the more flexible spring stack permitted a larger drift prior to yielding the bars.

Table 6.7 summarizes the results for this parameter and compares the results obtained by FE, and the CFE. The table shows good agreement between the results predicted using the closed form expressions and the results obtained from the FE analyses. Again, the largest errors are associated with the drift at fracture of the PT steel, with CFE under predicting the drift at fracture.

6.6.1.3 Initial stress (F_{pi})

Figures 6.8, 6.9, 6.10, 6.11 show the response for the cases where the initial stress in the PT bars is varied. As we apply more initial stress at the PT bars, the decompression moment increases since the force over the area increases at base of frame, so larger moment is needed. Further, the drift at yielding is decreasing since the bars will deform less before they yield.

Figure 6.8 to 6.11 also show that using flexible spring stack springs can alter the backbone curve leading to more drift even if we apply tremendous initial stress.

Table 6.8 summarizes the results for this parameter, and it shows that the CEF can accurately enough to predict the response for a range of initial prestress values.

6.6.1.4 Unbonded length (H_{unb})

Figures 6.12 and 6.13 illustrate the effects of decreasing the unbonded length of the PT steel for frames with zero eccentricity. The figures show that decreasing the unbonded

length increases the lateral stiffness of the frame and reduces the drift capacity at yielding of the PT bar. This is because the shorter bars have a higher axial stiffness than the longer bars.

Comparison of Figures 6.12 and 6.13 shows that introducing a flexible spring stack reduces the lateral stiffness even with a small unbonded length. Also, the drift capacity increases as flexible spring stack is introduced.

Figures 6.14 and 6.15 show the response of frames with intermediate eccentricity. As in earlier plots, we can see that successive yielding of the bars is still occurring, and the introduction of the flexible spring increased the drift at yielding of PT bars.

The results of the initial stress F_{pi} parameter study are shown in Table 6.9. This table shows that the error between the CFE and FE results is small.

6.6.2 Results for the second group

6.6.2.1 Relative stiffness (γ_k)

Figure 6.17-(a) shows the backbone curve of F-38 under pushover load. After decompression, the force at the PT bar increases until it reaches 0.75 F_{py} which corresponds to the clamping of the spring stack. Once clamping occurs, the spring element in the FE model no longer deforms, and this causes a sudden increase in the force of the PT bar as seen in Figure 6.17-(b). Correspondingly, F-38 exhibits increased lateral stiffness after the clamping of the spring stack as seen in Figure 6.17-(a). Figure 6.17-(c) shows the force at the gap element. This figure shows that this gap element starts to carry force after the clamping of the spring stack. In fact, the gap element must carry

all the force developed in the PT bar after clamping without permitting the spring stack deform further.

Figure 6.16 shows the effects of changing the relative stiffness of the spring stack for frames with zero eccentricity. Unlike the response attained earlier in Section 6.6.1.1, the spring stack clamps at a load level of 0.75 the yield stress of the steel.

Interestingly, the frames increase in stiffness after the clamping of the spring stack. However, the clamping occurs at different drifts since the γ_k for each frame is different, with larger drifts found when more flexible spring stacks are used.

Figure 6.18 shows the moment drift response of F-44, and it indicates that the frame started with decompression. Then, the first spring stack reached clamping followed by yielding of the PT bar. The process of successive clamping and yielding happens to all the PT groups. However, each clamping is followed by gain in the stiffness whereas each yielding of the PT bar is followed by a reduction in the lateral stiffness.

Figure 6.19 shows the response of frames with intermediate eccentricity. Similar to the results in Figure 6.18, the frames are exhibiting multiple occurrence of clamping and yielding. The frames gain stiffness due to each spring stack clamping, followed by a loss of stiffness due to yielding of the PT bar. Also, we can notice that using flexible stack of springs led to more drift and less lateral stiffness after the gap opening. The results for this parameter variation are summarized in Table 6.10.

6.7 CONCLUSIONS

1. The closed form expressions derived in Chapter 3 display an excellent agreement with the FE results. However, the error of drift at bar fracture becomes higher for large drifts because the CFE were simplified using the small deformation theory.
2. Even though a rocking frame has constant member dimensions and PT steel area, connecting the PT steel in series with a spring stack having variable stiffness could change the backbone curve under lateral loads.
3. The use of flexible disc spring stack connected in series with the PT steel increases the drift capacity and delayes the onset of the PT steel yielding.
4. The use of flexible disc spring stack causes the prototype frames to have low lateral stiffness after the gap opening (DEC limit state) at the base. In contrast, the use of stiff disc spring stack increases the lateral stiffness.
5. When the PT steel was extended to the roof of the prototype frames, some frames displayed large drifts without reaching the nominal moment capacity of the frame (i.e. PT steel yielding). However, the parametric study showed that limiting the height of the PT bars to only the first floor instead of the roof would reduce the lateral drift at yielding of the PT bars.

   This phenomenon suggests that the use of spring stacks could eliminate the need to extend the PT bars to higher floor levels. This offers two significant advantages:

   - In standard rocking frame with full height post-tensioning, all the structural elements of columns and braces below the anchorage point of

the PT bars must be designed to accommodate the large PT force that develops during the application of the lateral load. However, limiting the height of the PT bars to, for example, the first floor would eliminate the need to design the elements above the first floor for these larger forces.

- Limiting the PT bars to lower stories would require less total length of PT bars.

The disadvantage of limiting the PT bars to only lower floor levels is that the PT steel is unable to assist with self-centering the floor above the anchorage point if they encounter permanent lateral deformations (floors 2 and 3 in Figures 6.20 and 6.21.

6. When the spring stack has finite travel capacity, clamping can occur leading to increase in the lateral stiffness and sudden increase in PT steel force.

Table 6.1: Analysis matrix (relative stiffness of the spring stack γ_k).

Frame	$F_{pi}=0.5F_y$	T_{pi}	$\sum T_{pi}$	H_w	L_f	Number of bars	A_p	e_p	e_p/L_w	H_{unb}	K_p	K_s	K_s/K_p
1	72.5	172	172	396	120	3	2.37	0	0	396	174	35	0.2
2	72.5	172	172	396	120	3	2.37	0	0	396	174	87	0.5
3	72.5	172	172	396	120	3	2.37	0	0	396	174	174	1
4	72.5	172	172	396	120	3	2.37	0	0	396	174	347	2
5	72.5	172	172	396	120	3	2.37	0	0	396	174	868	5
6	72.5	172	172	396	120	3	2.37	0	0	396	174	-	-
7	72.5	57	172	396	120	1-1-1	0.79	30-0-30	0.25-0-0.25	396	58	12	0.2
8	72.5	57	172	396	120	1-1-1	0.79	30-0-30	0.25-0-0.25	396	58	29	0.5
9	72.5	57	172	396	120	1-1-1	0.79	30-0-30	0.25-0-0.25	396	58	58	1
10	72.5	57	172	396	120	1-1-1	0.79	30-0-30	0.25-0-0.25	396	58	116	2
11	72.5	57	172	396	120	1-1-1	0.79	30-0-30	0.25-0-0.25	396	58	289	5
12	72.5	57	172	396	120	1-1-1	0.79	30-0-30	0.25-0-0.25	396	58	-	-
- No spring													

Table 6.2: Analysis matrix: relative stiffness of the spring stack γ_k

(spring stack clamps at PT stress of 0.75 F_{py}).

Frame	$F_{pi}=0.5F_y$	T_{pi}	$\sum T_{pi}$	H_w	L_f	Number of bars	A_p	e_p	e_p/L_w	H_{unb}	K_p	K_s	K_s/K_p
37	72.5	172	172	396	120	3	2.37	0	0	396	174	35	0.2
38	72.5	172	172	396	120	3	2.37	0	0	396	174	87	0.5
39	72.5	172	172	396	120	3	2.37	0	0	396	174	174	1
40	72.5	172	172	396	120	3	2.37	0	0	396	174	347	2
41	72.5	172	172	396	120	3	2.37	0	0	396	174	868	5
6	72.5	172	172	396	120	3	2.37	0	0	396	174	-	-
43	72.5	57	172	396	120	1-1-1	0.79	30-0-30	0.25-0-0.25	396	58	12	0.2
44	72.5	57	172	396	120	1-1-1	0.79	30-0-30	0.25-0-0.25	396	58	29	0.5
45	72.5	57	172	396	120	1-1-1	0.79	30-0-30	0.25-0-0.25	396	58	58	1
46	72.5	57	172	396	120	1-1-1	0.79	30-0-30	0.25-0-0.25	396	58	116	2
47	72.5	57	172	396	120	1-1-1	0.79	30-0-30	0.25-0-0.25	396	58	289	5
12	72.5	57	172	396	120	1-1-1	0.79	30-0-30	0.25-0-0.25	396	58	-	-
- No spring													

Table 6.3: Analysis matrix: length of the frame L_f.

Frame	$F_{pi}=0.5F_y$	T_{pi}	H_w	L_f	Number of bars	A_p	e_p	e_p/L_w	H_{unb}	K_p	K_s	K_s/K_p
13	72.5	172	396	90	3	2.37	0	0	396	174	87	0.5
14	72.5	172	396	90	3	2.37	0	0	396	174	347	2
2	72.5	172	396	120	3	2.37	0	0	396	174	87	0.5
4	72.5	172	396	120	3	2.37	0	0	396	174	347	2
15	72.5	172	396	150	3	2.37	0	0	396	174	87	0.5
16	72.5	172	396	150	3	2.37	0	0	396	174	347	2
17	72.5	57	396	90	1-1-1	0.79	30-0-30	0.25-0-0.25	396	58	29	0.5
18	72.5	57	396	90	1-1-1	0.79	30-0-30	0.25-0-0.25	396	58	116	2
8	72.5	57	396	120	1-1-1	0.79	30-0-30	0.25-0-0.25	396	58	29	0.5
10	72.5	57	396	120	1-1-1	0.79	30-0-30	0.25-0-0.25	396	58	116	2
19	72.5	57	396	150	1-1-1	0.79	30-0-30	0.25-0-0.25	396	58	29	0.5
20	72.5	57	396	150	1-1-1	0.79	30-0-30	0.25-0-0.25	396	58	116	2

Table 6.4: Analysis matrix: initial stress F_{pi}.

Frame	%F_{pi}	F_{pi}	T_{pi}	H_w	L_f	Number of bars	A_p	e_p	e_p/L_w	H_{unb}	K_p	K_s	K_s/K_p
21	0.3Fy	43.5	103	396	120	3	2.37	0	0	396	174	87	0.5
22	0.3Fy	43.5	103	396	120	3	2.37	0	0	396	174	347	2
2	0.5Fy	72.7	172	396	120	3	2.37	0	0	396	174	87	0.5
4	0.5Fy	72.5	172	396	120	3	2.37	0	0	396	174	347	2
23	0.7Fy	101.5	241	396	120	3	2.37	0	0	396	174	87	0.5
24	0.7Fy	101.5	241	396	120	3	2.37	0	0	396	174	347	2
25	0.3Fy	43.5	34	396	120	1-1-1	0.79	30-0-30	0.25-0-0.25	396	58	29	0.5
26	0.3Fy	43.5	34	396	120	1-1-1	0.79	30-0-30	0.25-0-0.25	396	58	116	2
8	0.5Fy	72.7	57	396	120	1-1-1	0.79	30-0-30	0.25-0-0.25	396	58	29	0.5
10	0.5Fy	72.5	57	396	120	1-1-1	0.79	30-0-30	0.25-0-0.25	396	58	116	2
27	0.7Fy	101.5	80	396	120	1-1-1	0.79	30-0-30	0.25-0-0.25	396	58	29	0.5
28	0.7Fy	101.5	80	396	120	1-1-1	0.79	30-0-30	0.25-0-0.25	396	58	116	2

Table 6.5: Analysis matrix: height of the unbonded length H_{unb}.

Frame	$F_{pi}=0.5F_y$	T_{pi}	H_w	L_f	Number of bars	A_p	e_p	e_p/L_w	H_{unb}	K_p	K_s	K_s/K_p
29	72.5	172	396	120	3	2.37	0	0	132	521	260	0.5
30	72.5	172	396	120	3	2.37	0	0	132	521	1041	2
31	72.5	172	396	120	3	2.37	0	0	264	260	130	0.5
32	72.5	172	396	120	3	2.37	0	0	264	260	521	2
2	72.5	172	396	120	3	2.37	0	0	396	174	87	0.5
4	72.5	172	396	120	3	2.37	0	0	396	174	347	2
33	72.5	57	396	120	1-1-1	0.79	30-0-30	0.25-0-0.25	132	174	87	0.5
34	72.5	57	396	120	1-1-1	0.79	30-0-30	0.25-0-0.25	132	174	347	2
35	72.5	57	396	120	1-1-1	0.79	30-0-30	0.25-0-0.25	264	87	43	0.5
36	72.5	57	396	120	1-1-1	0.79	30-0-30	0.25-0-0.25	264	87	174	2
8	72.5	57	396	120	1-1-1	0.79	30-0-30	0.25-0-0.25	396	58	29	0.5
10	72.5	57	396	120	1-1-1	0.79	30-0-30	0.25-0-0.25	396	58	116	2

Table 6.6: Analyses results: relative stiffness γ_k.

Frame	$Mdec$ (kips-in)			Θdec (%)		$Mllp$ (kips-in)			Θllp (%)			Mfp (kips-in)			Θfp (%)		
	CFE	FE	Error %	CFE	FE	CFE	FE	Error %	CFE	FE	Error %	CFE	FE	Error %	CFE	FE	Error %
1	859	859	0.0	0.0	0.0	1718	1718	0	5.6	5.6	0.0	1896	1902	-0.3	25.5	27.1	-5.9
2	859	859	0.0	0.0	0.0	1718	1718	0	2.8	2.8	0.0	1896	1902	-0.3	22.7	24.2	-6.2
3	859	859	0.0	0.0	0.0	1718	1718	0	1.9	1.9	0.0	1896	1902	-0.3	21.7	23.0	-5.7
4	859	859	0.0	0.0	0.0	1718	1718	0	1.4	1.4	0.0	1896	1902	-0.3	21.2	22.8	-7.0
5	859	859	0.0	0.0	0.0	1718	1718	0	1.1	1.1	0.0	1896	1902	-0.3	20.9	22.4	-6.7
6	859	859	0.0	0.0	0.0	1718	1718	0	0.9	0.9	0.0	1896	1902	-0.3	20.7	22.2	-6.8
7	859	859	0.0	0.0	0.0	1527	1528	-0.1	3.7	3.8	-2.6	1855	1847	0.4	17.7	19	-6.8
8	859	859	0.0	0.0	0.0	1527	1528	-0.1	1.9	1.9	0.0	1839	1847	-0.4	15.6	16.5	-5.4
9	859	859	0.0	0.0	0.0	1527	1528	-0.1	1.2	1.2	0.0	1844	1853	-0.4	14.9	16.2	-8.0
10	859	859	0.0	0.0	0.0	1527	1528	-0.1	0.9	0.9	0.0	1847	1855	-0.4	14.5	16	-9.3
11	859	859	0.0	0.0	0.0	1527	1528	-0.1	0.7	0.7	0.0	1849	1855	-0.3	14.3	15.5	-7.7
12	859	859	0.0	0.0	0.0	1527	1528	-0.1	0.6	0.6	0.0	1850	1855	-0.2	14.1	15.5	-9.0

Table 6.7: Analyses results: length of the frame L_f.

Frame	M_{dec} (kips-in)			Θ_{dec} (%)		M_{llp} (kips-in)			Θ_{llp} (%)			M_{fp} (kips-in)			Θ_{fp} (%)		
	CFE	FE	Error %	CFE	FE	CFE	FE	Error %	CFE	FE	Error %	CFE	FE	Error %	CFE	FE	Error %
13	644	645	-0.2	0.0	0.0	1288	1290	-0.2	3.7	3.7	0.0	1422	1461	-2.7	29.2	31.2	-6.4
14	644	645	-0.2	0.0	0.0	1288	1290	-0.2	1.9	1.9	0.0	1422	1461	-2.7	27.4	29.9	-8.4
2	859	859	0.0	0.0	0.0	1718	1718	0.0	2.8	2.8	0.0	1896	1902	-0.3	22.7	24.2	-6.2
4	859	859	0.0	0.0	0.0	1718	1718	0.0	1.4	1.4	0.0	1896	1902	-0.3	21.2	22.8	-7.0
15	1073	1075	-0.2	0.0	0.0	2147	2149	-0.1	2.2	2.2	0.0	2370	2387	-0.7	18.5	20.0	-7.5
16	1073	1075	-0.2	0.0	0.0	2147	2149	-0.1	1.1	1.1	0.0	2370	2387	-0.7	17.3	18.9	-8.5
17	644	645	-0.2	0.0	0.0	1145	1145	0.0	2.5	2.5	0.0	1379	1392	-0.9	20.4	22.3	-8.5
18	644	645	-0.2	0.0	0.0	1145	1145	0.0	1.2	1.2	0.0	1385	1392	-0.5	19.0	20.7	-8.2
8	859	859	0.0	0.0	0.0	1527	1528	-0.1	1.9	1.9	0.0	1839	1847	-0.4	15.6	16.5	-5.5
10	859	859	0.0	0.0	0.0	1527	1528	-0.1	0.9	0.9	0.0	1847	1855	-0.4	14.5	16.0	-9.4
19	1073	1074	-0.1	0.0	0.0	1909	1909	0.0	1.5	1.5	0.0	2299	2310	-0.5	12.6	13.3	-5.3
20	1073	1074	-0.1	0.0	0.0	1909	1909	0.0	0.7	0.7	0.0	2309	2316	-0.3	11.7	12.6	-7.1

Table 6.8: Analyses results: initial stress F_{pi}.

Frame	M_{dec} (kips-in)			Θ_{dec} (%)		M_{llp} (kips-in)			Θ_{llp} (%)			M_{fp} (kips-in)			Θ_{fp} (%)		
	CFE	FE	Error %	CFE	FE	CFE	FE	Error %	CFE	FE	Error %	CFE	FE	Error %	CFE	FE	Error %
21	515	517	-0.4	0.0	0.0	1718	1718	0.0	3.9	3.9	0.0	1896	1909	-0.7	23.7	25.4	-6.7
22	515	517	-0.4	0.0	0.0	1718	1718	0.0	2.0	2.0	0.0	1896	1909	-0.7	21.7	23.5	-7.7
2	859	859	0.0	0.0	0.0	1718	1718	0.0	2.8	2.8	0.0	1896	1902	-0.3	22.7	24.2	-6.2
4	859	859	0.0	0.0	0.0	1718	1718	0.0	1.4	1.4	0.0	1896	1902	-0.3	21.2	22.8	-7.0
23	1202	1204	-0.2	0.0	0.0	1718	1718	0.0	1.7	1.7	0.0	1896	1909	-0.7	21.7	23.5	-7.7
24	1202	1204	-0.2	0.0	0.0	1718	1718	0.0	0.8	0.8	0.0	1896	1909	-0.7	20.7	22.6	-8.4
25	515	517	-0.4	0.0	0.0	1451	1453	-0.1	2.6	2.6	0.0	1849	1854	-0.3	16.3	17.8	-8.4
26	515	517	-0.4	0.0	0.0	1451	1453	-0.1	1.3	1.3	0.0	1852	1854	-0.1	14.9	16.4	-9.1
8	859	859	0.0	0.0	0.0	1527	1528	-0.1	1.9	1.9	0.0	1839	1847	-0.4	15.6	16.5	-5.5
10	859	859	0.0	0.0	0.0	1527	1528	-0.1	0.9	0.9	0.0	1847	1855	-0.4	14.5	16.0	-9.4
27	1202	1225	-1.9	0.0	0.0	1603	1632	-1.8	1.1	1.1	0.0	1853	1884	-1.6	14.9	15.9	-6.3
28	1202	1225	-1.9	0.0	0.0	1603	1632	-1.8	0.5	0.5	0.0	1859	1884	-1.3	14.1	15.1	-6.6

Table 6.9: Analyses results: height of the unbonded length H_{unb}.

Frame	M_{dec} (kips-in)			Θ_{dec} (%)		M_{llp} (kips-in)			Θ_{llp} (%)			M_{fp} (kips-in)			Θ_{fp} (%)		
	CFE	FE	Error %	CFE	FE	CFE	FE	Error %	CFE	FE	Error %	CFE	FE	Error %	CFE	FE	Error %
29	859	859	0.0	0.0	0.0	1718	1718	0.0	0.9	0.9	0.0	1896	1891	0.3	7.9	8.6	-8.1
30	859	859	0.0	0.0	0.0	1718	1718	0.0	0.4	0.4	0.0	1896	1906	-0.5	7.4	8.0	-7.5
31	859	859	0.0	0.0	0.0	1718	1718	0.0	1.9	1.9	0.0	1896	1949	-2.7	15.6	16.9	-7.7
32	859	859	0.0	0.0	0.0	1718	1718	0.0	0.9	0.9	0.0	1896	1955	-3.0	14.5	15.8	-8.2
2	859	859	0.0	0.0	0.0	1718	1718	0.0	2.8	2.8	0.0	1896	1902	-0.3	22.7	24.2	-6.2
4	859	859	0.0	0.0	0.0	1718	1718	0.0	1.4	1.4	0.0	1896	1902	-0.3	21.2	22.8	-7.0
33	859	859	0.0	0.0	0.0	1527	1527	0.0	0.6	0.6	0.0	1851	1854	-0.2	5.3	5.7	-7.0
34	859	859	0.0	0.0	0.0	1527	1527	0.0	0.3	0.3	0.0	1853	1854	-0.1	4.9	5.3	-7.5
35	859	859	0.0	0.0	0.0	1527	1527	0.0	1.2	1.2	0.0	1851	1854	-0.2	10.5	11.5	-8.7
36	859	859	0.0	0.0	0.0	1527	1552	-1.6	0.6	0.6	0.0	1853	1884	-1.6	9.8	10.4	-5.8
8	859	859	0.0	0.0	0.0	1527	1528	-0.1	1.9	1.9	0.0	1839	1847	-0.4	15.6	16.5	-5.5
10	859	859	0.0	0.0	0.0	1527	1528	-0.1	0.9	0.9	0.0	1847	1855	-0.4	14.5	16.0	-9.4

Table 6.10: analyses results: relative stiffness of the spring stack γk

(spring stack clamps at PT bar stress of 0.75 F_{py}).

Frame	M_{dec} (kips-in)			Θ_{dec} (%)		M_{llp} (kips-in)			Θ_{llp} (%)			M_{fp} (kips-in)			Θ_{fp} (%)			M_{fc} (kips-in)			Θ_{fc} (%)		
	CFE	FE	Error %	CFE	FE	CFE	FE	Error %	CFE	FE	Error %	CFE	FE	Error %	CFE	FE	Error %	FE	CFE	Error %	CFE	FE	Error %
37	859	860.6	-0.1	0.0	0.0	1718.3	1718.6	0	3.3	3.3	0.0	1896.0	1895.5	0.0	22.8	24.3	-6.2	1290.9	1288.7	-0.2	2.8	2.8	0.0
38	859	860.6	-0.1	0.0	0.0	1718.3	1718.6	0	1.9	1.9	0.0	1896.0	1895.5	0.0	21.6	23.1	-6.5	1290.9	1288.7	-0.2	1.4	1.4	0.0
39	859	860.6	-0.1	0.0	0.0	1718.3	1718.6	0	1.4	1.4	0.0	1896.0	1895.5	0.0	21.2	22.7	-6.6	1290.9	1288.7	-0.2	0.9	0.9	0.0
40	859	860.6	-0.1	0.0	0.0	1718.3	1718.6	0	1.2	1.2	0.0	1896.0	1895.5	0.0	21.0	22.5	-6.7	1290.9	1288.7	-0.2	0.7	0.7	0.0
41	859	860.6	-0.1	0.0	0.0	1718.3	1718.6	0	1.0	1.0	0.0	1896.0	1895.5	0.0	20.8	22.4	-7.1	1290.9	1288.7	-0.2	0.5	0.5	0.0
42	859	860.6	-0.1	0.0	0.0	1718.3	1718.6	0	0.9	0.9	0.0	1896.0	1895.5	0.0	20.7	22.3	-7.2	1290.9	1288.7	-0.2	0.4	0.4	0.0
43	859	860.6	-0.1	0.0	0.0	1427.9	1428.2	0.0	2.2	2.2	0.0	1850.5	1850.6	0.0	15.6	16.8	-7.1	1193.2	1193.2	0.0	1.9	1.9	0.0
44	859	860.6	-0.1	0.0	0.0	1447.8	1449.3	-0.1	1.2	1.2	0.0	1852.9	1853.2	0.0	14.7	16.0	-8.1	1193.2	1193.2	0.0	0.9	0.9	0.0
45	859	860.6	-0.1	0.0	0.0	1467.7	1470.5	-0.2	0.9	0.9	0.0	1853.8	1853.3	0.0	14.5	15.6	-7.1	1193.2	1193.2	0.0	0.6	0.6	0.0
46	859	860.6	-0.1	0.0	0.0	1495.5	1496.9	-0.1	0.79	0.78	1.28	1854.3	1853.3	0.1	14.3	15.4	-7.1	1193.2	1193.2	0.0	0.4	0.4	0.0
47	859	860.6	-0.1	0.0	0.0	1513.8	1515.3	-0.1	0.7	0.7	0.0	1854.5	1855.9	-0.1	14.2	15.3	-7.2	1193.2	1193.2	0.0	0.3	0.3	0.0
48	859	860.6	-0.1	0.0	0.0	1527.3	1528.5	-0.1	0.6	0.6	0.0	1854.7	1855.9	-0.1	14.2	15.2	-6.6	1193.2	1193.2	0.0	0.3	0.3	0.0

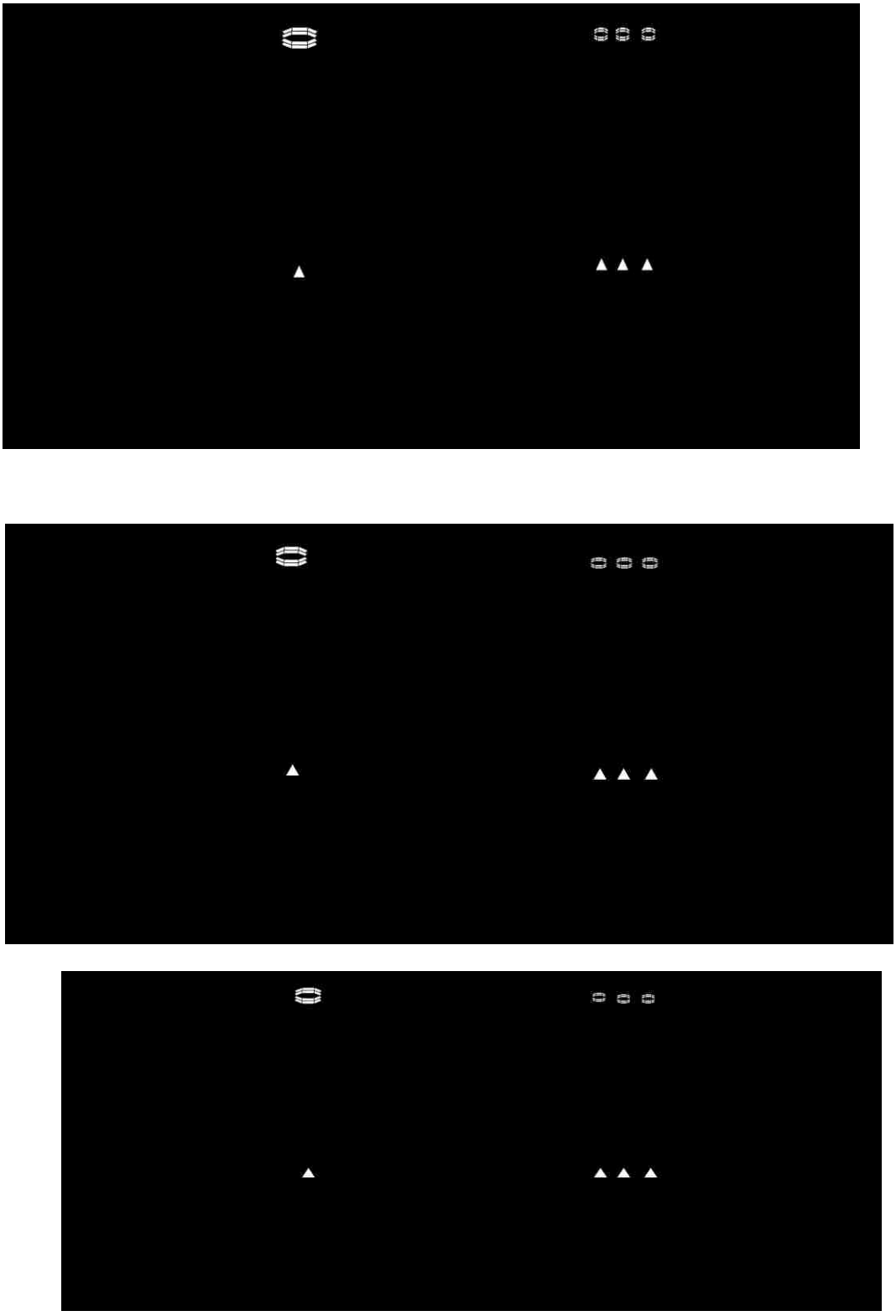

Figure 6.1: Length of the frame L_f in this parametric study where γ_k is ranging from 0.2 to 5.

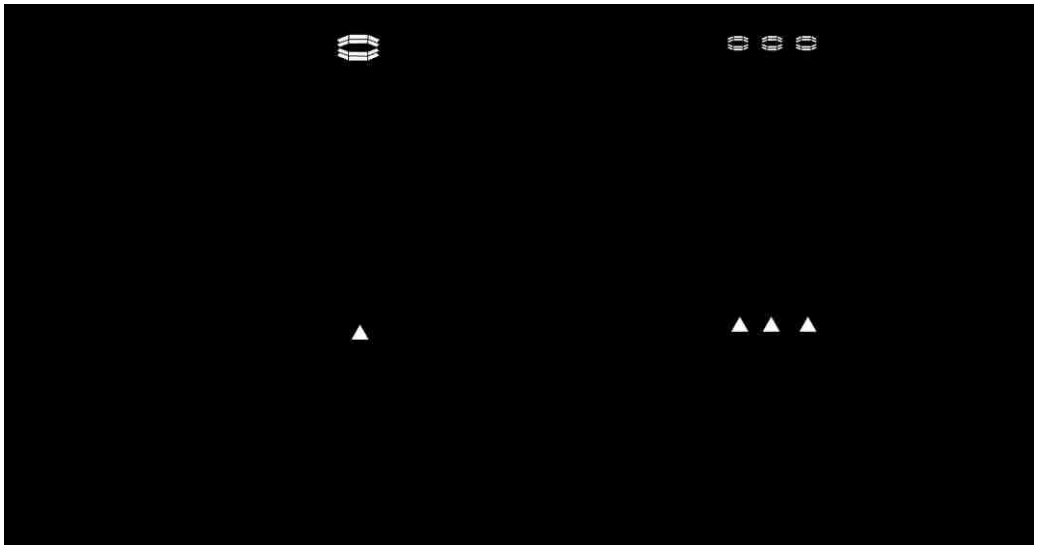

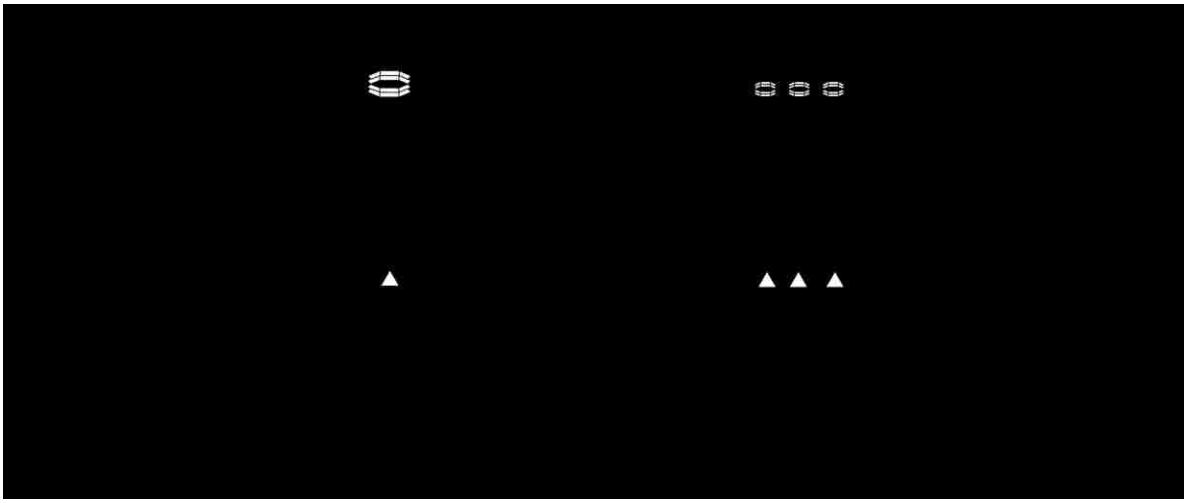

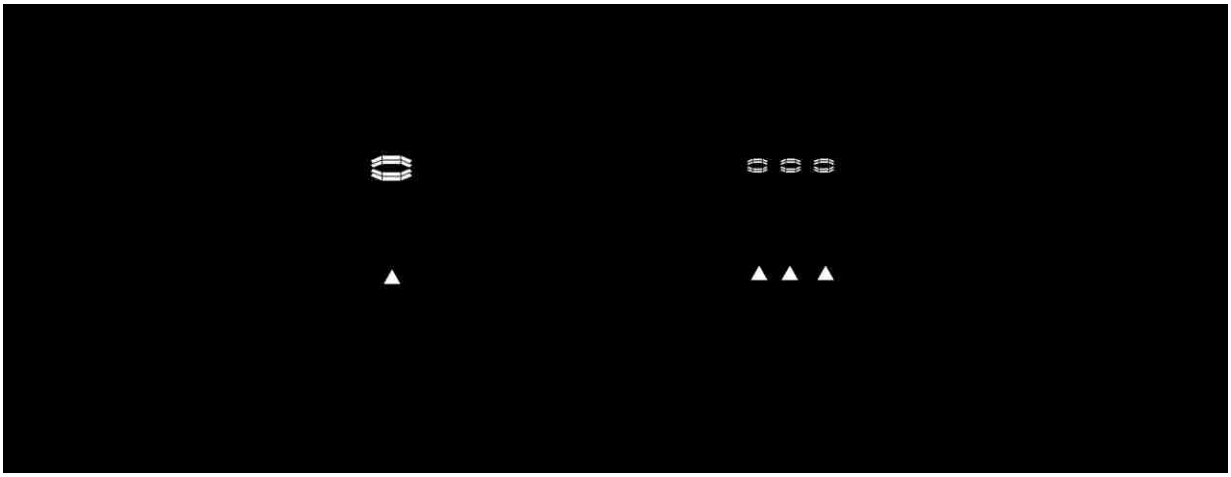

Figure 6.2: Height of the PT steel H_{unb} where γ_k is ranging from 0.2 to 5.

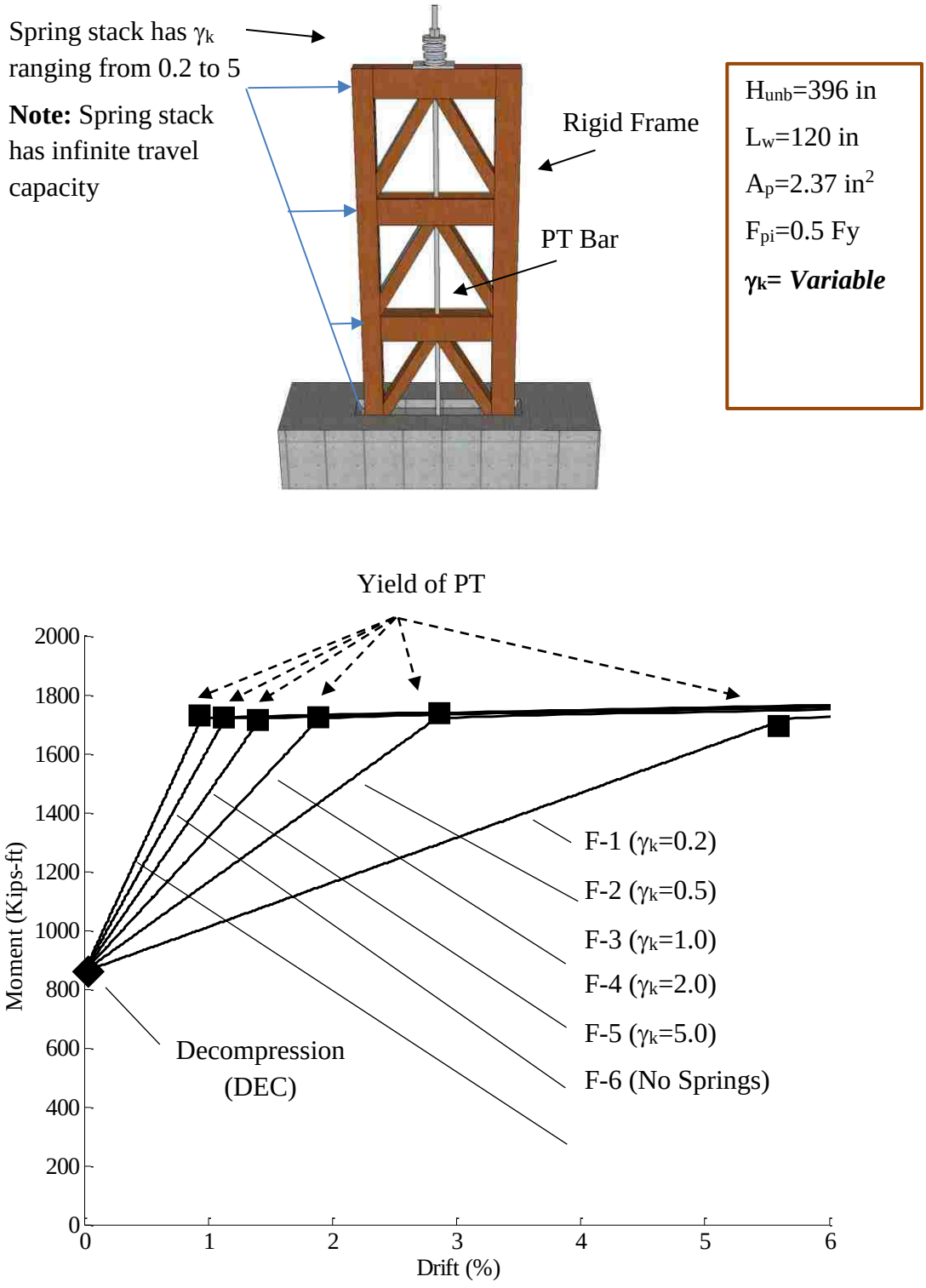

Figure 6.3: Effects of the relative stiffness γ_k on the response of frames with zero eccentricity (spring stack has infinite travel capacity).

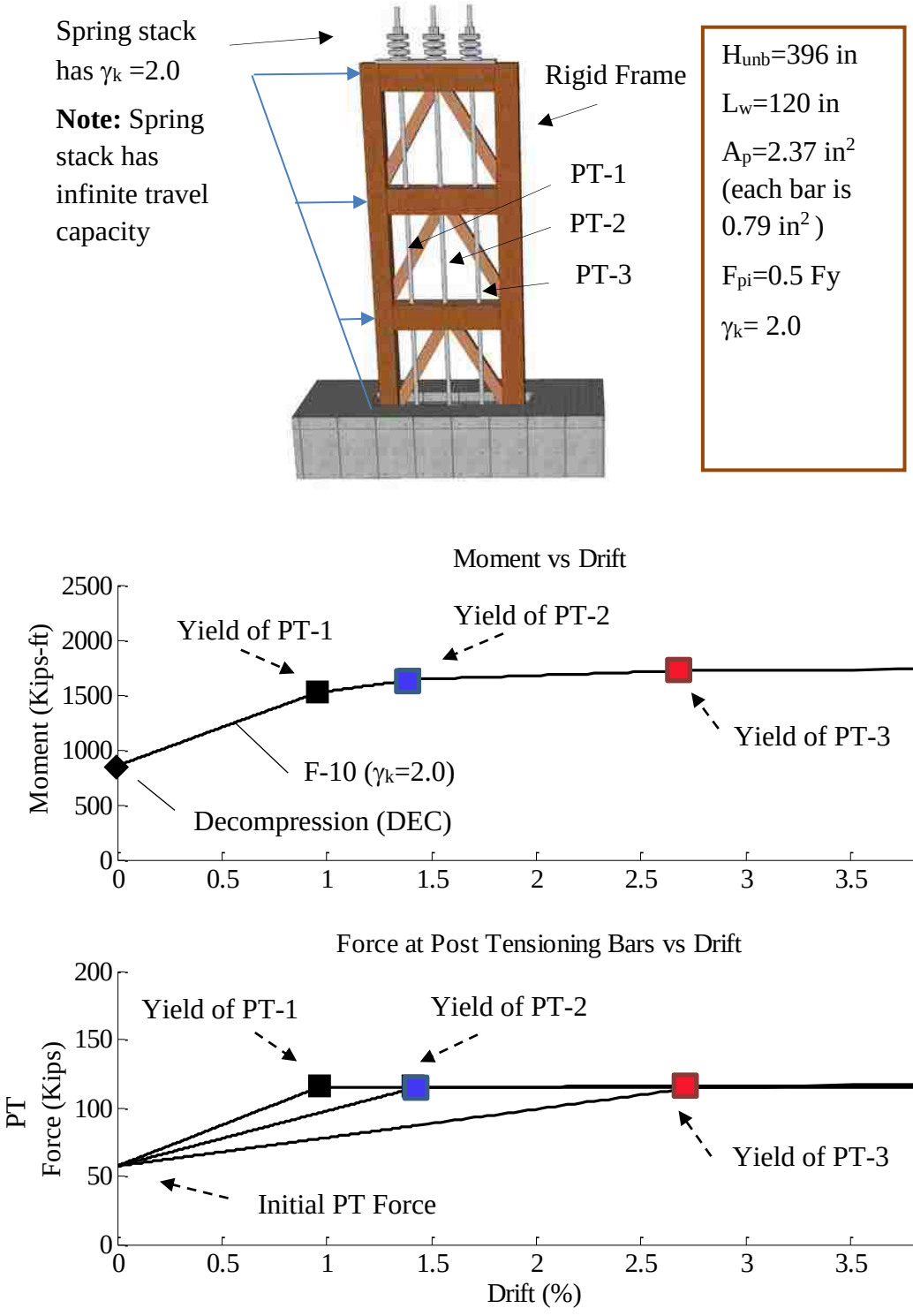

Figure 6.4: Response of frame F-10 under pushover load (spring stack has infinite travel capacity).

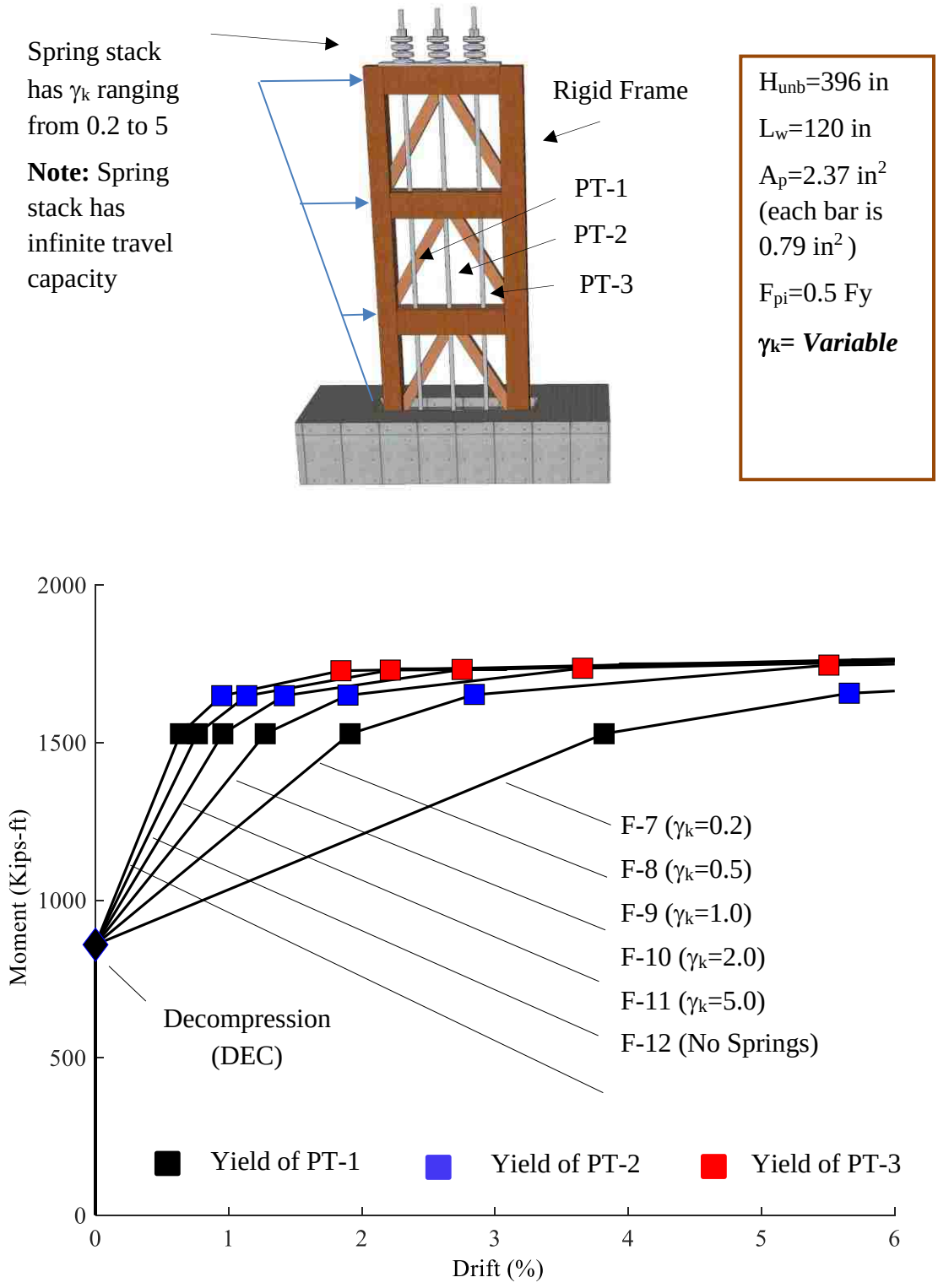

Figure 6.5: Effects of the relative stiffness γ_k on the response of frames with intermediate eccentricity (spring stack has infinite travel capacity).

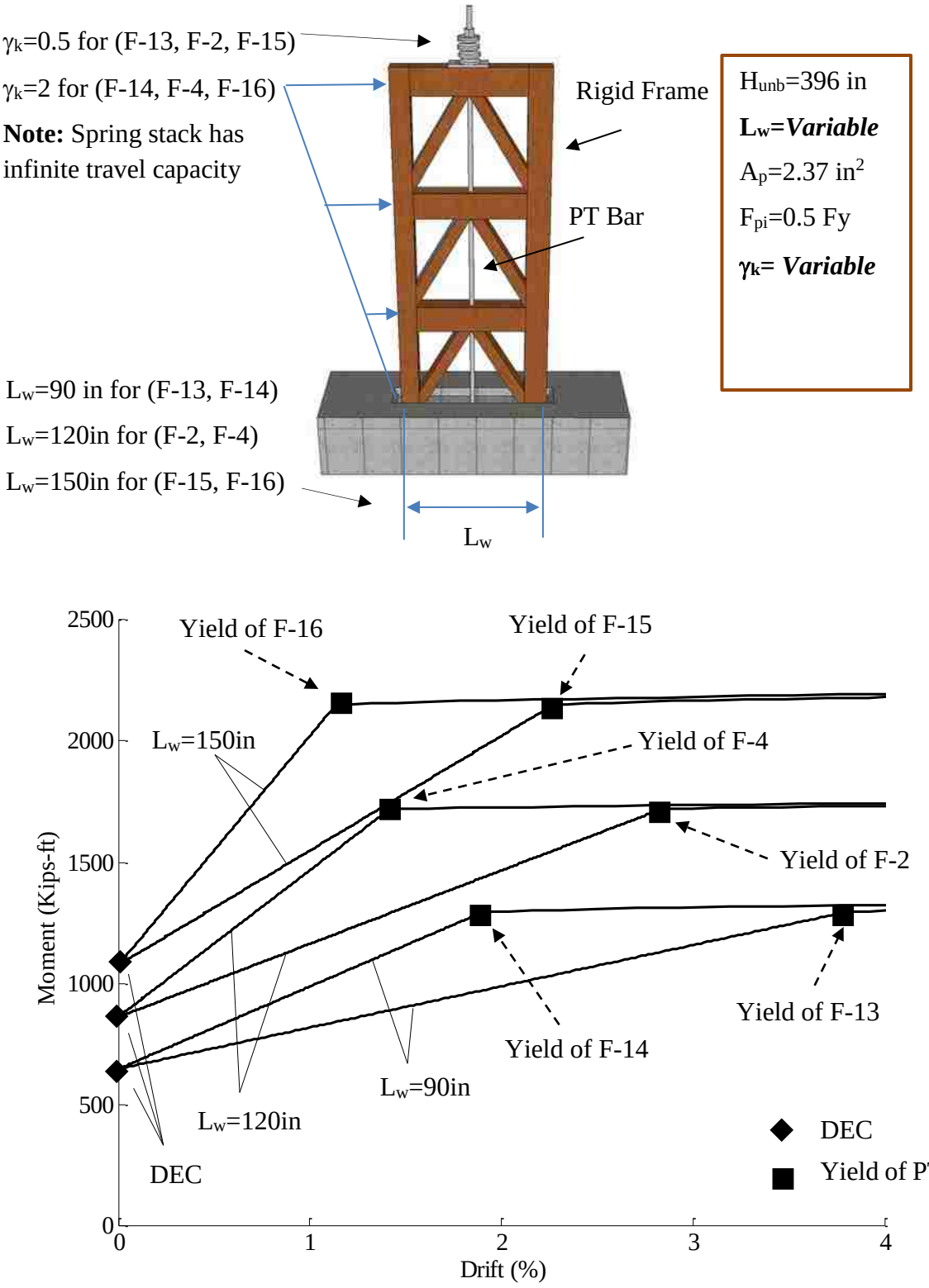

Figure 6.6: Effects of the frame length L_f on the response of frames with zero eccentricity (spring stack has infinite travel capacity).

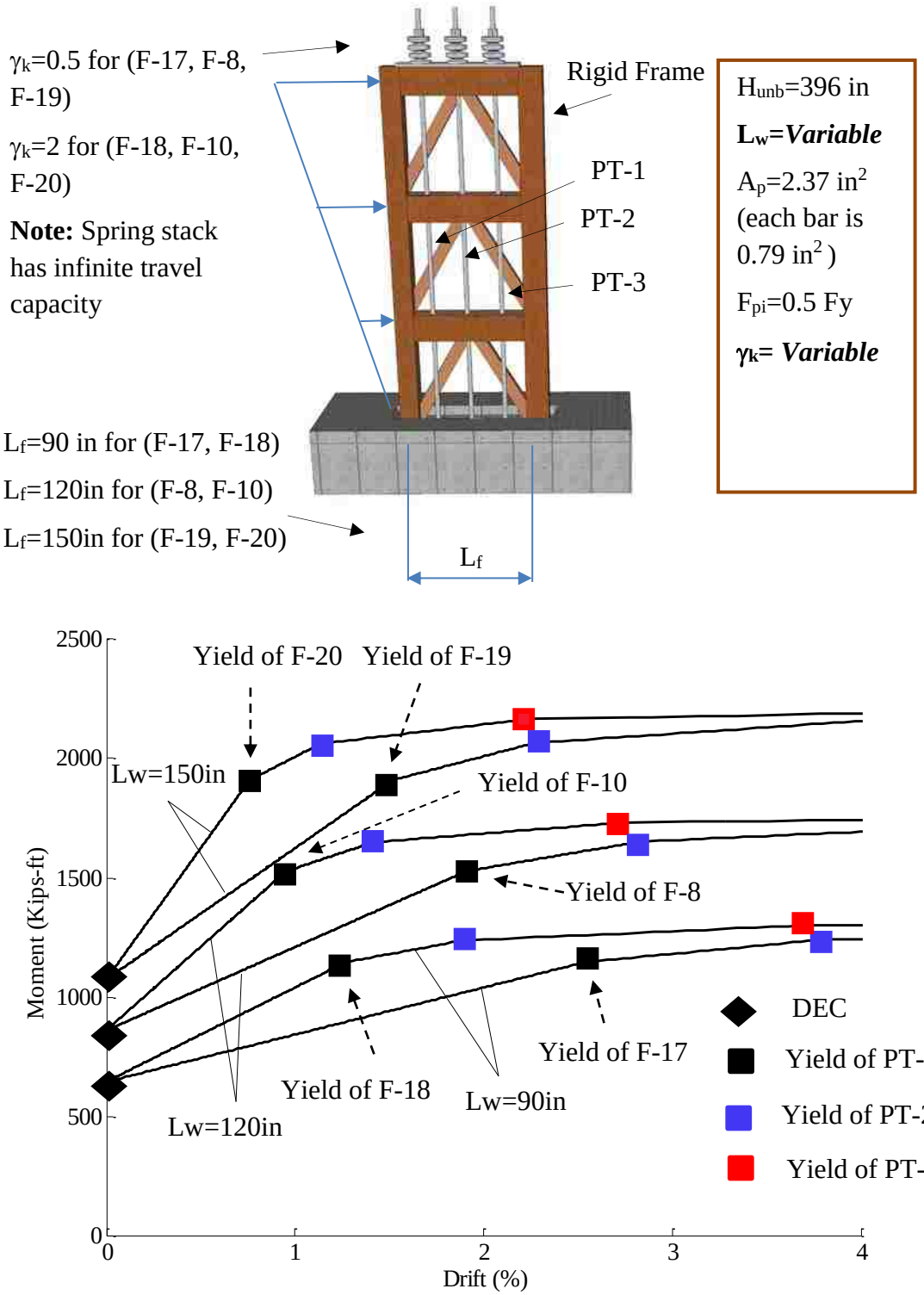

Figure 6.7: Effects of the frame length L_f on the response of frames with intermediate eccentricity (spring stack has infinite travel capacity).

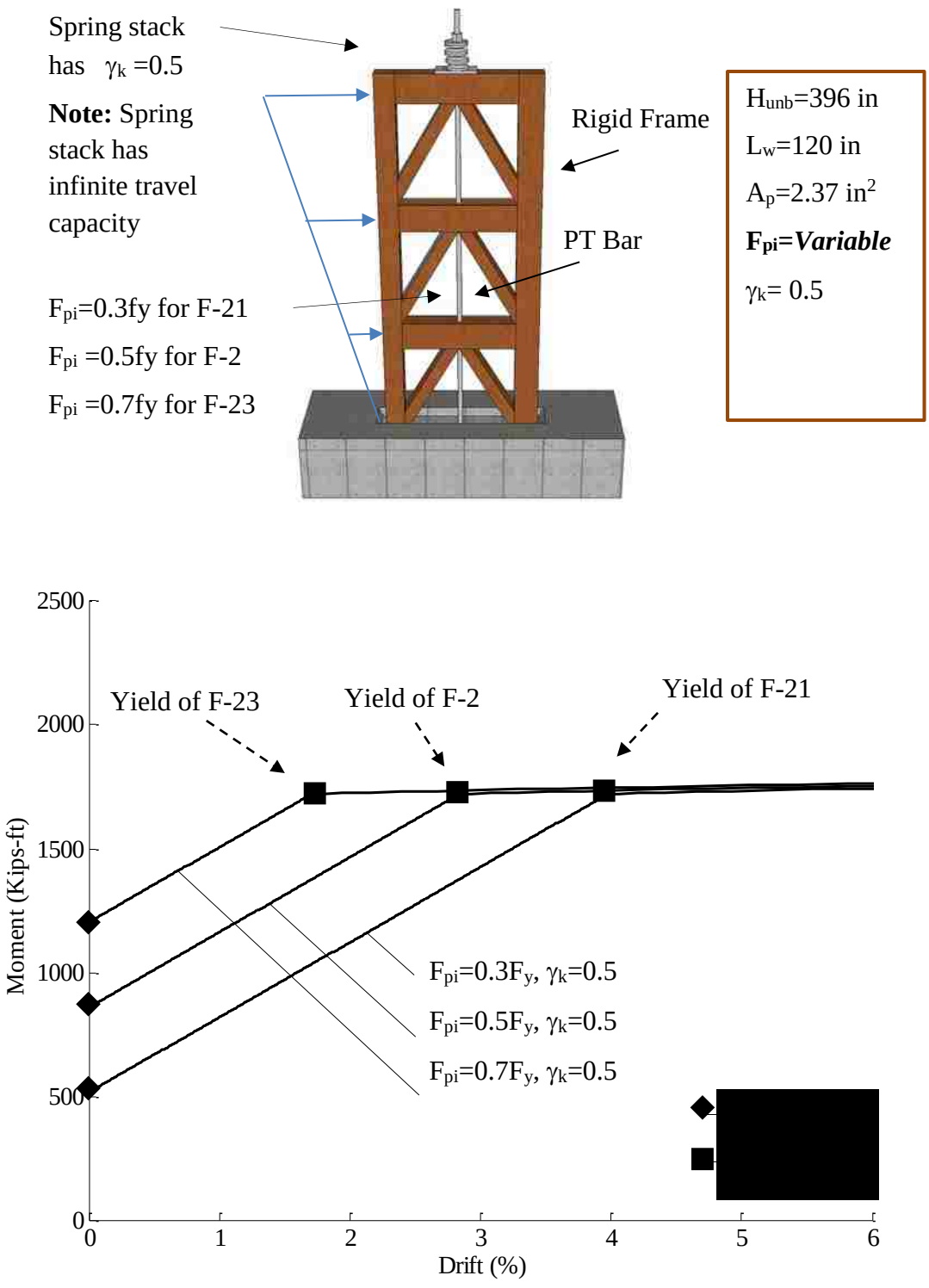

Figure 6.8: Effects of the initial stress on the response of frames with zero eccentricity and γ_k=0.5 (spring stack has infinite travel capacity).

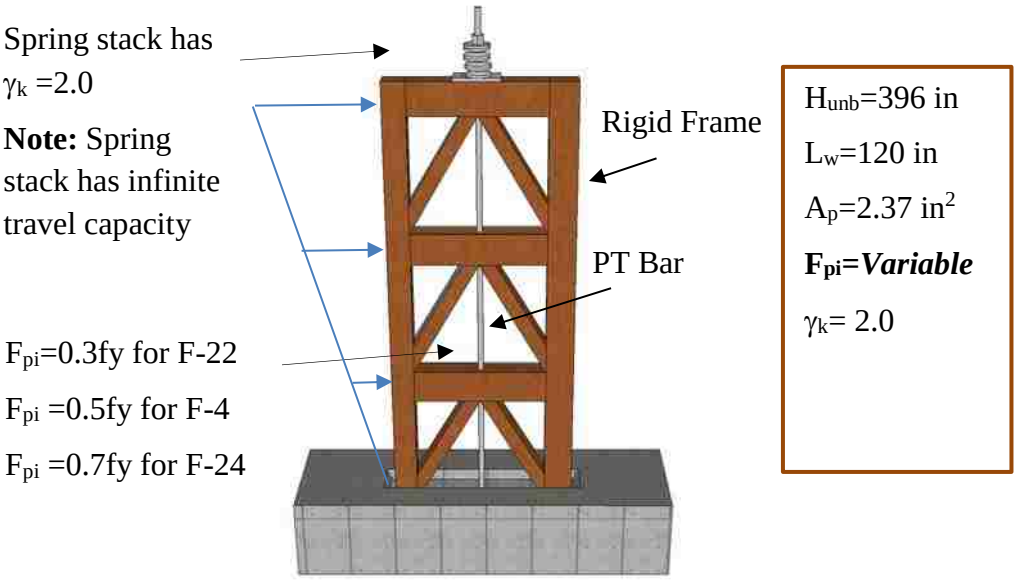

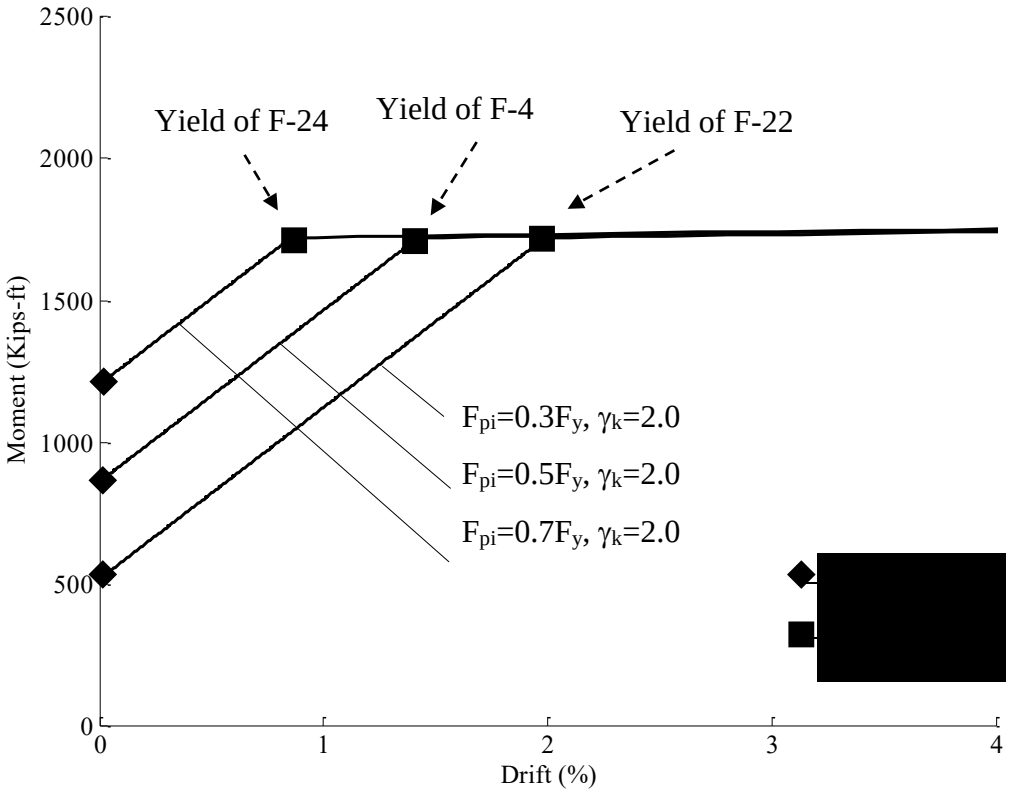

Figure 6.9: Effects of the initial stress on the response of frames with zero eccentricity and γ_k=2.0 (spring stack has infinite travel capacity).

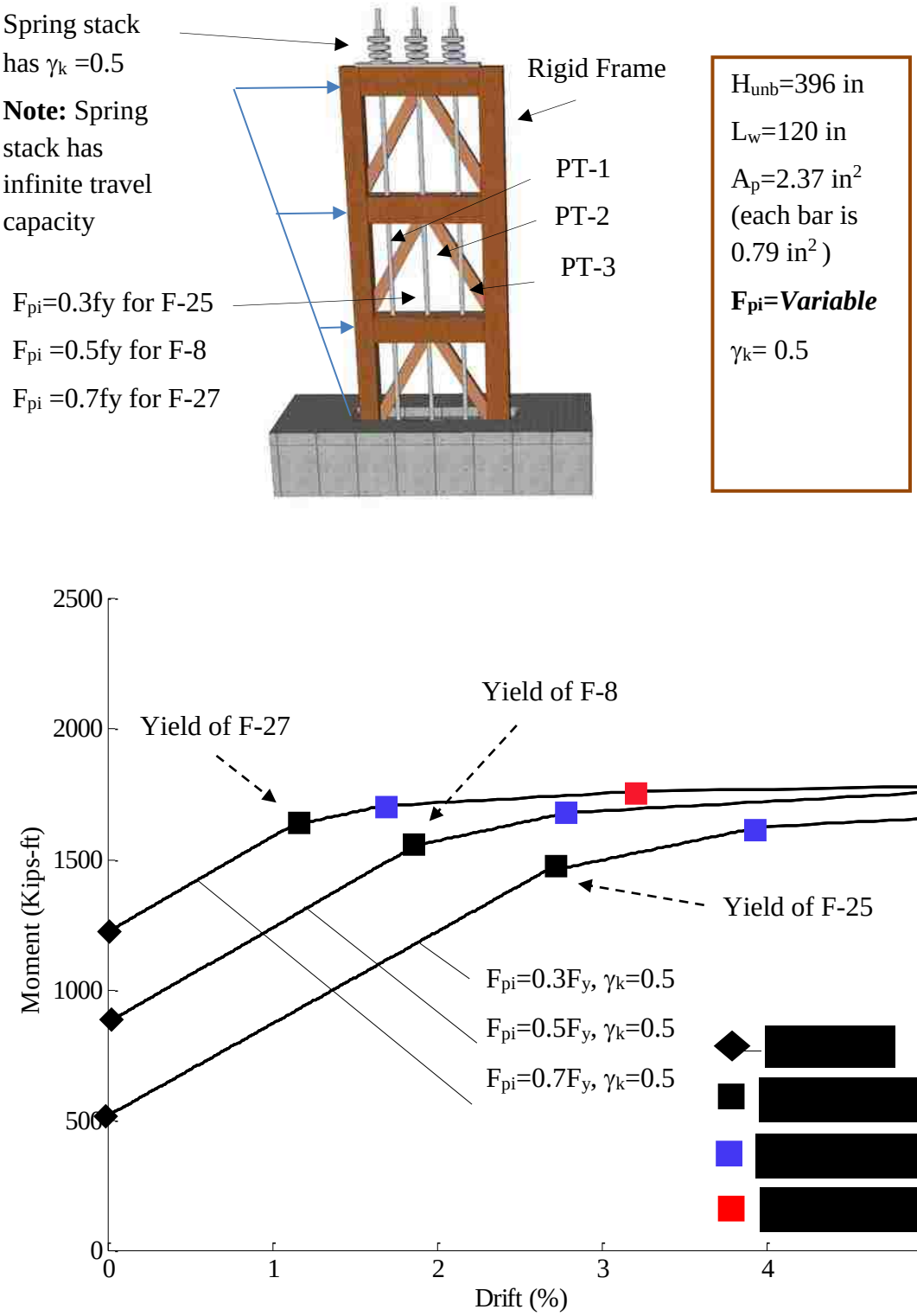

Figure 6.10: Effects of the initial stress on the response of frames with zero eccentricity and γ_k=0.5 (spring stack has infinite travel capacity).

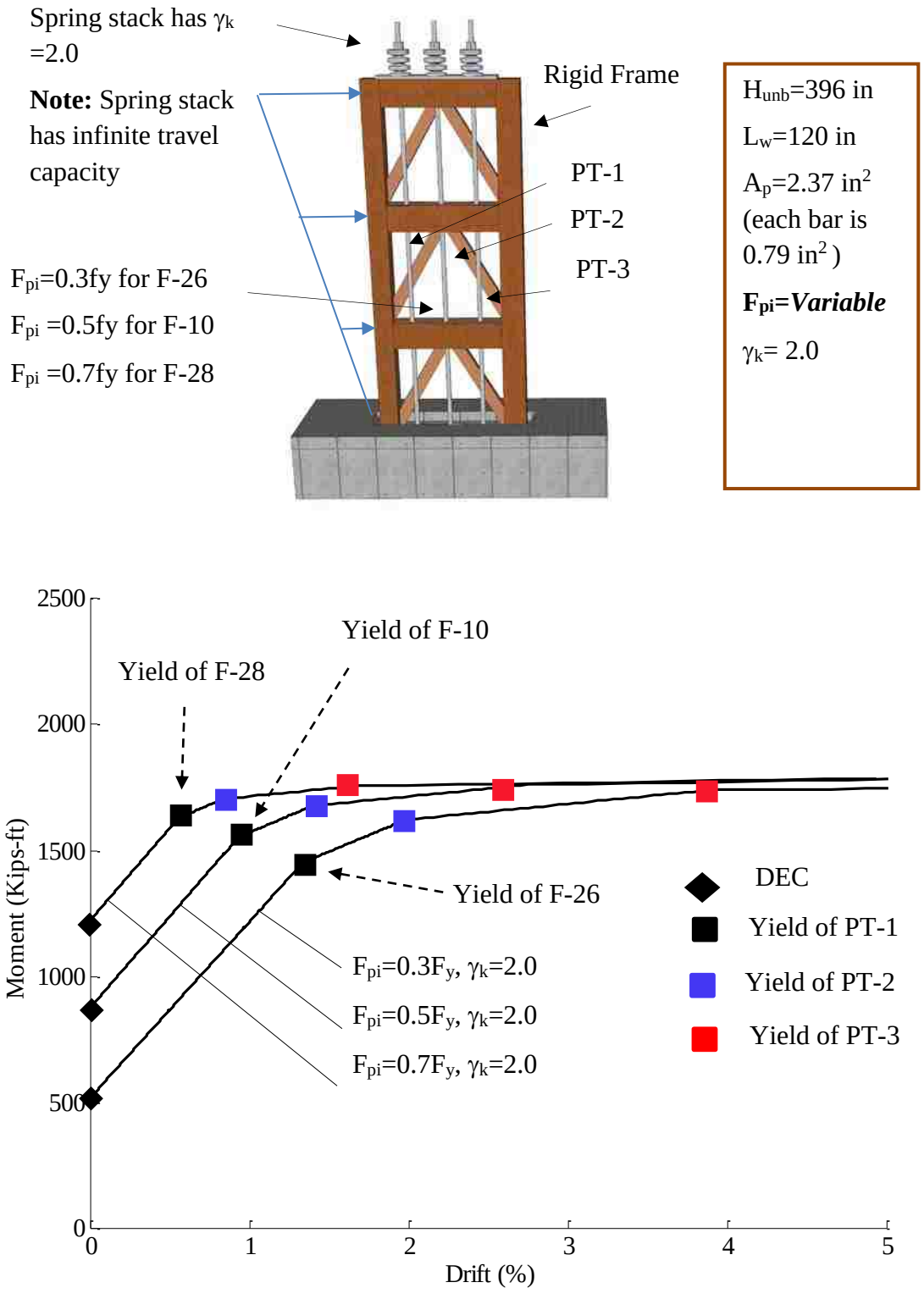

Figure 6.11: Effects of the initial stress on the response of frames with intermediate eccentricity and γ_k=2.0 (spring stack has infinite travel capacity).

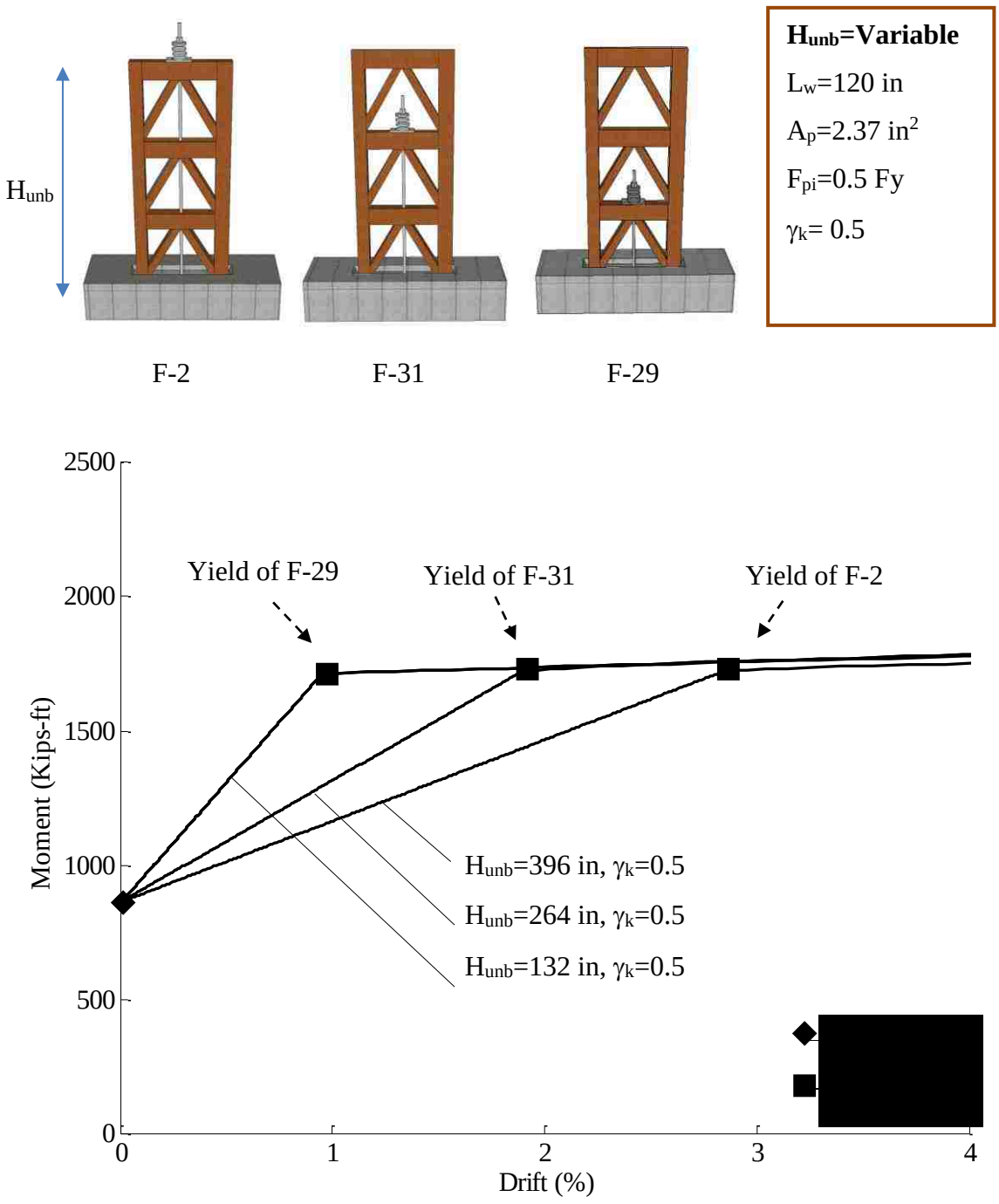

Figure 6.12: Effects of the unbonded length H_{unb} on the response of frames with zero eccentricity and γ_k=0.5 (spring stack has infinite travel capacity).

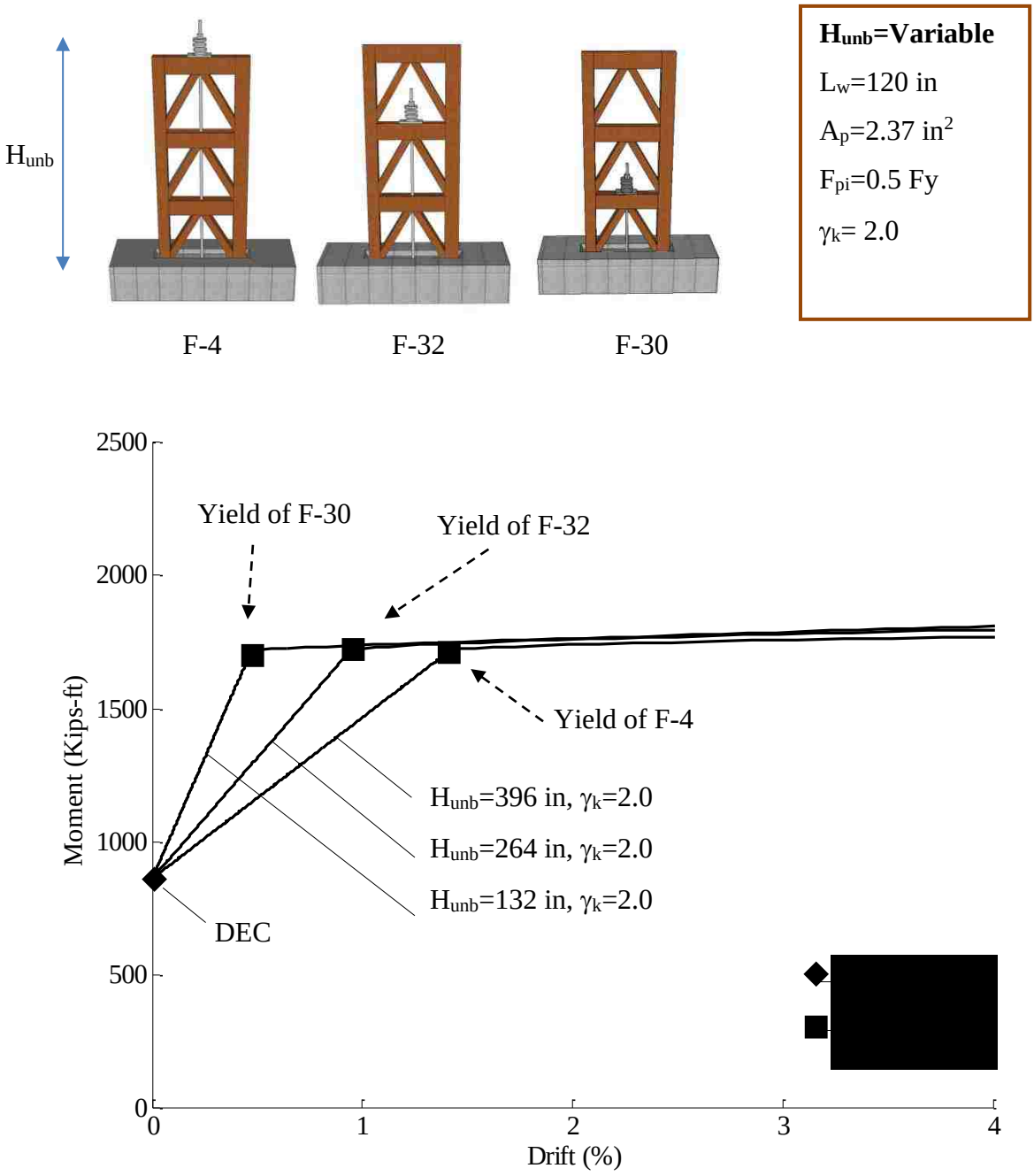

Figure 6.13: Effects of the unbonded length H_{unb} on the response of frames with zero eccentricity and γ_k=2.0 (spring stack has infinite travel capacity).

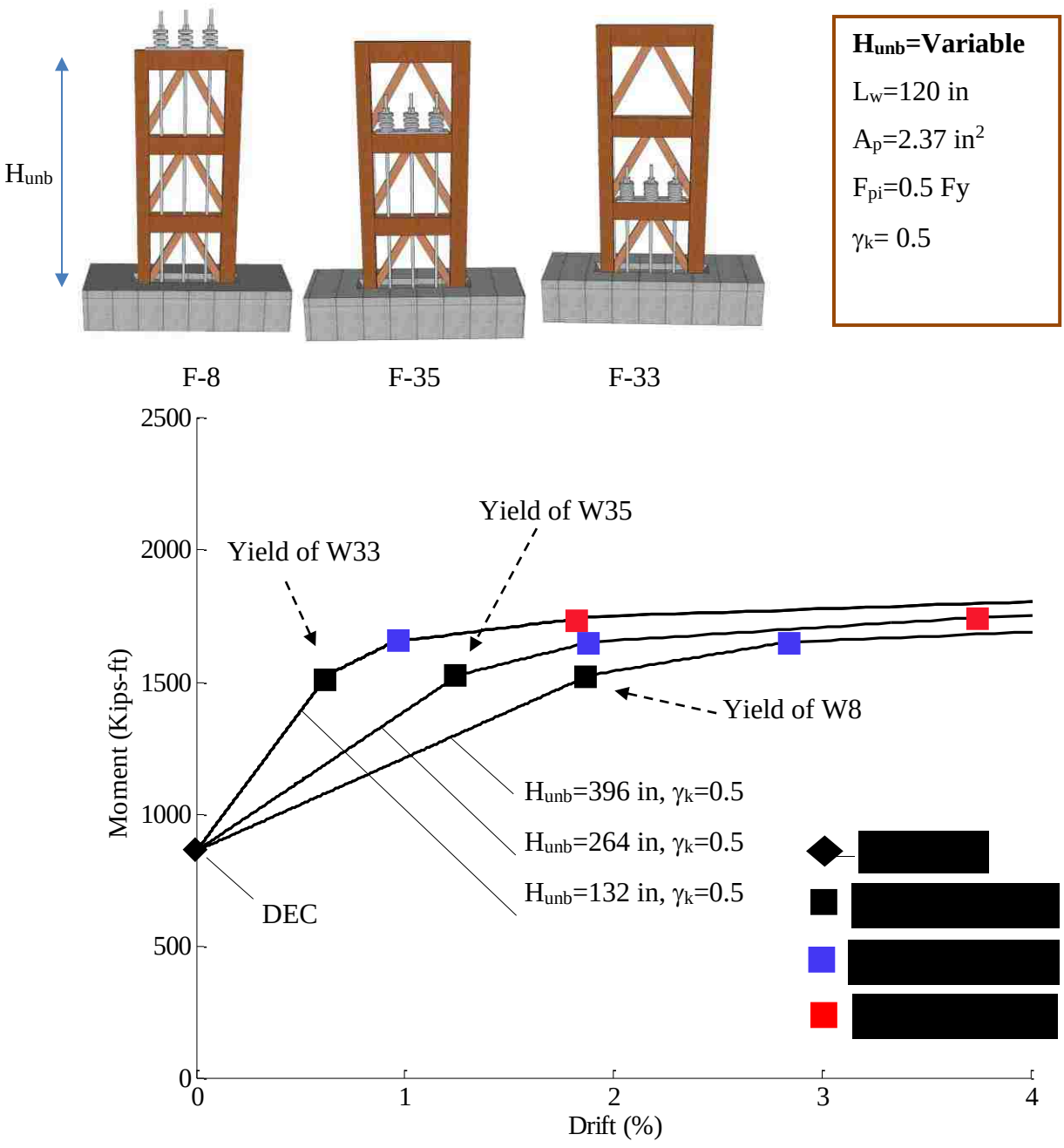

Figure 6.14: Effects of the unbonded length H_{unb} on the response of frames with intermediate eccentricity and γ_k=0.5 (spring stack has infinite travel capacity).

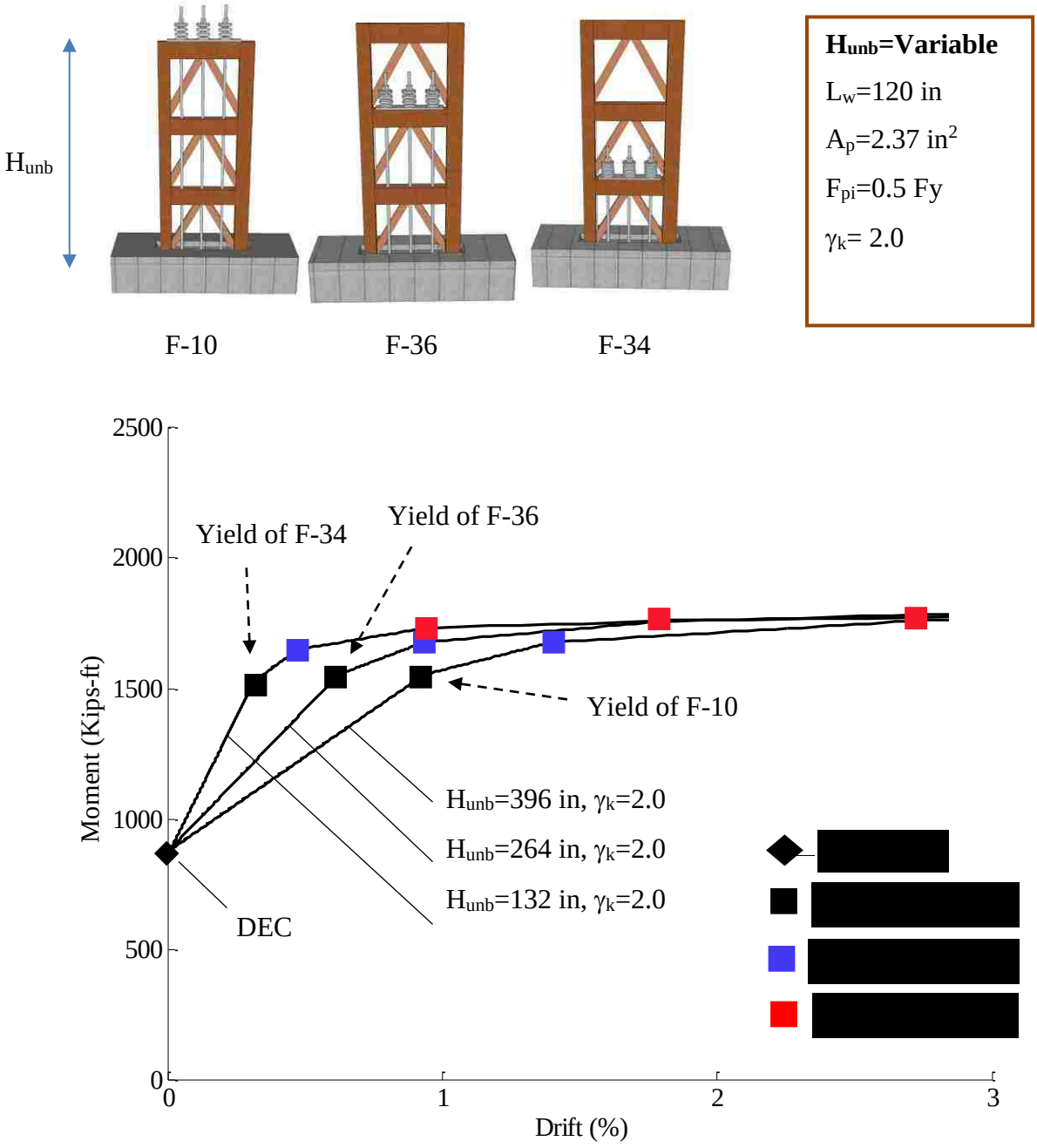

Figure 6.15: Effects of the unbonded length H_{unb} on the response of frames with intermediate eccentricity and γ_k=2.0 (spring stack has infinite travel capacity).

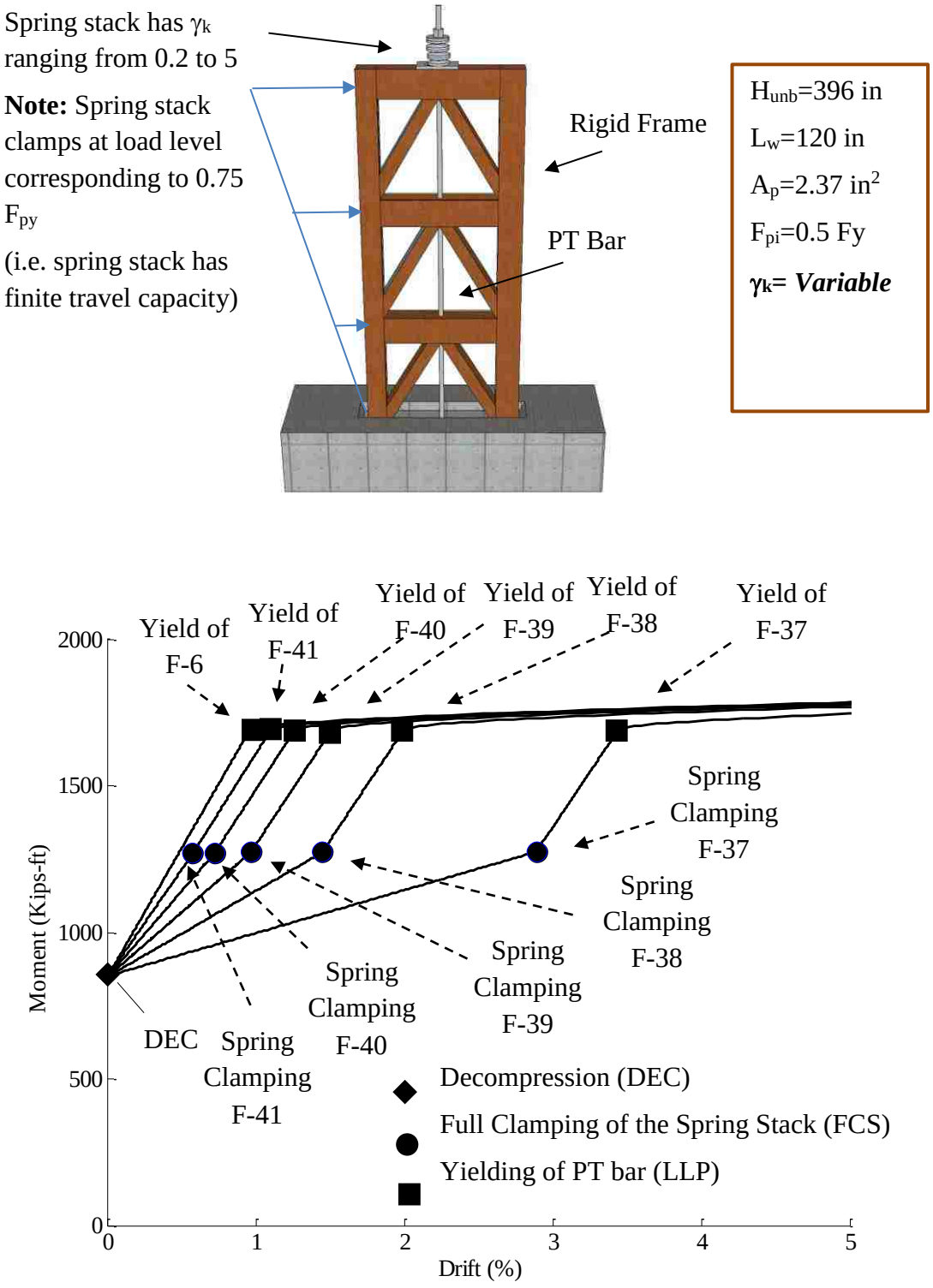

Figure 6.16: Effects of the relative stiffness γ_k on the response of frames with zero eccentricity (spring stack clamps at PT stress of 0.75 F_{py}).

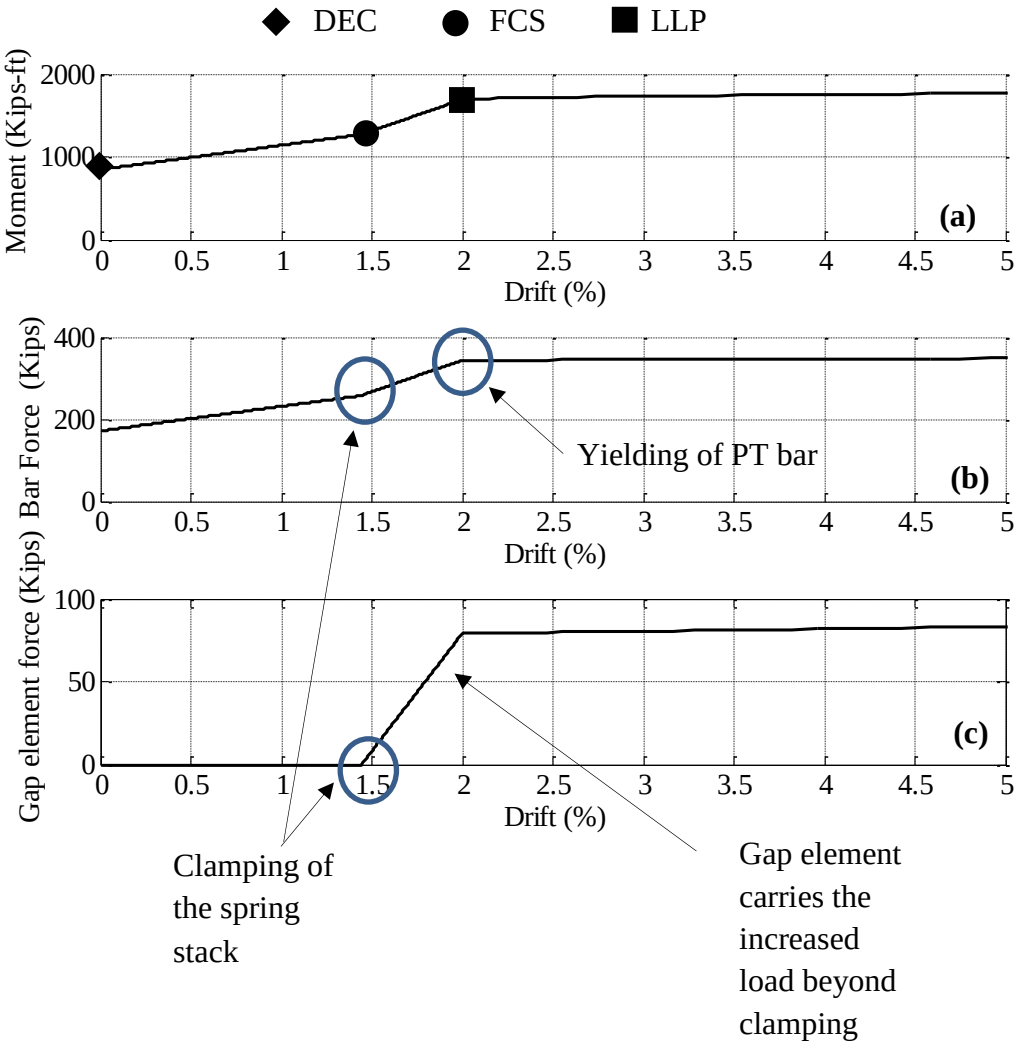

Figure 6.17: Response F-38 to pushover load: (a) Moment-drift history; (b) Force at the PT bar vs drift; (c) Force at the gap element that represented the clamping mechanism.

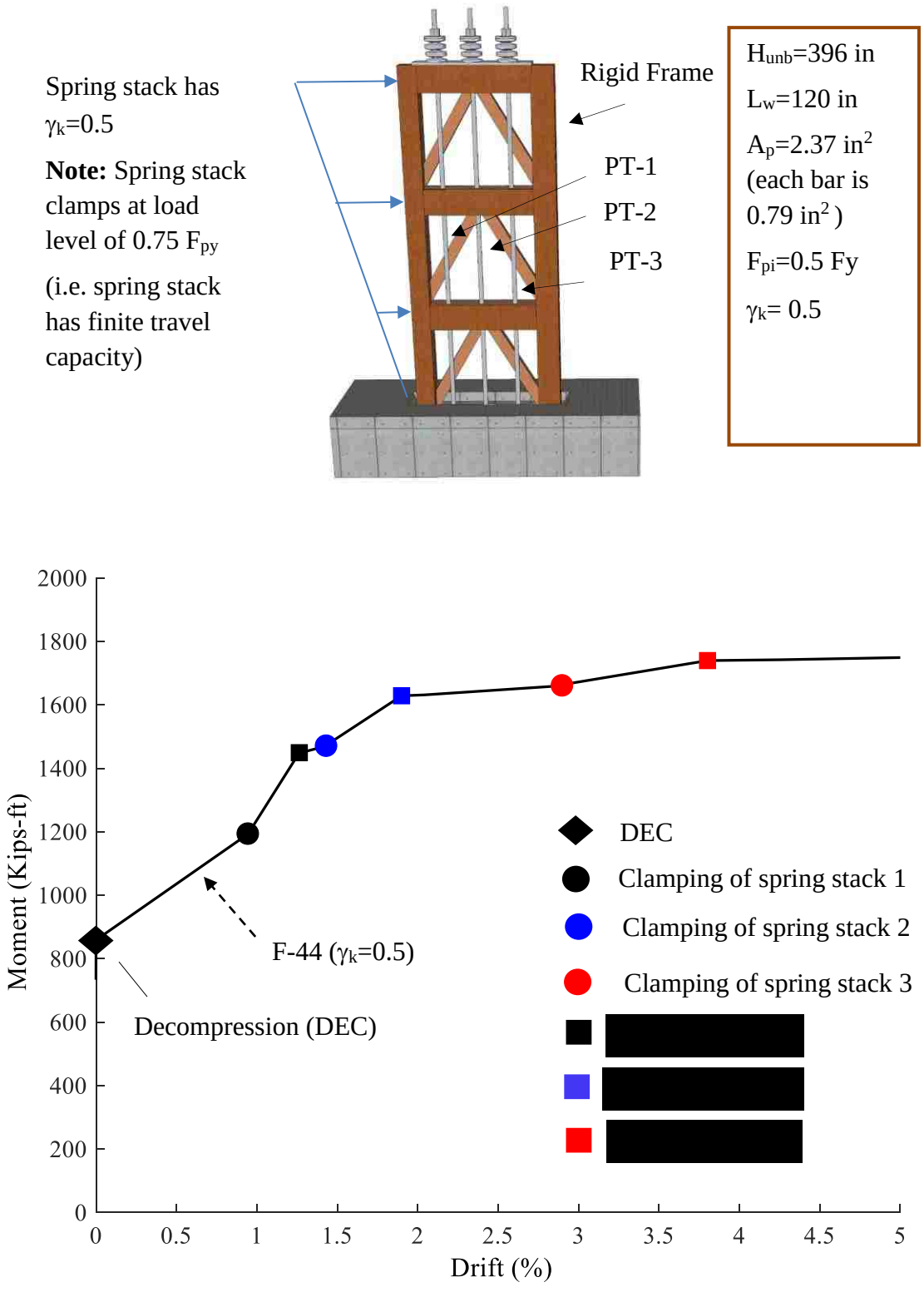

Figure 6.18: Moment-drift response of F-44
(spring stack clamps at PT bar stress of 0.75 F_{py}).

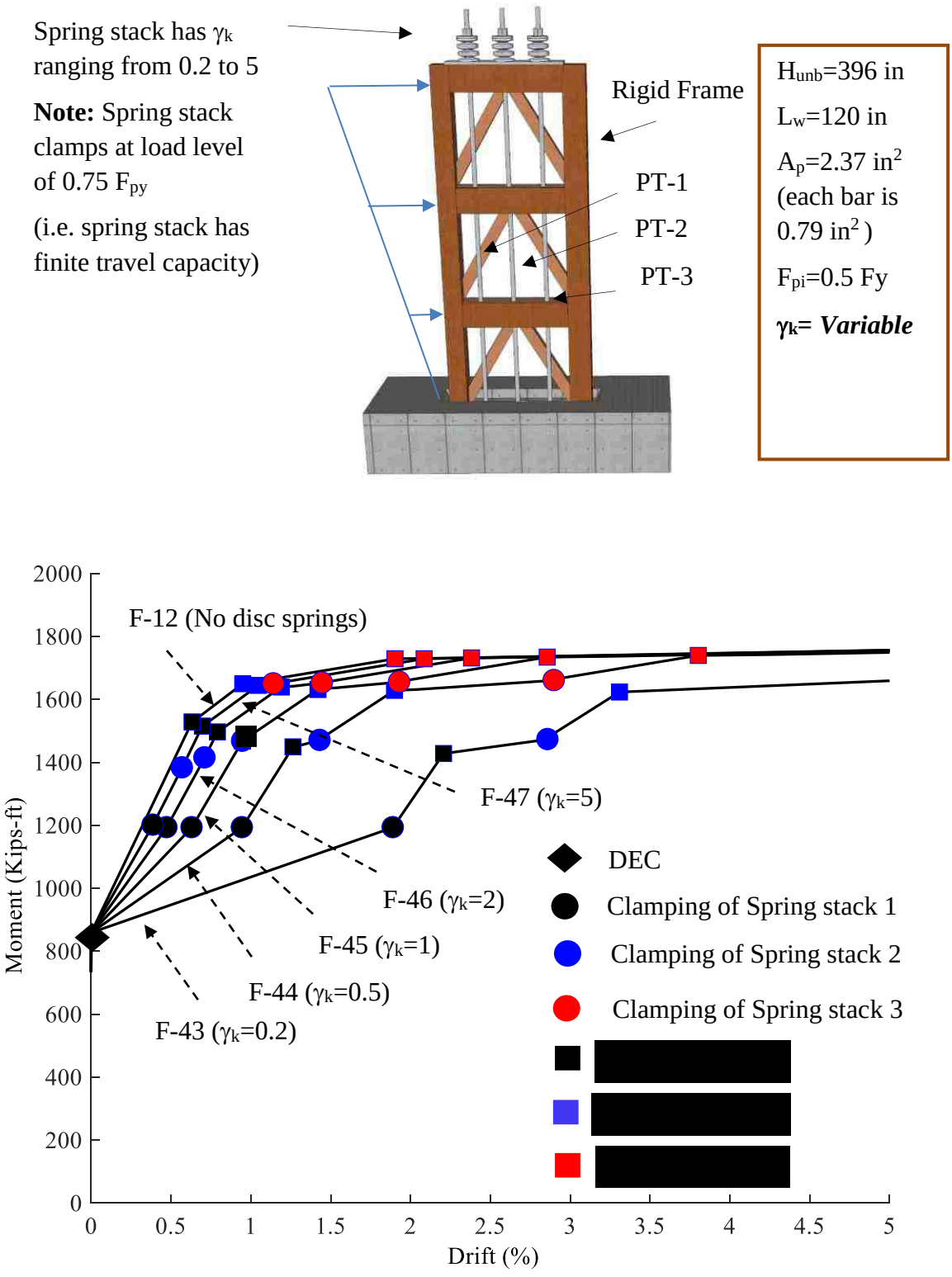

Figure 6.19: Effects of the relative stiffness γ_k on the response of frames with zero eccentricity (spring stack has finite travel capacity).

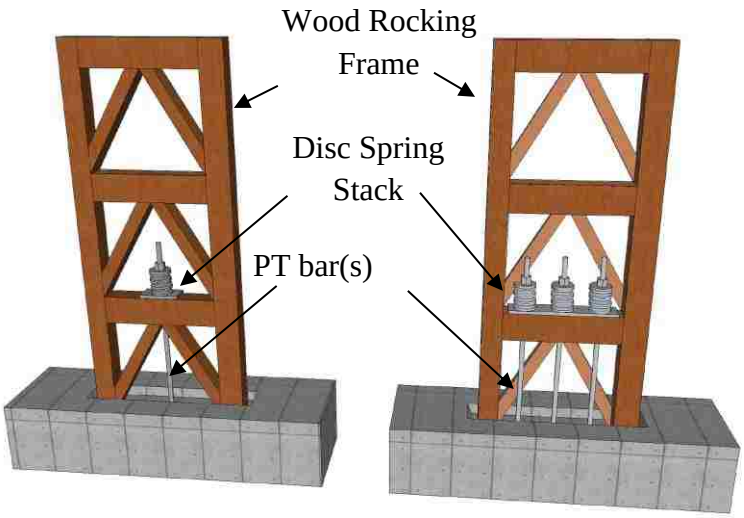

Figure 6.20: Prototype frames where the PT bars are extended to the first floor instead of the roof.

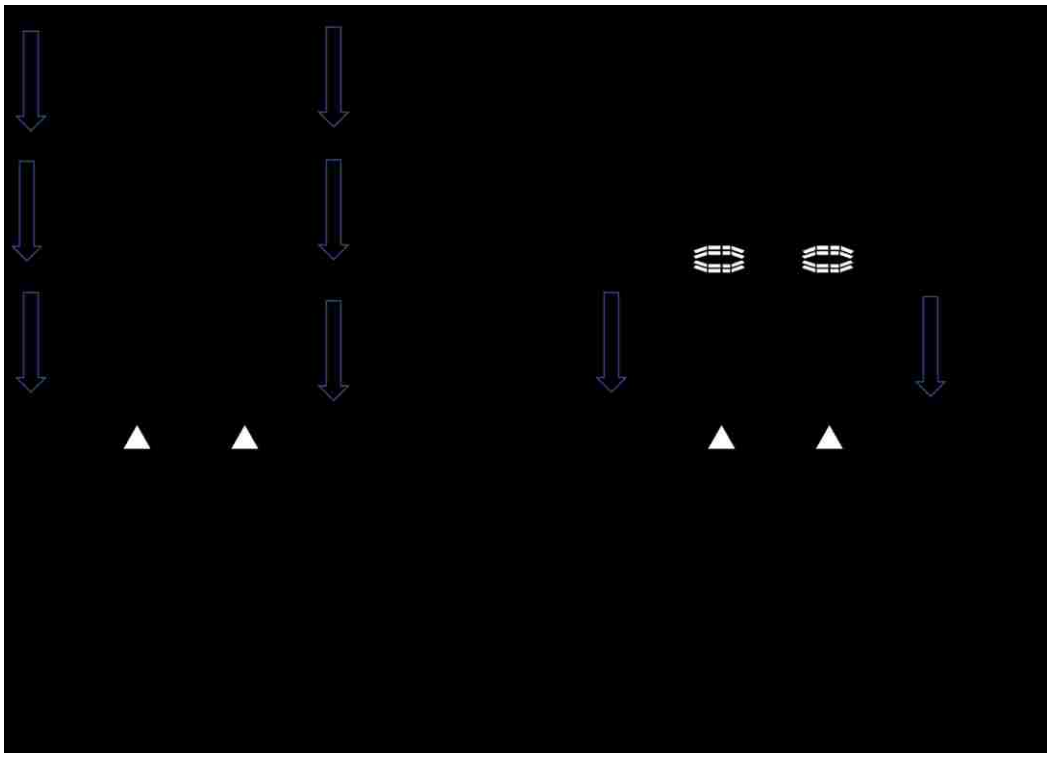

Figure 6.21: Benefits of extending the PT bars to lower floors.

CHAPTER 7

NONLINEAR DYNAMIC ANALYSIS

7.1 INTRODUCTION

This chapter presents the results of the nonlinear dynamic analysis of the prototype frames. The frames were subjected to a set of actaul recorded ground motions scaled to the Design Based Earthquake (DBE) and the Maximum Considered Earthquake (MCE) levels. A toatl of 44 ground motion records were considered.

Note that presenting the complete time history responses for all the ground motions would be impractical. Instead, the results of this chapter are presented in two parts: The first part focuses on the nonlinear time history response of frames F-1, F-4, F-37, and F-40 to the Hector Mine earthquake. This enables a close look at the time history response parameters of interest to determine if they are expected. The second part presents a summary of the peak responses of all the prototype frames having zero eccentricity and listed in Tables 6.1 and 6.2.

7.2 FE MODEL

Figures 7.1 and 7.2 show the FE models used in the dynamic analyses. Note that these FE modes are based on previous FE model developed by Chancellor (2014) for steel rocking frames, but the actual model is updated here to account for the spring stack and the clamping associated with it. Figure 7.1 shows the model for frames with spring stack with infinite travel capacity. Figure 7.2 shows the model for frames with spring stacks with finite

travel capacity. The FE models shown in Figures 7.1 and 7.2 are similar to the FE models described in Chapter 4 for the static pushover analyses with a few changes in rocking frame modeling, support assignment, PT steel modeling, and the allocation of the gravity loads as desribed in the following sections.

7.2.1 Rocking frame modeling

The prototype rocking frames are modeled as elastic as shown in Figures 7.1 and 7.2. The joints between the beam-column elements are assumed to be rigid. The beam column elements have uniform cross-sectional dimensions of 30×7 inches. The modulus of elasticity of the elements is 900,000 psi.

7.2.2 Support assignment

Figures 7.1 and 7.2 show the modified support layout of the FE model used in the dynamic analyses. In contrast to the static FE model developed in Chapter 4, this model permits a vertical gap opening at both the left and the right supports under the action of the dynamic loads. This layout follows the work done by Chancellor (2014) for steel rocking frames.

7.2.3 PT bar modeling

The PT bar is modeled as a corotational truss element (i.e. the local axies of the element are updated according to the deformed position) to account for the nonlinear geometry during the response. However, the static FE model developed in Chapter 4 neglected these

effects. The corotational element is assumed to be massless and connected through the nodes shown in Figures 7.1 and 7.2.

7.2.4 Lean on column

To capture the secondary moment due to P-Δ effects, a lean on column is used in the dynamic FE model (Chancellor 2014). The column is an elastic beam-column connecting the nodes 24 to 27 and pinned to the ground as shown in Figures 7.1 and 7.2. The nodes of the lean-on-column are constrained horizontally to the rocking frame using an equal displacement constraint (Chancellor 2014).

7.2.5 Mass calculation and assignment

Figures 7.1 and 7.2 show the location of the masses assigned to the dynamic FE model. The mass allocated to the rocking frame represents the mass collected by its tributary area. The lean on column picks up the remaining floor mass.

Since there are two rocking frames in the X-direction of the prototype building, half of the building mass goes to the dynamic FE model and thus, the results in this chapter including the base shear and the bending moments are half of the total values for the entire prototype building. Note that the mass assigned to the FE model includes the dead load of the prototype building and 25% of the live load.

7.2.6 Solution and time stepping methods

Performing the transient analysis of the prototype frames followed these steps:

1. The eigensolver is used to find the natural frequencies of the FE model, and this serves two purposes. First, knowing the required time step to avoid aliasing. Second, using the natural frequencies in calculating Rayleigh damping parameters. Table 7.1 lists the natural frequencies and the corresponding periods of the prototype frame.

2. An unconditionally stable Newmark integrator with γ=0.5 and β=0.25 are implemented.
3. Newton line search algorithm is used to solve the nonlinear equations with an energy increment test having a tolerance of 10E-8. The parameters of the line search method were used so that Bisection line search is implemented with MaxETA=0.2, MinETA=0.1 and a maximum number of iterations of 1000. The line search algorithm had a search tolerance of 0.1, which is more conservative than the recommended value of 0.8 by (M.A. Crisfield 1991).
4. The time step is chosen to be 0.003 sec, which should provide reasonable accuracy since the period of the highest mode considered is 0.024 sec as shown in Table 7.1.

7.2.7 Damping

The FE model implements Rayleigh proportional damping to represent the energy dissipation during vibration. The damping ratios of the 1^{st} and the 4^{th} modes are assumed

to be 4% and 3.3% respectively. Thus, Rayleigh damping coefficients are (a_o= 0.9131) and (a_1=0.0003), leading to the damping ratios shown in Table 7.1. Note that 4% damping for the 1st mode is less than the given range (5-7%) for timber structures at the working stress level as given by Chopra (2007). The damping for the 4th mode is chosen so that it does not cause too much damping for other modes.

7.2.8 Ground motions selection and scaling

A total of 22-pair ground motions were used in the dynamic analyses of the prototype frames. These ground motions are the "Far-Field" record set given in the FEMA P695, and Table 7.2 lists the name, location, and the magnitude of these events.

The procedure of scaling the ground motions to the DBE, and the MCE according to the ASCE 7-10 is as follows. First, the records of the ground motions are available on (http://www.csuchico.edu/structural/researchdatabases/ground_motion_sets.shtml). Second, the eigensolver in OpenSEES (Mazzoni et al. 2006) was used to determine the fundamental period of the FE model (T). Third, the scaling factor for the DBE was chosen so that the mean value of the spectral acceleration for the periods ranging from 0.2T to 1.5T is equal the design spectral acceleration of site location. As a result, the scaling factors for the DBE and the MCE are determined to be 0.87 and 1.3 respectively.

7.3 TIME HISTORY RESPONSE OF HECTOR MINE EARTHQUAKE

This section presents the time history response of frames F-1, F-4, F-37 and F-40 to Hector Mine earthquake scaled to the DBE and the MCE levels. It noted that:

1. F-1 and F-4 have spring stacks with infinite travel capacities, whereas F-37 and F-40 have spring stacks with finite travel capacities;
2. F-1 and F-37 have relatively flexible spring stacks (γ_k=0.2), whereas F-4 and F-40 have relatively stiff spring stacks (γ_k=2).

The results below compare the response of F-1 with F-4 and F-37 with F-40. This is because the aim of this section is to understand the impact of the spring stack stiffness on the dynamic response.

7.3.1 Floor displacements and roof drift

Frames 1,4

Figures 7.3, 7.4, 7.5, and 7.6 show the floor displacements, and the roof drifts of F-1 and F-4 due to the DBE. In general, the figures demonstrate that the peak displacements and drifts of F-1 (γ_k=0.2) were larger than the peaks of F-4 (γ_k=2). Indeed, the peak floor displacements of F-1 were 27%, 33%, and 29% greater than F-4 peak floor displacement. Notice that having a relatively flexible spring stack such as the case for F-1 causes the frame to have small lateral stiffness after the gap opening. Thus, F-1 is expected to undergo more lateral displacement than F-4 assuming that both are subjected to the same lateral

force, and the gap at the base of the frame is opened. This could explain why F-1 experienced larger peaks than F-4.

Figures 7.7, 7.8, 7.9, and 7.10 present the floor displacements and the drifts of F-1 and F-4 due to to the MCE. As expected, we can see that the peak responses are higher than the DBE level. Also, the peak responses for F-1 are still larger than F-4. In fact, the peak floor displacements of F-1 were 8%, 9%, and 9% greater than F-4 peaks. These increased values are less than the increases in peak floor displacements obtained under the DBE.

Interestingly, the plots show that when the gap at the base of the frame opens, the natural period of F-1 is slightly longer than F-4, which is as expected because F-1 has less lateral stiffness after the gap opening.

Frames 37,40

Figures 7.11, 7.12, 7.13, 7.14 show the floor displacements, and the roof drifts of F-37 and F-40 due to the DBE. The figures illustrate that the peak responses of F-37 are larger than that of F-40. Also, it could be noticed that the responses of F-37 and F-40 are exactly similar to that of F-1 and F-4 under the same earthquake because the DBE was not high enough to cause clamping of the spring stack.

Figures 7.15, 7.16, 7.17, and 7.18 show the response of F-37 and F-40 due to the MCE, and again the response under the MCE is larger than the DBE. Again, the peak responses of F-37 are greater than F-40. Notice again that the natural period of F-37 is slightly longer than F-40 since F-37 has less lateral stiffness after the gap opening.

It is observed that F-1 and F-37 responses under the MCE decay more quickly than F-4 and F-40. It is important to note that F-4 and F-40 experienced yielding of the PT steel which should reduce the PT force, and thus the decompression moment M_{dec}. This would make it easier for F-4 and F-40 to rotate as a rigid body after a significant loss of the PT force. The implication of this reduction in the PT force is that the small lateral forces acting on the rocking frame by the end of the ground motion can easily cause the gap at the base of the frame to open and lead to large lateral displacements due to the rigid body rotation. However, F-1 and F-37 did not experience yielding, and thus the decompression moment remains the same by the end of the ground motion. As a result, the small lateral forces acting on the frame by the end of the ground motion will not cause the gap to open, and the frame will vibrate without any rigid body rotations. This explains why F-1 and F-4 response seem to decay quickly, while F-4 and F-40 seem to continue vibrating with larger amplitudes by the end of the ground motion.

7.3.2 PT Force

Frames 1,4

Figure 7.19 shows the force at the PT bar of F-1 and F-4 due to the DBE. The figure implies that the peak PT force of F-1 is smaller than that of F-4. The reason is that F-1 has a flexible spring stack (γ_k=0.2) that leads to a reduction in the effective stiffness of the assembly (Accorsi and Sarisley 1990), whereas the F-4 has stiff spring stack (γ_k=2) leading to increase the stiffness and the peak PT force.

The difference between the peak PT forces developed in F-1 and F-4 becomes more apparent when the MCE is applied. As shown in Figure 7.20, the peak PT force of F-4 has significantly increased that it eventually reached the yield stress. As a result, F-4 encountered a loss in the PT force due to this yielding, but the PT force of F-1 remains the same.

Frames 37,40

Figure 7.21 shows the PT force developed in F-37 and F-40 due to the DBE, and it can be seen that it is similar to that of F-1 and F-4 shown in Figure 7.19 since the DBE was not enough to cause clamping of the spring stack.

However, the force response due to the MCE is shown in Figure 7.22. Interestingly, both of F-4 and F-40 experienced yielding of the PT bar as shown in Figures 7.22 and 7.20, but it appears that F-40 experienced more PT loss than F-4.

7.3.3 Spring stack force and displacement

Frames 1,4

Figures 7.23, and 7.24 show the spring stack force and the corresponding displacement under the DBE. The spring stack of F-40 experienced large peak force, but less peak displacement in comparison with F-1. This discrepancy comes as expected since F-4 has stiff spring stack (γ_k=2).

Figures 7.25 and 7.26 show the spring stack force and the corresponding displacement under the MCE level. It can be seen that the spring stack force is equal to the force of the PT bar shown in Figure 7.20 because the FE model connects the spring stack and the PT bar in series. Also, the spring stack force drops as yielding occurs at PT bar of F-4. Additionally, the spring stack experienced some relaxation by having a negative displacement due to the reduction of the PT force due to yielding. Again, the spring stack of F-4 experienced more force and less displacement. Moreover, it does capture the decrease in the PT force due to yielding.

Frames 37, 40

Figures 7.27 and 7.28 show the spring stack force and the corresponding displacement due to the DBE. The response is similar to that of F-1 and F-4 because the spring stack did not clamp during the DBE.

Figures 7.29 and 7.30 show the response under the MCE. It can be seen that the spring stack of F-40 has reached its maximum travel capacity (clamping) due to the increased force at the PT bar. Also, the force at the spring stack does not increase once clamping occurs. In fact, Figure 7.31 shows that the gap element picks up the additional load beyond clamping and prevents the spring stack from deforming.

Figure 7.30 reveals that the spring stack of F-40 did not return to its initial static position of equilibrium since the force at the PT bar was reduced due to the yielding. F-37 experienced more peak displacement and less peak PT force, but no damage by yielding.

7.3.4 Overturning moment vs. roof drift

Frames 1,4

Figure 7.32 shows the recorded overturning moment of F-1 and F-4 versus the roof drift due to DBE. We can see that F-4 has more stiffness after the DEC limit state since it has a spring stack that is stiffer than F-1. Also, no hysteretic behavior in either F-1 or F-4 is present because no yielding occurred under the DBE level.

On the contrary, the response under the MCE is different and is shown in Figure 7.33. The figure demonstrates that the MCE caused the PT steel of F-4 to yield leading to the hysteresis loop shown. Also, the figure indicates that the drop in the PT force of F-4 caused the decompression moment to be less and this explains the secondary backbone curve of F-4 shown in Figure 7.33.

In contrast to F-4, the PT steel of F-1 did not yield, and there was no loss in the PT force as illustrated in Figure 7.33. It is clear that both of F-1 and F-4 recentered after the earthquake ended.

Frames 37,40

Figure 7.34 shows the response of F-37 and F-40 under the DBE. Both of F-37 and F-40 follow the same responses of F-1 and F-4 shown in Figure 7.32 since the DBE did not induce clamping of the spring stack.

Figure 7.35 shows the response to the MCE, and it indicates that the PT bar of F-40 experienced yielding that led to the hysteretic behavior shown. However, we can see that

the clamping of the spring stack caused some gain in stiffness after the gap opening (marked with an arrow in Figure 7.35), which complies with the findings of the parametric study presented in Chapter 6.

Figure 7.35 shows that the DEC moment becomes smaller after yielding of F-40 steel, and this leads to the secondary backbone path. However, the remaining PT force was larger enough to cause recentering of the rocking frame by the end of the earthquake.

7.3.5 Vertical reaction at supports

Frames 1,4

Figures 7.36 and 7.37 present the vertical reactions at the base of F-1 and F-4 under DBE. The figures show that the supports are originally in compression due to the initial PT force and the gravity loads on the rocking frame. Also, the supports carry compression loads only as intended when building the FE model. Note that the gap at the base of the frame opens when the reaction is zero. Now, the peak reactions of F-4 are larger than that of F-1, and the reason is that F-4 developed more PT force during its response due to stiff springs.

Figures 7.38 and 7.39 present the response due to the MCE level. The frames exhibit more reactions than the DBE level, but the peak reaction of F-4 is still larger than F-1.

Frames 37,40

Figures 7.40 and 7.41 show the vertical reactions at the base of F-37 and F-40 under the DBE. The response is the same to the response of F-1 and F-4 shown in Figures 7.36, 7.37 because there was no clamping of the spring stack during the earthquake.

Figures 7.42 and 7.43 show the vertical reaction at the base of F-37 and F-40 under the MCE. We can see that the peak vertical reaction at F-40 is larger than the peak vertical reaction of F-37 because the peak PT force developed in F-40 is greater than F-37. Moreover, the reactions are greater than the once obtained under the DBE. Notice that while F-4 and F-40 developed more peak vertical reactions under the MCE, their response has a lower amplitude than F-1 and F-4 by the end of the ground motion. This is because both of F-4 and F-40 experienced a reduction of the PT force due to yielding, which reduces the vertical reaction at the supports.

7.3.6 Vertical gap at supports

Frames 1,4

Figures 7.44 and 7.45 show the vertical displacement of the left and the right supports due to the DBE. We can see that the peak displacement for F-1 is larger than F-4.

Figures 7.46 and 7.47 show the vertical displacement due to the MCE level. It is greater than the DBE response, but the peak vertical displacement of F-1 is still bigger than F-4.

Frames 37,40

Figures 7.48 and 7.49 show the vertical displacement due to the DBE, and it is equal to that of F-1 and F-4 for the same DBE as shown in Figures 7.44 and 7.45. However, Figures 7.50, 7.51 demonstrate the response under the MCE, and the same trend could be seen that F-37 has larger peak vertical displacement than F-40.

Note that F-4 and F-40 have more frequent gap opening than F-1 and F-37 under the MCE. This is explained by the fact that the yielding of the PT steel reduces the decompression moment. Thus, it was easier for F-4 and F-40 to open the gap at the base of the frame even with small lateral force.

7.3.7 Brace forces

Figures 7.52 and 7.53 show the first story brace forces of F-1, F-4, F37, and F-40 under the DBE. All braces were originally in compression due to the initial PT force besides the gravity loads on the rocking frame. We see that the tension force in the braces is too small because the base of the column is free to move laterally and vertically when the gap at the base of the frame opens. Figures 7.54and 7.55 show the response due to the MCE, and the peak forces are higher than the DBE.

7.3.8 Base shear and overturning moment history

Frames 1,4

Figures 7.56 and 7.57 show the base shear and the overturning moment of F-1 and F-4 under the DBE. In general, the peak overturning moment and base shear of F-1 are less

than F-4 under the DBE. Indeed, peak base shear for F-1 is 20% less, while the overturning moment is 14% less.

Figures 7.58 and 7.59 show the base shear and the overturning moment of F-1 and F-4 under the MCE. The peak base shear for F-1 is 9% higher than F-4, while the overturning moment is 21% less.

Frames 37,40

Figures 7.60 and 7.61 show the base shear and the overturning moment history response of F-37 and F-40 under the DBE, and it is similar to the base shear and overturning moment of F-1 and F-4 under the DBE. This similarity is attributed to the fact that no clamping of the spring stack occurred under the DBE.

On the other hand, the response under the MCE in Figures 7.62 and 7.63 show that F-37 developed more peak base shear and less peak overturning moment than F-40.

7.3.9 Floor accelerations

Figures 7.64, 7.65, 7.66 and 7.67 show the floor accelerations of F-1 and F-4 due to the DBE with the ground motion time history, which are similar to that of F-37 and F-40 shown in Figures 7.68, 7.69 and 7.70. Under the DBE, the peak floor accelerations of F-1 and F-37 are less than the peaks of F-4 and F-40. Note that this is consistent with the previous finding that the peak base shear for F-1 and F-37 were less than F-4 and F-40 peaks for the DBE.

Also, the results for the MCE with the ground motion history are shown in Figures 7.71, 7.72, 7.73 and 7.74 for F-1 and F-40 and Figures 7.75, 7.76and 7.77 for F-37 and F-40. The peaks of the floor accelerations for F-1 and F-37 are larger than F-4 and F-40 under the MCE. Again, this is consistent with the finding that the peak base shear for F-1 and F-4 is larger than the other frames.

7.4 PEAK RESPONSES

This section summarizes the peak responses of the prototype frames (F-1, F-4, F-6, F-37, F-40, and F-43) to the entire set of 44 Far-Field ground motion record given in the FEMA P695. The above frames are in three groups:

1) F-1 and F-4 have spring stacks with infinite travel capacities (i.e. spring does not clamp);
2) F-37 and F-40 have spring stacks with finite travel capacities (i.e. spring does clamp);
3) F-6 is a standard rocking frame without disc springs.

It is noted that F-1 and F-37 have spring stack with γ_k=0.2, while F-4 and F-40 have spring stack with γ_k=2.0. The peak responses of interest are the followings: (1) base shear; (2) overturning moment; (3) roof drift; (4) maximum PT force (5) residual PT force; (6) inter-story drifts; (7) storiy displacements; and, (8) roof acceleration.

7.4.1 Base shear

F-1, F-4, and F-6

Figure 7.78 shows the peak recorded base shear for F-1, F-4, and F-6 due to the 22-pair ground motions scaled to the DBE. The figure illustrates that the peak base shear of different frames is essentially the same for the given ground motions are applied.

Figure 7.79 shows the maximum recorded base shear of F-1, F-4, and F-6 under the MCE. As expected, the figure shows that peak base shear under the MCE is larger than the DBE.

F-37, F-40, and F-6

Figure 7.80 shows the peak base shear of F-37, F-40, and F-6 under the DBE. It worth mentioning that under certain earthquakes scaled to the MCE, (EQ ID =11 in Figure 7.82 for example) the peak recorded base shear of F-40 is different from F-4 peak base shear. This difference means that the clamping of the spring stack of F-40 during the response could affect the peak base shear.

Table 7.3 lists the average peak base shear and the standard deviation of the 22-pair ground motions. In general, the frames with flexible spring stack (γ_k=0.2) developed slightly less peak shear.

7.4.2 Overturning moment

F-1, F-4, and F-6

Figure 7.82 shows the peak recorded the overturning moment of F-1, F-4, and F-6 due to the DBE. In most cases, the peak overturning moment of F-1 is less than that of F-4 and F-6, and this is because the peak PT force of F-1 is always less.

Figure 7.83 shows the peak recorded overturning moment under the MCE. Although F-1, F-4, and F-6 experienced an increase in the peak overturning moment due to the MCE, F-1 experienced the smallest increase. This is because the PT steel of F-1 experienced the smallest increase in the peak force due to its relatively flexible spring stack.

F-37, F-40, and F-6

Figure 7.84 shows the peak overturning moment of F-37 and F-40 under the DBE. In a similar manner to F-1 and F-4, the peak overturning moment of F-37 is less than that of F-40 and F-6 since the peak PT force of F-37 is less.

Figure 7.85 shows the peak recorded overturning moment at the base of F-37, F-40, and F-6 due to the MCE. In general, the peak overturning moment under the MCE is larger than the peak overturning moment under the DBE. It is noted that F-37 continues at have the least peak overturning moment.

Table 7.4 lists the average peak recorded overturning moments due to the Far-Field record set. Ingeneral, frames with flexible spring stack (γ_k=0.2) developed less peak overturning moment.

7.4.3 Maximum and residual PT force

F-1, F-4, and F-6

Figure 7.85 shows the maximum recorded PT force during the 22-pair ground motions scaled to the DBE. The figure follows the trend that F-1 always exhibits the lowest increase in the PT force, while F-6 encounters the largest increase. However, Figure 7.87 shows that F-6 reached the yield stress in 4 out of the 44 ground motions, while F-1 and F-4 never experienced yielding in any of the ground motions.

Figure 7.88 shows the maximum PT force due to MCE ground motion level. The figure indicates that the MCE in general induced more peak PT force than the DBE. Also, as illustrated in Figure 7.89, F-6 encountered yielding in 20 out of the 44 ground motions, while F-4 encountered yielding in 11 of them. However, the figure shows that the residual PT force of F-4 was always larger than that of F-6.

Interestingly, Figure 7.89 showes that F-6 fully lost its PT force three times, but F-1 never yielded in any of the ground motions. This shows that the more flexible the spring stack, the less maximum PT force is developed provided that the rocking frames are pushed laterally the same magnitude.

F-37, F-40, and F-6

Figure 7.90 shows the peak PT force developed during the DBE response of F-37, F-40, and F-6. In a similar manner to the previous F-1 and F-4, the maximum developed PT force is less for the frame that has flexible spring stack. As a matter of fact, we can see in Figure

7.91 that F-6 encounters yielding in 4 out of 44 ground motions, whereas F-40 yielded in only one of them and F-37 never yielded. Note that F-4 in Figure 7.87 never yielded in any of the ground motions, but F-37 in Figure 7.91 yielded once because of the clamping of the spring stack that suddenly increases the PT force and causes yielding.

Figure 7.92 shows the maximum PT force under the MCE, and it implies that the MCE induced more peak PT force. In particular, F-40 reached yielding in 14 out of the 44 ground motions as seen in Figure 7.93 and one of these cases caused a total loss of the PT force. Still, F-37 like F-1; it never yielded, and the residual PT force always equals the initial force.

Table 7.5 lists the average peak PT forces due to the 44-pair ground motions. In general, the frames with flexible spring stack (γ_k=0.2) developed less peak PT force.

7.4.4 Roof drift

F-1, F-4, and F-6

Figure 7.94 shows the maximum recorded drift due to the DBE. The figure indicates that even with different spring stack stiffnesses, F-1 and F-4 have exhibited the same response if the ground motion does not push the frames far beyond their decompression (DEC) limit state.

Figure 7.95 shows the maximum recorded roof drift due to the MCE. The peaks are higher than the peaks obtained under the DBE. However, most frames were pushed far beyond their DEC limit state under the MCE, and this led to the results shown in Figure 7.95.

F-37, F-40, and F-6

Figure 7.96 shows the maximum recorded drift due to the DBE. However, some earthquakes caused clamping of the spring stack and led to slightly different results than F-1 and F-4.

Figure 7.97 shows the response due to the MCE, and it can be seen that the maximum drifts are generally larger than the DBE.

Table 7.7 lists the average peak recorded roof drifts due to the 22-pair ground motions. In general, frames with flexible spring stack (γ_k=0.2) underwent larger roof drift. This behavior is expected since frames with flexible spring stacks have small lateral stiffness after the gap opening.

7.4.5 Roof acceleration

Figures 7.98 and 7.99 show the peak roof acceleration of F-1, F-4, and F-6 under the DBE and the MCE. It can be seen that the peak responses are essentially very close. Figures 7.100 and 7.101 show the peak roof acceleration of F-37, F-40, and F-6 under the DBE and the MCE. As expected, the figures indicate that the peaks are higher for the MCE than the DBE.

Table 7.6 lists the average peak recorded floor acceleration due to the 22-pair ground motions. The table shows that the average roof drift is similar. However, the average for the MCE is larger than the DBE.

7.4.6 Maximum inter-story drift and displacement

Figures 7.102, 7.103, 7.104, 7.105, 7.106 and 7.107 show the maximum recorded interstory drifts and the corresponding floor displacements of F-1 and F-4 under the DBE. Figures 7.108, 7.109, 7.110, 7.111, 7.112 and 7.113 show the peak drifts and the corresponding floor displacement under the MCE for F-1 and F-4. The response is generally higher for the MCE than the DBE.

Figures 7.114, 7.115, 7.116, 7.117, 7.118 and 7.119 show the peak drifts and the corresponding floor displacements of F-37 and F-10 under the DBE. Figures 7.120, 7.121, 7.122, 7.123, 7.124 and 7.125 display the response the MCE. Notice that under low intensity seismic load, especially for the cases where F-6 did not reach the LLP limit state, the response of F-1, F-4, F-37, F-40, and F-6 matches. This is expected because these frames have the same backbone curves up to the DEC limit state (i.e. before the DEC limit state, all deformations are elastic, and there is no rigid body rotation). Thus, the low intensity seismic load would push F-1, F-4, F-37, F-40, and F-6 to the same peak lateral displacement since their backbone curves are similar in this special case. However, if the seismic load is causing the frames to go far beyond their DEC limit state, their backbone curves would diverge and lead to different peak lateral displacements.

7.5 AVERAGE PEAK RESPONSES

Note that peak responses presented in Section 7.4 are only for F-1, F-4, F-6, F-37, and F-40 to keep the discussion focused. However, this section presents the average peak response of the entire frames with zero eccentricity listed in Tables 6.1 and 6.2 due to the 22-pair ground motions scaled to the DBE and MCE.

Figure 7.126 shows the average peak response of the first group in Table 6.1, which has spring stacks with infinite travel capacities. The followings are noticed: (1) the peak average base shear has negligible increase; (2) under both the DBE and MCE, the average overturning moment and the PT force is reduced with the reduction of the spring stack stiffness; and, (3) the average peak roof acceleration and roof drift have negligible change.

Figure 2.127 shows the average peak response of the second group shown in Table 6.2, which have spring stacks with finite travel capacities. Notice that the same observations mentioned above apply to this figure. In fact, the differences between Figures 7.126 and 7.127 are barely dsitingushable. It is important to notice that frames with flexible spring stacks, γ_k=0.2 for example, have the same peak average value for all the response quantities whether we allow the spring stack clamping or not as shown in Tables 7.3, 7.4, 7.5, and 7.6. This is because these frames never reached the LLP limit state (yielding of the PT steel) during the ground motion because of the flexible spring stack.

7.6 CONCLUSIONS

1. The dynamic analyses show that even though a set of rocking frames have the same dimensions and PT steel area, adding a disc spring stack with variable stiffness could alter the dynamic response of each frame.
2. Frames with flexible spring stacks are likely to develop less peak PT force during the ground motions. This was explained by the fact that adding the spring stack reduces the effective stiffness of the assembly (Accorsi and Sarisley 1990).
3. The dynamic analyses show that even though significant ground motions are applied to the frames, the residual PT force of frames having flexible spring stacks is always more than other frames with stiff spring stack. In fact, the frames with γ_k=0.2 (i.e. flexible spring stack) had never experienced yielding in any of the ground motions in this study. This is attributed to the flexible spring stack.
4. The dynamic analyses demonstrate that the moment hysteresis loop for a frame with γ_k=0.2 (flexible spring stack) is likely to be flat after the frame decompression, while the hysteresis loop of a frame with γ_k=2.0 (stiff spring stack) is steeper under the same circumstances.
5. The clamping of the spring stack during the ground motions caused a sudden increase in the PT force. Interestingly, the moment hysteresis loop of frames where the spring stack clamped during the dynamic response has shown to gain lateral stiffness after clamping.

Table 7.1: Natural frequencies and damping ratios.

Mode	Frequency (Hz)	Period (sec)	Damping Ratio (%)
1	11.8	0.529	4.0
2	34.9	0.187	1.8
3	62.8	0.100	1.6
4	209.4	0.030	3.3
5	314.1	0.026	3.7
6	314.1	0.024	3.9

Table 7.2: ATC-63 far-field ground motion set (Haselton 2008).

EQ ID	Name	Year	Magnitude	PEER-NGA Sequence Number	1st Component	2nd Component	Peak Ground Acceleration (g)	Peak Ground Velocity (cm/sec)
1-2	Northridge	1994	6.7	953	NORTHR/MUL009	NORTHR/MUL279	0.52	63
3-4	Northridge	1994	6.7	960	NORTHR/LOS000	NORTHR/LOS270	0.48	45
5-6	Duzce, Turkey	1999	7.1	1602	DUZCE/BOL000	DUZCE/BOL090	0.82	62
7-8	Hector Mine	1999	7.1	1787	HECTOR/HEC000	HECTOR/HEC090	0.34	42
9-10	Imperial Valley	1979	6.5	169	IMPVALL/H-DLT262	IMPVALL/H-DLT352	0.35	33
11-12	Imperial Valley	1979	6.5	174	IMPVALL/H-E11140	IMPVALL/H-E11230	0.38	42
13-14	Kobe, Japan	1995	6.9	1111	KOBE/NIS000	KOBE/NIS090	0.51	37
15-16	Kobe, Japan	1995	6.9	1116	KOBE/SHI000	KOBE/SHI090	0.24	38
17-18	Kocaeli, Turkey	1999	7.5	1158	KOCAELI/DZC180	KOCAELI/DZC270	0.36	59
19-20	Kocaeli, Turkey	1999	7.5	1148	KOCAELI/ARC000	KOCAELI/ARC090	0.22	40
21-22	Landers	1992	7.3	900	LANDERS/YER270	LANDERS/YER360	0.24	52
23-24	Landers	1992	7.3	848	LANDERS/CLW-LN	LANDERS/CLW-TR	0.42	42
25-26	Loma Prieta	1989	6.9	752	LOMAP/CAP000	LOMAP/CAP090	0.53	35
27-28	Loma Prieta	1989	6.9	767	LOMAP/G03000	LOMAP/G03090	0.56	45
29-30	Manjil, Iran	1990	7.4	1633	MANJIL/ABBAR--L	MANJIL/ABBAR--T	0.51	54
31-32	Superstition Hills	1987	6.5	721	SUPERST/B-ICC000	SUPERST/B-ICC090	0.36	46
33-34	Superstition Hills	1987	6.5	725	SUPERST/B-POE270	SUPERST/B-POE360	0.45	36
35-36	Cape Mendocino	1992	7.0	829	CAPEMEND/RIO270	CAPEMEND/RIO360	0.55	44
37-38	Chi-Chi, Taiwan	1999	7.6	1244	CHICHI/CHY101-E	CHICHI/CHY101-N	0.44	115
39-40	Chi-Chi, Taiwan	1999	7.6	1485	CHICHI/TCU045-E	CHICHI/TCU045-N	0.51	39
41-42	San Fernando	1971	6.6	68	SFERN/PEL090	SFERN/PEL180	0.21	19
43-44	Friuli, Italy	1976	6.5	125	FRIULI/A-TMZ000	FRIULI/A-TMZ270	0.35	31

Table 7.3: Average peak base shear due to the Far-Field ground motion set.

	Relative stiffness γ_k	DBE		MCE	
		Mean (kips)	**Standard Deviation (kips)**	**Mean (kips)**	**Standard Deviation (kips)**
Spring stack has infinite travel capacity	γ_k=0.2	109.0	26.1	154.0	47.0
	γ_k=0.5	111.2	27.1	157.9	44.0
	γ_k=1.0	113.5	27.7	159.2	46.2
	γ_k=2.0	113.7	27.0	157.5	43.4
Spring stack has finite travel capacity	γ_k=0.2	109.0	26.1	154.0	47.0
	γ_k=0.5	111.2	27.1	158.2	44.7
	γ_k=1.0	113.5	27.7	158.4	44.6
	γ_k=2.0	114.0	26.9	157.7	44.3

Table 7.4: Average peak overturning moment due to the Far-Field record set.

	Relative stiffness γ_k	**DBE**		**MCE**	
		Mean (kips.in)	**Standard Deviation (kips.in)**	**Mean (kips.in)**	**Standard Deviation (kips.in)**
Spring stack has infinite travel capacity	γ_k=0.2	17218	643	18397	1107
	γ_k=0.5	18253	1242	20480	2099
	γ_k=1.0	19107	1624	22062	2623
	γ_k=2.0	19980	2249	23194	2679
Spring stack has finite travel capacity	γ_k=0.2	17218	643	18397	1107
	γ_k=0.5	18253	1242	21006	2865
	γ_k=1.0	19224	1899	22585	3018
	γ_k=2.0	20144	2573	23572	2801

Table 7.5: Average peak PT force due to the Far Field record set.

	Relative stiffness γ_k	DBE		MCE	
		Mean (kips)	**Standard Deviation (kips)**	**Mean (kips)**	**Standard Deviation (kips)**
Spring stack has infinite travel capacity	γ_k=0.2	191.0	10.7	210.7	18.5
	γ_k=0.5	208.2	20.7	245.4	35.1
	γ_k=1.0	222.5	27.1	271.8	43.8
	γ_k=2.0	237.0	37.5	290.6	44.7
Spring stack has finite travel capacity	γ_k=0.2	191.0	10.7	210.7	18.5
	γ_k=0.5	208.2	20.7	254.2	47.8
	γ_k=1.0	224.4	31.7	280.5	50.4
	γ_k=2.0	239.7	42.9	297.0	46.7

Table 7.5: Average peak roof acceleration due to the Far-Field record set.

	Relative stiffness γ_k	DBE		MCE	
		Mean (g)	**Standard Deviation (g)**	**Mean (g)**	**Standard Deviation (g)**
Spring stack has infinite travel capacity	γ_k=0.2	0.802	0.255	1.246	0.427
	γ_k=0.5	0.817	0.275	1.252	0.408
	γ_k=1.0	0.836	0.281	1.269	0.407
	γ_k=2.0	0.826	0.270	1.251	0.407
Spring stack has finite travel capacity	γ_k=0.2	0.802	0.255	1.246	0.427
	γ_k=0.5	0.817	0.275	1.256	0.409
	γ_k=1.0	0.836	0.281	1.263	0.402
	γ_k=2.0	0.826	0.270	1.250	0.411

Table 7.6: Average peak roof drifts due to the Far-Field record set.

	Relative stiffness γ_k	DBE		MCE	
		Mean (%)	**Standard Deviation (%)**	**Mean (%)**	**Standard Deviation (%)**
Spring stack has infinite travel capacity	γ_k=0.2	1.192	0.585	2.236	0.943
	γ_k=0.5	1.171	0.581	2.188	0.923
	γ_k=1.0	1.127	0.525	2.122	0.936
	γ_k=2.0	1.118	0.559	2.096	0.957
Spring stack has finite travel capacity	γ_k=0.2	1.192	0.585	2.236	0.943
	γ_k=0.5	1.171	0.581	2.171	0.898
	γ_k=1.0	1.128	0.527	2.114	0.932
	γ_k=2.0	1.117	0.558	2.079	0.934

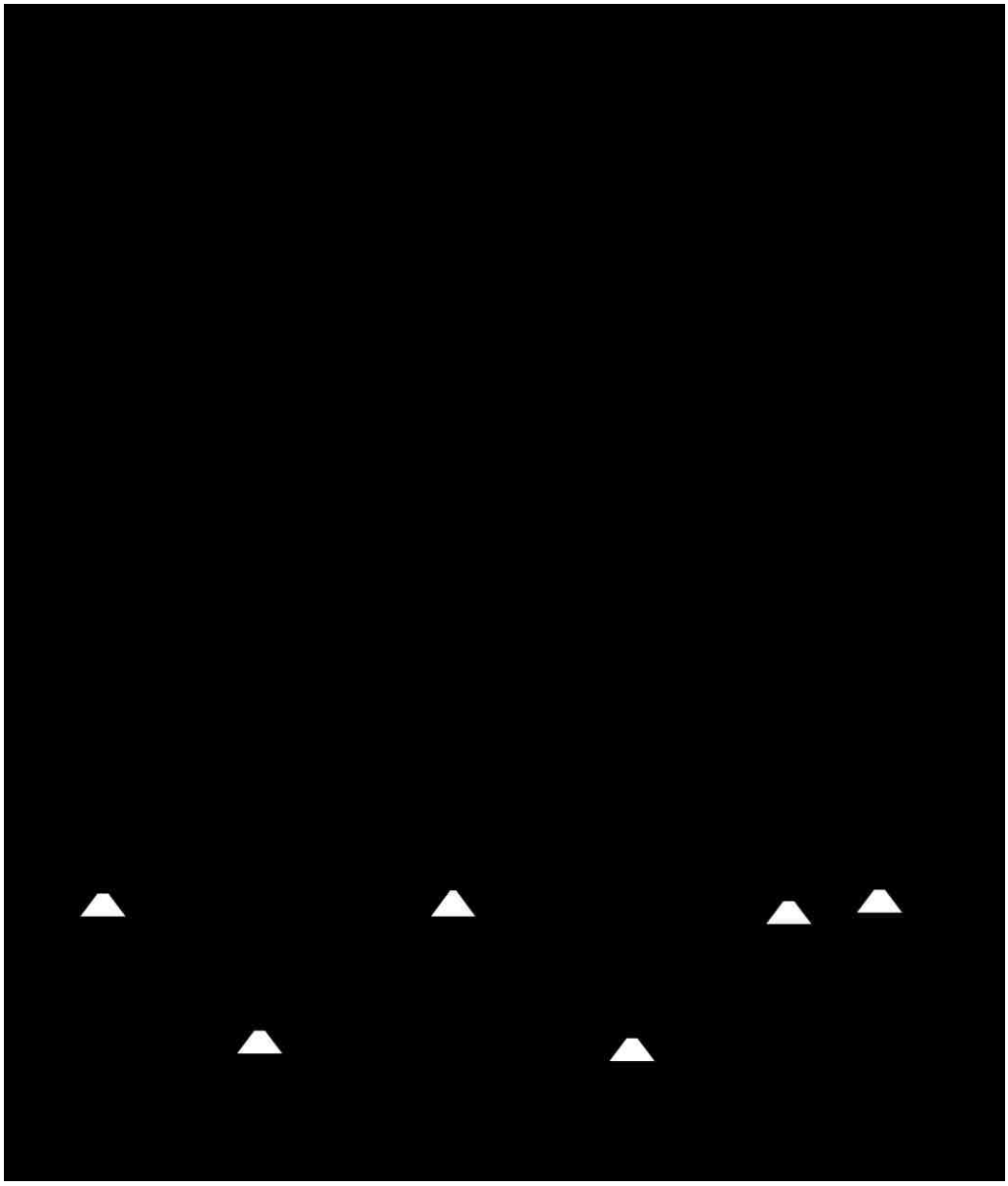

Figure 7.1: FE model for frames with spring stack with infinite travel capacity.

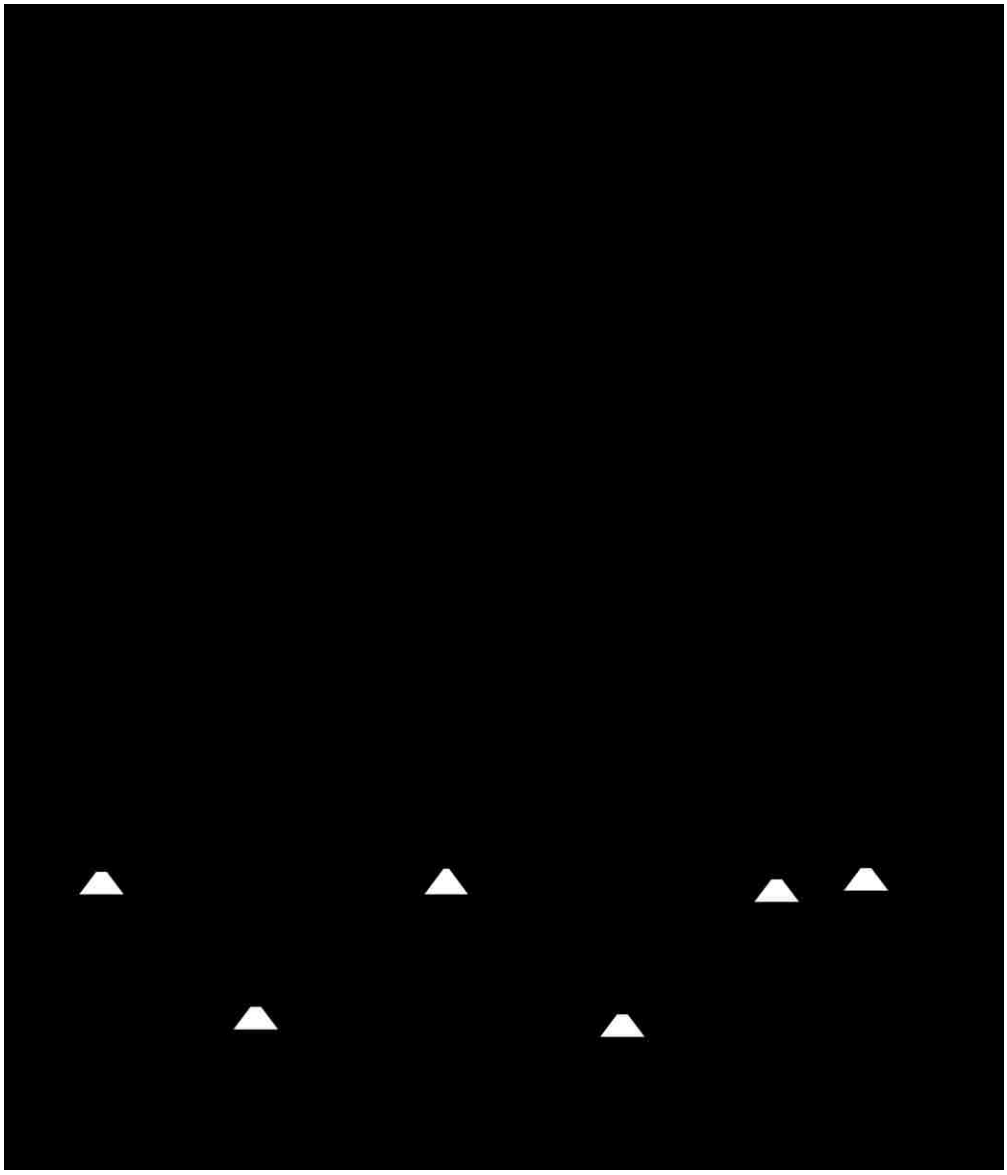

Figure 7.2: FE model for frames with spring stack with finite travel capacity.

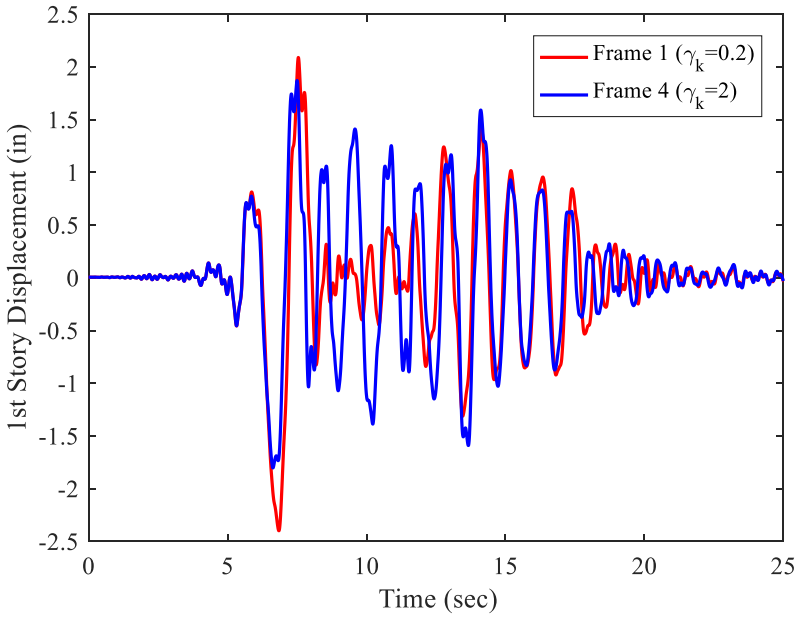

Figure 7.3: 1st story displacement of F-1 and F-4 under Hector Mine earthquake scaled to the DBE level (spring stack has infinite travel capacity).

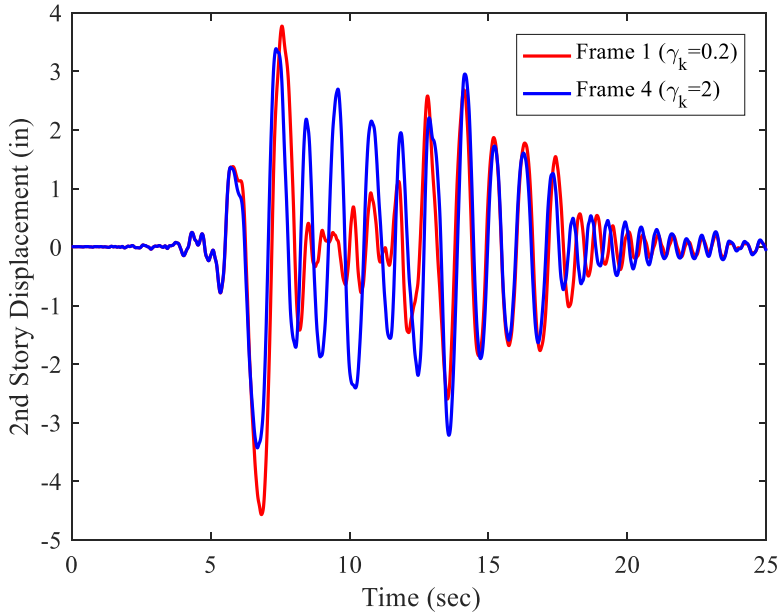

Figure 7.4: 2nd story displacement of F-1 and F-4 under Hector Mine earthquake scaled to the DBE level (spring stack has infinite travel capacity).

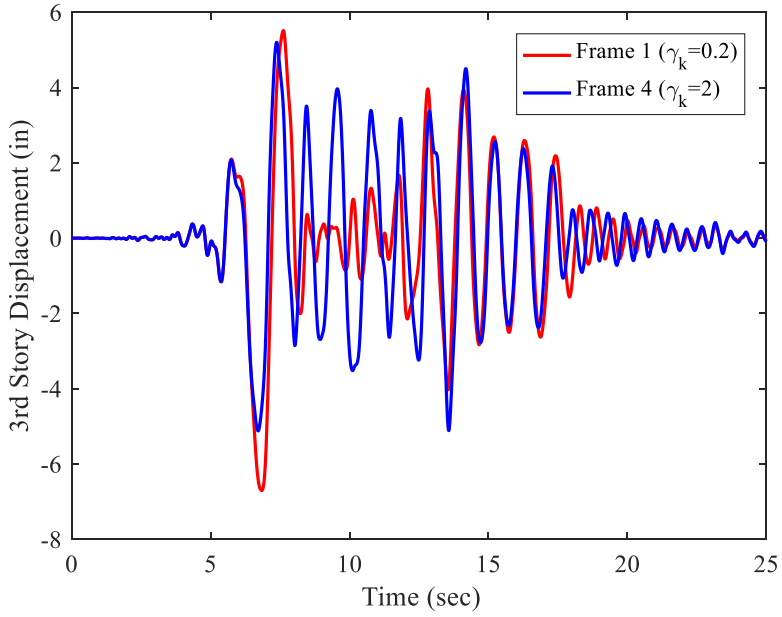

Figure 7.5: 3rd story displacement of F-1 and F-4 under Hector Mine earthquake scaled to the DBE level (spring stack has infinite travel capacity).

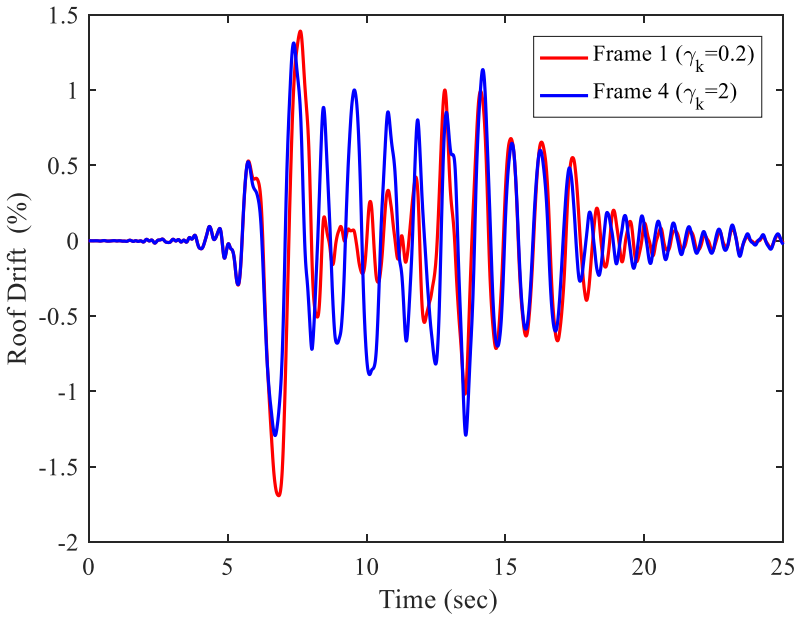

Figure 7.6: Roof drift of F-1 and F-4 under Hector Mine earthquake scaled to the DBE level (spring stack has infinite travel capacity).

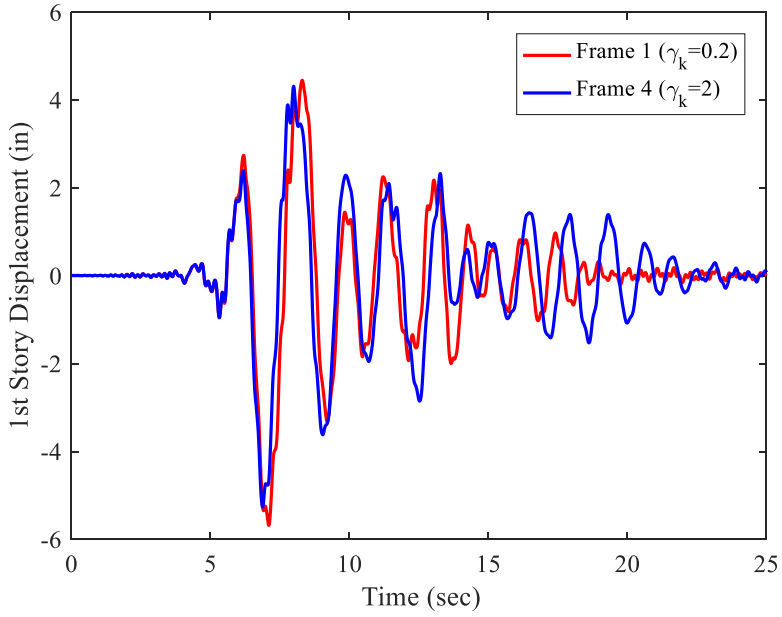

Figure 7.7: 1st story displacement of F-1 and F-4 under Hector Mine earthquake scaled to the MCE level (spring stack has infinite travel capacity).

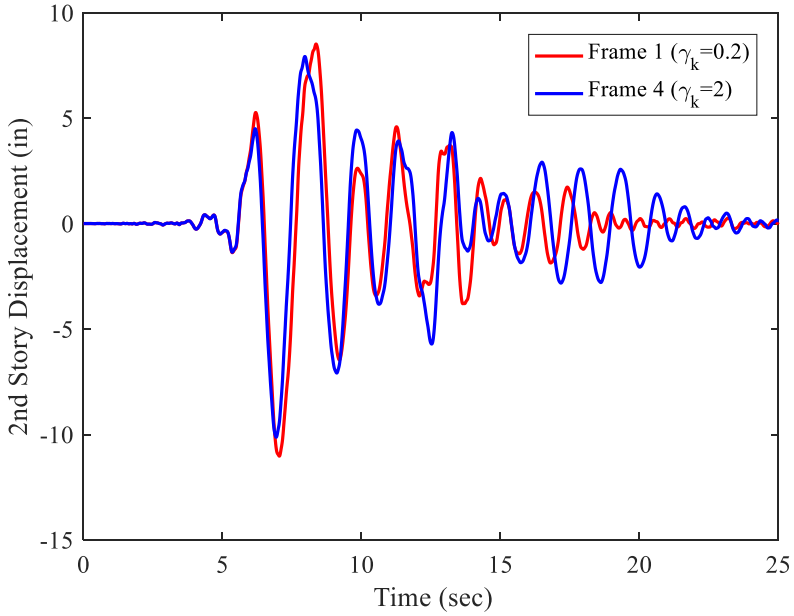

Figure 7.8: 2nd story displacement of F-1 and F-4 under Hector Mine earthquake scaled to the MCE level (spring stack has infinite travel capacity).

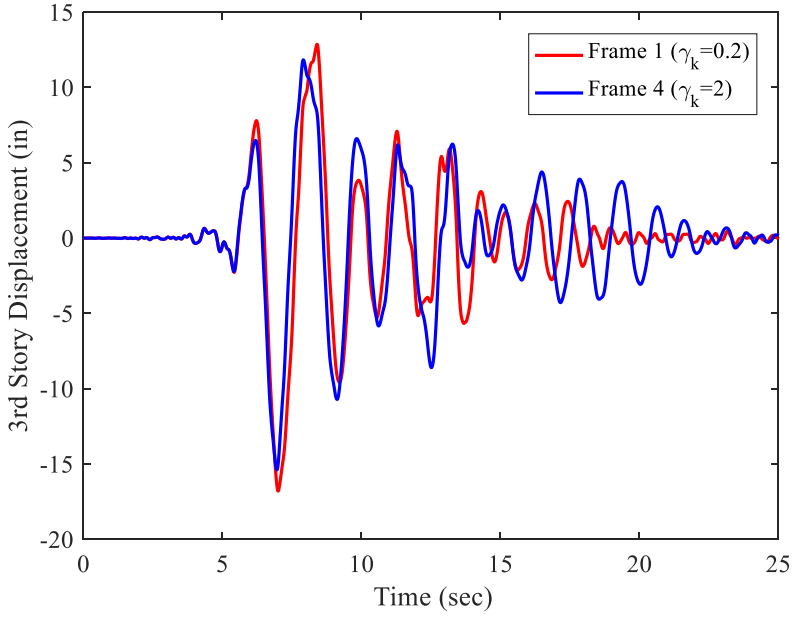

Figure 7.9: 3rd story displacement of F-1 and F-4 under Hector Mine earthquake scaled to the MCE level (spring stack has infinite travel capacity).

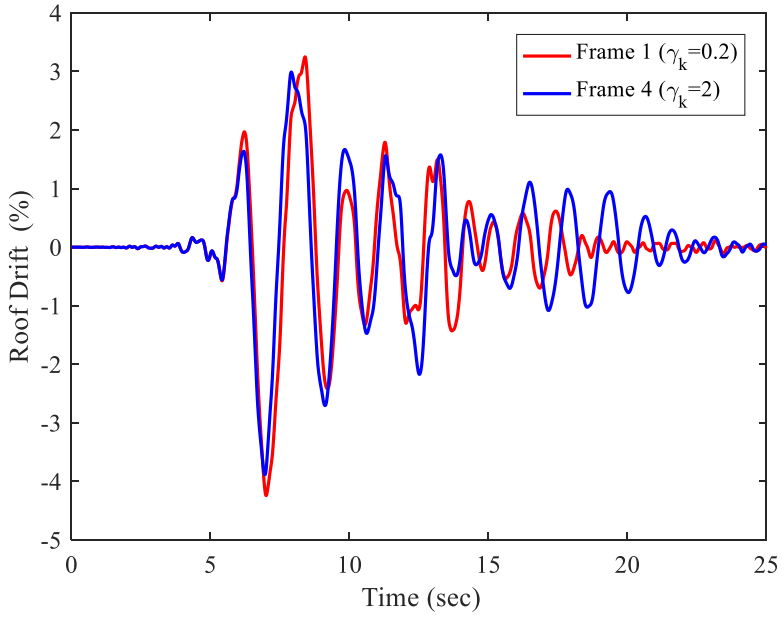

Figure 7.10: Roof drift of F-1 and F-4 under Hector Mine earthquake scaled to the MCE level (spring stack has infinite travel capacity).

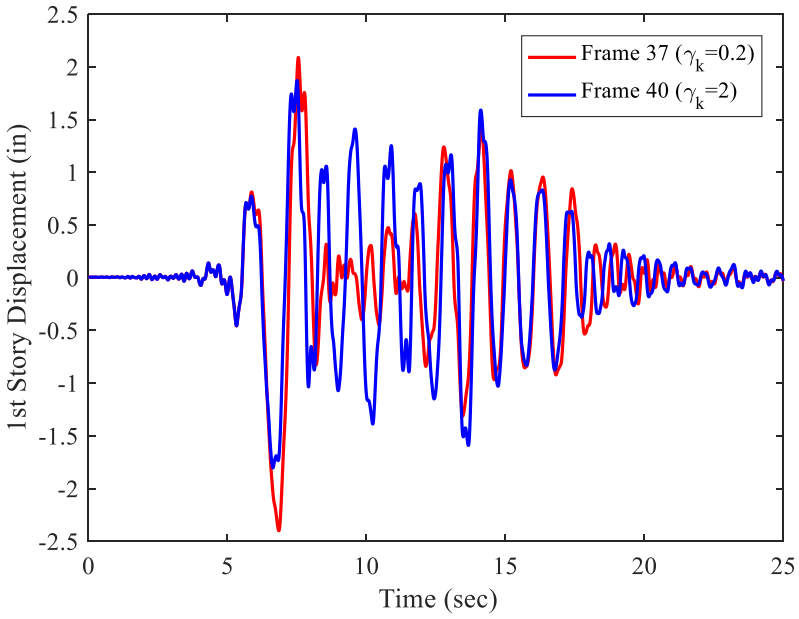

Figure 7.11: 1st story displacement of F-37 and F-40 under Hector Mine earthquake scaled to the DBE level (spring stack has finite travel capacity).

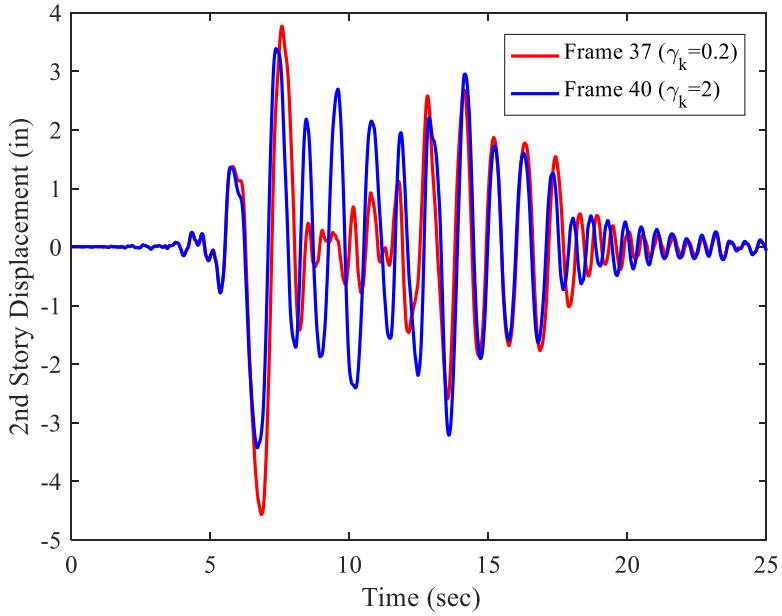

Figure 7.12: 2nd story displacement of F-37 and F-40 under Hector Mine earthquake scaled to the DBE level (spring stack has finite travel capacity).

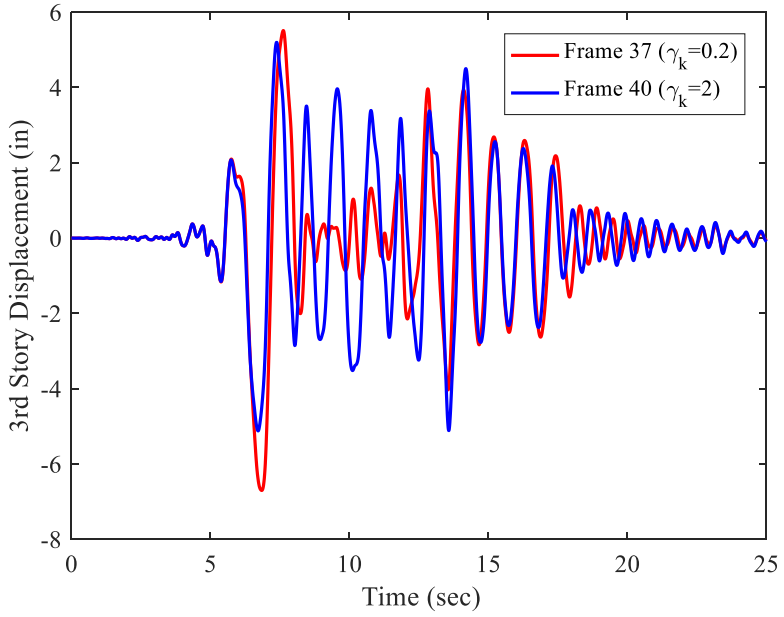

Figure 7.13: 3rd story displacement of F-37 and F-40 under Hector Mine earthquake scaled to the DBE level (spring stack has finite travel capacity).

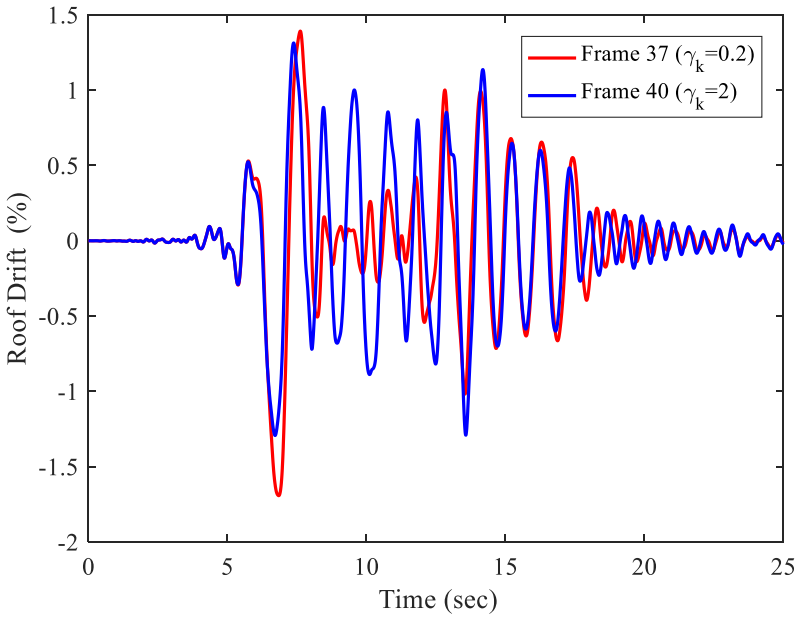

Figure 7.14: Roof drift of F-37 and F-40 under Hector Mine earthquake scaled to the DBE level (spring stack has finite travel capacity).

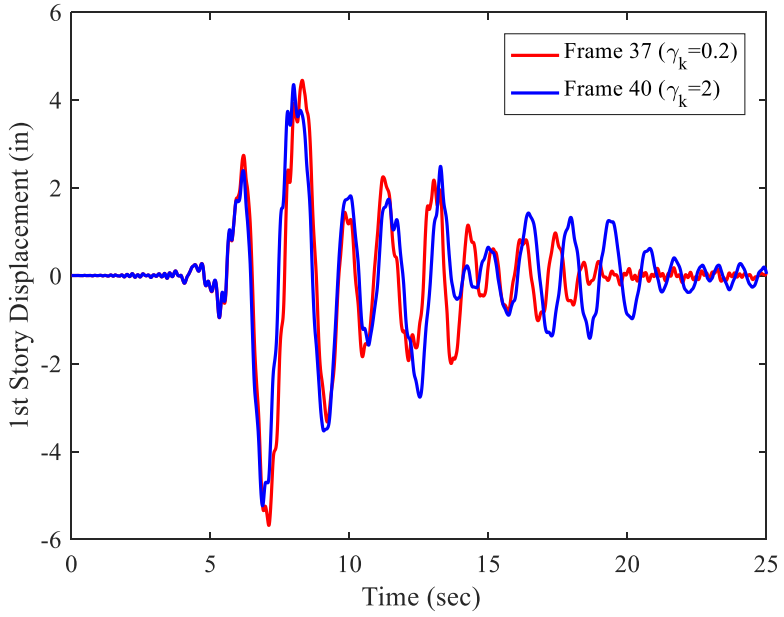

Figure 7.15: 1st story displacement of F-37 and F-40 under Hector Mine earthquake scaled to the MCE level (spring stack has finite travel capacity).

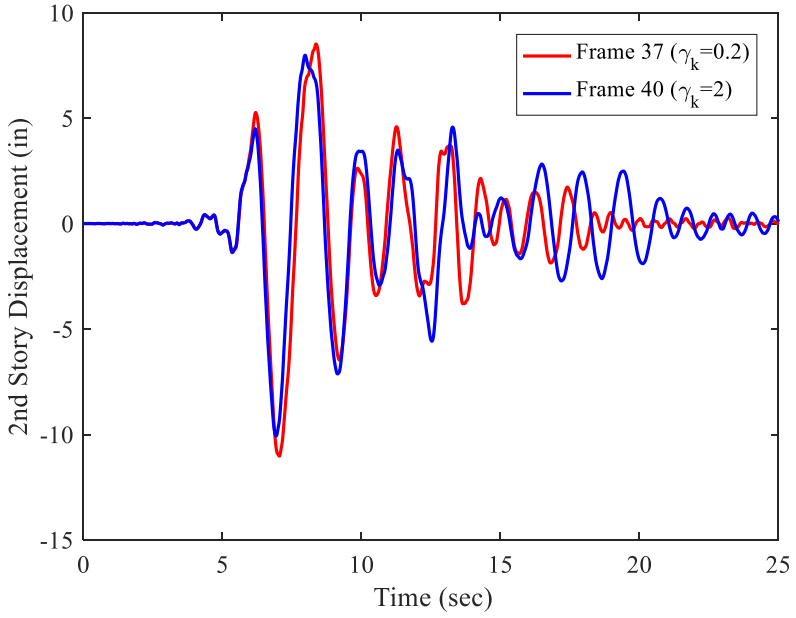

Figure 7.16: 2nd story displacement of F-37 and F-40 under Hector Mine earthquake scaled to the MCE level (spring stack has finite travel capacity).

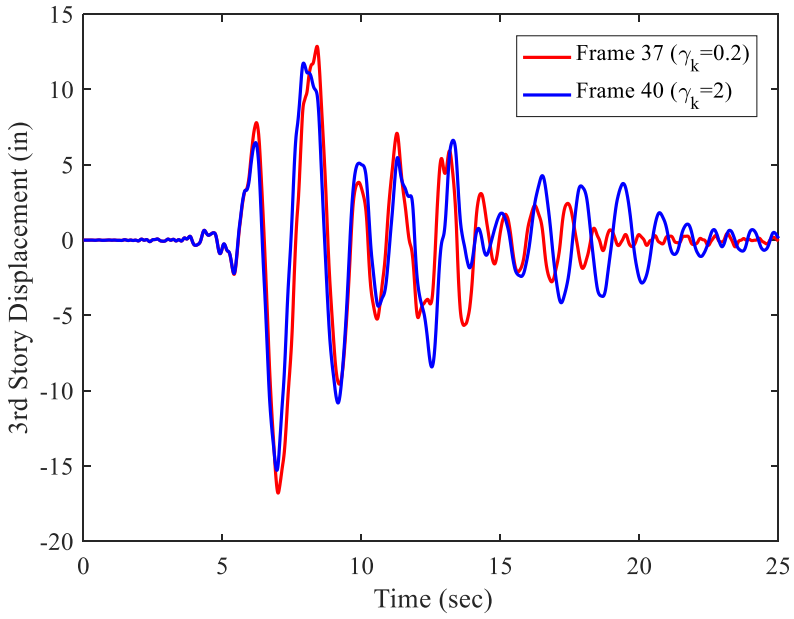

Figure 7.17: 3rd story displacement of F-37 and F-40 under Hector Mine earthquake scaled to the MCE level (spring stack has finite travel capacity).

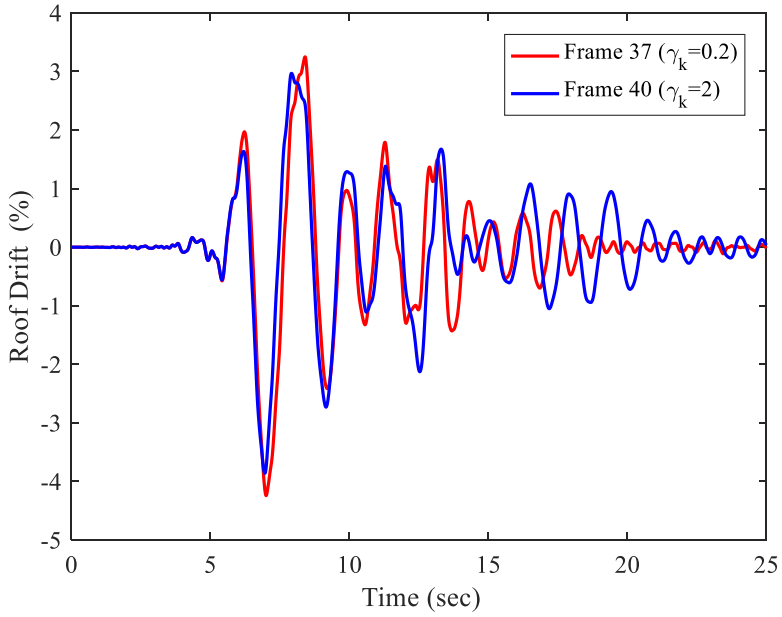

Figure 7.18: Roof drift of F-37 and F-40 under Hector Mine earthquake scaled to the MCE level (spring stack has finite travel capacity).

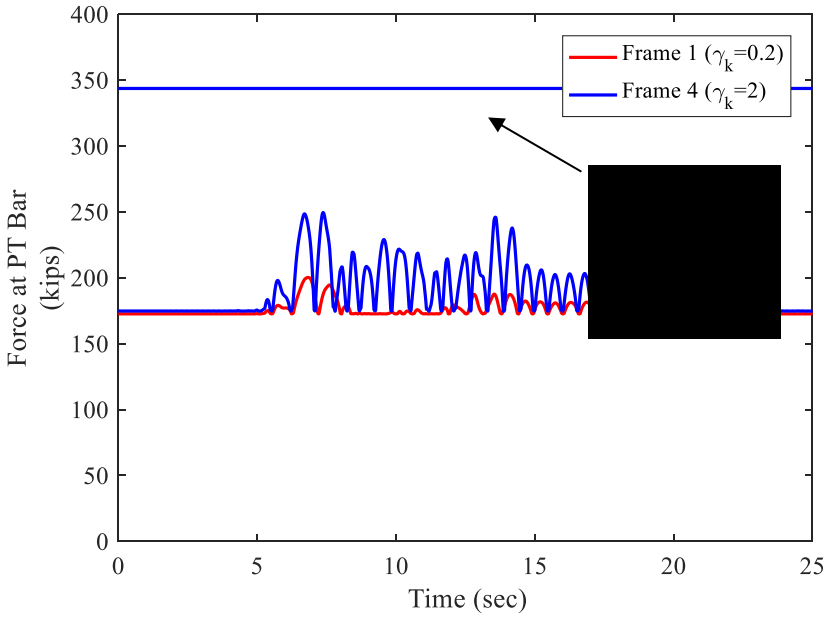

Figure 7.19: Force at the PT bar of F-1 and F-4 under Hector Mine earthquake scaled to the DBE level (spring stack has infinite travel capacity).

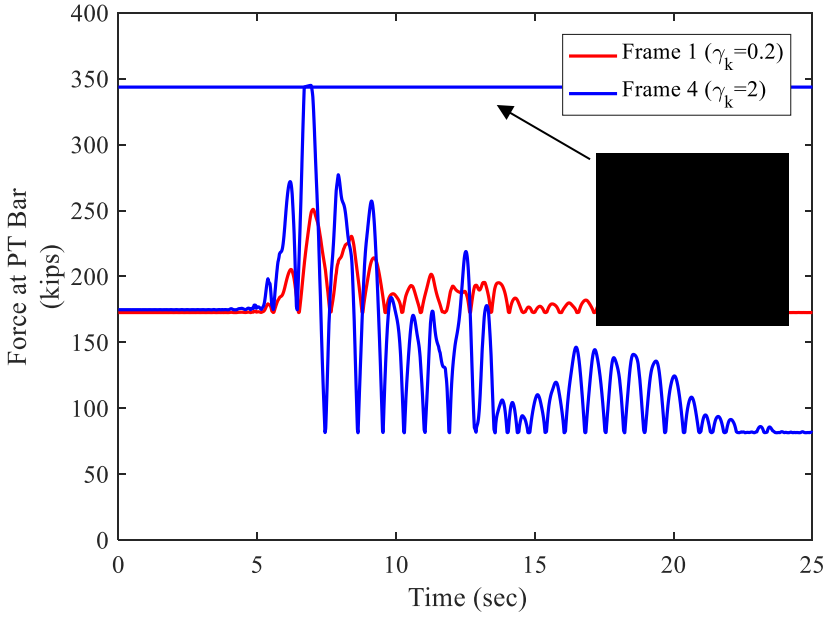

Figure 7.20: Force at PT bar of F-1 and F-4 under Hector Mine earthquake scaled to the MCE level (spring stack has infinite travel capacity).

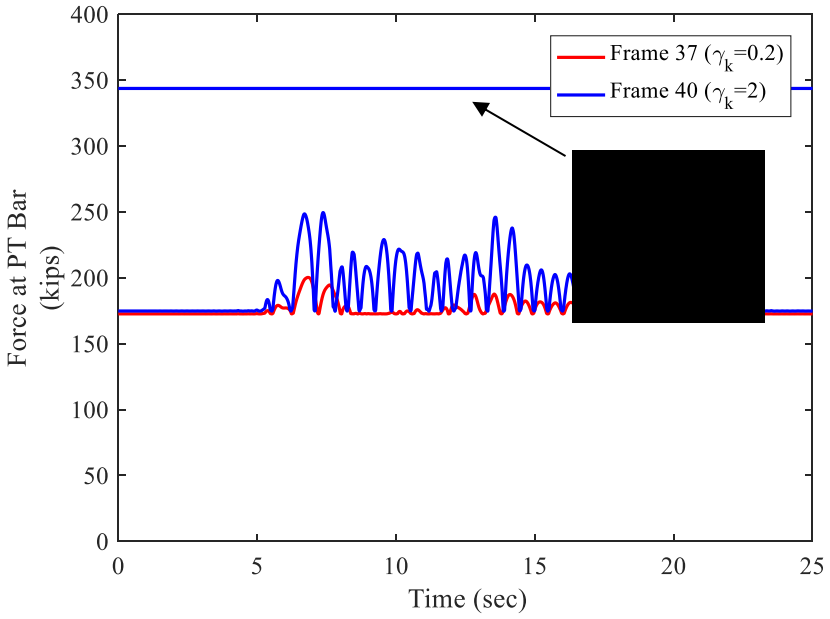

Figure 7.21: Force at PT bar of F-37 and F-40 under Hector Mine earthquake scaled to the DBE level (spring stack has finite travel capacity).

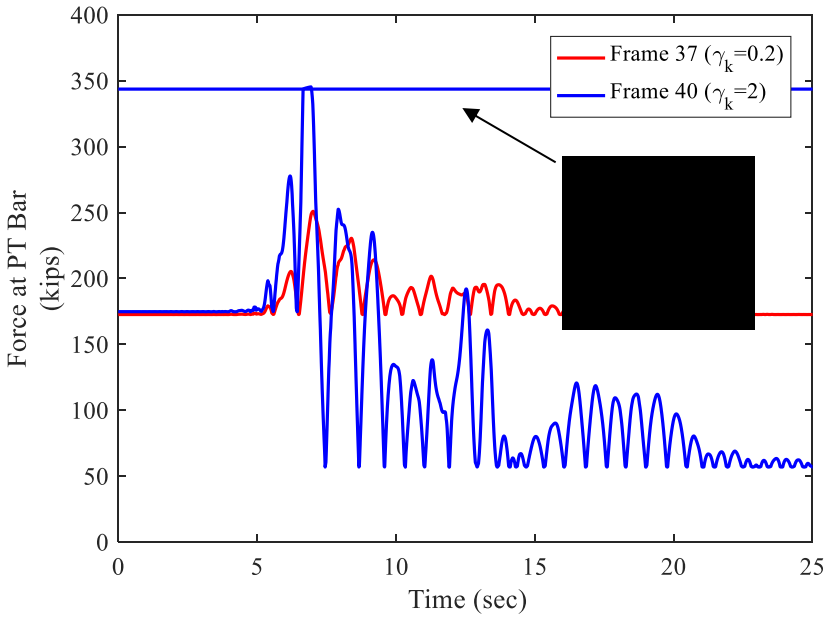

Figure 7.22: Force at PT bar of F-37 and F-40 under Hector Mine earthquake scaled to the MCE level (spring stack has finite travel capacity).

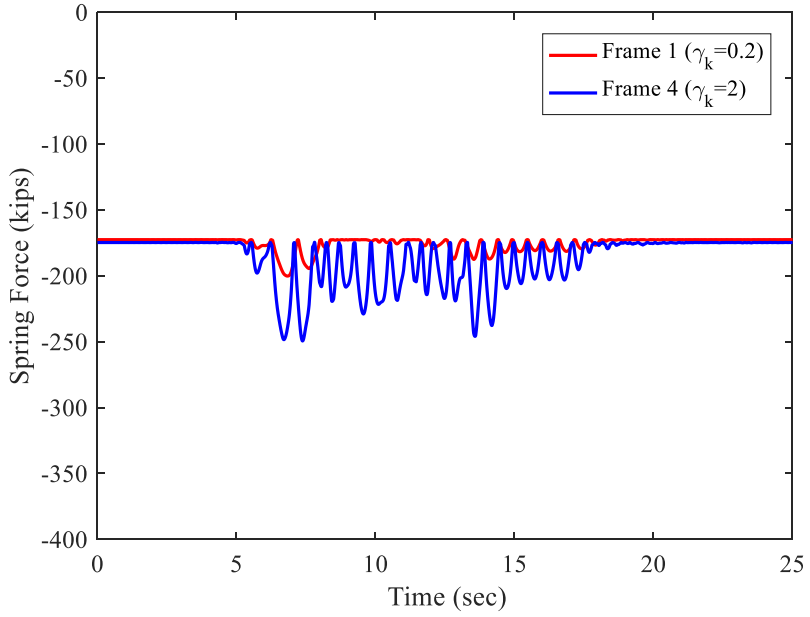

Figure 7.23: Force at spring stack of F-1 and F-4 under Hector Mine earthquake scaled to the DBE level (spring stack has infinite travel capacity).

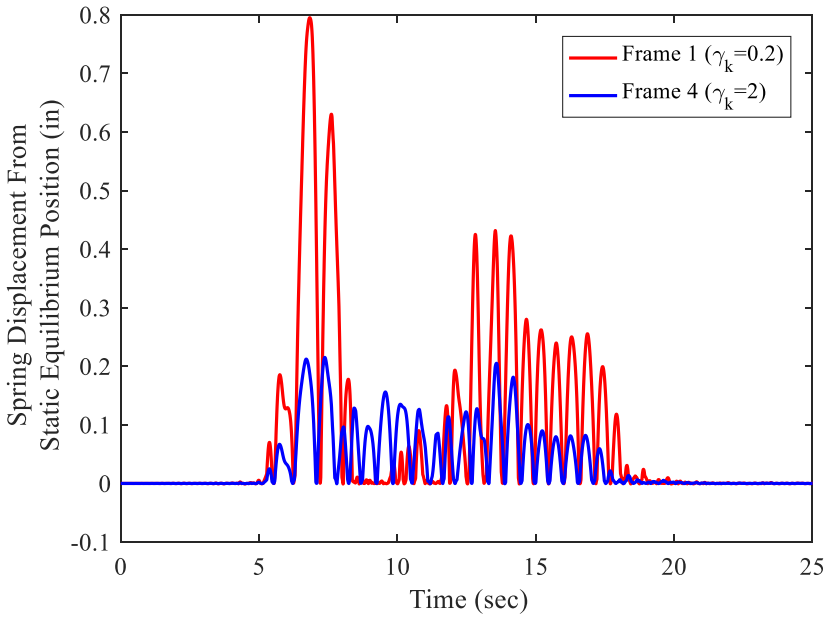

Figure 7.24: Spring stack displacement from the static position of equilibrium of F-1 and F-4 under Hector Mine earthquake scaled to the DBE level (spring stack has infinite travel capacity).

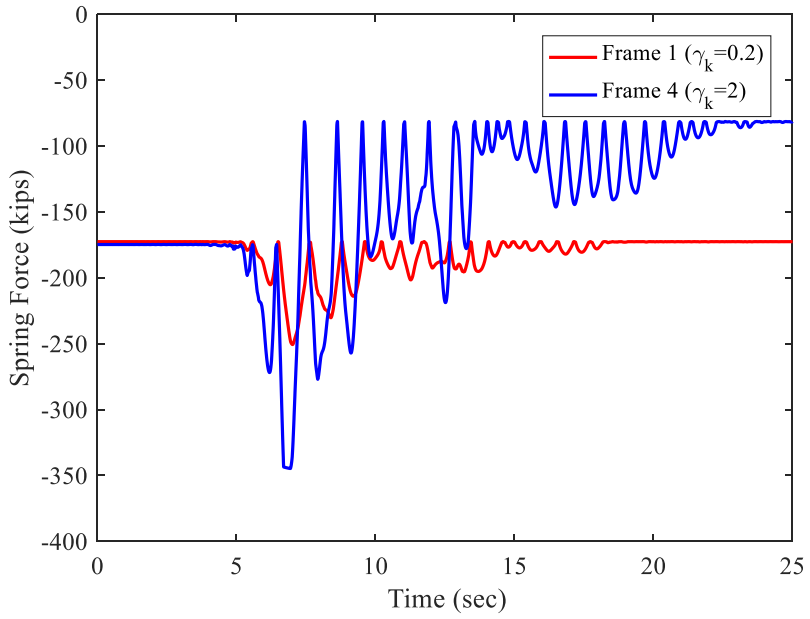

Figure 7.25: Force at spring stack of F-1 and F-4 under Hector Mine earthquake scaled to the MCE level (spring stack has infinite travel capacity).

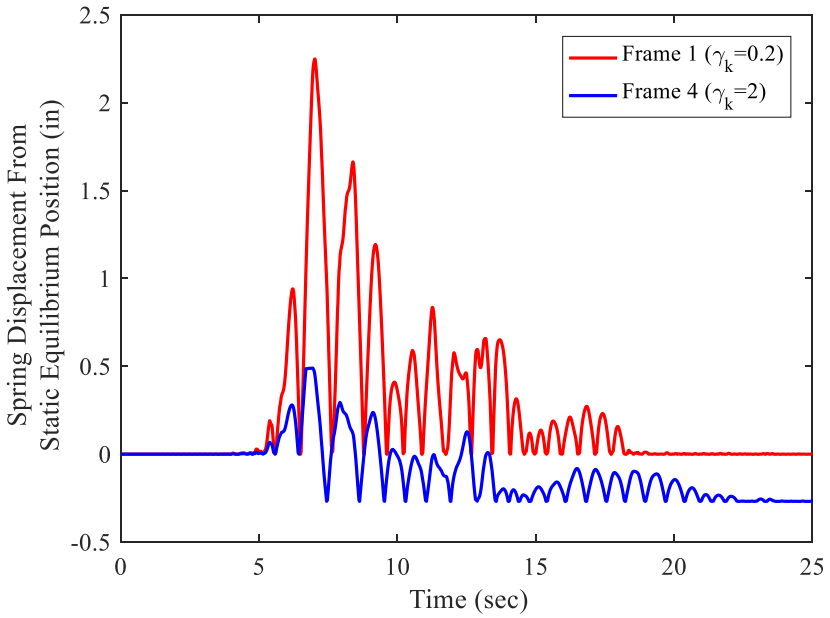

Figure 7.26: Spring stack displacement from the static position of equilibrium of F-1 and F-4 under Hector Mine earthquake scaled to the MCE level (spring stack has infinite travel capacity).

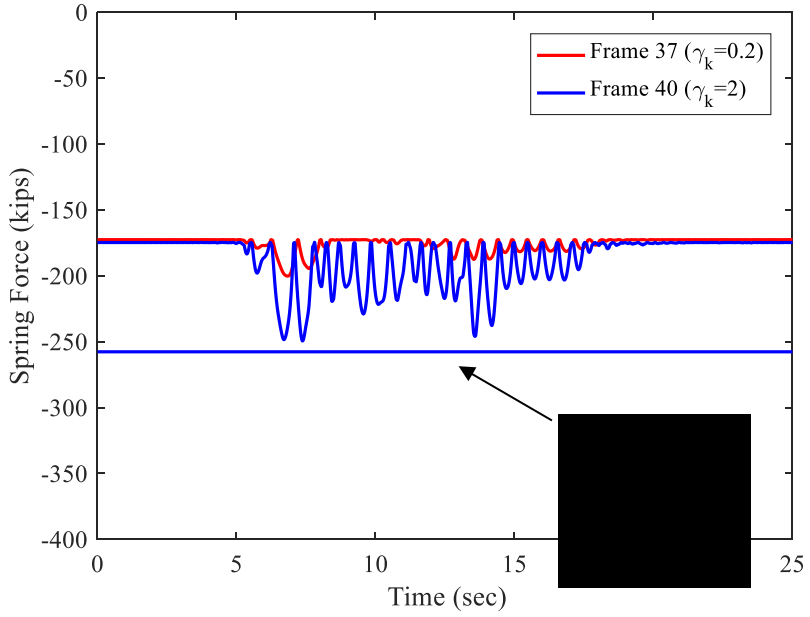

Figure 7.27: Spring stack force of F-37 and F-40 under Hector Mine earthquake scaled to the DBE level (spring stack has finite travel capacity).

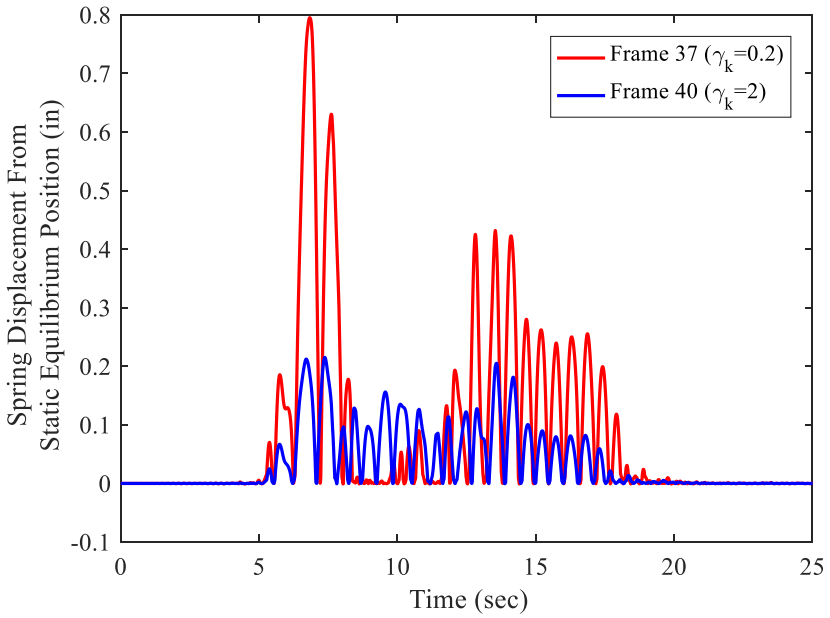

Figure 7.28: Spring stack displacement from the static position of equilibrium of F-37 and F-40 under Hector Mine earthquake scaled to the DBE level (spring stack has finite travel capacity).

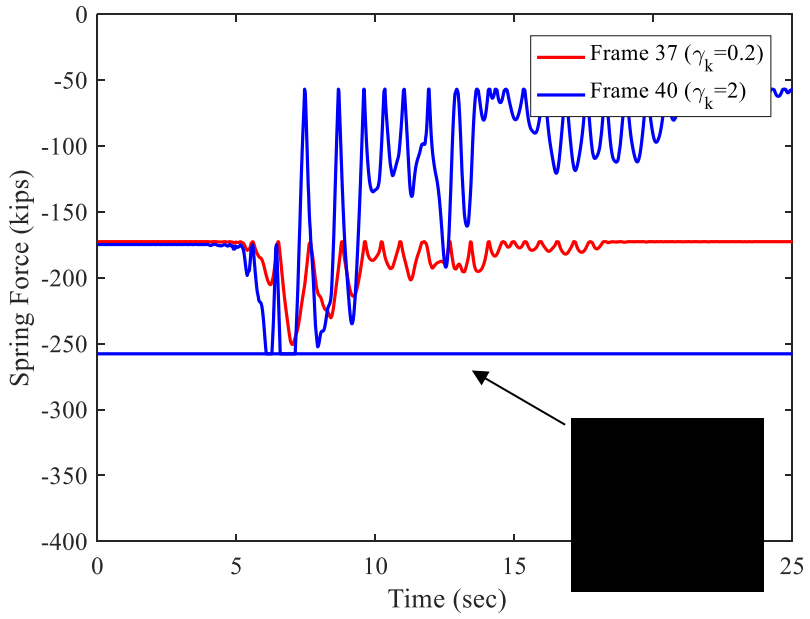

Figure 7.29: Spring stack force of F-37 and F-40 under Hector Mine earthquake scaled to the MCE level (spring stack has finite travel capacity).

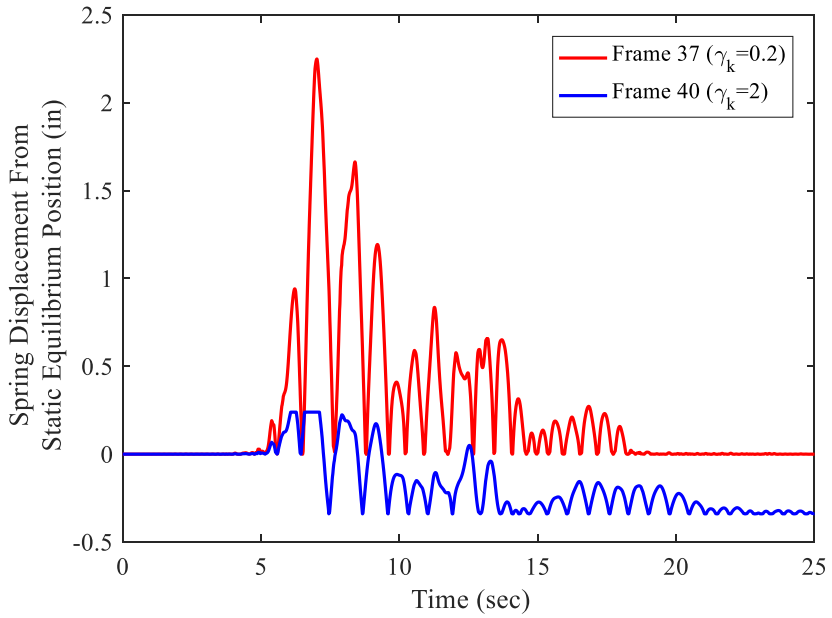

Figure 7.30: Spring stack displacement from the static position of equilibrium of F-37 and F-40 under Hector Mine earthquake scaled to the MCE level (spring stack has finite travel capacity).

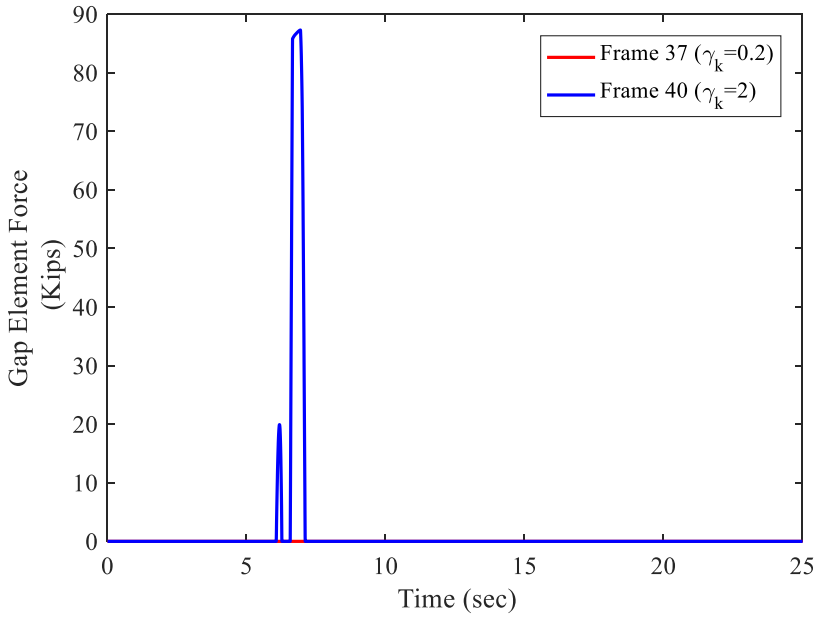

Figure 7.31: Gap element force of F-37 and F-40 under Hector Mine earthquake scaled to the MCE level (spring stack has finite travel capacity).

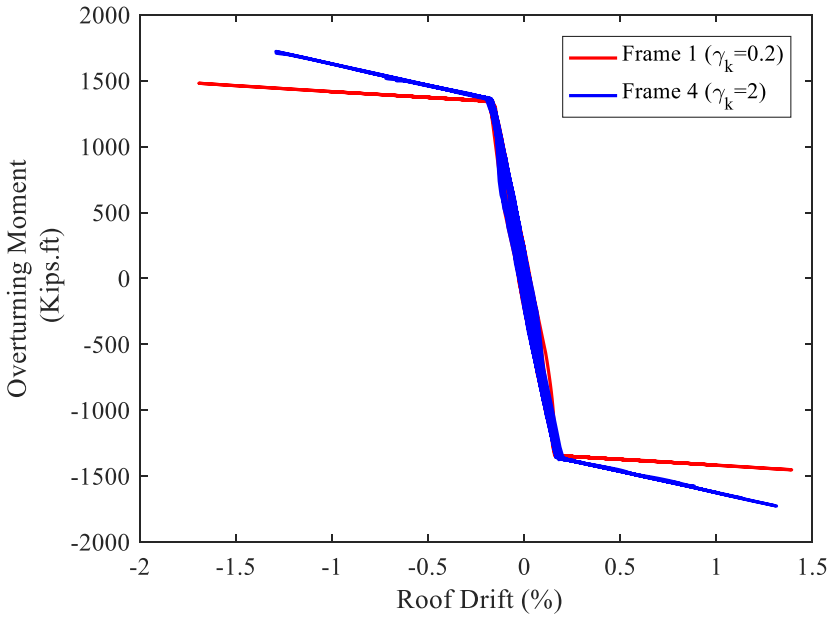

Figure 7.32: Overturning moment vs. roof drift of F-1 and F-4 under Hector Mine earthquake scaled to the DBE level (spring stack has infinite travel capacity).

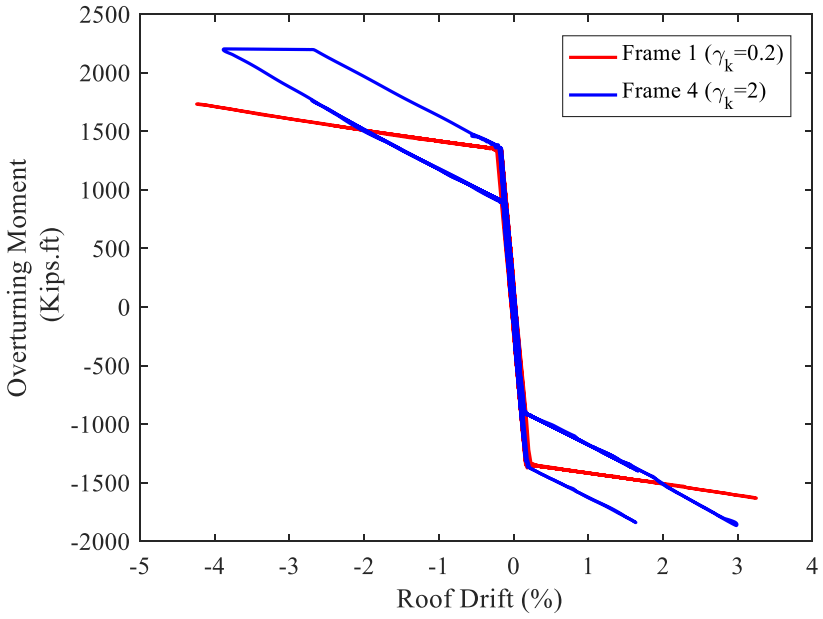

Figure 7.33: Overturning moment vs. roof drift of F-1 and F-4 under Hector Mine earthquake scaled to the MCE level (spring stack has infinite travel capacity).

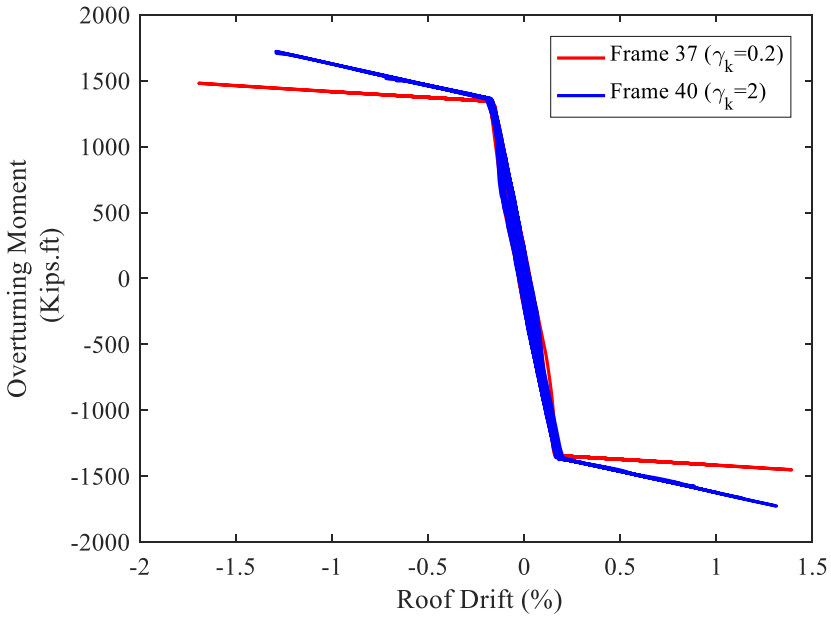

Figure 7.34: Overturning moment vs. roof drift of F-37 and F-40 under Hector Mine earthquake scaled to the DBE level (spring stack has finite travel capacity).

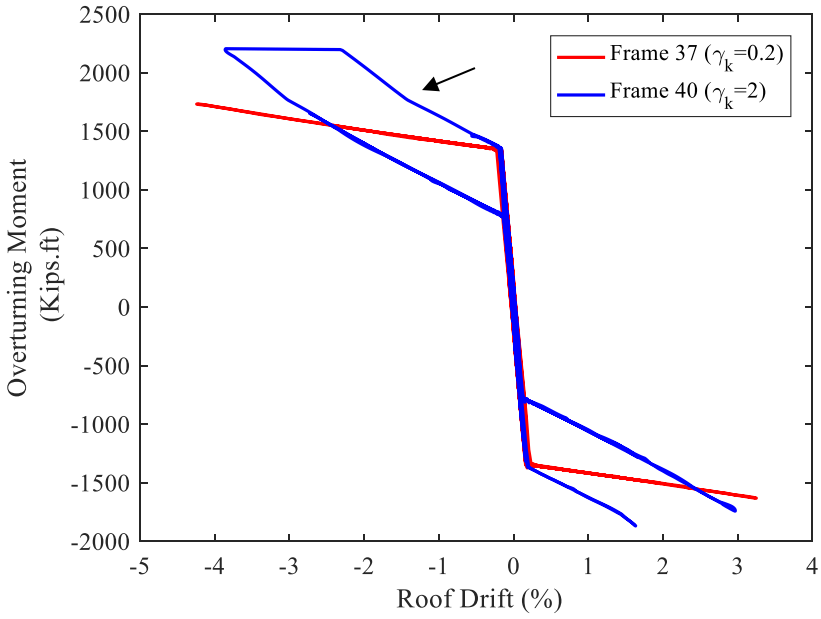

Figure 7.35: Overturning moment vs. roof drift of F-37 and F-40 under Hector Mine earthquake scaled to the MCE level (spring stack has finite travel capacity).

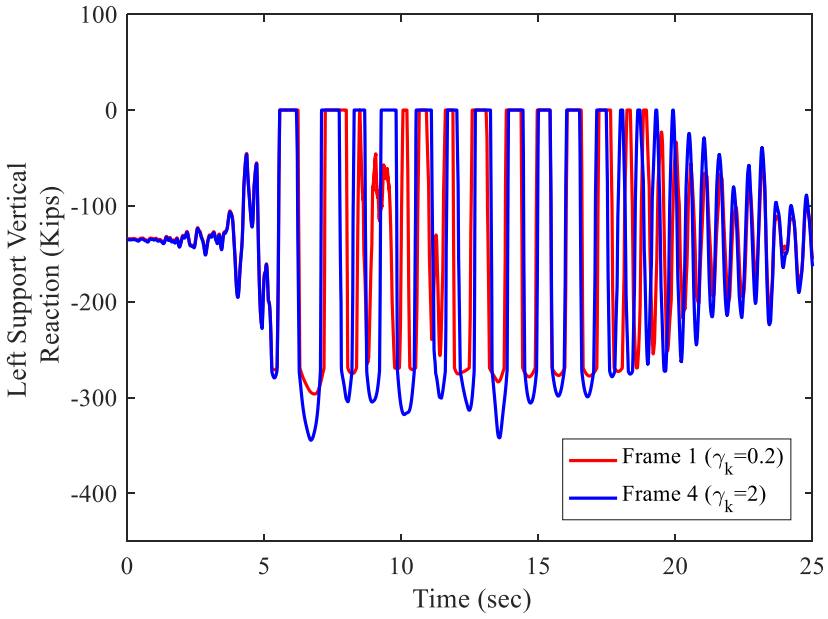

Figure 7.36: Left support vertical reaction of F-1 and F-4 under Hector Mine earthquake scaled to the DBE level (spring stack has infinite travel capacity).

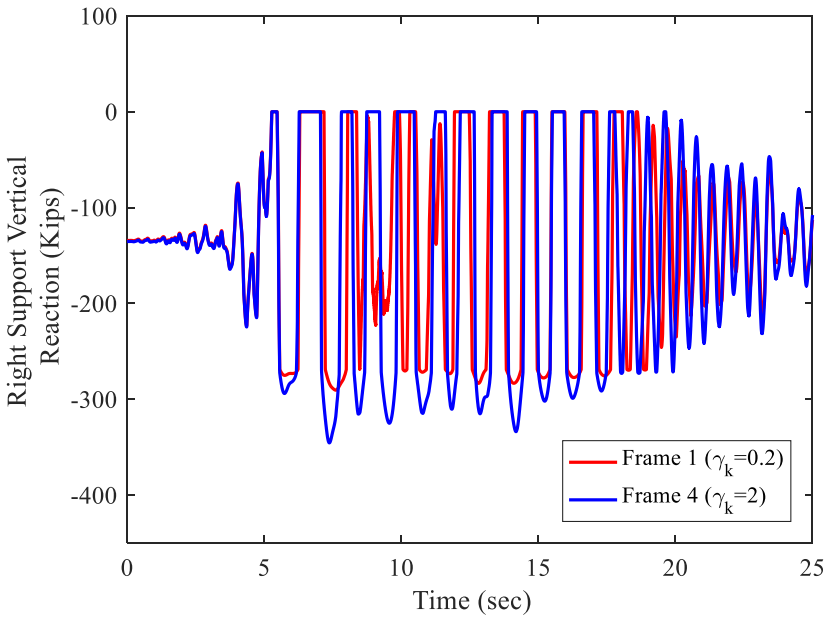

Figure 7.37: Right support vertical reaction of F-1 and F-4 under Hector Mine earthquake scaled to the DBE level (spring stack has infinite travel capacity).

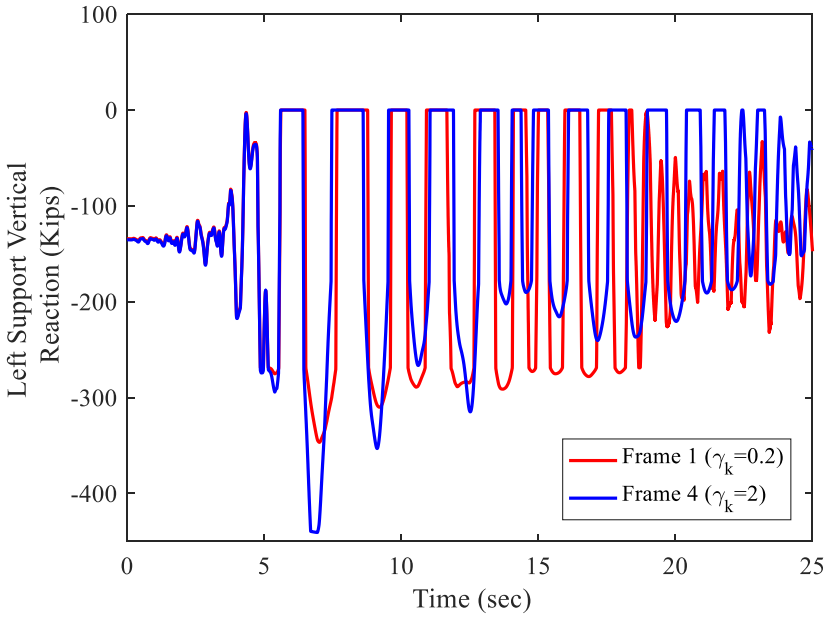

Figure 7.38: Left support vertical reaction of F-1 and F-4 under Hector Mine earthquake scaled to the MCE level (spring stack has infinite travel capacity).

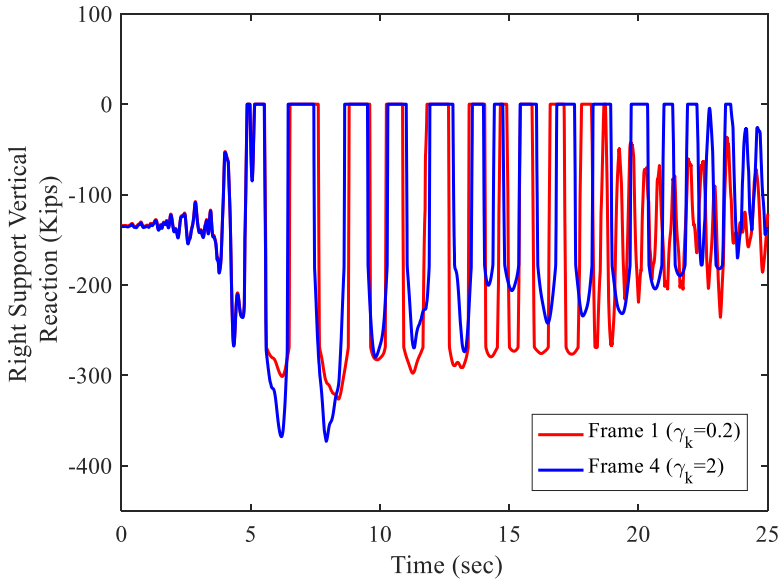

Figure 7.39: Right support vertical reaction of F-1 and F-4 under Hector Mine earthquake scaled to the MCE level (spring stack has infinite travel capacity).

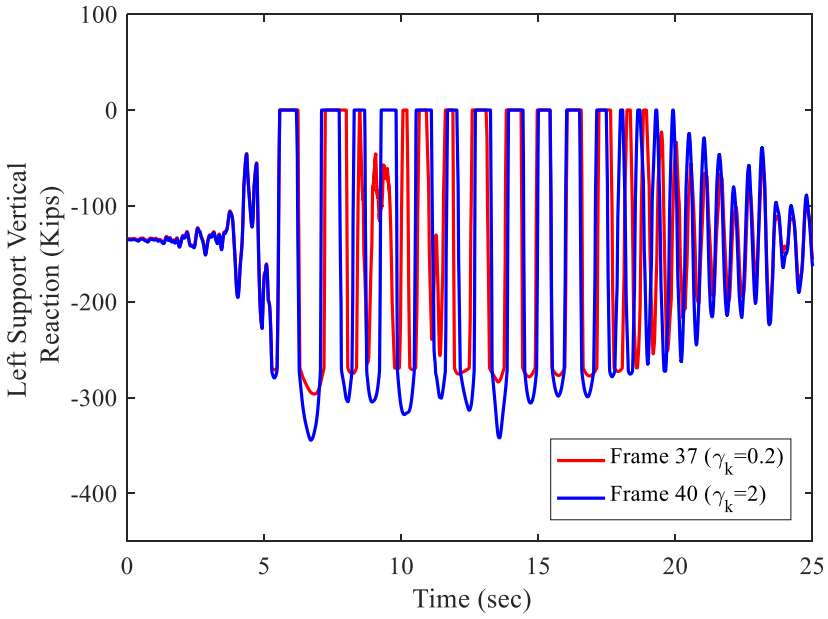

Figure 7.40: Left support vertical reaction of F-37 and F-40 under Hector Mine earthquake scaled to the DBE level (spring stack has finite travel capacity).

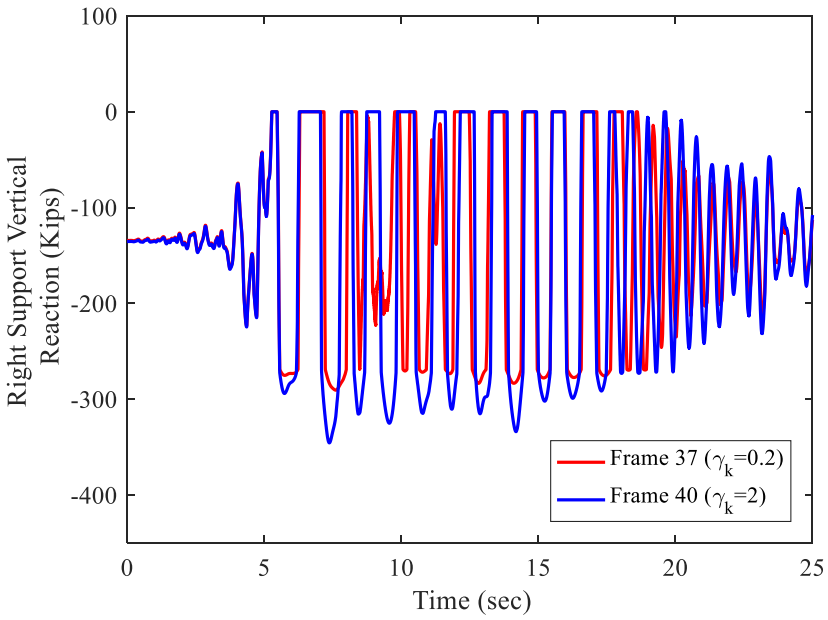

Figure 7.41: Right support vertical reaction of F-37 and F-40 under Hector Mine earthquake scaled to the DBE level (spring stack has finite travel capacity).

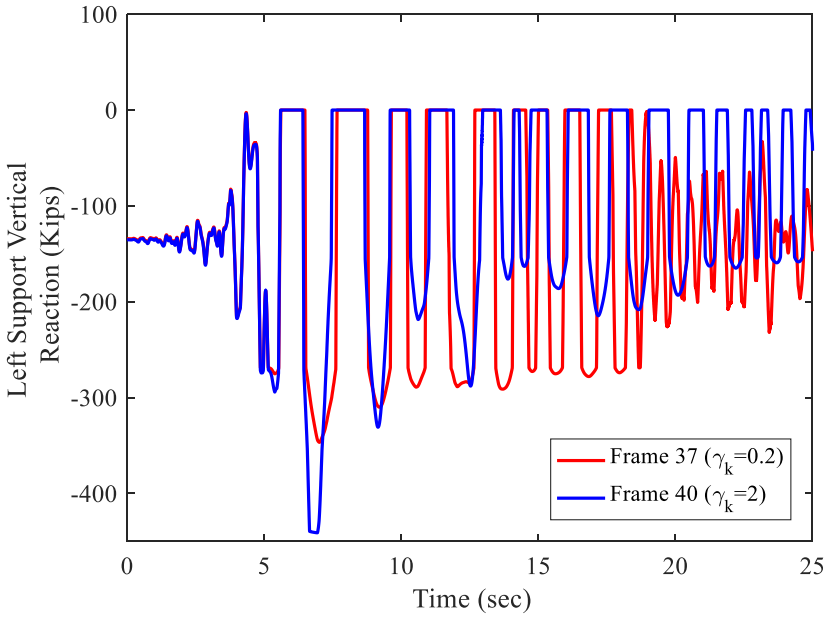

Figure 7.42: Left support vertical reaction of F-37 and F-40 under Hector Mine earthquake scaled to the MCE level (spring stack has finite travel capacity).

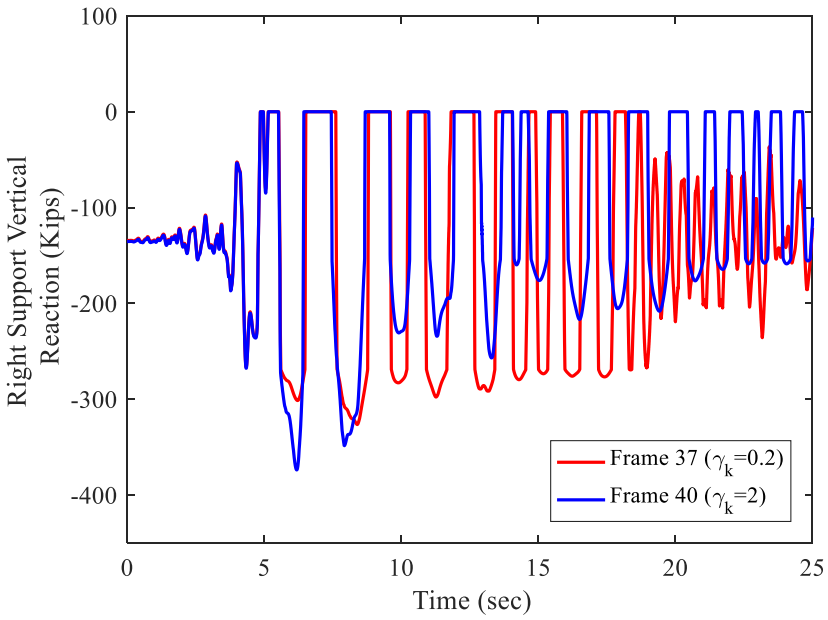

Figure 7.43: Right support vertical reaction of F-37 and F-40 under Hector Mine earthquake scaled to the MCE level (spring stack has finite travel capacity).

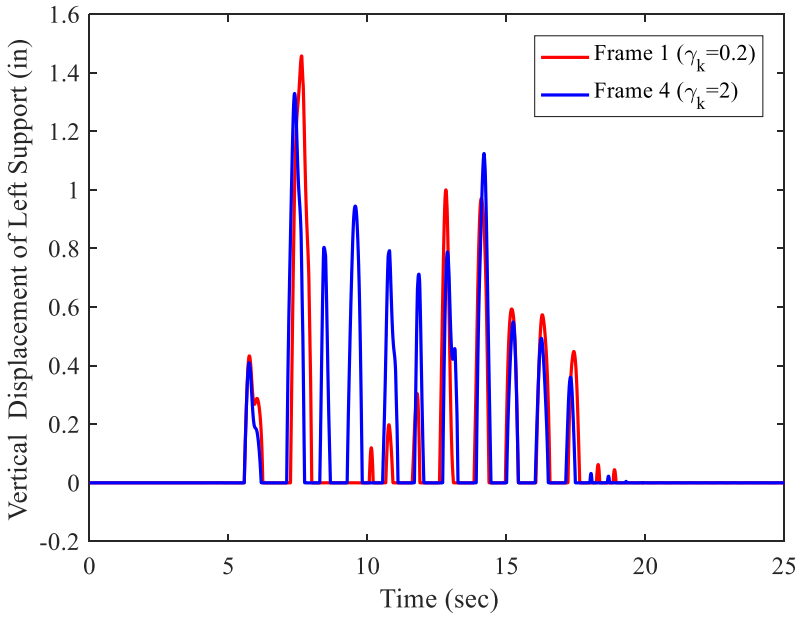

Figure 7.44: Left support vertical displacement of F-1 and F-4 under Hector Mine earthquake scaled to the DBE level (spring stack has infinite travel capacity).

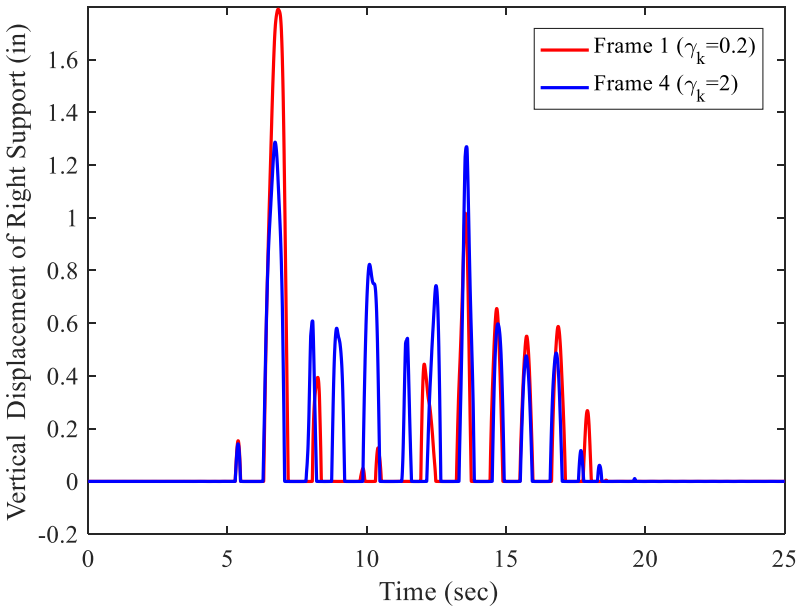

Figure 7.45: Right support vertical displacement of F-1 and F-4 under Hector Mine earthquake scaled to the DBE level (spring stack has infinite travel capacity).

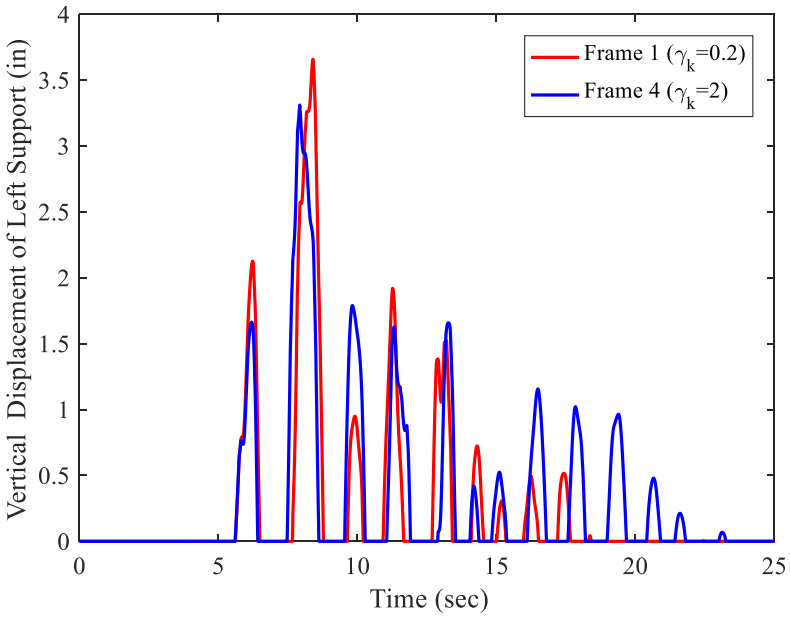

Figure 7.46: Vertical displacement of the left support of F-1 and F-4 under Hector Mine earthquake scaled to the MCE level (spring stack has infinite travel capacity).

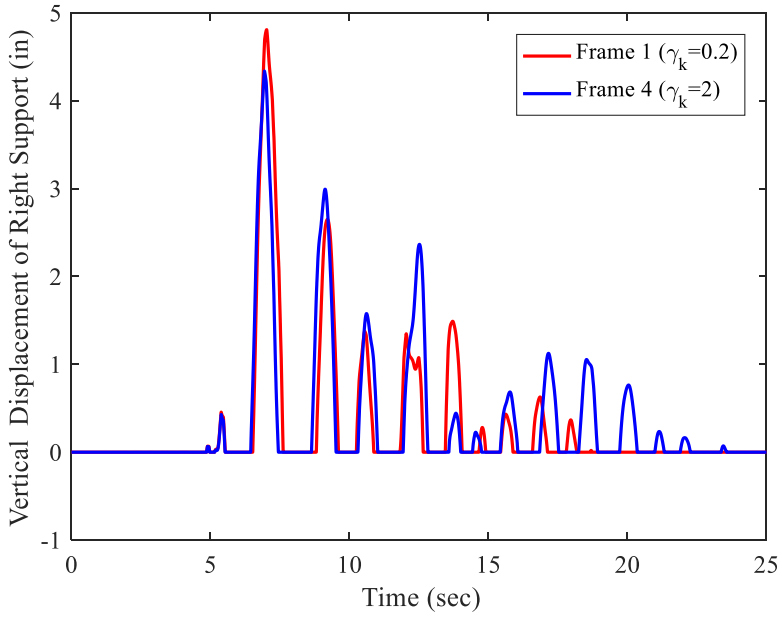

Figure 7.47: Vertical displacement of right support of F-1 and F-4 under Hector Mine earthquake scaled to the MCE level (spring stack has infinite travel capacity).

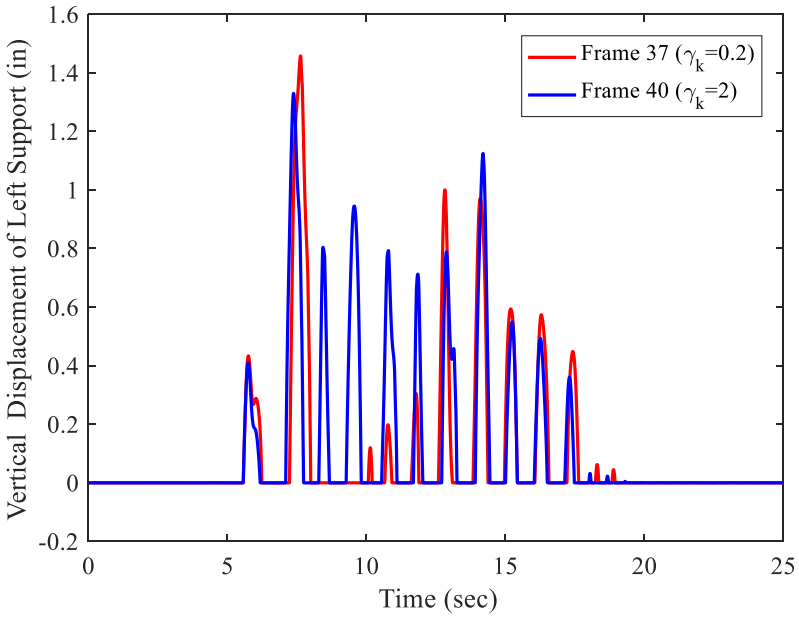

Figure 7.48: Vertical displacement of the left support of F-37 and F-40 under Hector Mine earthquake scaled to the DBE level (spring stack has finite travel capacity).

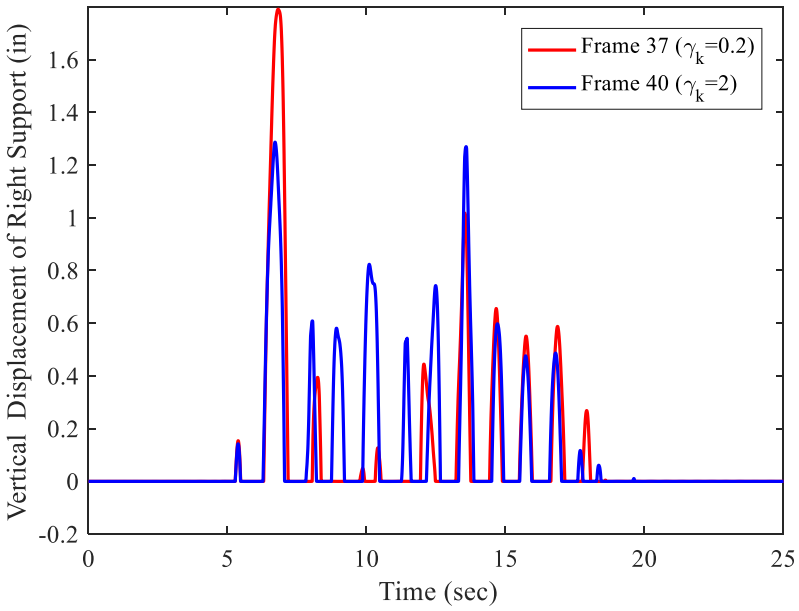

Figure 7.49: Vertical displacement of the right support of F-37 and F-40 under Hector Mine earthquake scaled to the DBE level (spring stack has finite travel capacity).

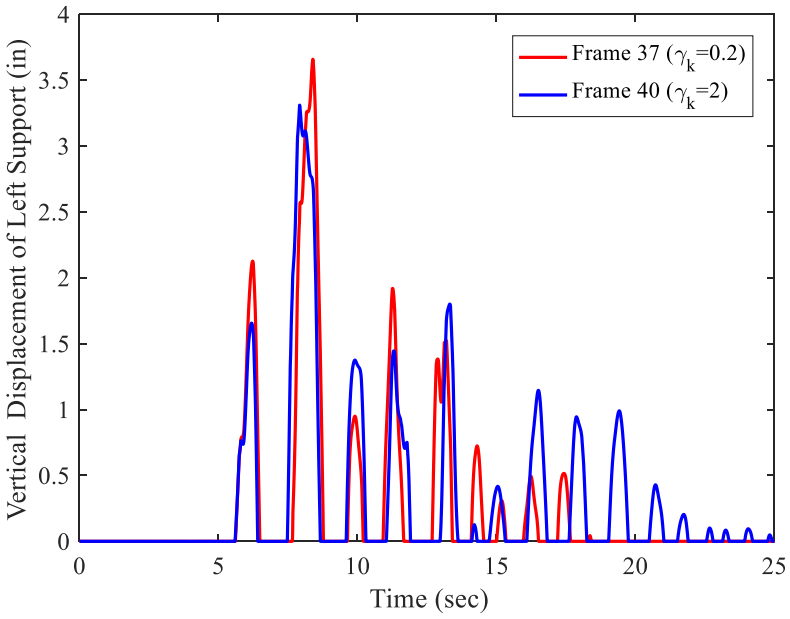

Figure 7.50: Vertical displacement of the left support of F-37 and F-40 under Hector Mine earthquake scaled to the MCE level (spring stack has finite travel capacity).

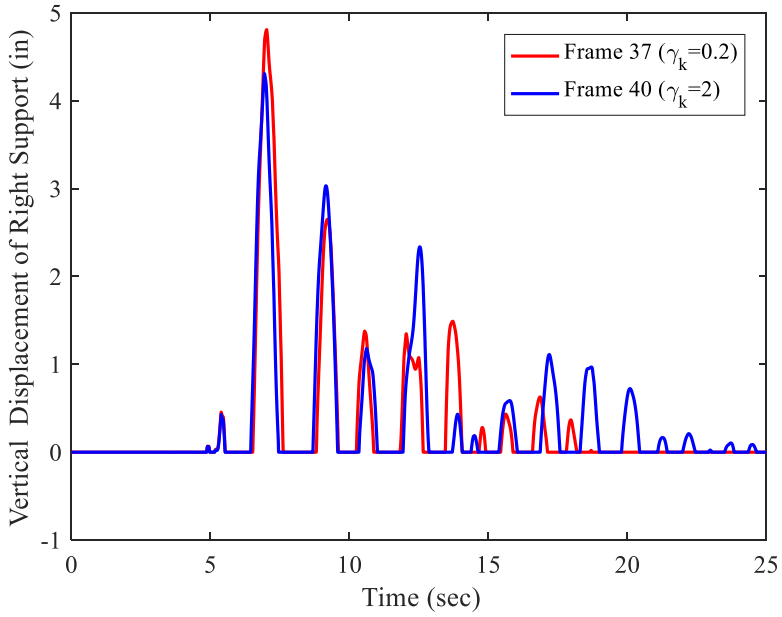

Figure 7.51: Vertical displacement of the right support of F-37 and F-40 under Hector Mine earthquake scaled to the MCE level (spring stack has finite travel capacity).

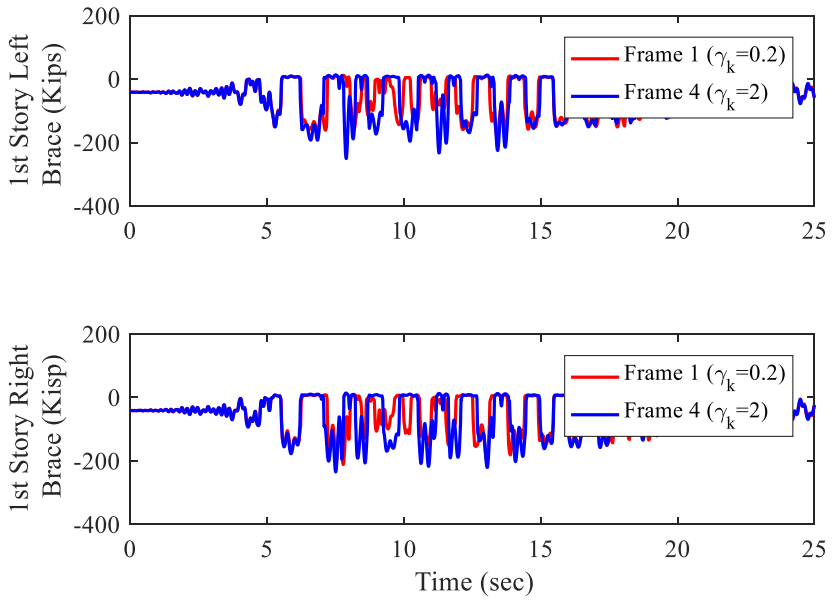

Figure 7.52: 1st story brace forces of F-1 and F-4 under Hector Mine earthquake scaled to the DBE level (spring stack has infinite travel capacity).

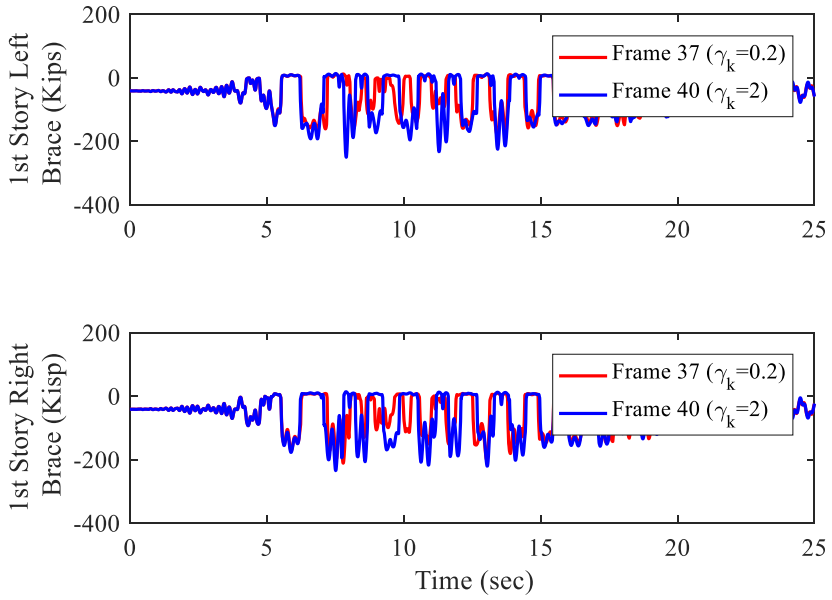

Figure 7.53: 1st story brace forces of F-37 and F-40 under Hector Mine earthquake scaled to the DBE level (spring stack has finite travel capacity).

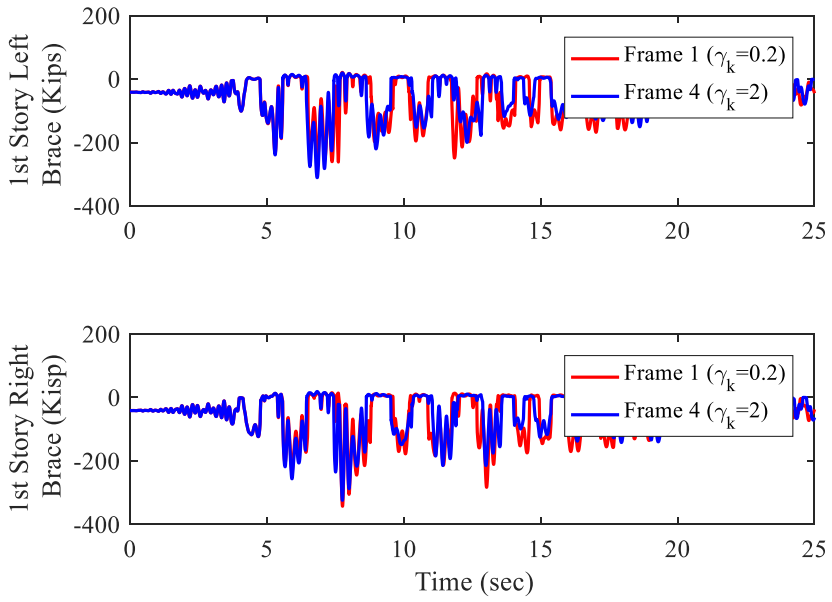

Figure 7.54: 1st story brace forces of F-1 and F-4 under Hector Mine earthquake scaled to the MCE level (spring stack has infinite travel capacity).

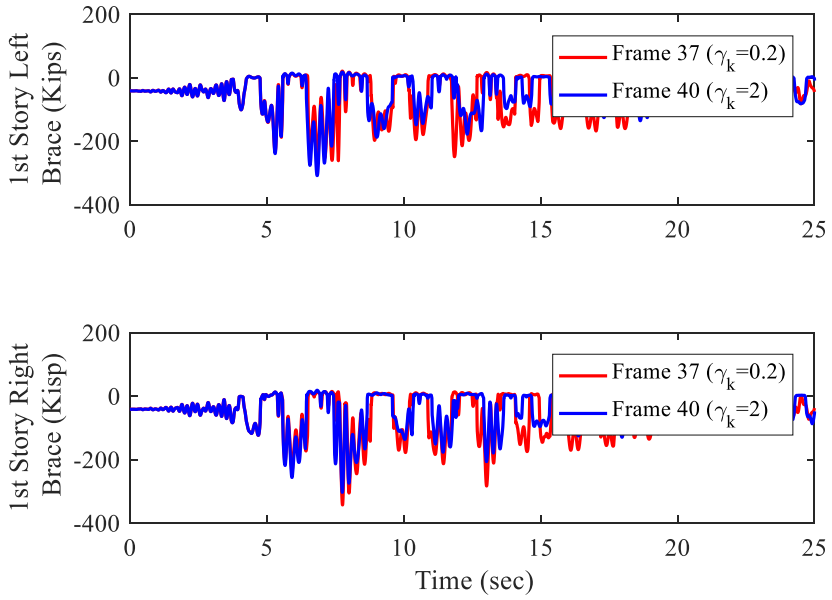

Figure 7.55: 1st story brace forces of F-37 and F-40 under Hector Mine earthquake scaled to the MCE level (spring stack has finite travel capacity).

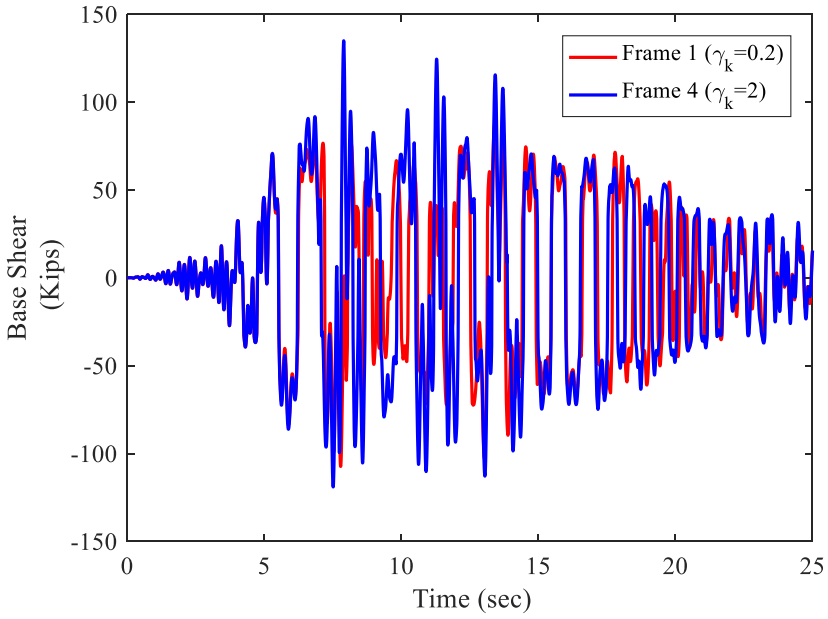

Figure 7.56: Base shear of F-1 and F-4 under Hector Mine earthquake scaled to the DBE level (spring stack has infinite travel capacity).

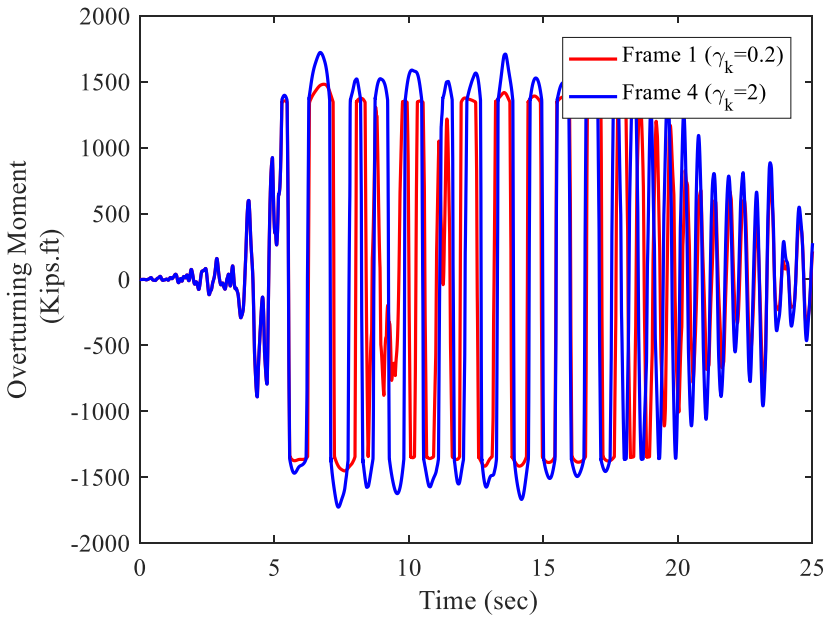

Figure 7.57: Overturning moment of F-1 and F-4 under Hector Mine earthquake scaled to the DBE level (spring stack has infinite travel capacity).

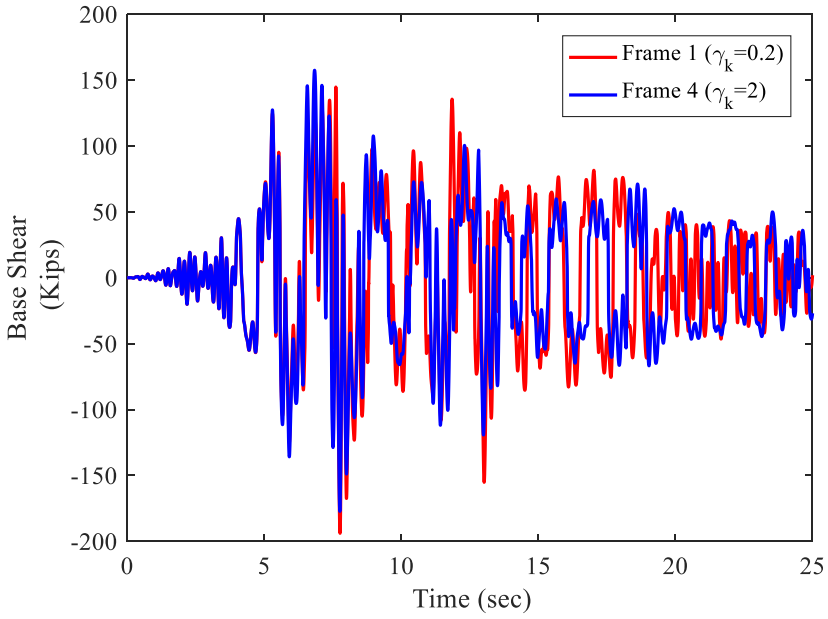

Figure 7.58: Base shear of F-1 and F-4 under Hector Mine earthquake scaled to the MCE level (spring stack has infinite travel capacity).

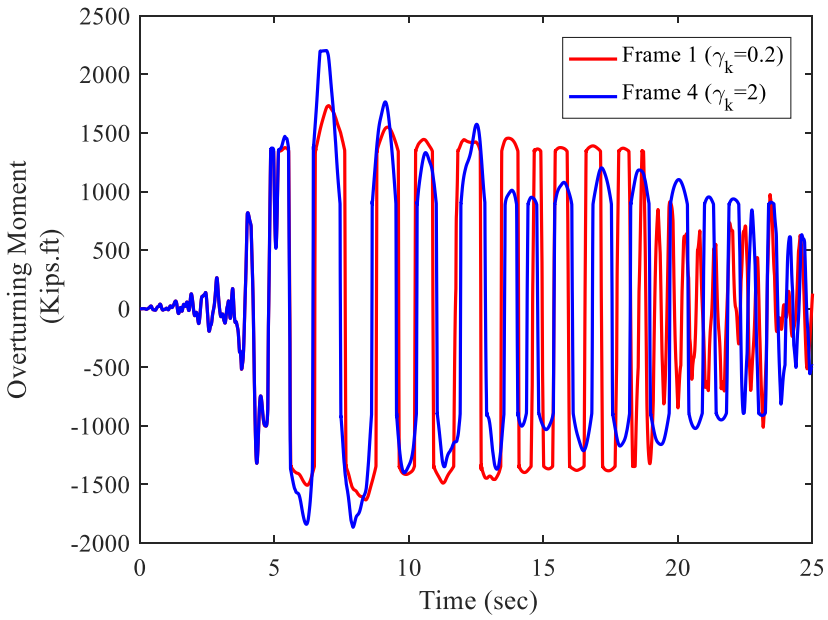

Figure 7.59: Overturning moment of F-1 and F-4 under Hector Mine earthquake scaled to the MCE level (spring stack has infinite travel capacity).

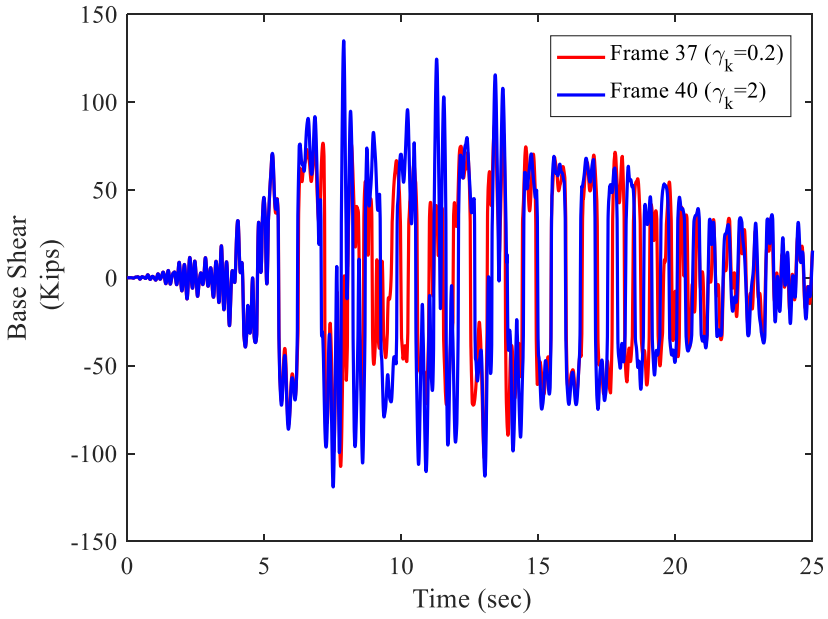

Figure 7.60: Base shear of F-37 and F-40 under Hector Mine earthquake scaled to the DBE level (spring stack has finite travel capacity).

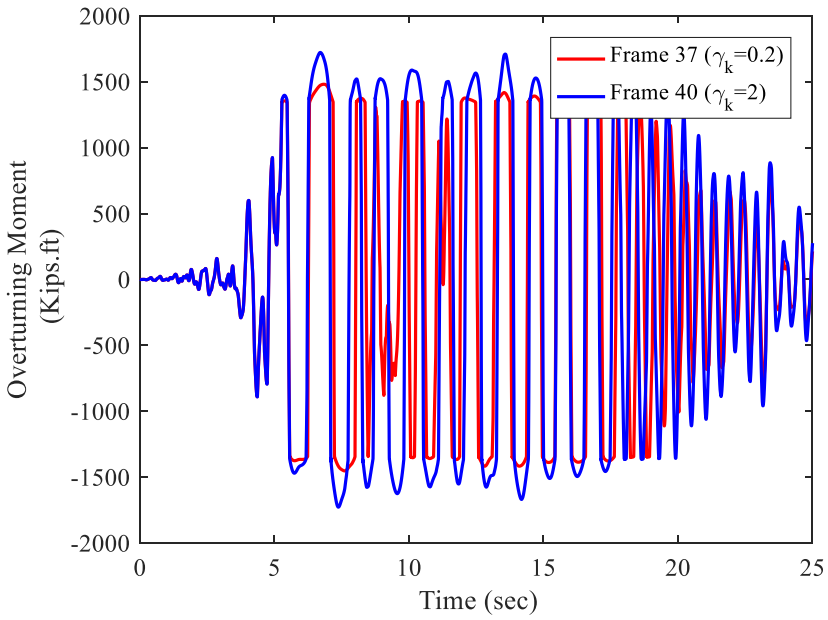

Figure 7.61: Overturning moment of F-37 and F-40 under Hector Mine earthquake scaled to the DBE level (spring stack has finite travel capacity).

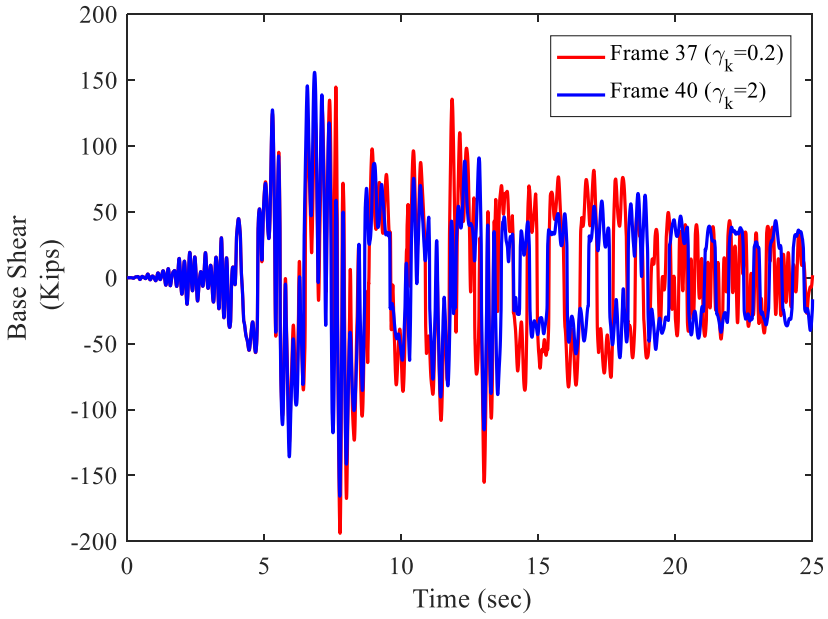

Figure 7.62: Base shear of F-37 and F-40 under Hector Mine earthquake scaled to the MCE level (spring stack has finite travel capacity).

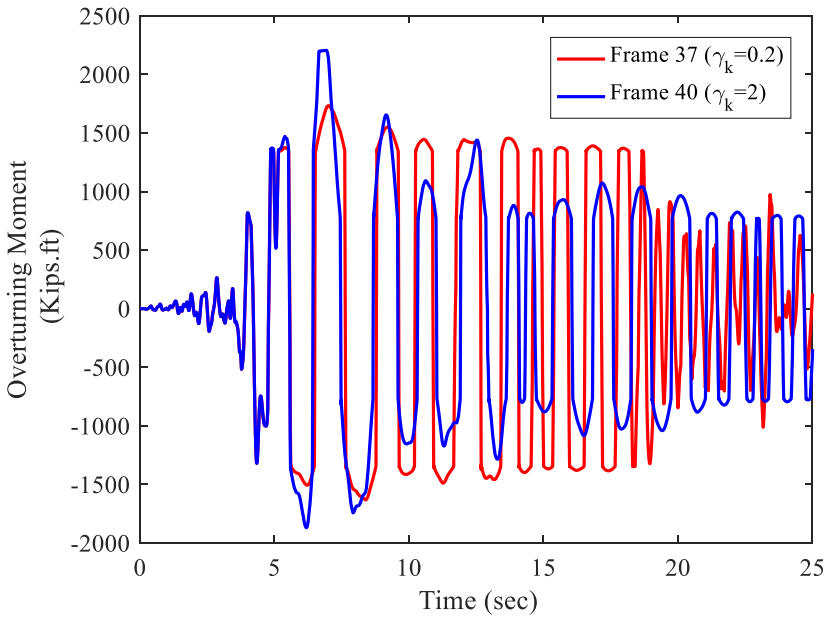

Figure 7.63: Overturning moment of F-37 and F-40 under Hector Mine earthquake scaled to the MCE level (spring stack has finite travel capacity).

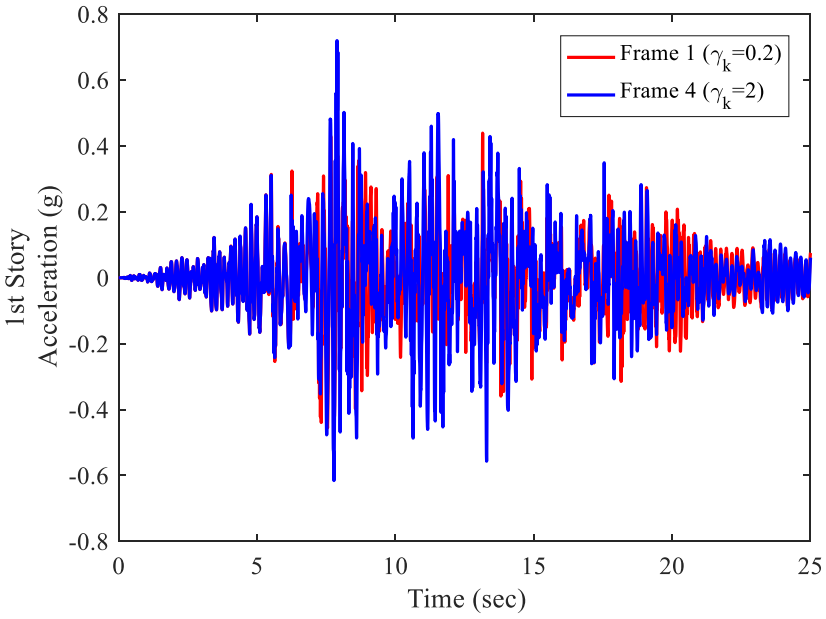

Figure 7.64: 1st story acceleration of F-1 and F-4 under Hector Mine earthquake scaled to the DBE level (spring stack has infinite travel capacity).

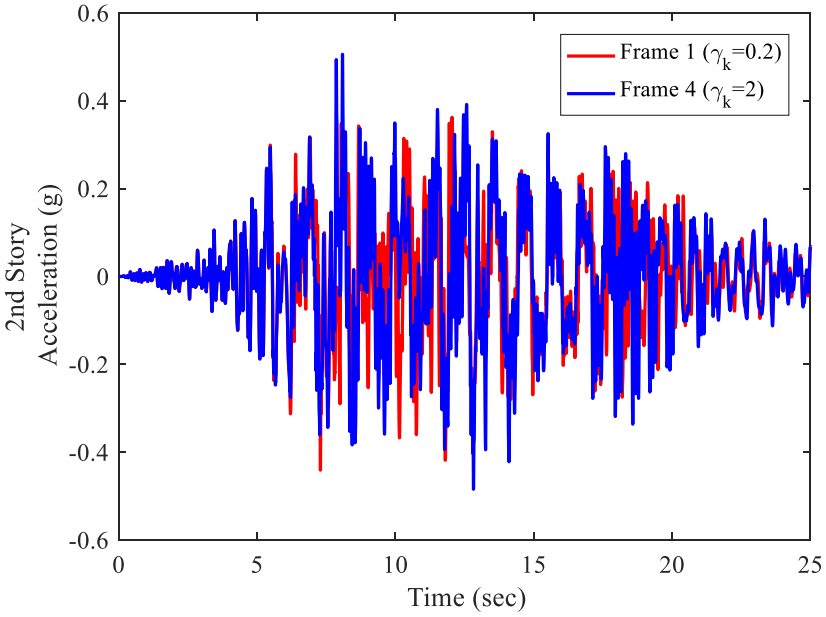

Figure 7.65: 2nd story acceleration of F-1 and F-4 under Hector Mine earthquake scaled to the DBE level (spring stack has infinite travel capacity).

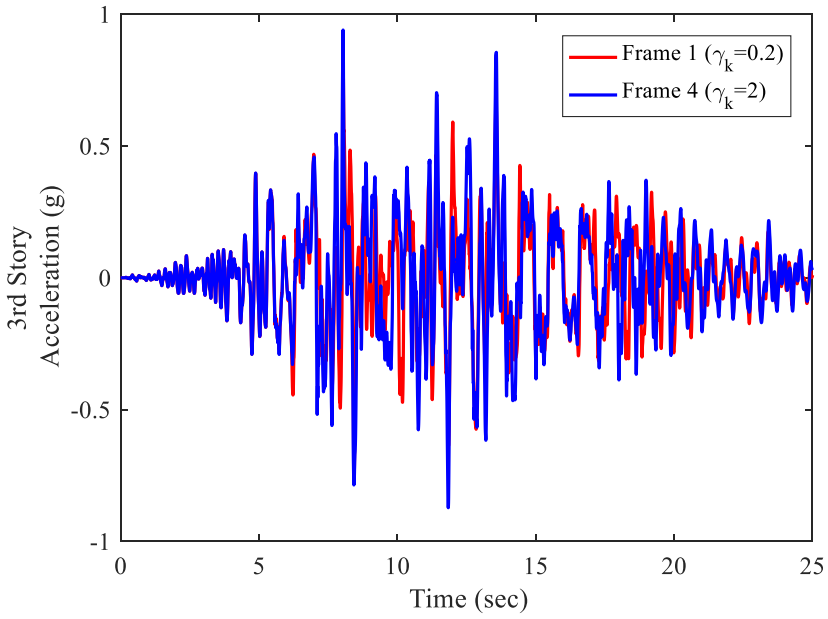

Figure 7.66: 3rd story acceleration of F-1 and F-4 under Hector Mine earthquake scaled to the DBE level (spring stack has infinite travel capacity).

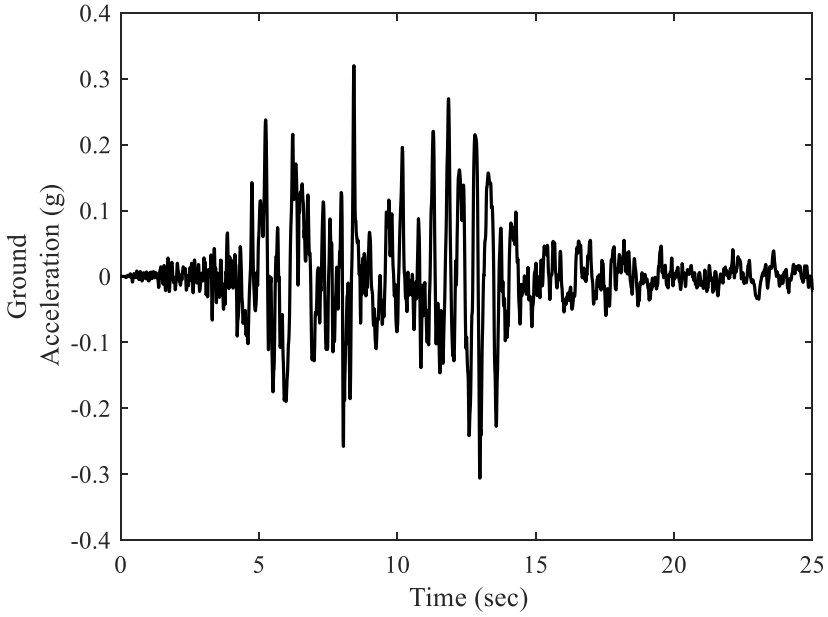

Figure 7.67: Ground acceleration of Hector Mine earthquake scaled to the DBE.

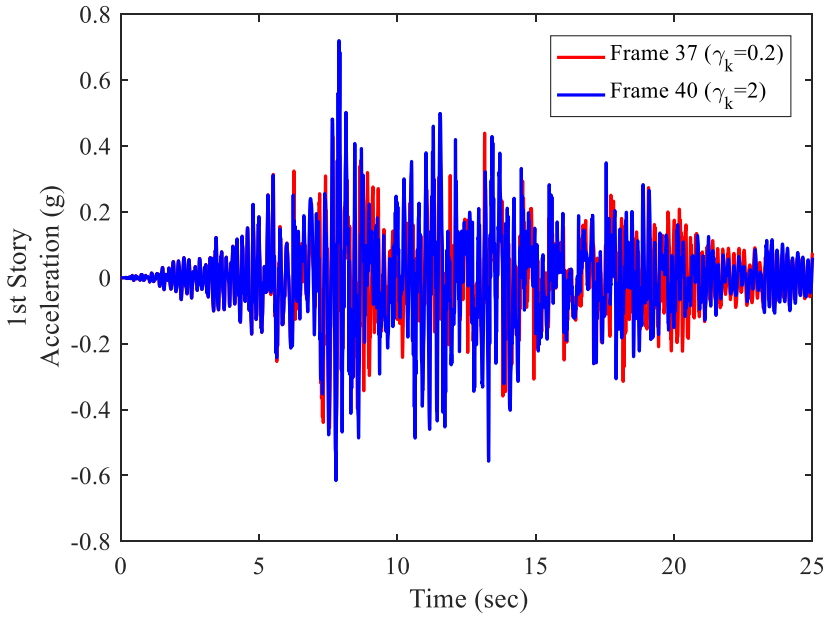

Figure 7.68: 1st story acceleration of F-37 and F-40 under Hector Mine earthquake scaled to the DBE level (spring stack has finite travel capacity).

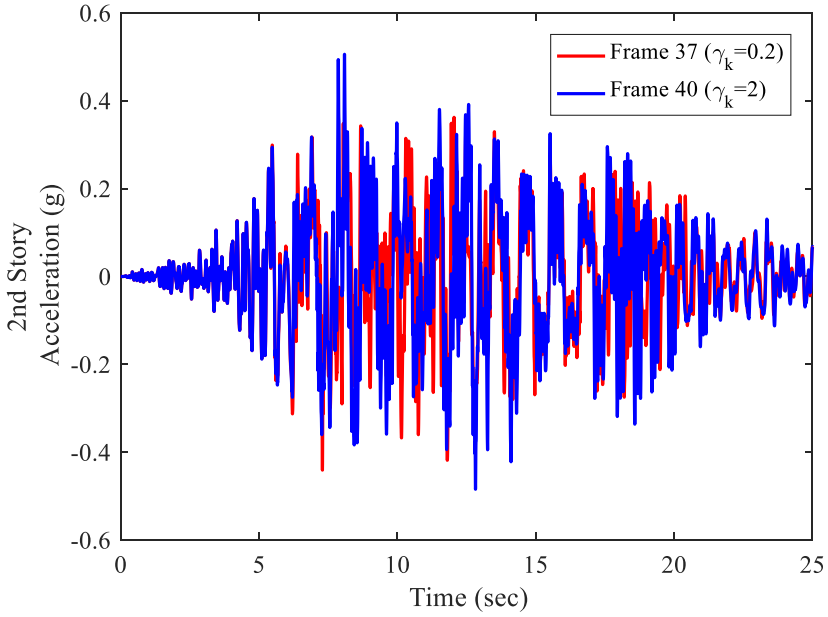

Figure 7.69: 2nd story acceleration of F-37 and F-40 under Hector Mine earthquake scaled to the DBE level (spring stack has finite travel capacity).

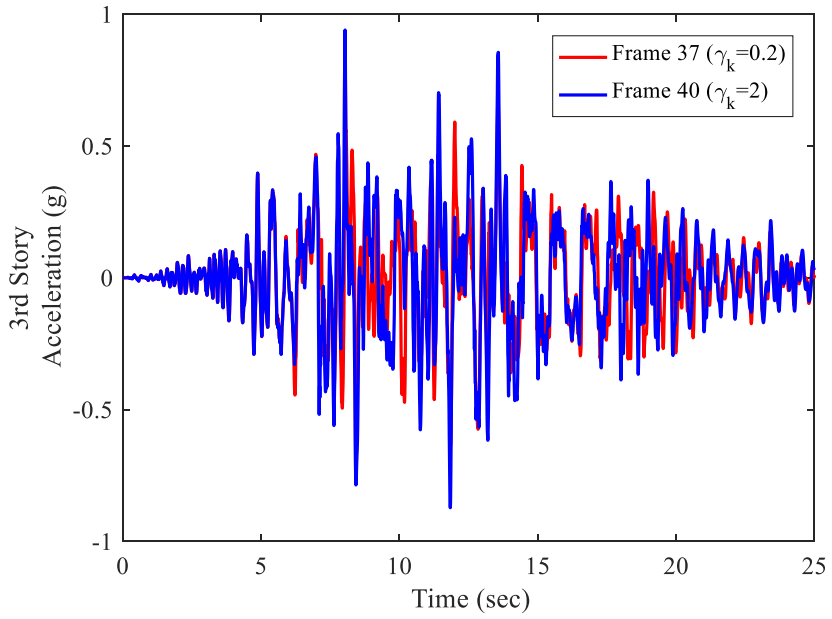

Figure 7.70: 3rd story acceleration of F-37 and F-40 under Hector Mine earthquake scaled to the DBE level (spring stack has finite travel capacity).

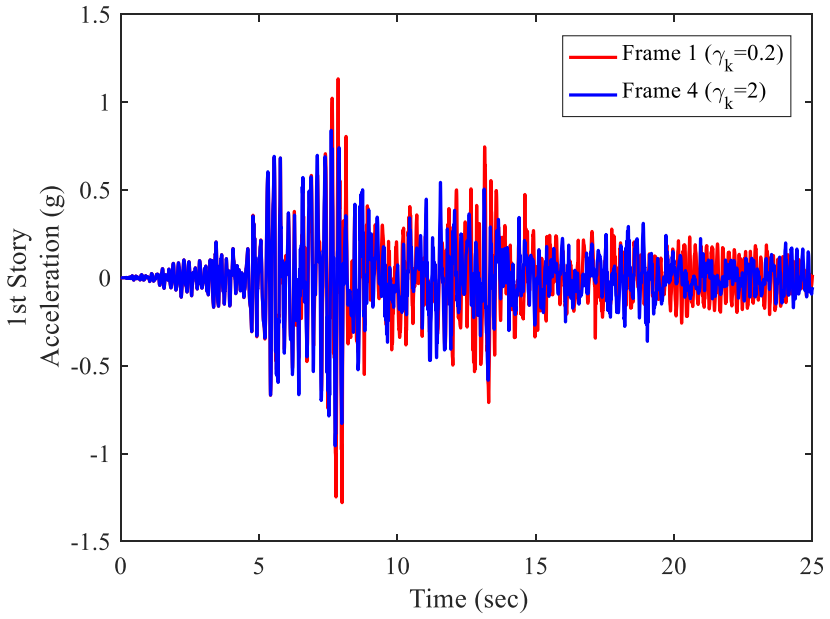

Figure 7.71: 1st story acceleration of F-1 and F-4 under Hector Mine earthquake scaled to the MCE level (spring stack has infinite travel capacity).

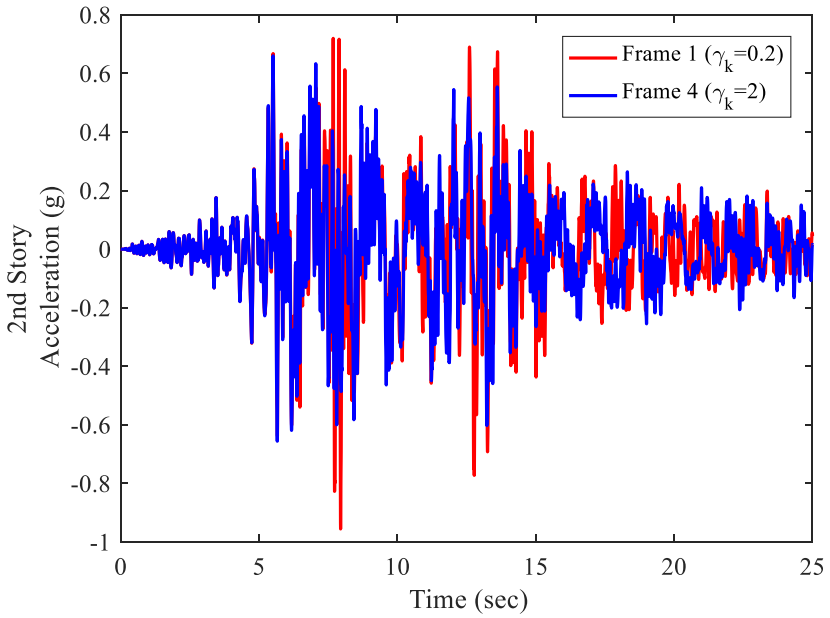

Figure 7.72: 2nd story acceleration of F-1 and F-4 under Hector Mine earthquake scaled to the MCE level (spring stack has infinite travel capacity).

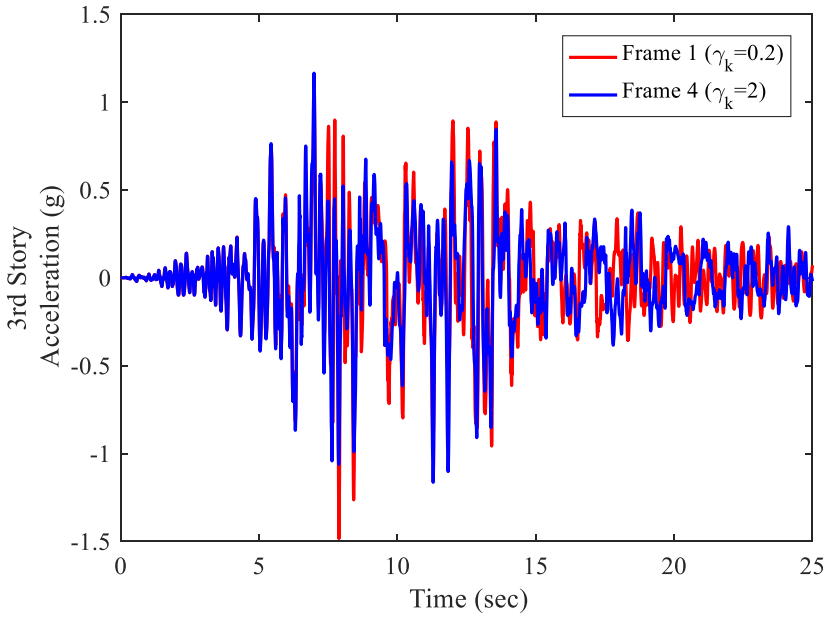

Figure 7.73: 3rd story acceleration of F-1 and F-4 under Hector Mine earthquake scaled to the MCE level (spring stack has infinite travel capacity).

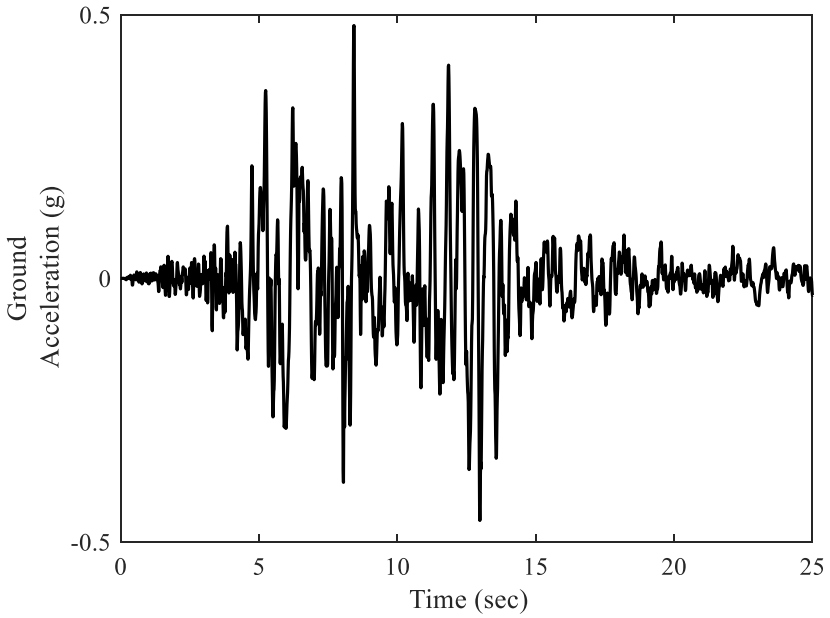

Figure 7.64: Ground acceleration of Hector Mine earthquake scaled to the MCE.

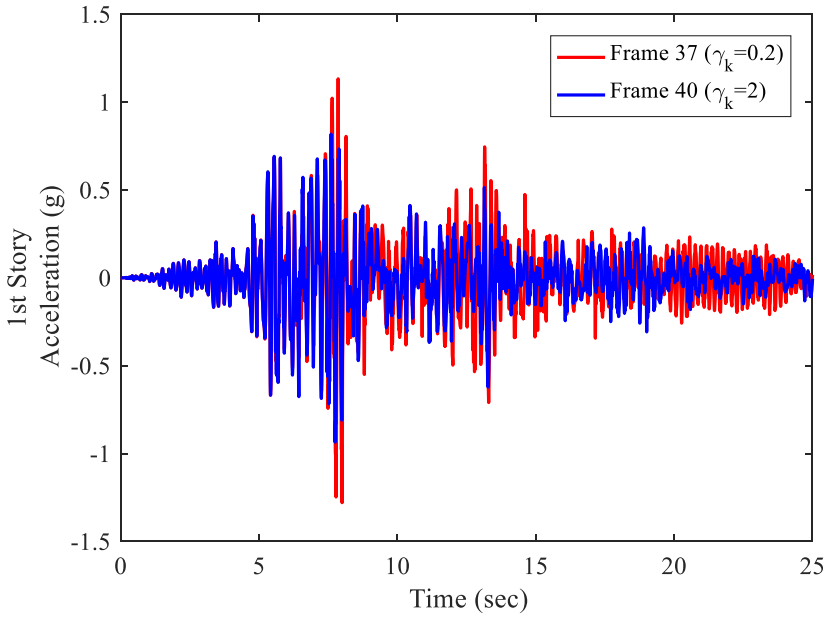

Figure 7.75: 1st story acceleration of F-37 and F-40 under Hector Mine earthquake scaled to the MCE level (spring stack has finite travel capacity).

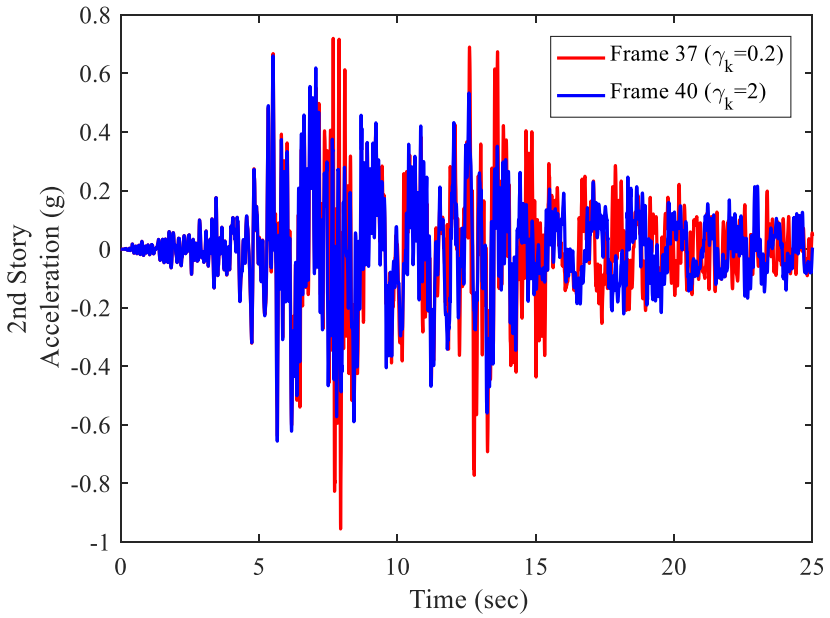

Figure 7.76: 2nd story acceleration of F-37 and F-40 under Hector Mine earthquake scaled to the MCE level (spring stack has finite travel capacity).

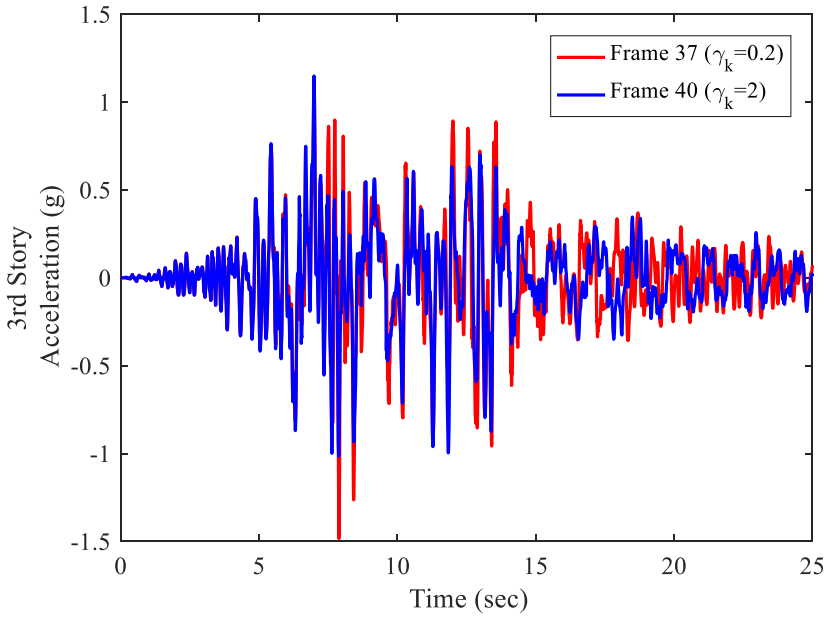

Figure 7.77: 3rd story acceleration of F-37 and F-40 under Hector Mine earthquake scaled to the MCE level (spring stack has finite travel capacity).

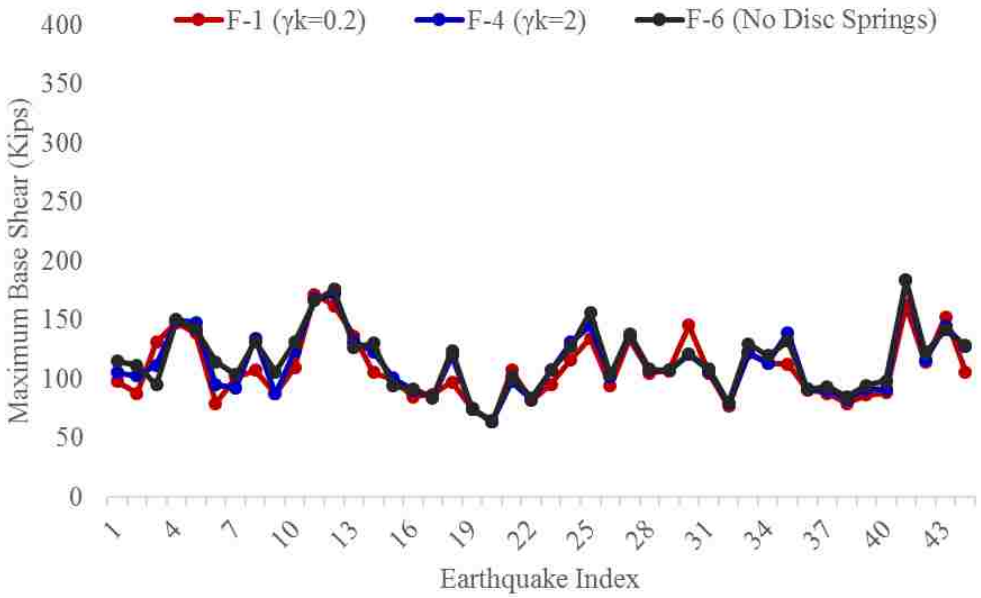

Figure 7.78: Maximum base shear of F-1, F-4, and F-6 under the DBE ground motions (spring stack has infinite travel capacity).

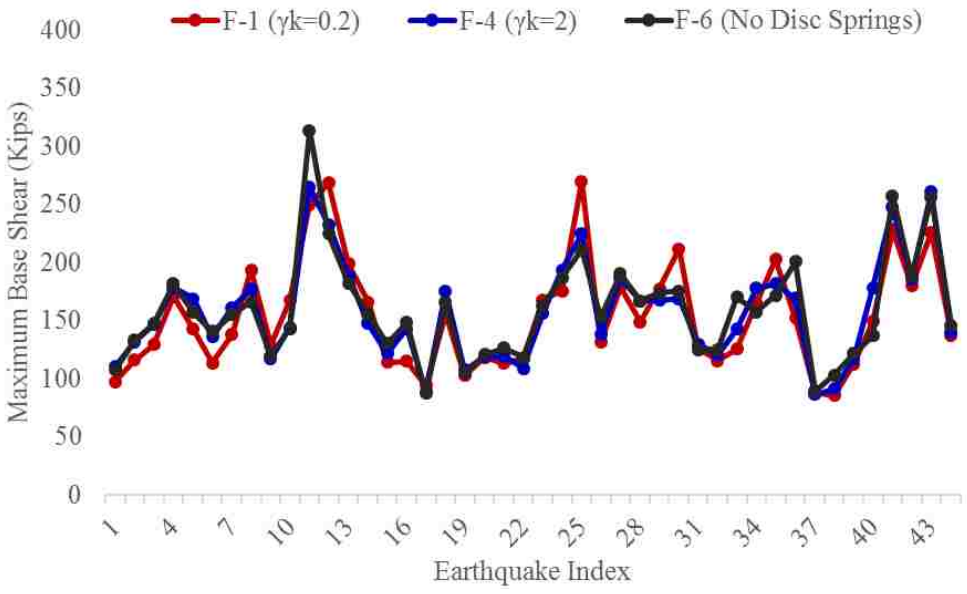

Figure 7.79: Maximum base shear of F-1, F-4, and F-6 under the MCE ground motions (spring stack has infinite travel capacity).

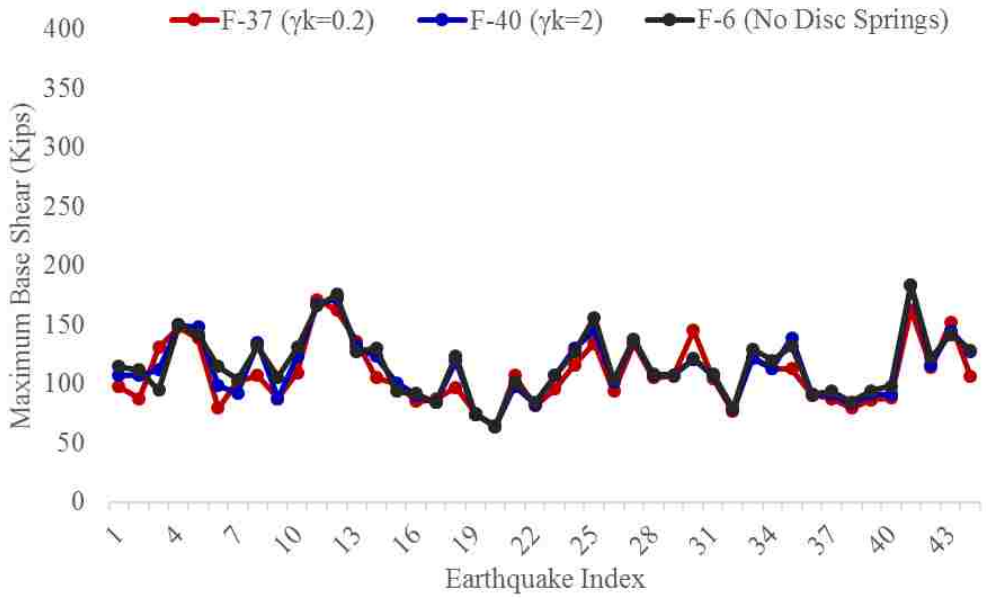

Figure 7.80: Maximum base shear of F-37, F-40, and F-6 under the DBE ground motions (spring stack has finite travel capacity).

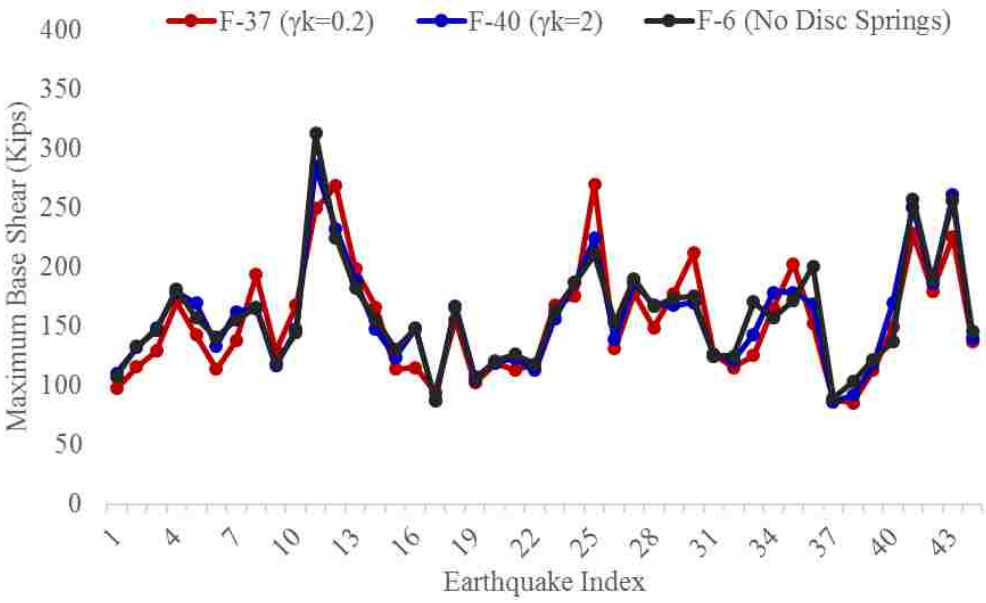

Figure 7.81: Maximum base shear of F-37, F-40, and F-6 under the MCE ground motions (spring stack has finite travel capacity).

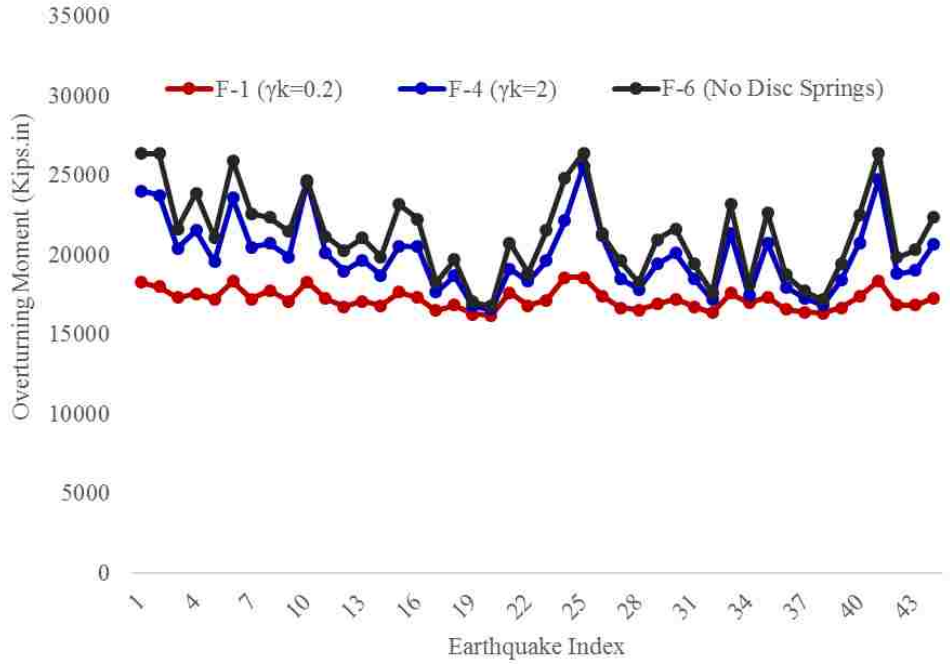

Figure 7.82: Maximum overturning moment of F-1, F-4, and F-6 under the DBE ground motions (spring stack has infinite travel capacity).

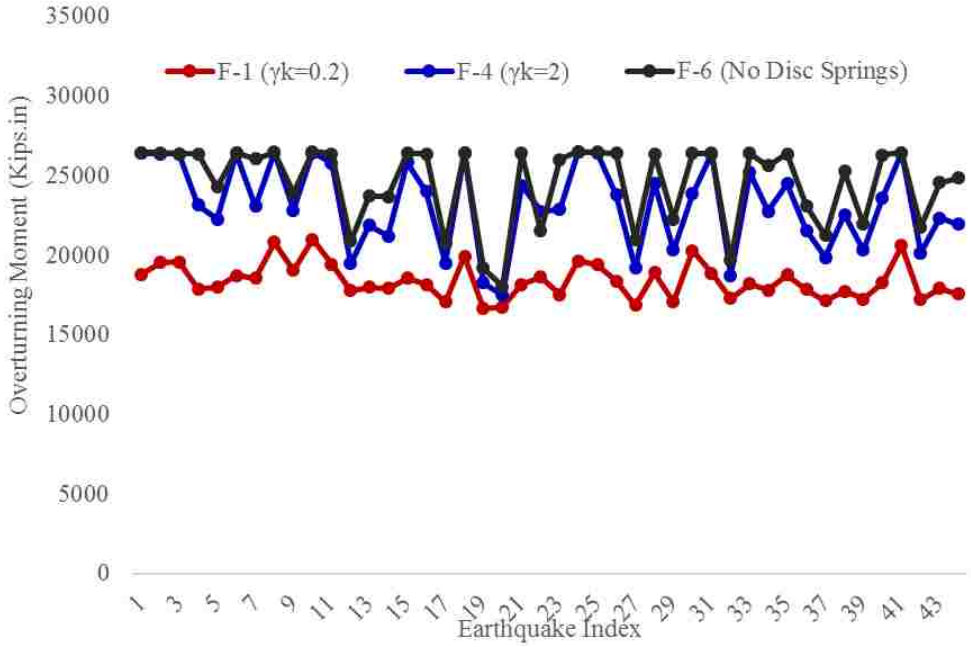

Figure 7.83: Maximum overturning moment of F-1, F-4, and F-6 under the MCE ground motions (spring stack has infinite travel capacity).

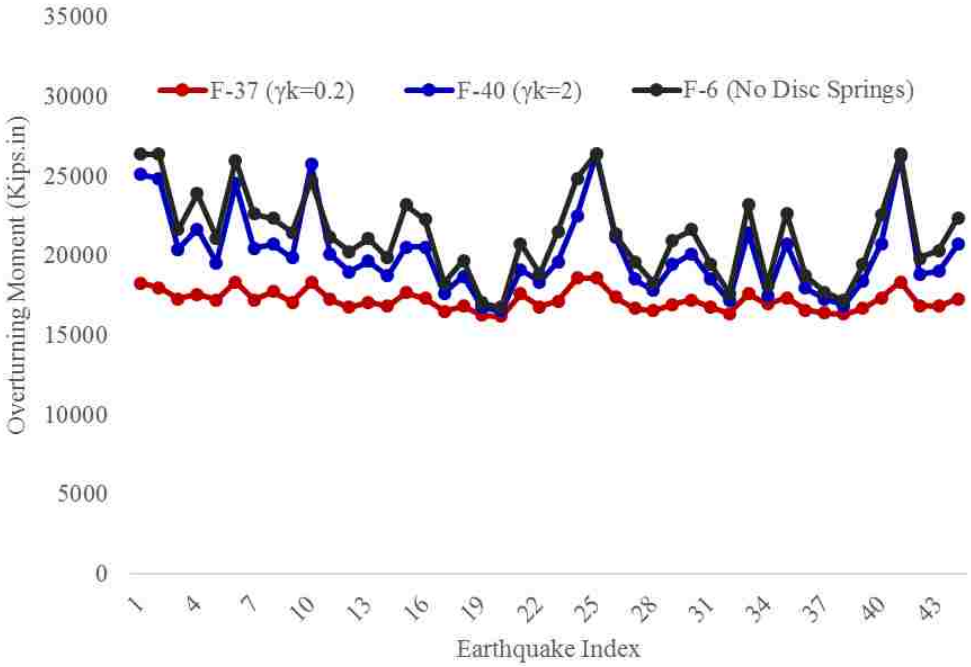

Figure 7.84: Maximum overturning moment of F-37, F-40, and F-6 under the MCE ground motions (spring stack has finite travel capacity).

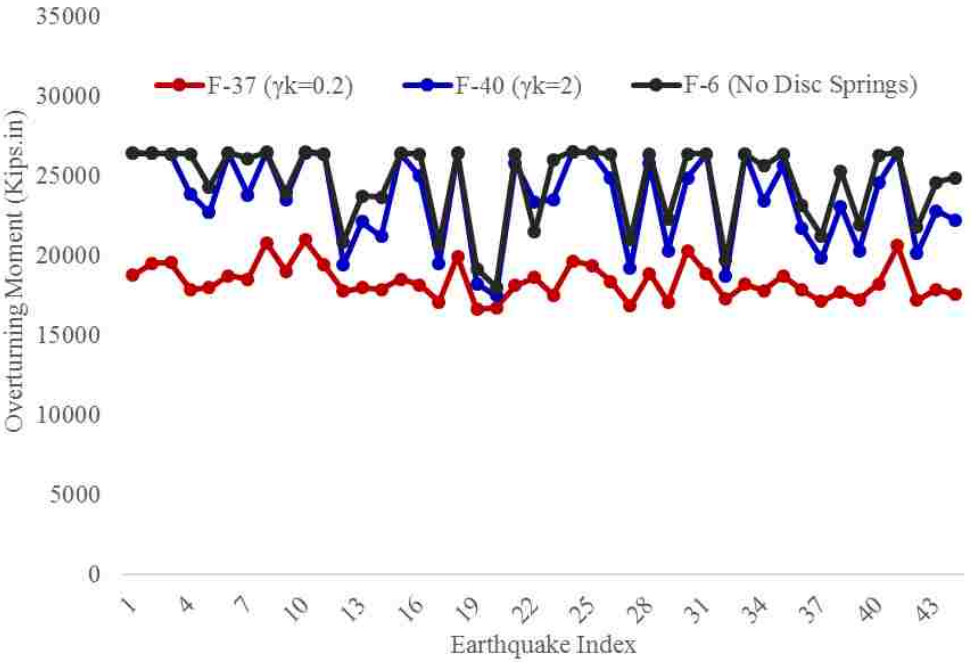

Figure 7.85: Maximum overturning moment of F-37, F-40, and F-6 under the DBE ground motions (spring stack has finite travel capacity).

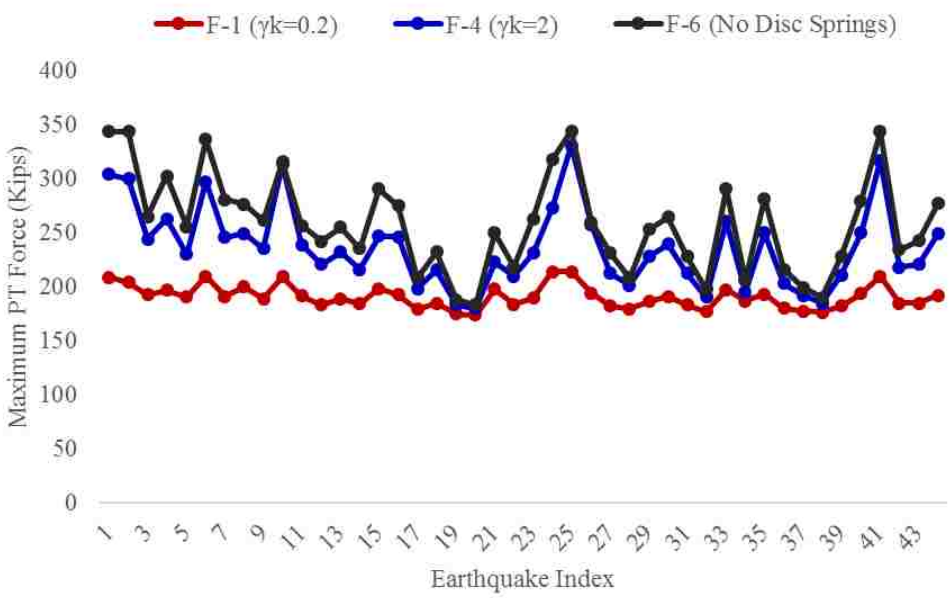

Figure 7.86: Maximum PT force of F-1, F-4, and F-6 under the DBE ground motions (spring stack has infinite travel capacity).

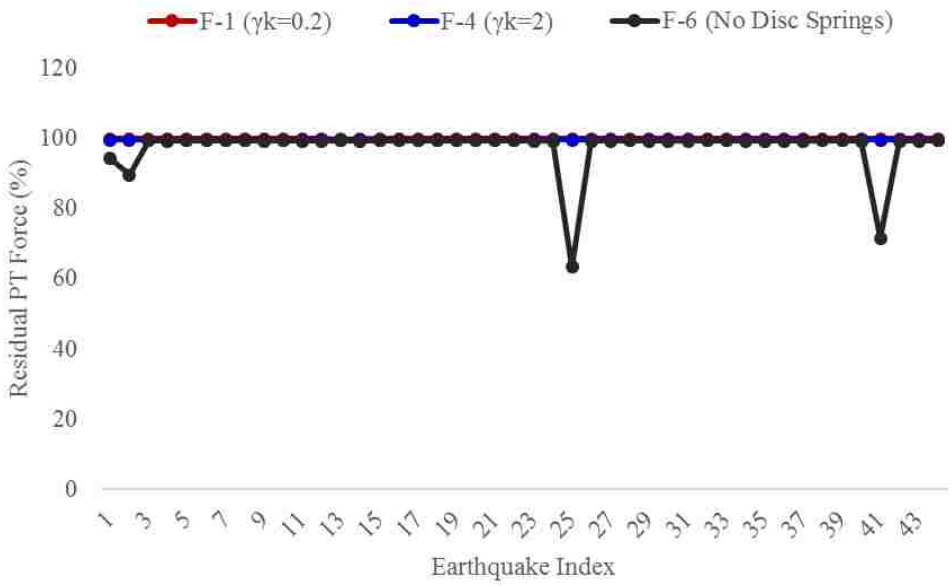

Figure 7.87: Residual PT force of F-1, F-4, and F-6 under the DBE ground motions (spring stack has infinite travel capacity).

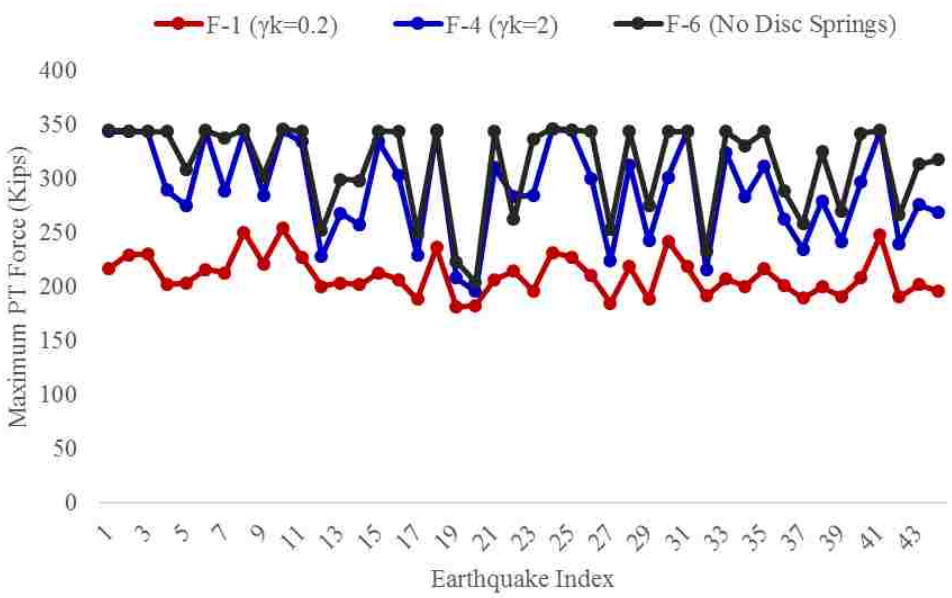

Figure 7.88: Maximum PT force of F-1, F-4, and F-6 under the MCE ground motions (spring stack has infinite travel capacity).

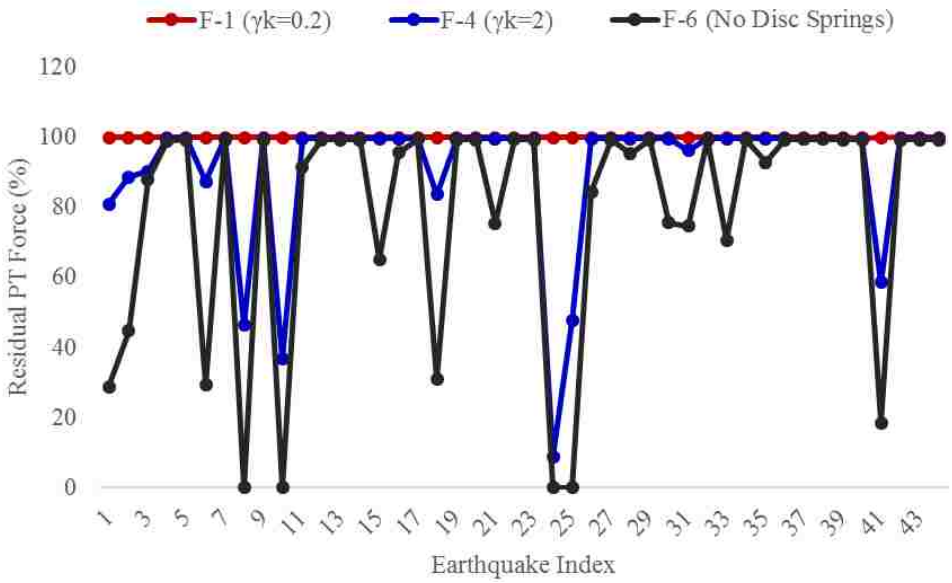

Figure 7.89: Residual PT force of F-1, F-4, and F-6 under the MCE ground motions (spring stack has infinite travel capacity).

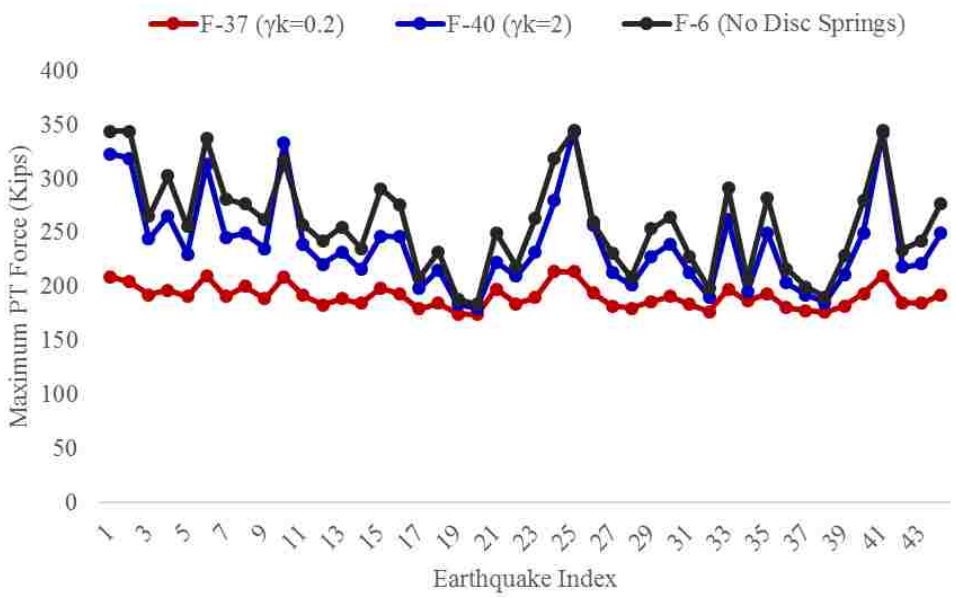

Figure 7.90: Maximum PT force of F-37, F-40, and F-6 under the DBE ground motions (spring stack has finite travel capacity).

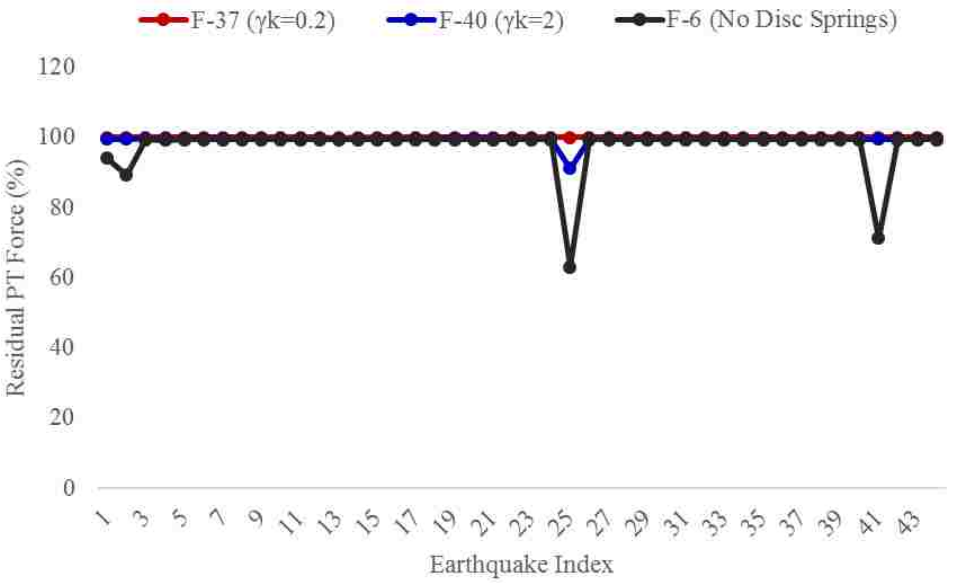

Figure 7.91: Residual PT force of F-37, F-40, and F-6 under the DBE ground motions (spring stack has finite travel capacity).

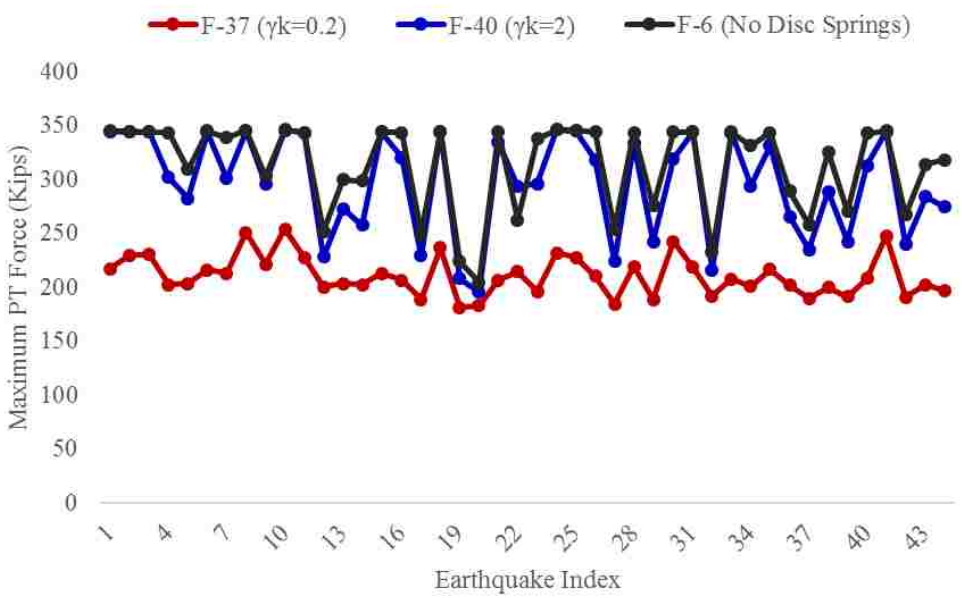

Figure 7.92: Maximum PT force of F-37, F-40, and F-6 under the MCE ground motions (spring stack has finite travel capacity).

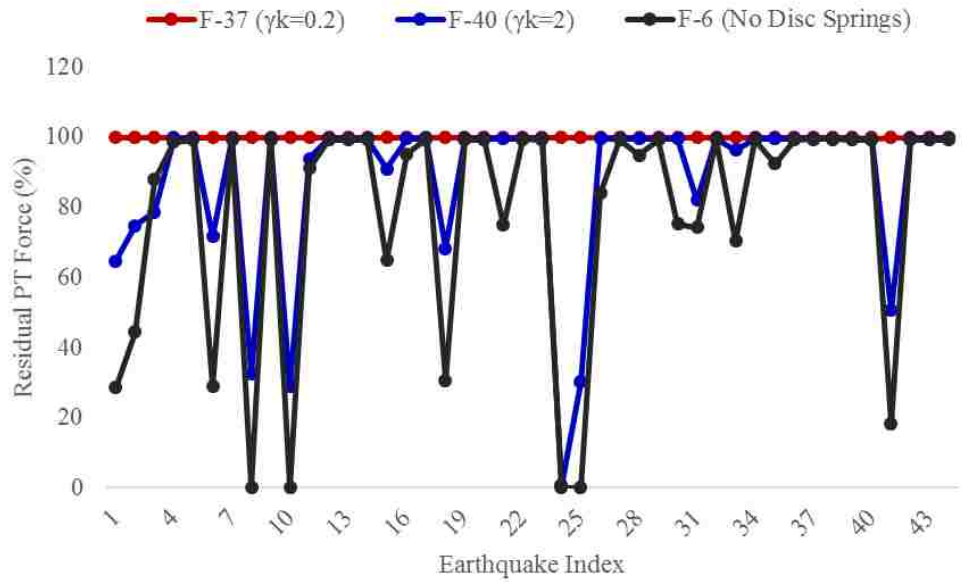

Figure 7.93: Residual PT force of F-37, F-40, and F-6 under the MCE ground motions (spring stack has finite travel capacity).

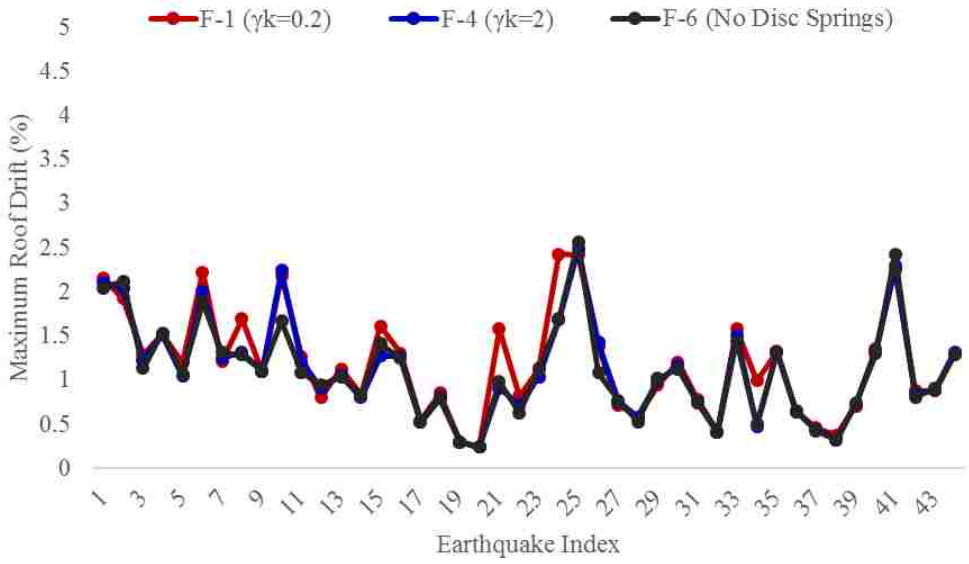

Figure 7.94: Maximum roof drift of F-1, F-4, and F-6 under the DBE ground motions (spring stack has infinite travel capacity).

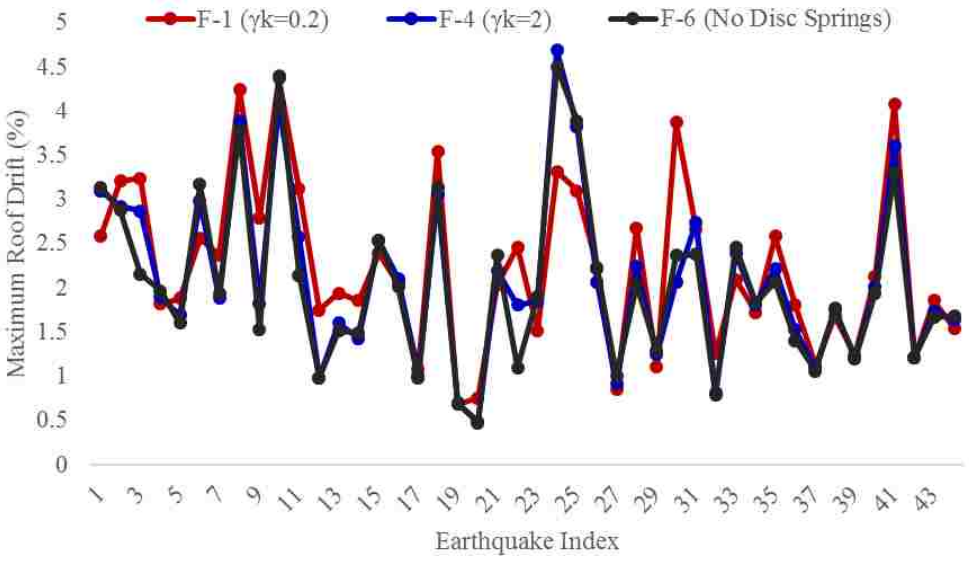

Figure 7.95: Maximum roof drift of F-1, F-4, and F-6 under the MCE ground motions (spring stack has infinite travel capacity).

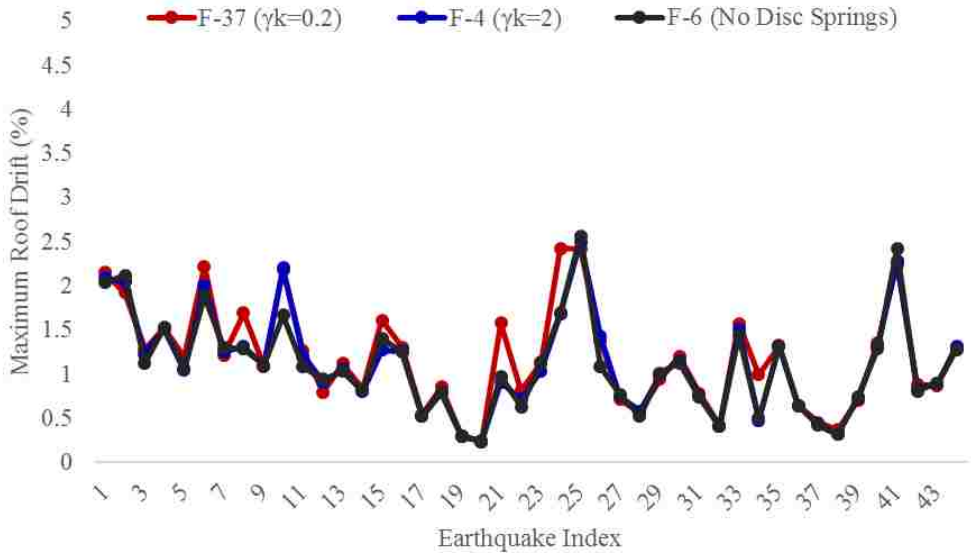

Figure 7.96: Maximum roof drift of F-37, F-40, and F-6 under the DBE ground motions (spring stack has finite travel capacity).

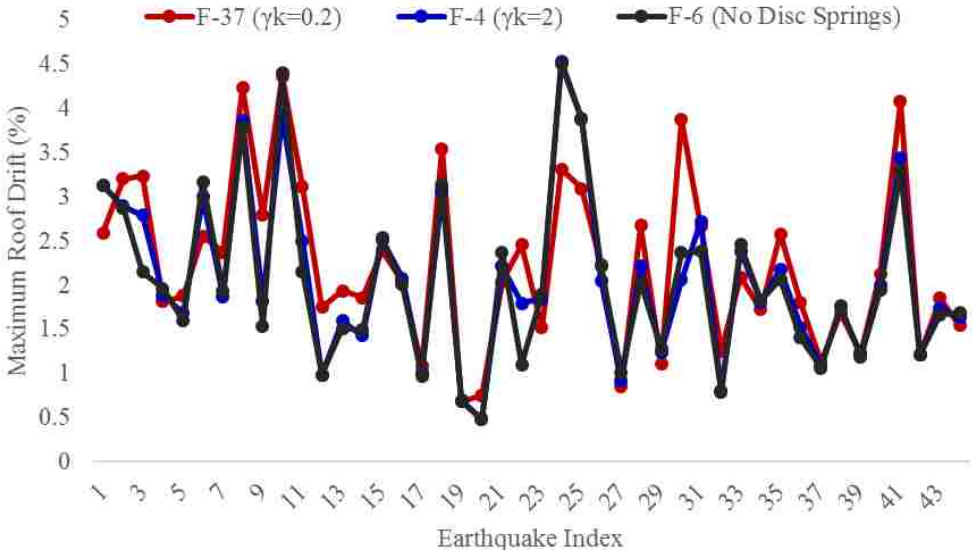

Figure 7.97: Maximum roof drift of F-37, F-40, and F-6 under the MCE ground motions (spring stack has finite travel capacity).

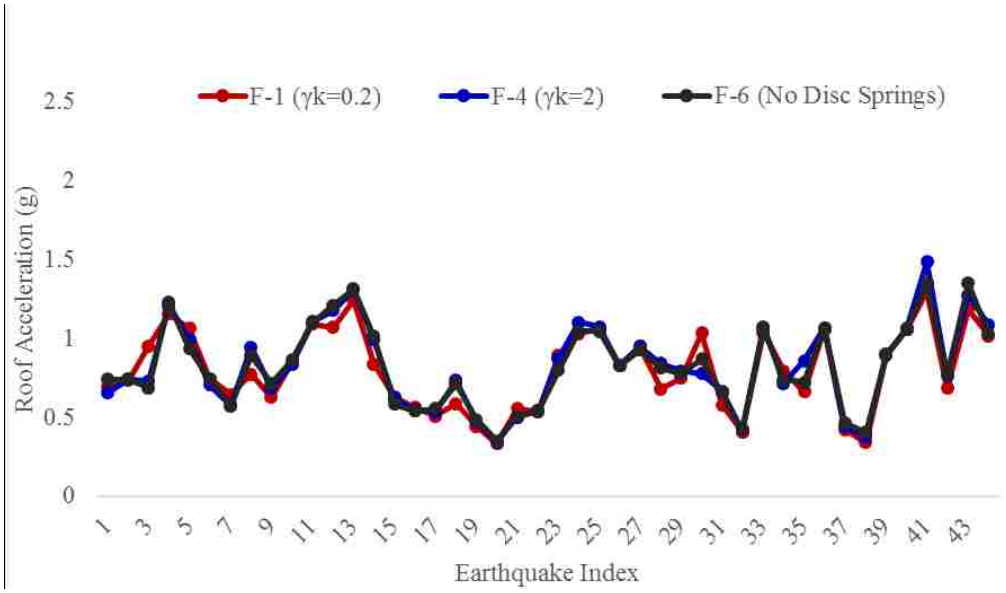

Figure 7.98: Maximum roof acceleration of F-1, F-4, and F-6 under the DBE ground motions (spring stack has infinite travel capacity).

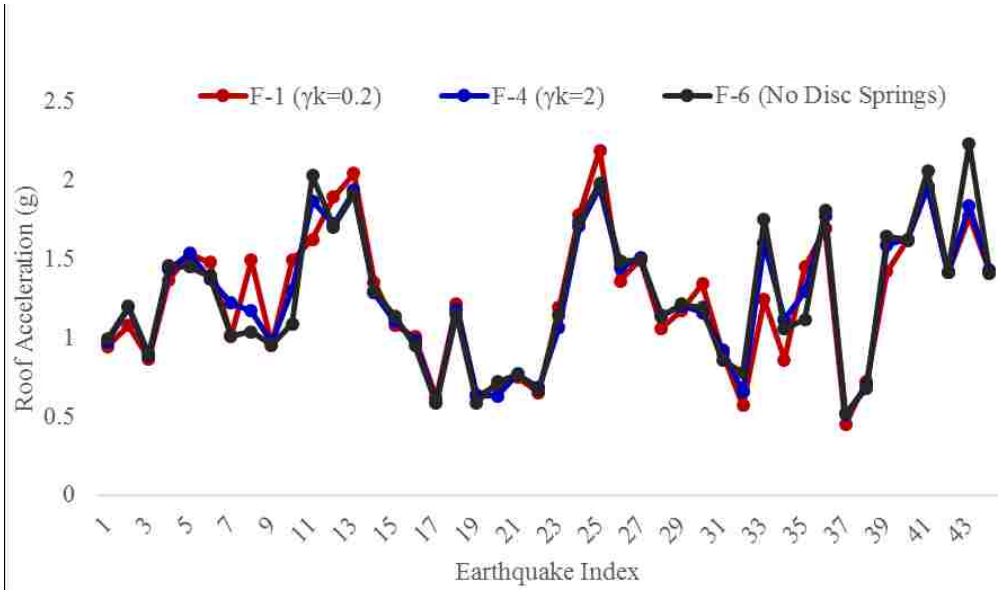

Figure 7.99: Maximum roof acceleration of F-1, F-4, and F-6 under the MCE ground motions (spring stack has infinite travel capacity).

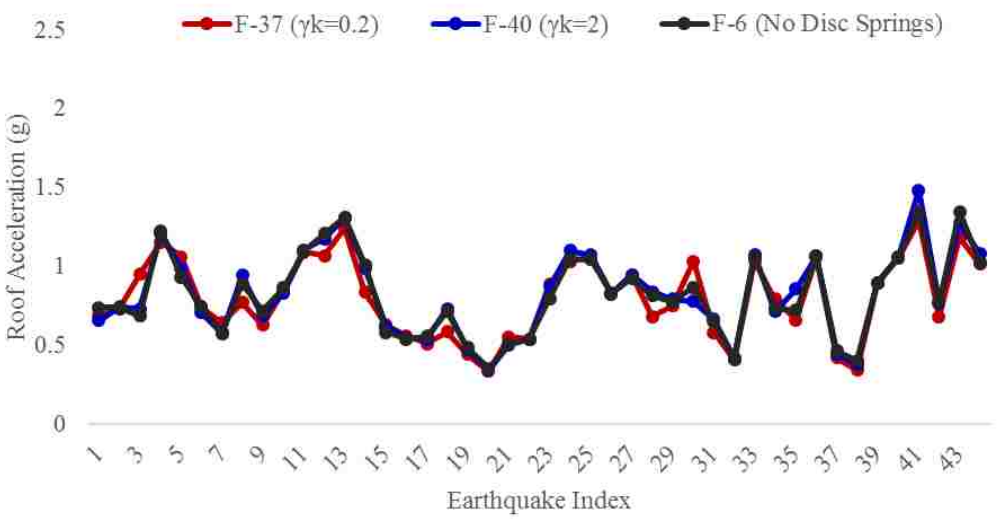

Figure 7.100: Maximum roof acceleration of F-37, F-40, and F-6 under the DBE ground motions (spring stack has finite travel capacity).

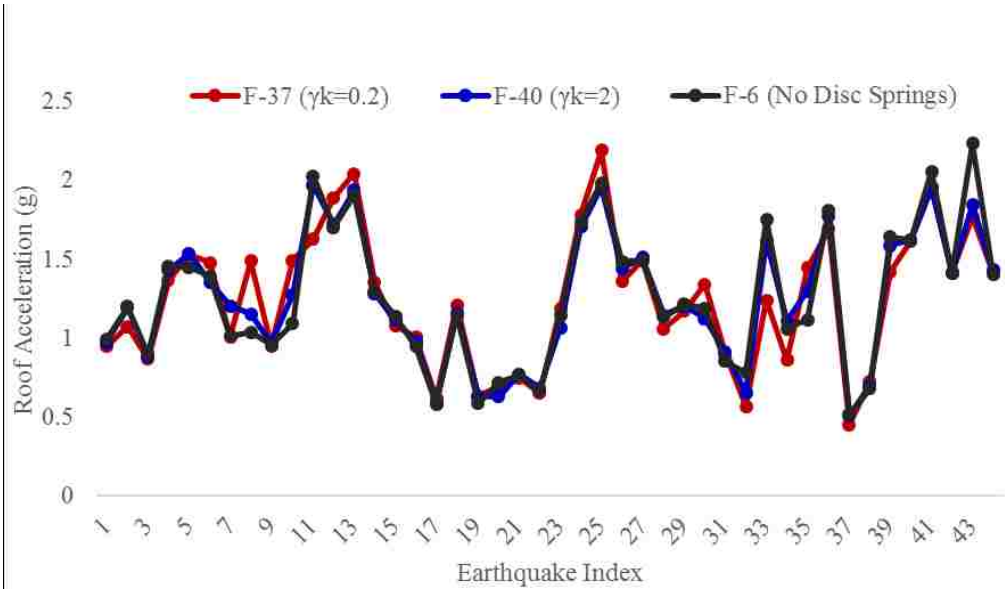

Figure 7.101: Maximum roof acceleration of F-37, F-40, and F-6 under the MCE ground motions (spring stack has finite travel capacity).

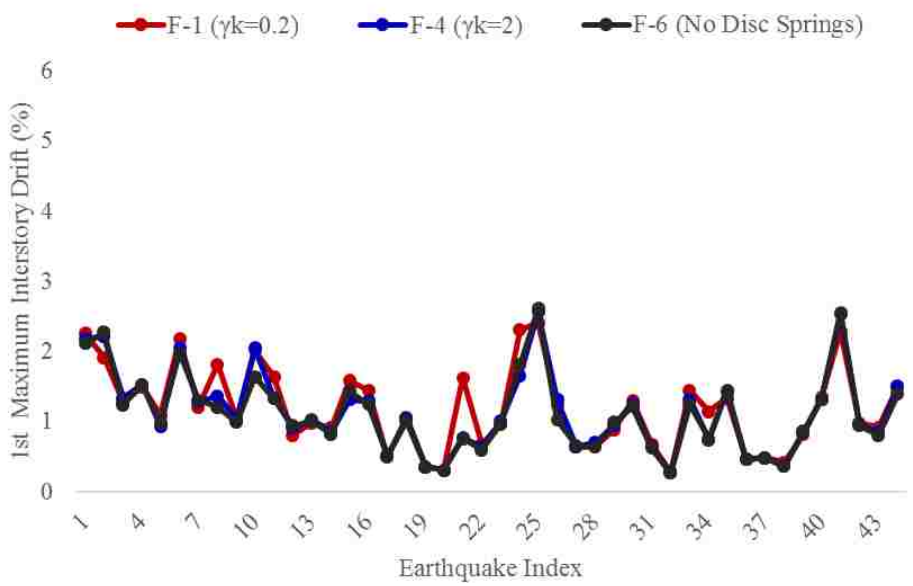

Figure 7.101: 1st peak interstory drift of F-1, F-4, and F-6 under the DBE ground motions (spring stack has infinite travel capacity).

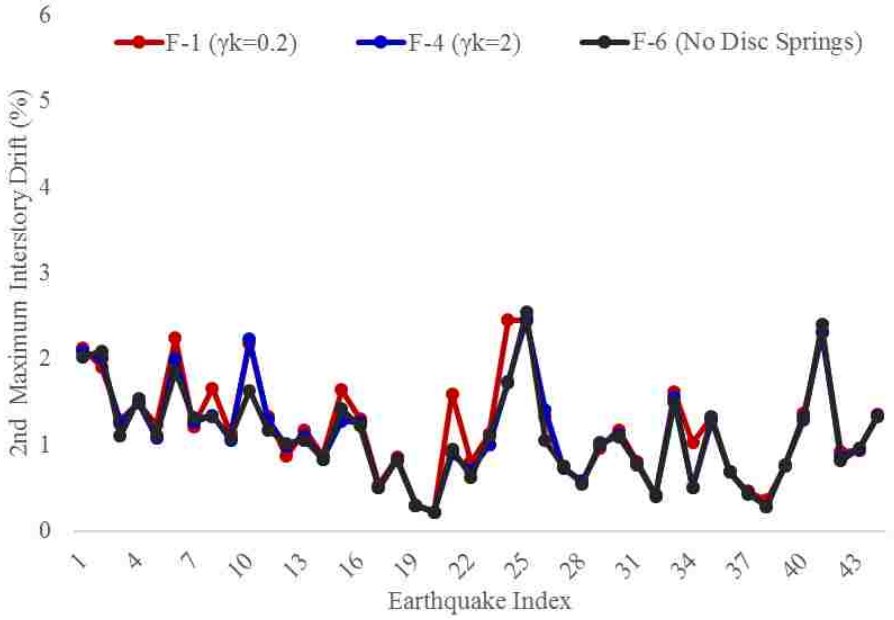

Figure 7.103: 2nd peak interstory drift of F-1, F-4, and F-6 under the DBE ground motions (spring stack has infinite travel capacity).

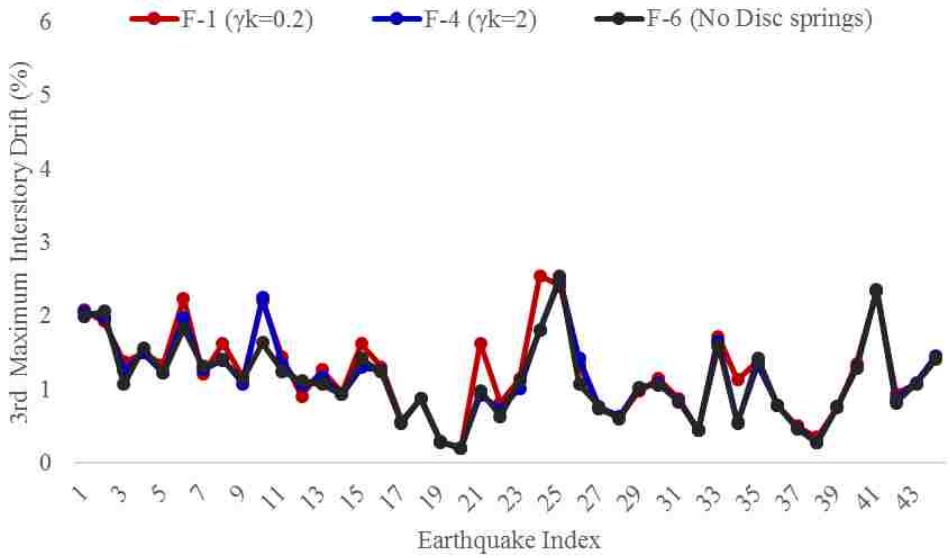

Figure 7.104: 3rd peak interstory drift of F-1, F-4, and F-6 under the DBE ground motions (spring stack has infinite travel capacity).

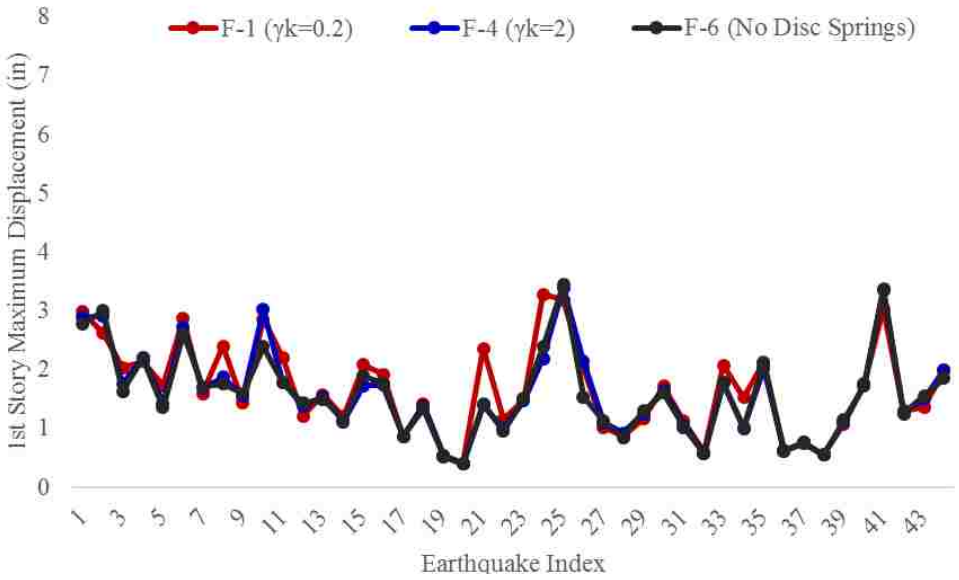

Figure 7.105: 1st story peak displacement of F-1, F-4, and F-6 under the DBE ground motions (spring stack has infinite travel capacity).

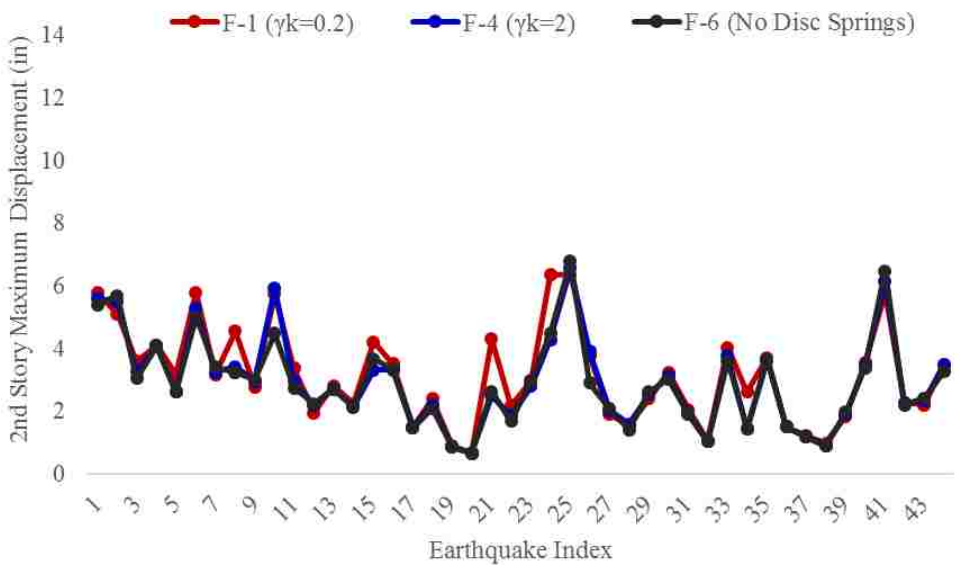

Figure 7.106: 2nd story peak displacement of F-1, F-4, and F-6 under the DBE ground motions (spring stack has infinite travel capacity).

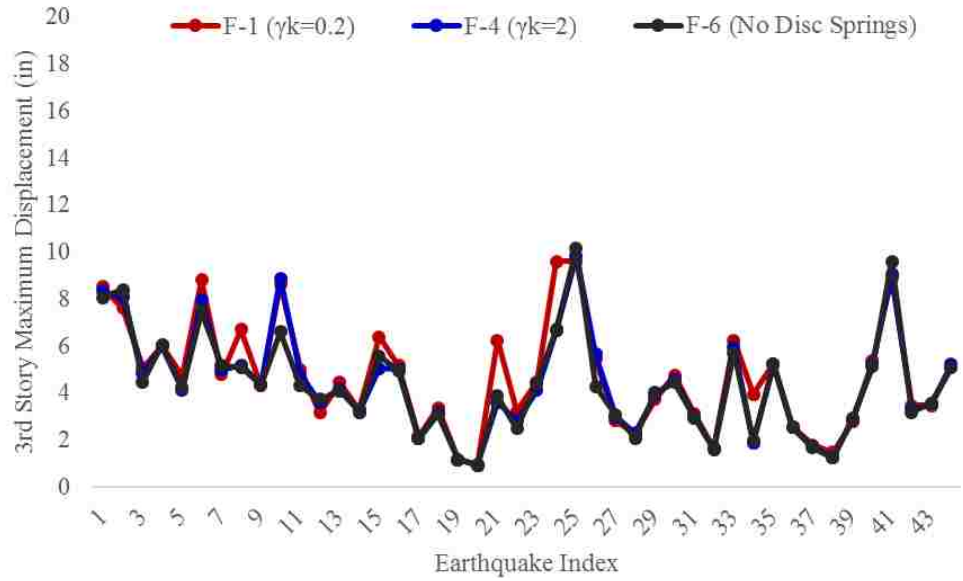

Figure 7.107: 3rd story peak displacement of F-1, F-4, and F-6 under the DBE ground motions (spring stack has infinite travel capacity).

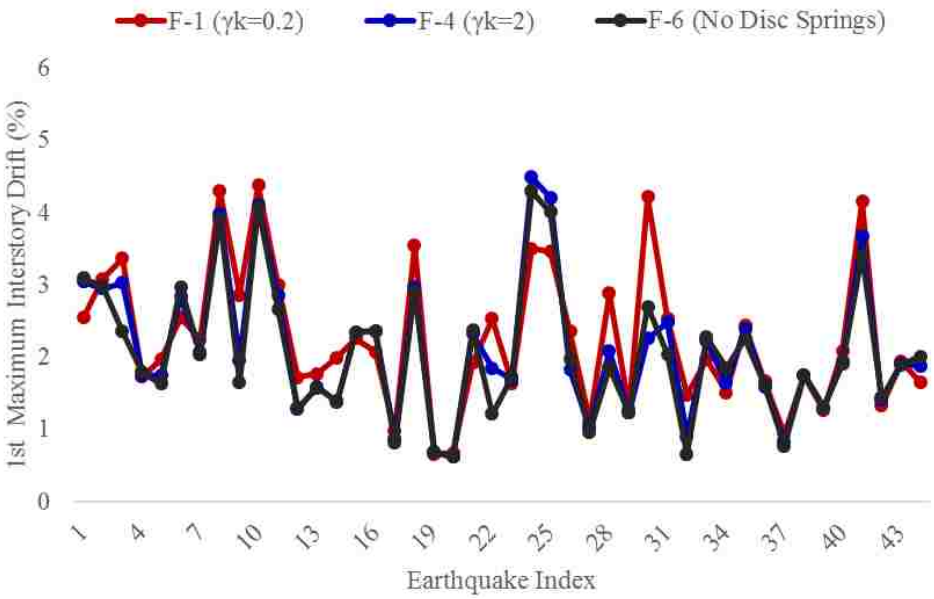

Figure 7.108: 1st maximum interstory drift of F-1, F-4, and F-6 under the MCE ground motions (spring stack has infinite travel capacity).

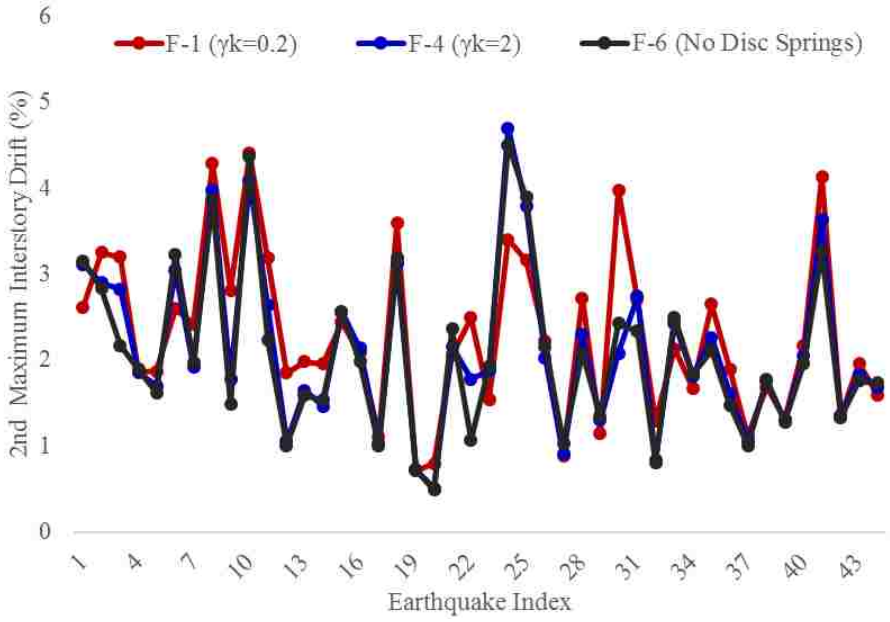

Figure 7.109: 2nd maximum interstory drift of F-1, F-4, and F-6 under the MCE ground motions (spring stack has infinite travel capacity).

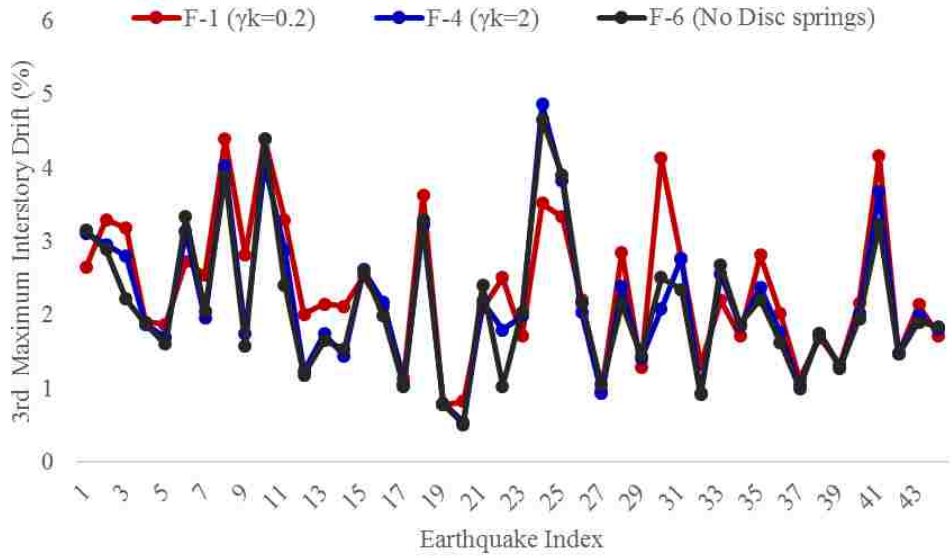

Figure 7.110: 3rd maximum interstory drift of F-1, F-4, and F-6 under the MCE ground motions (spring stack has infinite travel capacity).

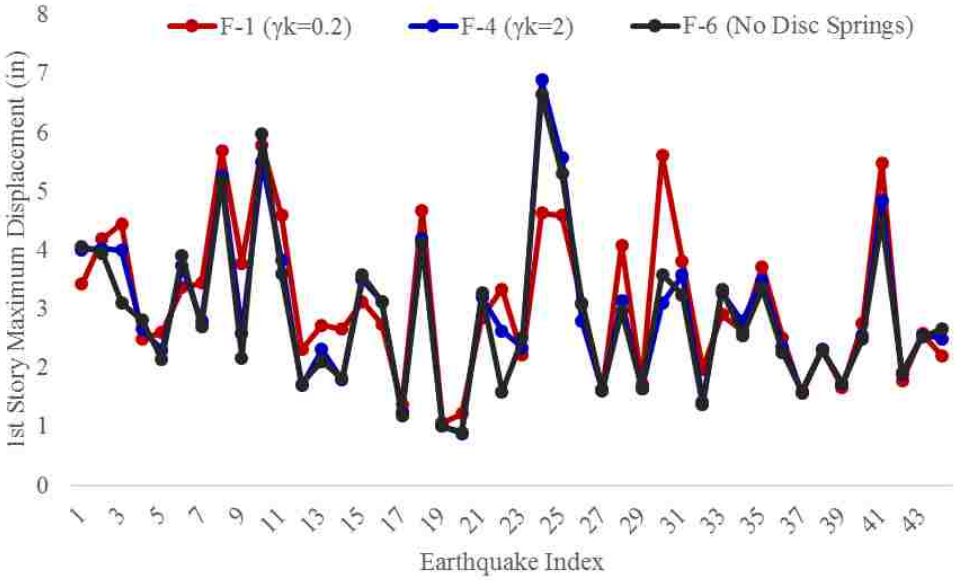

Figure 7.111: Maximum 1st story displacement of F-1, F-4, and F-6 under the MCE ground motions (spring stack has infinite travel capacity).

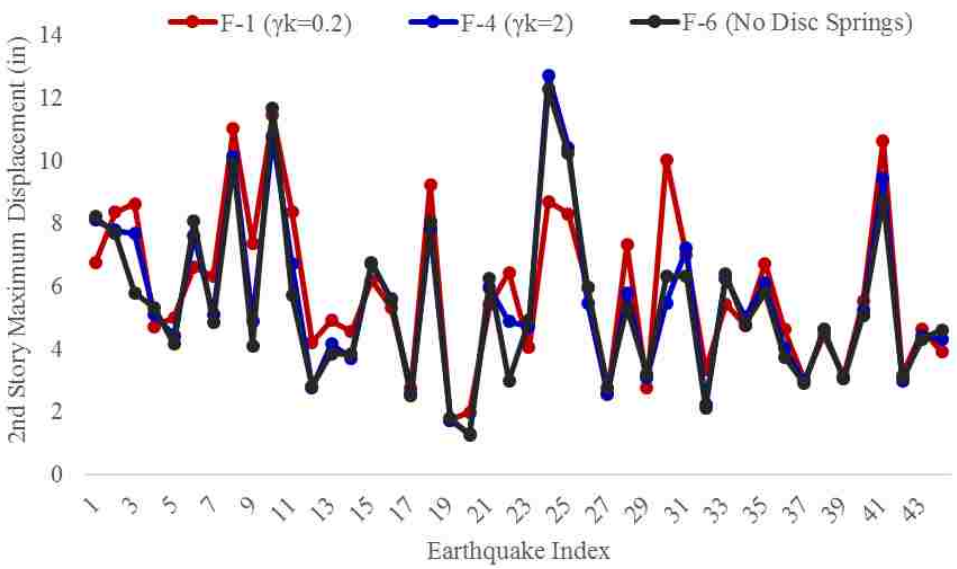

Figure 7.112: Maximum 2nd story displacement of F-1, F-4, and F-6 under the MCE ground motions (spring stack has infinite travel capacity).

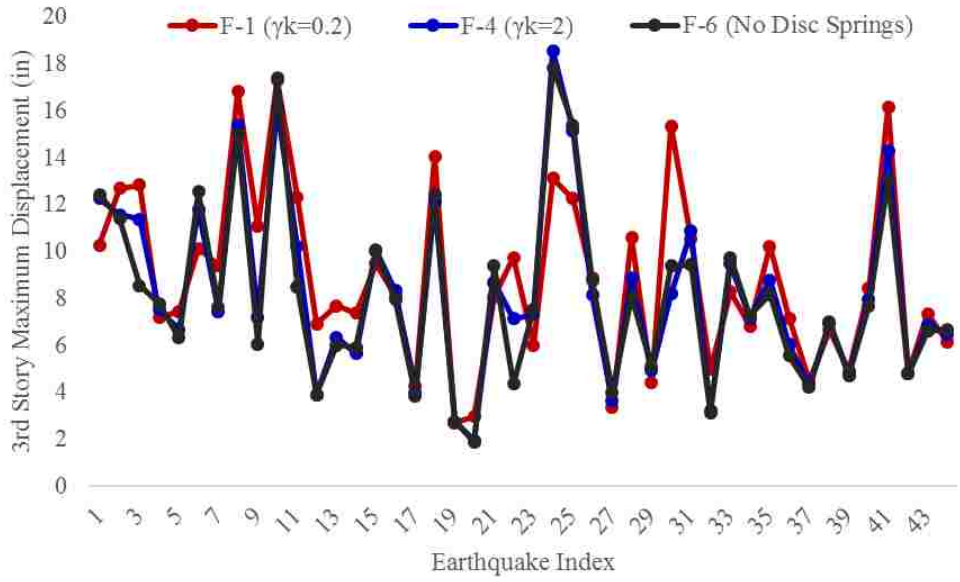

Figure 7.113: Maximum 3rd story displacement of F-1, F-4, and F-6 under the MCE ground motions (spring stack has infinite travel capacity).

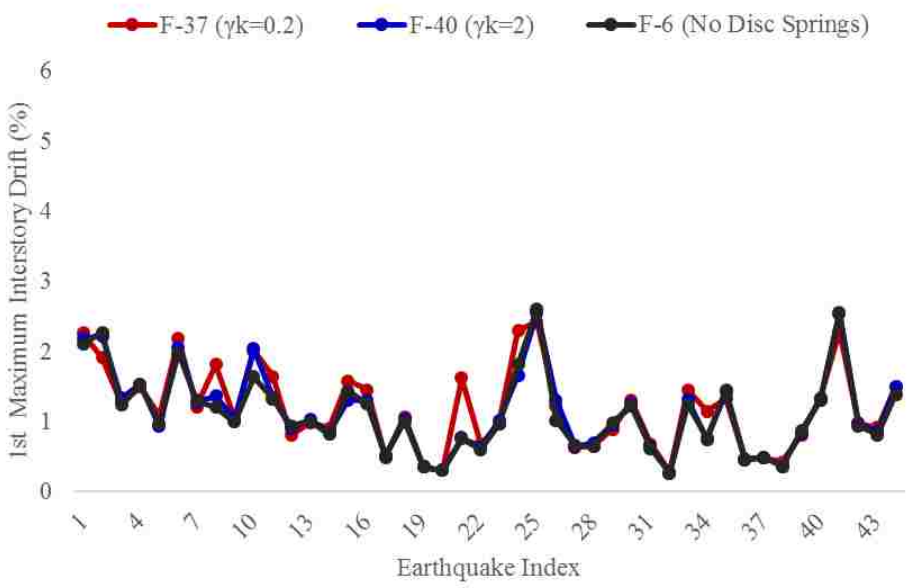

Figure 7.114: 1st maximum interstory drift of F-37, F-40, and F-6 under the DBE ground motions (spring stack has finite travel capacity).

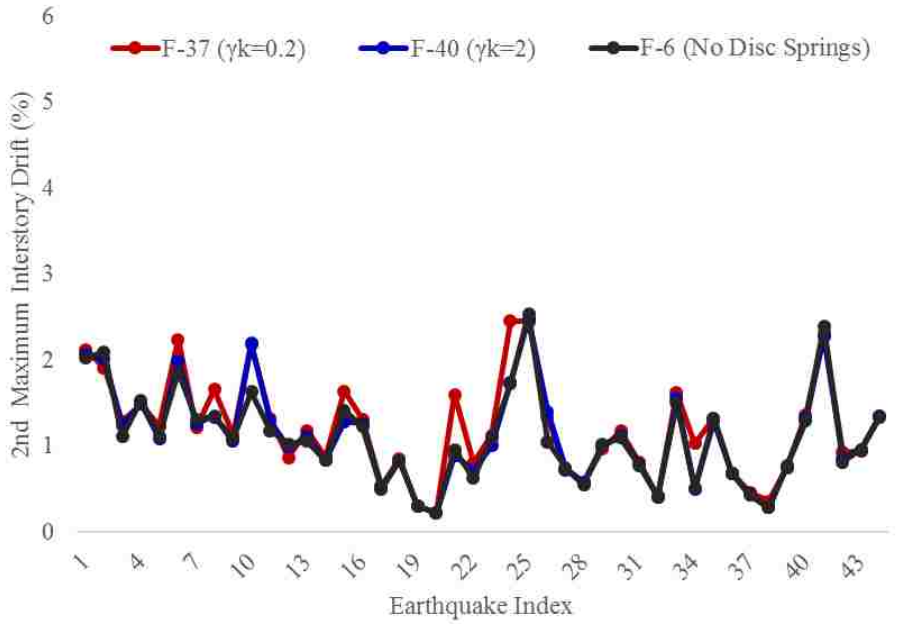

Figure 7.115: 2nd maximum interstory drift of F-37, F-40, and F-6 under the DBE ground motions (spring stack has finite travel capacity).

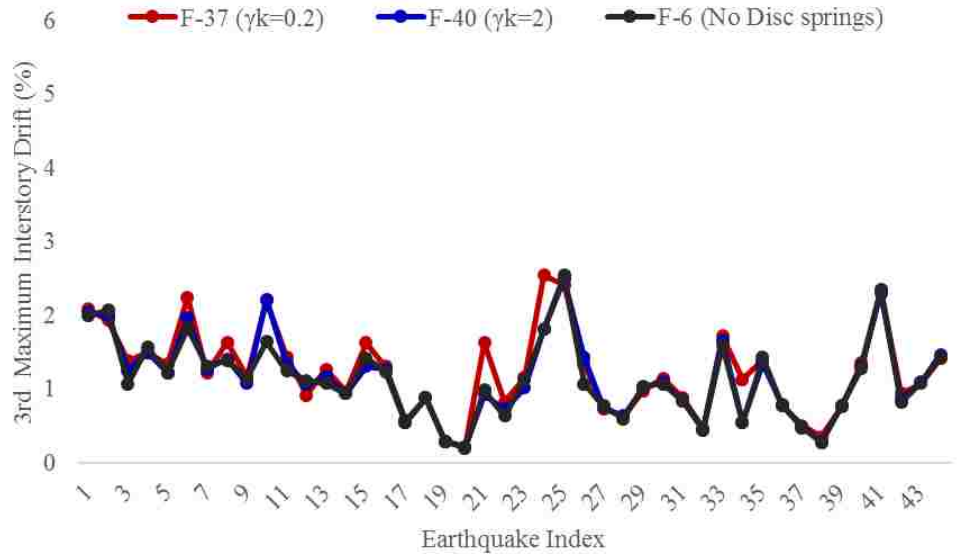

Figure 7.116: 3rd maximum interstory drift of F-37, F-40, and F-6 under the DBE ground motions (spring stack has finite travel capacity).

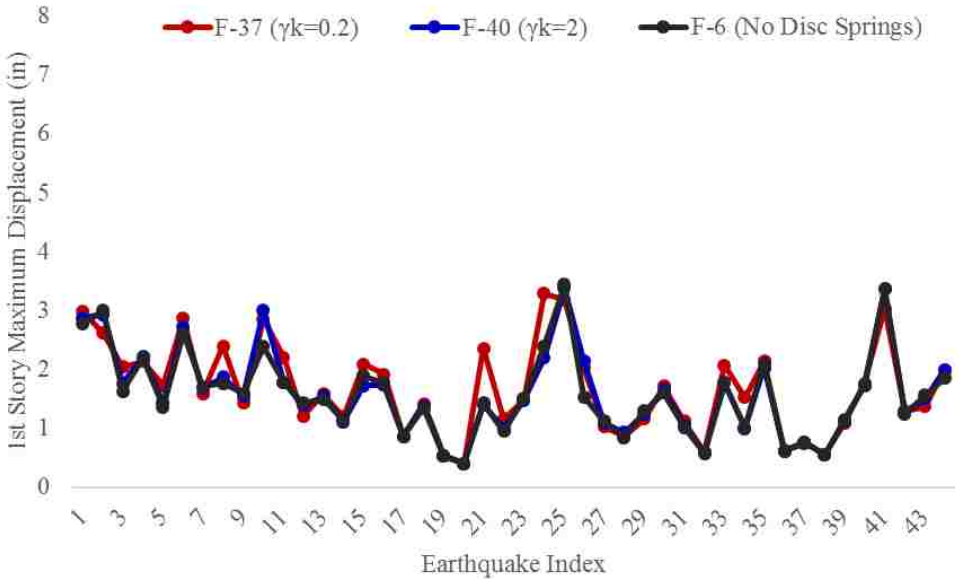

Figure 7.117: 1st maximum story displacement of F-37, F-40, and F-6 under the DBE ground motions (spring stack has finite travel capacity).

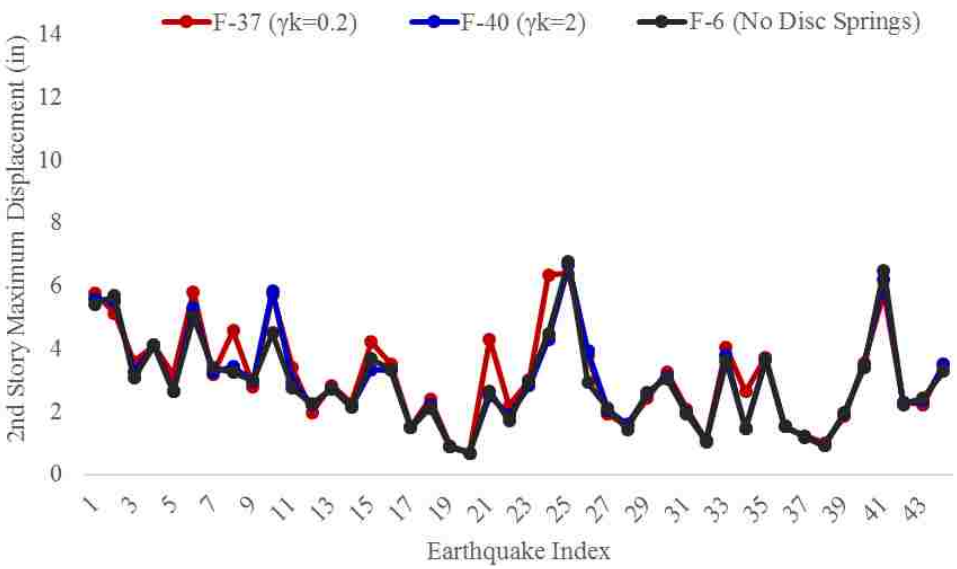

Figure 7.118: 2nd maximum story displacement of F-37, F-40, and F-6 under the DBE ground motions (spring stack has finite travel capacity).

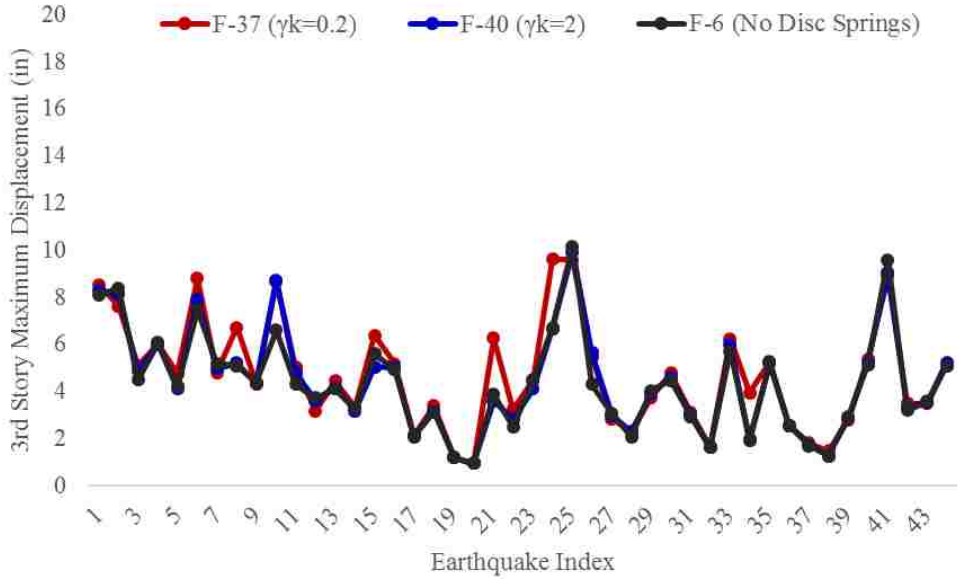

Figure 7.119: 3rd maximum story displacement of F-37, F-40, and F-6 under the DBE ground motions (spring stack has finite travel capacity).

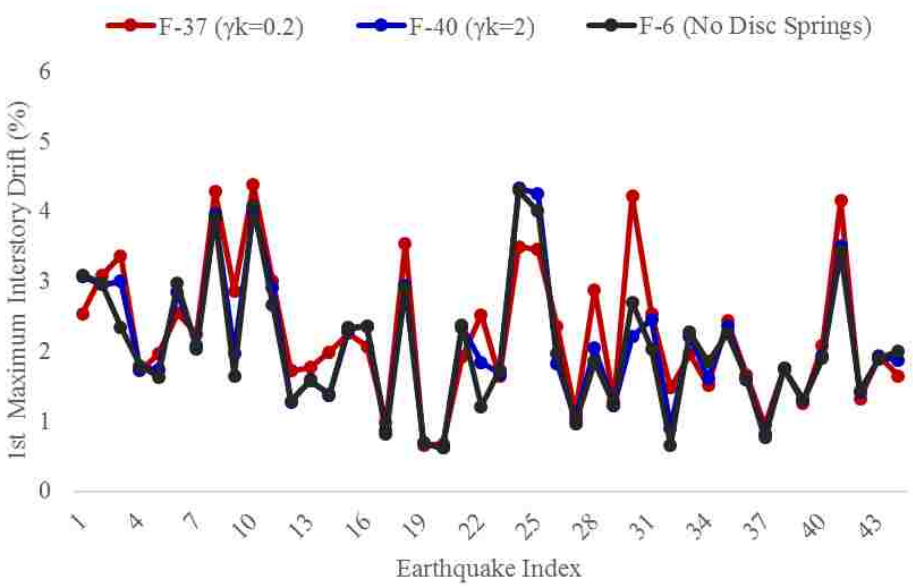

Figure 7.120: 1st maximum interstory drift of F-37, F-40, and F-6 under the MCE ground motions (spring stack has finite travel capacity).

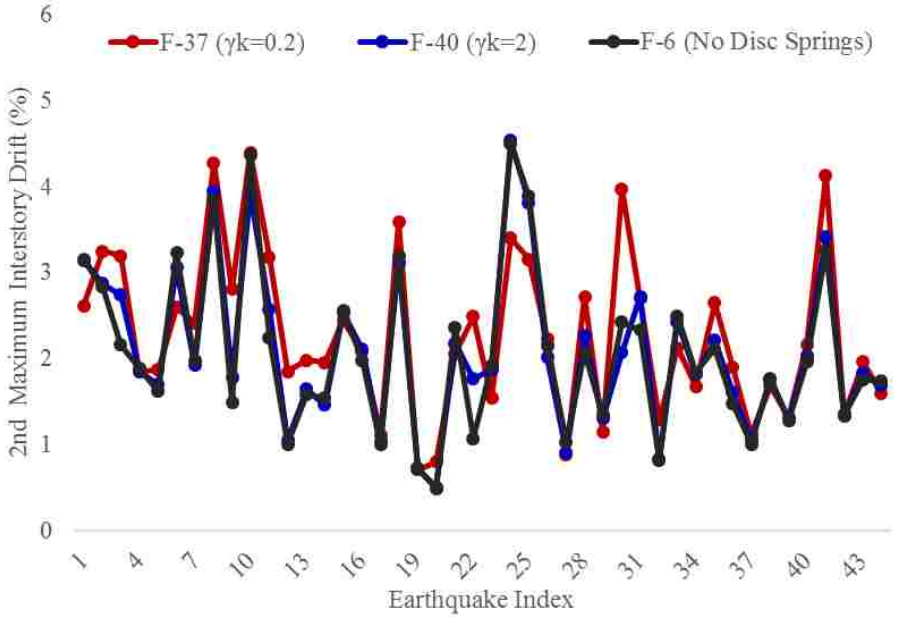

Figure 7.121: 2nd maximum interstory of F-37, F-40, and F-6 under the MCE ground motions (spring stack has finite travel capacity).

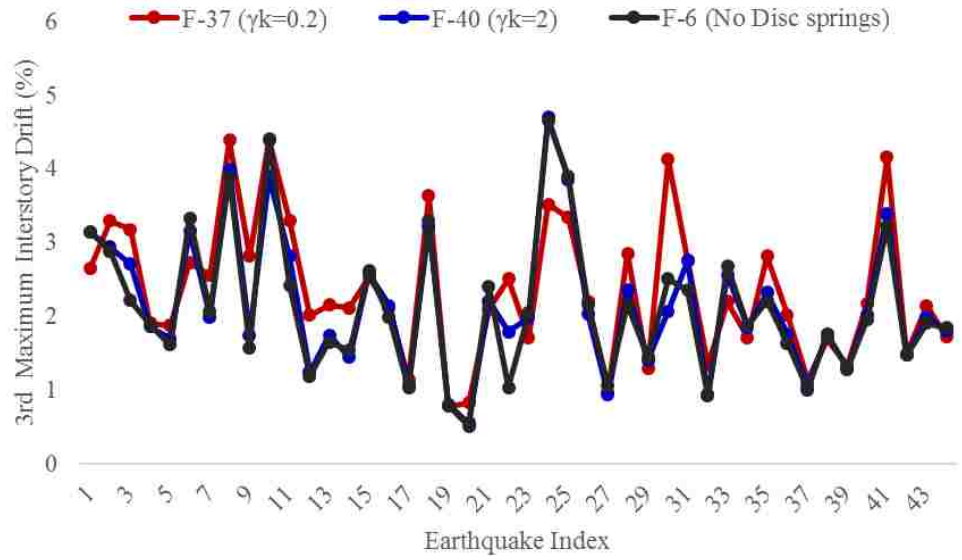

Figure 7.122: 3rd maximum interstory of F-37, F-40, and F-6 under the MCE ground motions (spring stack has finite travel capacity).

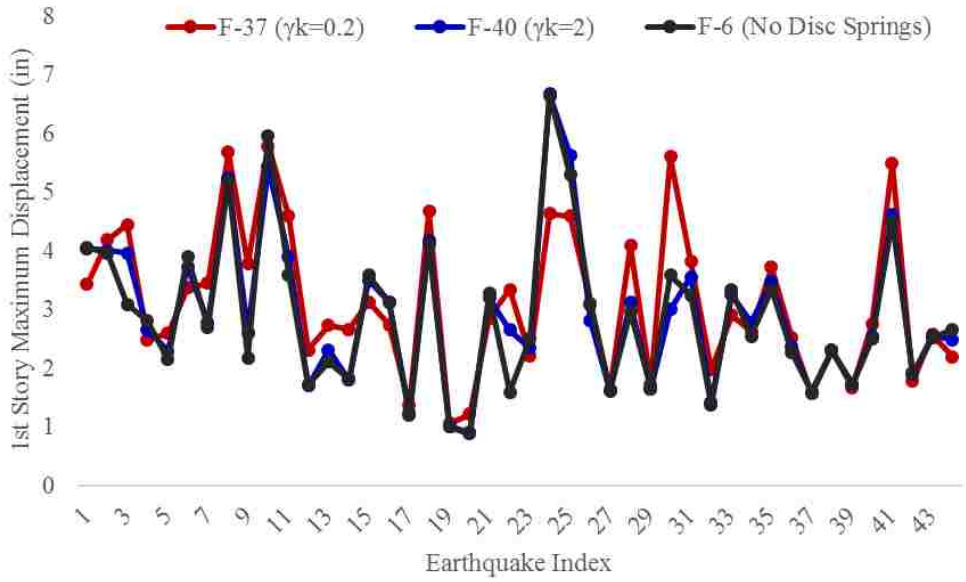

Figure 7.123: 1st story maximum displacement of F-37, F-40, and F-6 under the MCE ground motions (spring stack has finite travel capacity).

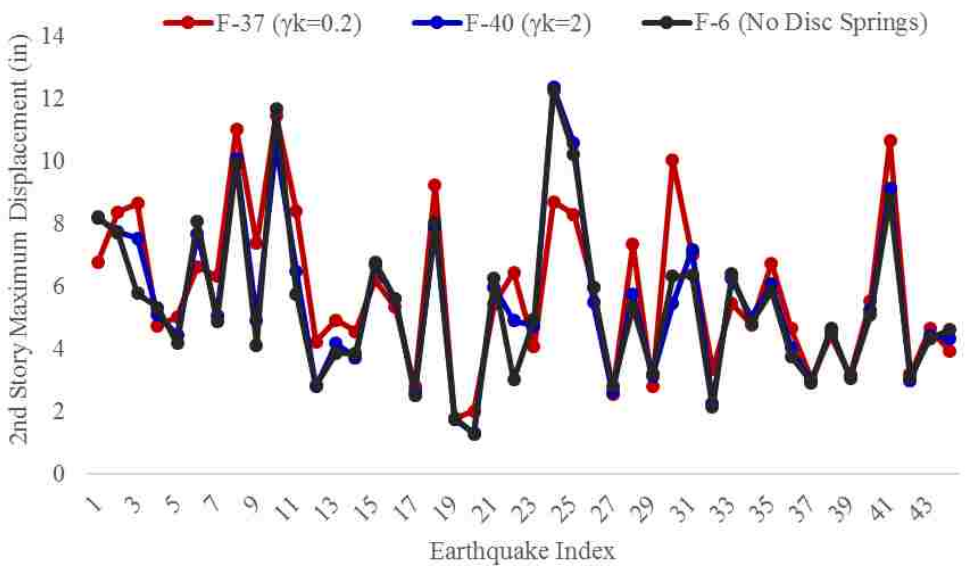

Figure 7.124: 2nd story maximum displacement of F-37, F-40, and F-6 under the MCE ground motions (spring stack has finite travel capacity).

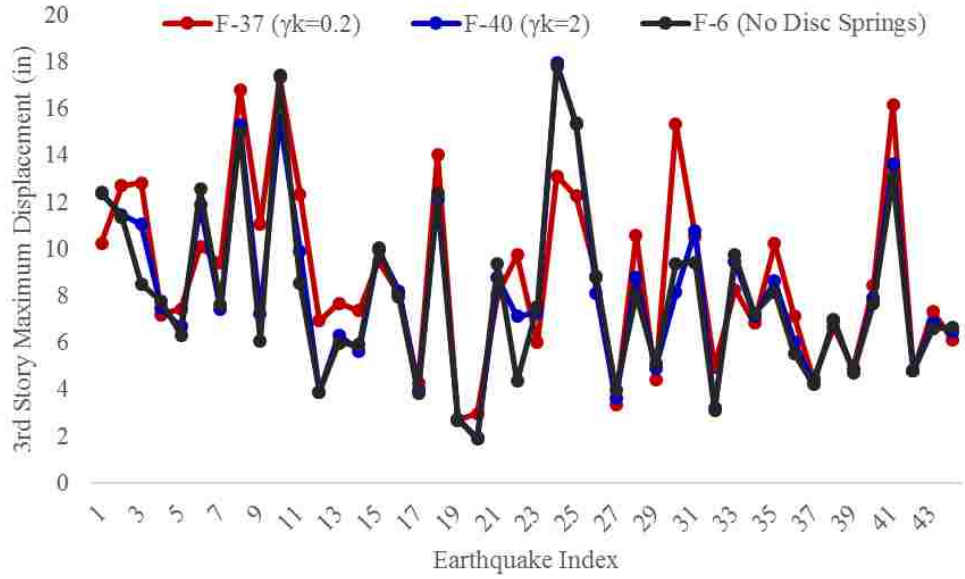

Figure 7.125: 3rd story maximum displacement of F-37, F-40, and F-6 under the MCE ground motions (spring stack has finite travel capacity).

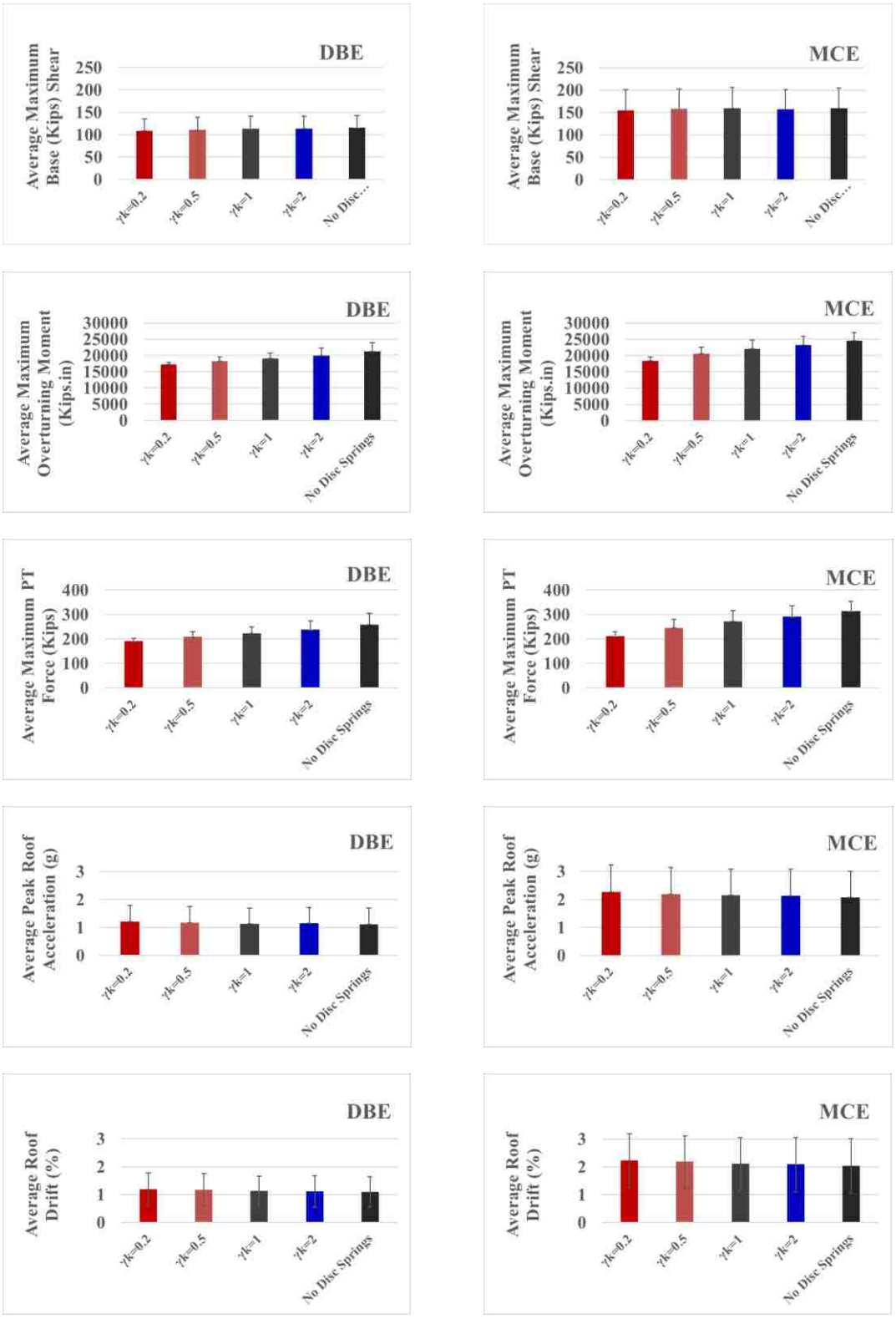

Figure 7.126: Average peak responses and the corresponding standard deviations for frames with zero eccentricity (spring stacks have infinite travel capacities).

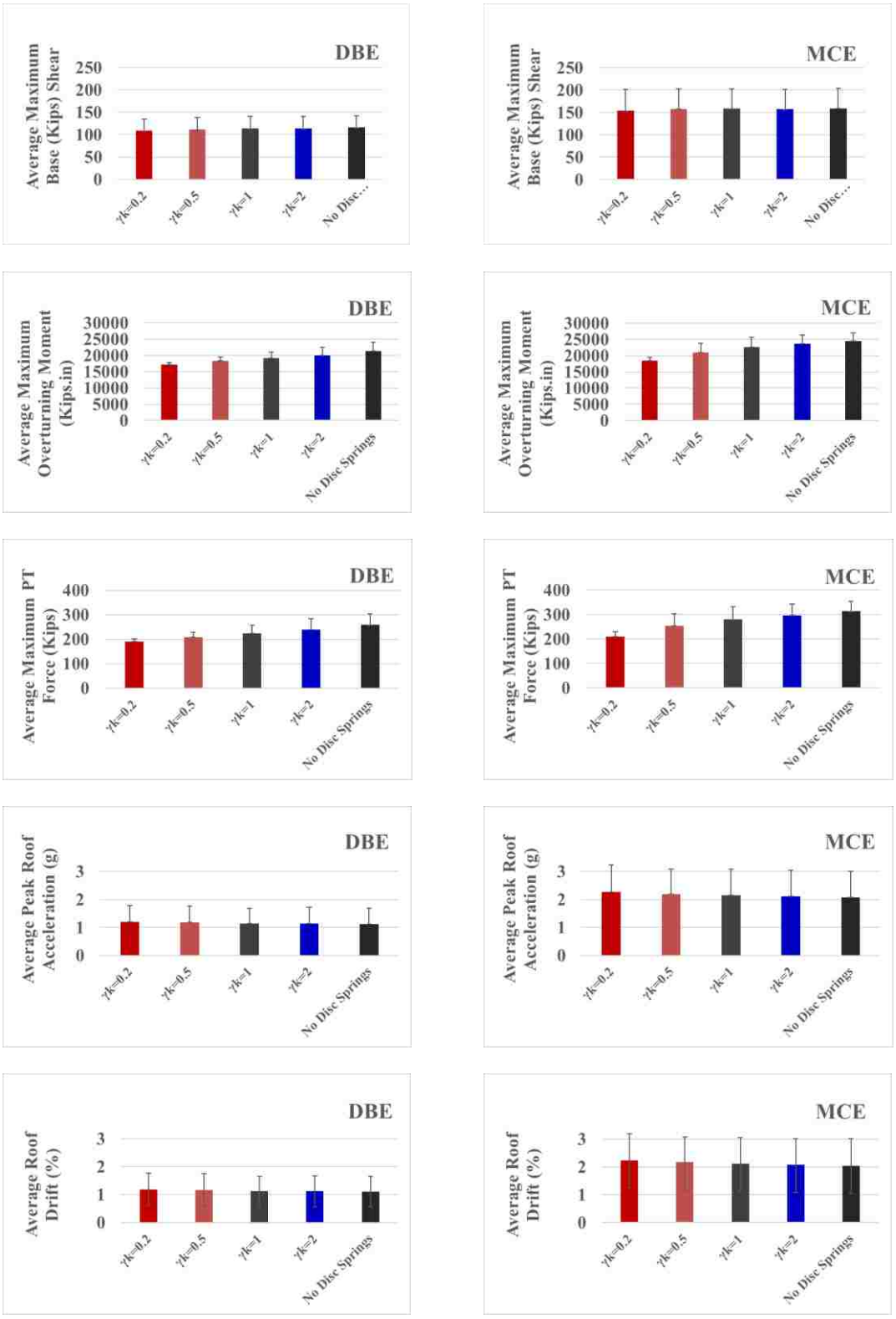

Figure 7.127: Average peak responses and the corresponding standard deviations for frames with zero eccentricity (spring stacks has finite travel capacities and clamps at 0.75 F_{py}).

CHAPTER 8

SUMMARY CONCLUSION AND FURTHER WORK

This chapter summarizes the results of the research and presents conclusions. Recommendations for future work are also given.

8.1 SUMMARY

Chapter 1 showed a scheme of the post-tensioned lateral force resistant systems. The literature indicates that these systems have large drift capacity and could be designed to reduce damage during extreme events. Also, these systems make use of the post-tensioning (PT) steel to provide self-centering force and eliminate the residual drift.

To make such systems available to developing communities that have no access to specialized PT equipment or highly trained workers, a simple manually post-tensioned self-centering system has been proposed. The system introduces spring element connected in series with the PT steel to facilitate the manual PT process. This also promotes more sustainable seismic resistant systems in that the systems are less prone to damage that requires extensive repair or demolition after a seismic event.

Chapter 2 presented the required background information on the relevant topics. Topics include a review of the rocking systems. Most importantly, a description of the disc spring elements used in this study. It highlights the essential characteristics of the disc springs, how do disc springs behave during compression loads, and how a single disc spring could provide a flexible way to gain different force-deformation response by stacking this spring in series or parallel.

Chapter 3 discusses the process underlying the derivation of the closed-form expressions. These equations were based on several assumptions to simplify the derivations. Two important cases were included in the derivation process. The first case included frames with spring stacks having infinite travel (deformation) capacities, while the second case included frames with spring stacks having finite travel capacities. It was shown that these two different cases have backbone curves with different shapes and the reason is the clamping of the spring stack. The equations in Chapter 3 show that the force at the PT steel is expected to increase as more lateral load is applied. Thus, the compression load on the spring stack also increases. This increase in the spring stack force causes it to shorten under the increased load, and once it reaches its full travel capacity, the backbone curve changes its response. This will not happen if the spring stack has unlimited travel capacity, or if the maximum compression load on the spring stack is less than the load that causes the stack to reach its full flat position.

Chapter 4 discusses the development of the FE model to represent the proposed system during static pushover loads. The foundation of the finite element model was based on a study completed in the literature. However, the current report updates the existing model to include the presence of the disc spring stack. A significant change to the existing FE model has been applied to account for the clamping of the spring stack during the pushover loads. The FE model includes several limit states such as decompression, yielding of the spring stack, clamping of the spring stack, fracture of the PT steel. Damage to the rocking frame components such as the columns, beams, and braces were excluded from the model, i.e. the frame itself was to remain elastic.

Chapter 5 presents the prototype building used in this thesis. This building is a wooden structure that was used in the literature to study the self-centering wood lateral resistant systems. It was also used here in this study. The building was assumed to be located in a region with moderate earthquake hazard. Analysis matrices for the parametric evaluation of rocking frame parameters were developed.

Chapter 6 presented the results the parametric study of the prototype frames. All frames were analyzed using both the FE model and the CFE, and the results were compared in a series of plots and tables. These results indicate that the CFE and the FE are, in general, in excellent agreement. The largest discrepancies occur in the prediction of the drift at PT bar fracture, with the CFE providing a conservative estimate of the drift as compared with the FE model. This is attributed to the small deformations assumptions used in the derivations of the CFE.

Chapter 7 develops the FE model and conducts the dynamic analysis of selected prototype frames. The finite element model in this chapter is an update of a previous model used to study the rocking steel frames. The original model was updated to include the modeling of the spring stack and the clamping mechanism associated with it. In contrast to the FE model developed in Chapter 4, this FE model includes the elastic deformations of the rocking frame. However, it continues to exclude possible damage to the rocking frame (i.e. the frame remains elastic). Chapter 7 also compares the results of selected prototype frames subjected to a set of ground motions. The goal was to examine how the spring stack influences the dynamic response. This chapter is divided into two parts. The first part presents the time history response of selected frames to the Hector Mine earthquake. The second part lists the peak responses of selected frames to the entire set of ground motions.

1.2 CONCLUSIONS

1.2.1 Static pushover analysis

1. Disc springs provide a flexible way to attain various force-deformation responses by combining multiple springs differently.
2. The literature shows that using a spring element connected in series with the PT bars can be used to reduce the PT loss associated with time dependent deformations like creep and shrinkage.
3. The closed form expressions derived in Chapter 3 display an excellent agreement with the FE results. The largest errors are for drift at bar fracture at large drifts because the CFE were simplified using the small deformation theory.
4. Even though a rocking frame has constant member dimensions and PT steel area, connecting the PT steel in series with a spring stack having variable stiffness can be used to modify the backbone curve under lateral loads.
5. The use of a flexible disc spring stack connected in series with the PT steel increases the drift capacity and delays the onset of the PT steel yielding.
6. The use of a flexible disc spring stack causes the prototype frames to have low lateral stiffness after the gap opening (DEC limit state) at the base. In contrast, the use of stiff disc spring stack increases the lateral stiffness after the gap opening.
7. When the PT steel was extended to the roof of the prototype frames, some frames displayed large drifts without reaching the nominal moment capacity of the frame (i.e. PT steel yielding). The parametric study showed that limiting the height of the PT bars to only the first floor instead of the roof would reduce the lateral drift at yielding of the PT bars. This observation suggests that the use of spring stacks

could eliminate the need to extend the PT bars to higher floor levels. This offers two possible advantages to explore in design: (1) In a standard rocking frame with full height post-tensioning, all the structural elements of columns and braces below the anchorage point of the PT bars must be designed to accommodate the large PT force that develops during the application of the lateral load. However, limiting the height of the PT bars to, for example, the first floor would eliminate the need to design the elements above the first floor for these larger forces; (2) Limiting the PT bars to lower stories would require less total length of PT bars.

8. When the spring stack has finite travel capacity, clamping can occur leading to increase in the lateral stiffness and sudden increase in PT steel force.

1.2.2 Dynamic Analysis

1. The dynamic analyses show that the use of disc spring stacks alters the dynamic response of rocking frames.
2. Rocking frames with flexible spring stacks in general develop less peak PT force during the ground motions.
3. Rocking frames with flexible spring stacks with maintain a higher residual force in the PT bars after an extreme seismic event as compared to rocking frames with relatively stiffer spring stacks. For the rocking frames and ground motions treated in this study, the frames with γ_k=0.2 (i.e. flexible spring stack) never experienced yielding in any of the ground motions.
4. The dynamic analyses demonstrate that the moment hysteresis loop for a frame with γ_k=0.2 (flexible spring stack) is likely to be flat after the frame

decompression, while the hysteresis loop of a frame with γ_k=2.0 (stiff spring stack) is steeper under the same circumstances.

5. The clamping of the spring stack during the ground motions caused a sudden increase in the PT force. Correspondingly, the moment hysteresis loop of frames where the spring stack clamped during the dynamic response has shown to gain lateral stiffness after clamping.

8.3 FUTURE WORK

Suggestions for future work include the following:

1. Additional design studies to more fully investigate the use of spring stacks in rocking wall assemblies.
2. Experimental studies (quasi-static pushover and dynamic tests) of rocking wall assemblies with flexible spring stacks.
3. Consideration of the use of replaceable energy dissipation devices.
4. Creep studies of rocking walls with flexible spring stacks.
5. Constructability studies of rocking walls with flexible spring stacks.

REFRENCES

"Spirol Disc Springs.", 2017 accessed 03/11, https://www.spirol.com/library/main_catalogs/SPIROL-Disc-Springs-us.pdf.

Timber Construction Manual 2012., edited by American Institute of Timber Construction. sixth ed. Wiley.

Accorsi, M. L. and Edward F. S. 1990. "Prestress Level in Stress-Laminated Timber Bridges."

Ceccotti, A., Sandhaas, C., Okabe, M., Yasumura, M., Minowa, C., & Kawai, N. (2013). SOFIE project–3D shaking table test on a seven-storey full-scale cross-laminated timber building. Earthquake Engineering & Structural Dynamics, 42(13), 2003-2021.

Chancellor, N. B., "Seismic Design and Performance of Self-Centering Concentrically-Braced Frames" (2014-a). *Theses and Dissertations*. 1705. http://preserve.lehigh.edu/etd/1705

Chancellor, N. B., Matthew R. Eatherton, David A. Roke, and Tuğçe Akbaş. 2014-b. "Self-Centering Seismic Lateral Force Resisting Systems: High Performance Structures for the City of Tomorrow." *Buildings* 4 (3): 520-548.

Haselton, Cahrles K. "ATC-63 Far-Field Ground Motion Set.", http://www.csuchico.edu/structural/researchdatabases/ground_motion_sets.shtml.

Gavric, Igor, Massimo Fragiacomo, Marjan Popovski, and Ario Ceccotti. 2014. "Behaviour of Cross-Laminated Timber Panels Under Cyclic Loads." In *Materials and Joints in Timber Structures*, 689-702: Springer.

Kurama, Y. C. 1997. "*Seismic Analysis, Behavior, and Design of Unbonded Post-Tensioned Precast Concrete Walls.*" Dissertation.

De Borst, R., Crisfield, M. A., Remmers, J. J., & Verhoosel, C. V. (2012). Nonlinear finite element analysis of solids and structures. John Wiley & Sons.

Mazzoni, Silvia, Frank McKenna, Michael H. Scott, and Gregory L. Fenves. 2006. "OpenSees Command Language Manual." *Pacific Earthquake Engineering Research (PEER) Center*.

Naraine, K., & Sinha, S. (1989). Behavior of brick masonry under cyclic compressive loading. *Journal of Structural Engineering*, *115*(6), 1432-1445.

Sarti, Francesco, Alessandro Palermo, and Stefano Pampanin. 2016a. "Quasi-Static Cyclic Testing of Two-Thirds Scale Unbonded Posttensioned Rocking Dissipative Timber Walls."

Sause, R., Ricles, J. M., Roke, D. A., Chancellor, N. B., & Gonner, N. P. (2010, July). Seismic performance of a self-centering rocking concentrically-braced frame. In Proceedings, 9th US national and 10th Canadian conference on earthquake engineering. Toronto, Ontario, Canada.

Srivastava, Sonam, "Analytical Lateral Load Response of Unbonded Post-Tensioned Cast-in-Place Concrete Special Structural Walls with Bonded or Debonded Longitudinal Mild Steel Reinforcement" (2013). *Theses and Dissertations*. 1115. http://preserve.lehigh.edu/etd/1115

Shigley, J. E., & Mischke, C. R. 1996. *Standard Handbook of Machine Design*. 2nd ed. McGraw-Hill.

Pessiki, S. (2017). *Sustainable Seismic Design*. Procedia Engineering, 171, 33-39.

Perez, Felipe J.; Pessiki, Stephen; and Sause, Richard, "Experimental and Analytical Lateral Load Response of Unbonded Post-Tensioned Precast Concrete Walls" (2004). *ATLSS Reports*. 45.

APPENDIX A

A.1.1 FRICTION OF THE SPRING STACK

As explained in Chapter 2, the disc spring stack has hysteretic behavior under cyclic loadings. Though, modeling the hysteretic behavior as a friction damper and using the friction coefficients given on the DIN 2092 (Schnorr, 2003) standards showed that such small friction of the spring stack does not significantly affect the dynamic response.

However, it worth mentioning that the values of friction given in the DIN standards are for spring stack that is lubricated to reduce friction and we expect the more friction to develop if no lubricant is present.

Our goal here will be to convert the area under the hysteresis loop of the spring stack to an equivalent column friction damper that can dissipate the same energy using the following steps.

- Find the hysteresis area under one cycle of force-deformation of the spring stack.
- Equate this area to a friction damper based on Coulomb model as seen in Equations A.1, A.2, A.3, A.4, and A.5.
- Now the friction damper dissipates the same amount of energy as the original spring stack as shown in in Figure (A.1).

$$\int_0^u (F_{sl} - F_{su})\, du = \int_0^u 2\, Fn\, du \tag{A.21}$$

$$F_{su}, F_{sl} = ks\, u \left(\frac{1}{1 \pm \mu m(n-1) \pm \mu r} \right) \tag{A.22}$$

$$\int_0^u ks\ u\ (\frac{1}{1-\mu m(n-1)-\mu r}-\frac{1}{1+\mu m(n-1)+\mu r})\ du=\int_0^u 2\ Fn\ du \quad \text{(A.23)}$$

$$ks\frac{u^2}{2}\left(\frac{1}{1-\mu m(n-1)-\mu r}-\frac{1}{1+\mu m(n-1)+\mu r}\right)=2\ Fn\ u \quad \text{(A.24)}$$

$$Fn=\frac{1}{4}\ ks\ u\left(\frac{1}{1-\mu m(n-1)-\mu r}-\frac{1}{1+\mu m(n-1)+\mu r}\right) \quad \text{(A.25)}$$

In Equation A.5, We can introduce the assumption that the amplitude of motion of the friction damper is equal to the travel capacity of the spring stack. However, a significant error would be introduced leading to large damping in the FE model especially if the amplitude of motion is less than the travel capacity. Even with the introduction of this error, the difference between the response would still be negligible as shown in Figure A.2.

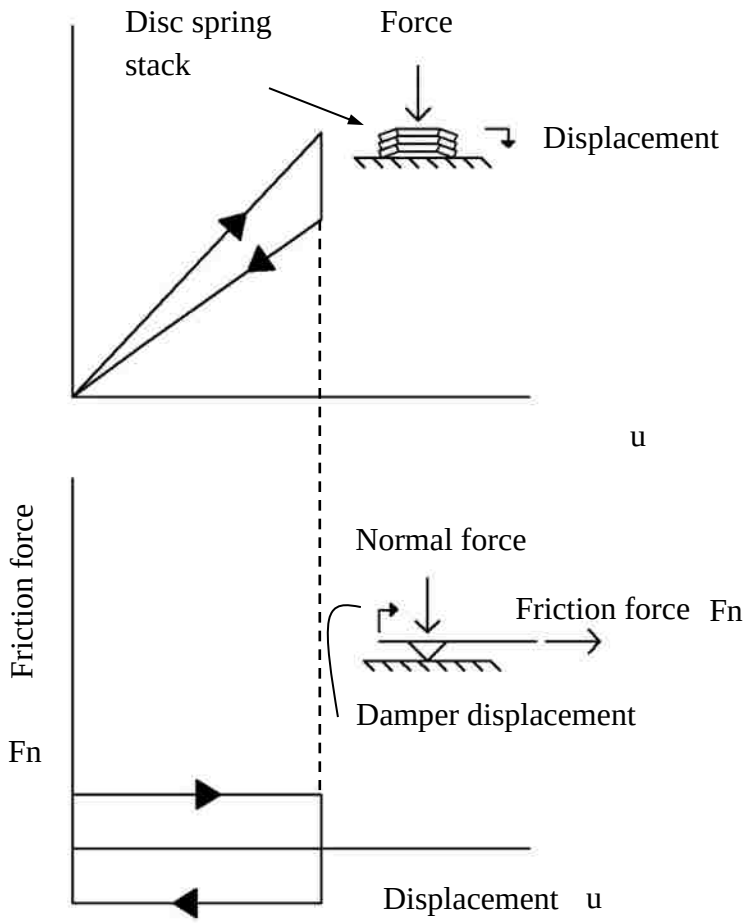

Figure A.1: Equating the energy dissipation of a single disc spring into an equivalent friction damper.

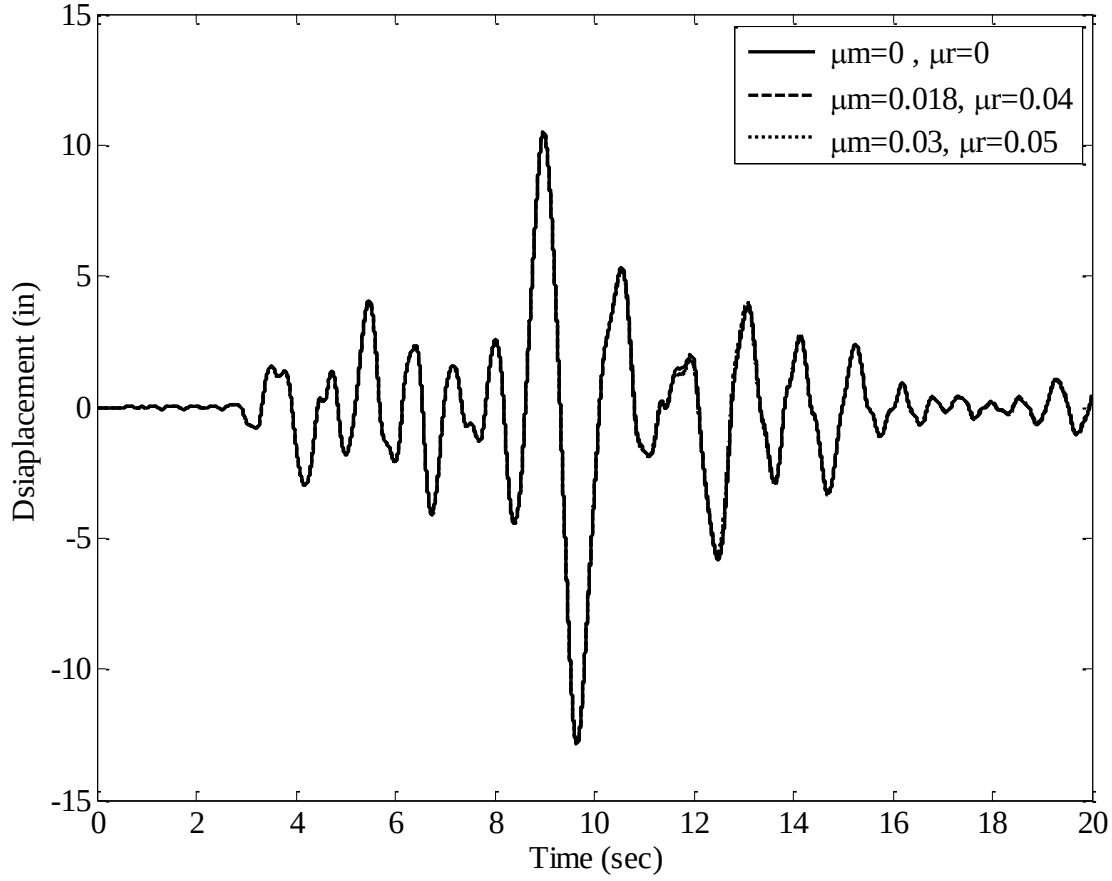

Figure A.2: Response under NORTHR/MUL009 earthquake for three cases: (a) no friction (μm=0, μr=0); (b) moderate friction (μm=0.018, μr=0.04) ; (c) and high friction (μm=0.03, μr=0.05).